Active Fluidic Control of a Cylinder in a Cross-Flow Using Synthetic Jet Actuation

Diarmuid Jackson

Department of Mechanical & Manufacturing Engineering

Parsons Building

University of Dublin, Trinity College

Dublin 2

Ireland

June 2016

A thesis submitted to the University of Dublin in partial fulfillment of the requirements for the degree of Ph.D.

Declaration

I declare that this thesis has not been submitted as an exercise for a degree at this or any other university and it is entirely my own work.

I agree to deposit this thesis in the University's open access institutional repository or allow the library to do so on my behalf, subject to Irish Copyright Legislation and Trinity College Library conditions of use and acknowledgement.

Diarmuid Jackson, June 2016

Abstract

The objective of this body of work is to establish the effectiveness of a simple synthetic jet actuator in modifying the drag forces experienced by a cylinder in a cross flow. This is achieved through the production of a virtual hydrodynamic wake structures, using a precisely controlled positioning system, high frequency strain measurements, flow visualisation (FV), high resolution whole field velocity, turbulence intensity and vorticity measurements through the use of particle image velocimetry (PIV). This is achieved using a circular cylinder in cross-flow with an embedded synthetic jet actuator (SJA) with a span-wise rectangular orifice (slot width = 0.05 cylinder diameter). Previous studies have investigated the effects of SJAs on producing a virtual hydrodynamic profile in the lee of a cylinder for a limited range of circumferential positions, and this study intends to cover a more comprehensive range of circumferential positions and determine the optimum operating conditions for drag reduction. A 20 mm diameter cylinder was placed in a cross-flow in a 400×120 mm test section of a closed loop water tunnel, with a Reynolds number in the subcritical flow regime, which corresponds to a well conditioned low turbulence flow, with minimal turbulence intensity and wall effects in the approaching flow. A span-wise finite-span synthetic jet orifice (0.05 x 2 cylinder diameters) is embedded in the cylinder. As the near field effects of a SJA on a cross flow is strongly influenced by velocity ratio of the free stream velocity to the orifice velocity during the expulsion stroke, the tests are carried out by maintaining a constant cross-flow velocity, while varying the velocity ratio. The circumferential location of the synthetic jet actuator can be continuously adjusted between 0 and 180 degrees, positioning the actuator upstream, inside and downstream of the separation zone, as well as facing directly up-stream and down-stream. The effects of varying velocity ratio over a series of cylinder angles on lift and drag forces was characterised using strain gauges to give force values. This allowed for

the creation of a map of effect, establishing the most effects SJA conditions to produce the maximum drag modification.

Flow visualisation (FV) is used on a selection of different SJA conditions, based on their ability to modify drag over either a consistent range of frequencies or to produce sudden spikes in drag modification. These are selected to identify the vortical structures responsible for modifying the wake. It was found that the SJA alters significantly the wake structures by the suppression of and / or altering the distance of roll-up of naturally forming vortices. In the case of drag increase, the formation distance is reduced, increasing wake oscillations, producing a larger pressure drag. In the case of drag reduction two primary profiles are identified; Type I supresses completely the natural formation of shedding vortices, with only a counter clock-wise vortex being formed by the SJA, that entrains high-energy fluid directly from the cross-flow, producing a highly turbulent asymmetric wake structure. Type II partially supresses the formation of naturally occurring vortices, instead producing a self sustaining wake structure that is not reliant on the direct entrainment of fluid from the cross-flow.

Particle image velocimetry measurements are carried out in the mid-plane to characterise and establish how the virtual hydrodynamic profile identified by FV interacts with the fluid streams passing over the cylinder. The virtual profiles allow for a controlled pressure recovery, capable of reducing drag by up to 20%, and substantially reducing the far-wake thickness and turbulence. This work presents an important building block in the production of a simple, robust, low-frequency fluidic control system that is capable of reducing drag and the effective length of a wake.

Acknowledgements

This thesis wouldn't have been possible without all the support I was given by the people around me. First and foremost I would like to thank my supervisor Dr.Tim Persoons for not only his continuous support, and guidance throughout my thesis, but also for bestowing upon me the honour of being his first Ph.D. student.
The second person I would like to thanks is Gordon O'Brien who without his practical knowledge it wouldn't have been possible to have constructed such an ambitious experimental setup.

A big thanks Mick Reilly, all the staff in the workshop and Gerry Byrne for the unbelievable amount of help and advice they have given me.

Over my time in the Parsons building, I was lucky to have been able get to meet some truly wonderful people. So a big thanks to Gerald, Seamus, Rudy, Jason, Eleonora, Richard, Maurice, Maeve, Sajad, Greg, Patrick, Guibing, Michael, Eoin and Kate for making my time at Trinity so special.

To my family I am ever grateful. To my father for constantly reading over my work, which was no small feat. To my mother for her constant advice, support, and many many lifts. last but not least I'd like to thank my wonderful girlfriend Simona for putting up with me incessant talking abound my work, and for always pretending to listen.

Contents

List of Figures

List of Tables

Nomenclature

ΔP	Pressure loss	$[Pa]$
$\overline{U}_O$	Average jet velocity	$[m/s]$
A	Area	$[m^2]$
A_{in}	Inlet area	$[m^2]$
A_{out}	Outlet area	$[m^2]$
A_{SJA}	Area of the orifice	$[m^2]$
D_d	Hydraulic diameter	$[m]$
d_P	Seeding particle diameter	$[m]$
D_{cyl}	Cylinder diameter	$[m]$
f	Frequency	$[Hz]$
F_D	Drag force	$[N]$
F_L	Lift Force	$[N]$
f_{SJA}	Synthetic jet actuator frequency	$[Hz]$
L	Characteristic length	$[m]$
L_c	Characteristic length of separation region	$[m]$
L_{cyl}	Characteristic diameter of the cylinder	$[m]$
L_{SJA}	Synthetic jet actuator stroke length	$[m]$
M	Mass	$[Kg/m^3]$
P	Pressure	$[Pa]$
P_w	Wetted perimeter	$[m]$
P_{dyn}	Dynamic pressure	$[Pa]$

Q_{pump}	Volumetric flow rate of water pump	$[m^3/s]$
Q_{SJA}	Volumetric flow rate of synthetic jet actuator	$[m^3/s]$
t	time	$[s]$
U	Relative velocity	$[m/s]$
U_O	Average orifice ejection velocity	$[m/s]$
U_p	Particle velocity	$[m/s]$
U_δ	Velocity within the boundary layer	$[m/s]$
U	Free-stream velocity	$[m/s]$
U_{max}	Maximum orifice ejection velocity	$[m/s]$
V	Volume	$[m^3]$
v	Local particle velocity	$[m/s]$
x	Distance along the chord	$[m]$
y	Normal distance from the surface	$[m]$

Dimensionless Numbers

σ_ε	Standard deviation	[-]
D_O/δ_{st}	Nominal thickness of Stoke layer	[-]
H_0/D_O	Orifice depth-to-diameter ratio	[-]
k_{SJA}	Usable area of the diaphragm	[-]
N_V	Number of vanes	[-]
N_{samp}	Number of samples	[-]
r_V	Vane radius	[-]
Re_{cr}	Critical Reynolds number	[-]
W_V	Vane width	[-]
ε_O	Sharpness of orifice exit, $\varepsilon = R/D_0$	[-]
C_D	Drag coefficient	[-]
C_F	Friction coefficient	[-]
C_L	Lift coefficient	[-]
C_p	Pressure coefficient	[-]

F^+	Dimensionless actuation frequency, $F^+ = f_{act}L/U_\infty$	[-]
K_d	Loss coefficient	[-]
K	Jet formation Constant	[-]
L_0/D_O	Dimensionless stroke Length	[-]
Re_{cyl}	Cylinder Reynolds numbers	[-]
Re_{SJA}	Synthetic jet Reynolds numbers	[-]
Re	Reynolds number	[-]
Sr	Strouhal number, $Sr = fD_H/\overline{U}_O$	[-]
St	Stokes number, $St = \sqrt{2\pi f {D_H}^2/\nu}$	[-]
V_R	Velocity ratio of U to U_O	[-]

Greek Symbols

α	Angle of attack	[*Degrees*]
α_{SJA}	Synthetic jet orifice angle	[*Degrees*]
$\Delta\rho$	Density difference	$[kg/m^3]$
δpx	Pixel displacement	[m]
δt	Time between interrogation windows	[s]
δ	Boundary layer thickness	$[m]$
Δ_p	Particle displacement	$[m]$
δ_t	Boundary layer thickness	$[m]$
δ_y	Distance from wall	$[m]$
ε_{st}	Stokes layer thickness	[m]
ε_{st}	Thickness of the Stokes layer	$[m]$
μ	Dynamic viscosity	$[kg/ms]$
ν	Kinematic viscosity	$[m^2/s]$
Ω	Thickness of the Stokes layer	[m]
ρ_f	Density of fluid	$[kg/m^3]$
ρ_p	Density of seeding particles	$[kg/m^3]$
σ	Surface tension	$[N/m]$

ϑ	Order of magnitude	[-]

Subscripts

∞	Bulk or infinity	[-]
cl	centerline	[-]
SJA	Synthetic jet actuator	[-]
s	separated region	[-]

Chapter 1

Introduction

Currently the world is looking towards greener energy conservation, and conversion systems to reduce fossil fuel-based systems. The International Energy Agency (IEA) predicts that massive investments in renewable power generation systems will be needed to reach their targeted Blue Map emission strategy by 2050, covering a wide range of technologies. In order to achieve this, renewable energy industries need to maximize their energy capture albites [20]. Some of the main issues facing renewable energy industries such as turbine farms include flow-induced vibrations, reduction of the large drag forces acting on structures, as well as decreasing the wake effects and interaction between adjacent turbines. One method of helping to achieve this goal is thought better fluidic control. Fluidic control (or flow control) is a fairly new technology that is one of the most pursued topics in the fields of fluid mechanics [21], as it allows a fluid to be altered from its natural flow state to a desired flow state, through the control of how a fluid traveling over an object. In structures such as wind a tidal turbine, the fluid forces cause structural failure through material fatigue and sudden excessive loading (Fig. 1.1), as well as large wake structures, limit the quantity of devices per area [22].

In regards to transport it results in high levels of drag that result in higher fuel cost. Lee *et al.* [23] described fluidic control as the production of a beneficial change in the boundary layer or free shear flows, with useful end results such as drag reduction, lift enhancement, mixing augmentation and flow induced noise suppression. As such fluidic control techniques focused mainly on mitigating flow separation through methods such as preventing adverse

Figure 1.1: Wind turbine in Wyoming that failed due to find loading [1]

pressure gradients or through the removal of sharp discontinuities in the flow boundary [24]. This is normally achieved thought passive or active fluidic control systems. Passive fluidic control is taken to be a system that is always present through all fluidic conditions and is normally a part of the designed or an addition to help improve flow efficient over a specific range of flow condition. However, this results in an effect being present at all times, resulting in possible efficiency reductions outside of the operating conditions. Lee *et al.* [23] describe active flow controls as the multi-disciplinary research area combining sense, actuation, flow physics and control with the objective of modifying flow fields characteristics to achieve a desired aerodynamic performance. Active flow control techniques are a relatively new technology that are becoming increasingly more popular due to their ability to, unlike passive systems alter the natural flow state into a desired flow state over a large range of flow conditions, while not causing negative effects when the system is operating outside of its operating parameters [21] ,[25]. Active fluidic control is achieved as active by leveraging and controlling the natural stability of a flow to obtain large effects with minimal input, and these effects are able to be removed when conditions are such that it is not desired that they be active. Active controls come in many forms, from large complex systems such a gears to tilt a turbine blade or thought small devices such as a synthetic jet actuator (SJA). Synthetic

jet actuators have started to become a major technology of significant interest in active flow control. Synthetic jets work by time periodic actuation and so allow for coupling of boundary layer instabilities at the separated region or the near wake to produce acoanda like attachment of the flow or at high reduced frequencies can completely prevent separation from taking place. It was found by Tensi *et al.* [26] that an optimized synthetic jet embedded in a cylinder could reduce the coefficient of drag by up to 30%.

Synthetic jets also have the advantage of not requiring piping systems to be installed as they are actuated using the surrounding fluid. They have a very simple design consisting of a chamber with an orifice and an oscillating diaphragm. For this reason they have become an attractive technology that can be easily embedded within the surface without needing any significant modifications to the body. The ability to match the frequencies of the jet to the cross flow has led to their use as flight controls. [27] placed synthetic jet actuators along the leading edges of a stingray U.A.V to control the pitch and roll at low angles of attack. The research of synthetic jets is still at an early stage with a lot of practical issues still to be determined and improved. [24], [25], [21].

The current research using synthetic jet actuators (SJA) for active fluid control hope to lead to more adaptive and cost-effective alternatives to existing fluidic control technologies currently in use for renewable power generation devices, which primarily offer a more crude control in response to variable flow conditions, such as the use of complex gear drives and motors to affect blade pitch, or complex surface geometries to attempt to reduce drag under certain operating conditions. For example, truck trailers being designed to reduce drag when traveling at a specific speed [28]). These existing systems are difficult to implement, add significantly to capital and maintenance costs and tend to operate optimally only under a limited range of conditions. By contrast, there are local active flow control methods under investigation that can offer much greater flexibility

1.1 Aims and objectives of the research

The main objective of this thesis is to determine the effect that a synthetic jet actuator embedded within a cylinder has on the drag forces experienced by the cylinder in a cross-flow. This will be done using an embedded finite span synthetic jet, to alter the flow condition around a cylinder through vortical interaction. Tests will be performed at a constant cylinder Reynolds number, with the synthetic jet actuator dimensionless stroke length, velocity ratio, and the jet orifice angle being modified.

The reason for selecting three different parameters was to build a map of synthetic jet effects over a large range of conditions. 192 separate jet conditions were looked at for this thesis, and as such it required that testing allowed for simple analysis of a large range of parameters and an increasingly more detailed analysis of the most interesting cases analysed.

This will be achieved by using a simple system to driving the synthetic jet that relies on reciprocal motion (which is similar to sinusoidal motion), aimed at producing a more practical method of actuation. This thesis will be using a water tunnel to get (i) better quality PIV images, and (ii) higher (i.e. more easily measured drag forces) drag forces.

Strain gauges will be used to directly measure the lift and drag forces acting on the cylinder, allowing for both instantaneous and average force measurements to be taken. Giving a map of the effects of a synthetic jet on the drag and lift forces, showing how potentially effective the synthetic jet is at modifying the forces.

When the jet force effects have been determined, the next aim will be to establish how this effect is achieved for a variety of conditions from drag increase to decrease. This is to be achieved using high-speed imaging.

The most interesting jet conditions from flow visualisation will be investigated using particle image velocimetry. Particle image velocimetry will be used measure flow velocity fields around the cylinder and the quantify how these are affected by the synthetic jet. It will

also be to establish the shape of the virtual hydrodynamic structure produced, and to then understand how it alter the flow around the cylinder to behave more like that of a simple aerofoil. This will be done by looking at the wake in terms of average velocity, average vorticity, and average turbulence intensity.

1.1.1 Outline of this thesis

Chapter 2 is a comprehensive literature review of the most important works relating to the understanding of synthetic jets actuators in terms of fluidic control over a cylinder. Chapter 3 lays out the large amount of equipment that had to be designed and built to the highest quality, on a limited budget, in order for this project to be possible. Chapter 4 describes the basis of the experimental work undertaken in the project and the basic test to characterise the water tunnel, the SJA actuator and all of the peripheral equipment used in testing. From this chapter the basic result for a cylinder in a cross flow and the synthetic jet actuating into a quiescent fluid are presented.

Chapters 5, 6, and 7 are the experimental chapters of this thesis, with each chapter focusing on an individual type of test. These chapters work as a refinement process, with chapter 5 looking a broad range of results, concentrated on identifying the affect that a synthetic jet has on the drag and lift forces experienced by the cylinder in a cross-flow. From this analysis it was possible to select was possible to select the most interesting results to look at in more detail using flow visualisation. Chapter 6 used flow visualisation to look in more depth at the effects of a synthetic jet actuator on the boundary layer and wake. Flow visualisation test allowed for the further refinement of test setups to be looked at using particle image velocimetry.

Chapter 7 examined the time average flow over the cylinder in terms of average velocity, average turbulence intensity, and average vorticity. Chapter 8 discusses the three experimental as one, and chapter 9 outlines the major conclusions of the thesis.

Chapter 2

Literature Review

2.1 External flow over submerged bodies

2.1.1 Flow over a flat plate

In the instance of fluid flow over a flat plate, it is possible to assess shear and pressure drag forces independently. In the case of a flat plate, parallel to the flow the drag produced is a result of shear forces only. Drag produced by the wall shear force τ_w and is independent of Pressure drag as $\theta = 90$. Conversely when the plate is positioned normal to the flow, drag is independent of skin friction as $\theta = 0$. Flow over a flat plate parallel to the flow is used to show the evolution of a boundary layer transitioning from laminar to transitional and finally to turbulent. If the x-axis is taken as the measurement along the surface of the plate from the leading edge in the direction of flow and y-axis as being the distance normal to the surface, δ as the boundary layer thickness, U_∞ as the free stream velocity, U is the x-component of the fluid velocity. The flow is assumed to be built up of layers adjacent to the surface. Due to the no-slip condition the fluid layer directly in contact with the surface will have a zero velocity, this fluid layer slows down the fluid molecules in the next layer and so on until at some distance δ where the effects are no longer felt and the free stream velocity returns to normal. As a result the U bounded by δ varies along the x-axis from $U = 0$ at $y = 0$ to near $U = U_\infty$ at y = δ. At y = δ it is usually assumed that $U = 0.99U_\infty$.

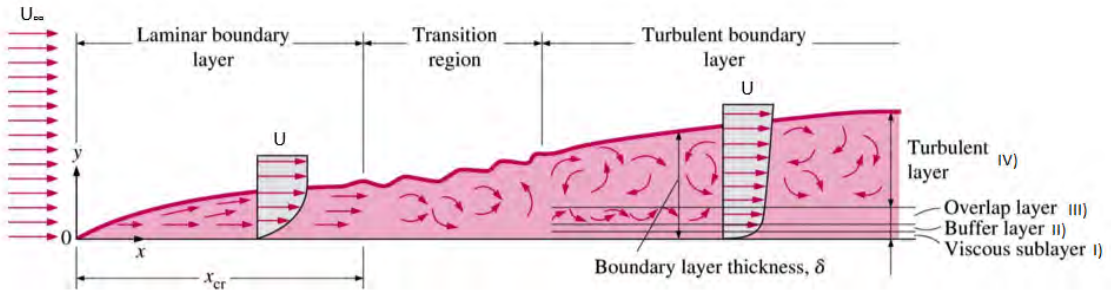

Figure 2.1: Flow over a flat plate [2]

The velocity profile in the turbulent flow has a slight change in velocity over its length encapsulated within the boundary layer except for a sharp drop in velocity near the surface, in comparison to the laminar flow, which has a more pronounced velocity change within the boundary layer. To better understand these differences, the turbulent flow regime can be split into four layers normal to the surface: I) the *Viscous sub layer* is a thin layer closest to the surface dominated by viscous forces, it has an almost linear velocity profile with nearly parallel flow. II) The *buffer layer* above the viscous layer is still primarily dominated by viscous effects, where turbulent effects are becoming more significant. III) the *Overlap layer* in which viscous effects are not yet dominant, but are more significant than that of the buffer layer, and IV) the *Turbulent layer* which spans the rest of the boundary layer where turbulent effects are dominant. [2], [29]

2.1.1.1 Frictional effect on a flat plate

As a flat plate is only subject to frictional drag, the drag coefficient is therefore equal to the frictional drag coefficient.

$$C_D = C_{D,Friction} = C_F \tag{2.1}$$

For laminar flow over a flat plate the C_F can be determined theoretical by solving numerically the linear momentum and the conservation of mass equations. This is not possible for a turbulent flow which must be determined though experimental testing and expressed by empirical correlations ([2]). In the case of the flat plate the drag forces can be looked at for the entire length using and *average friction coefficient* or for a specific location

using a *local friction factor*. In order to obtain the Average drag coefficient (Eq. 2.2) on a flat plate with enough length for turbulence to develop, but not long enough to be able to ignore the laminar layer, it is necessary to obtain the friction coefficient for both the laminar and turbulent regions.

$$C_F = \frac{1}{L}\int_0^{X_{cr}} C_{F\,x\,Laminar}\,dx + \int_{X_{cr}}^{L} C_{F\,x\,Turbulent}\,dx \tag{2.2}$$

The laminar region is taken from $0 \leq \mathrm{x} \leq x_{cr}$ and the turbulent region is $x_{cr} < x \leq L$. The transitional region is included within the turbulent region. By integrating the above equation and taking $Re_{cr} = 5x10^5$ give the average friction coefficient:

$$C_F = \frac{0.074}{Re_l^{1/5}} - \frac{1742}{Re_l}\, 5x10^5 \leq Re_l \leq 10^7 \tag{2.3}$$

2.1.1.2 Reynolds number on a flat plate

The point at which a flow over a flat plate will go form laminar to turbulent is dependent on the surface roughness, geometry, free stream velocity, and the properties of the fluid. The Reynolds number is used to determine flow regime:

$$Re = \frac{Inertial\,Forces}{Viscous\,Forces} = \frac{\rho U_\infty L}{\mu} = \frac{U_\infty L}{\nu} \tag{2.4}$$

Where Re is Reynolds number, ρ is the density, L is the characteristic linear dimension, μ is the dynamic viscosity, ν is the kinematic viscosity, and U_∞ is the velocity of fluid relative to the object
It is taken that for a flow going over a smooth flat plate the flow regime transitions from laminar to transitional at an Re $\cong 1x10^5$ and then to fully turbulent at a critical Reynolds number ($Re_x cr\%$) $\cong 3x10^6$.

2.1.2 Flow over a curved plate

The effects of separations can be clearly shows on a curved plate of zero thickness such as in figure 2.2, where at point A the velocity profile normal to the surface is zero due to the no-slip condition. This area of high pressure is known as the stagnation point. The boundary layer begins to grow as flow moves away form A. The flow moving through points B and C

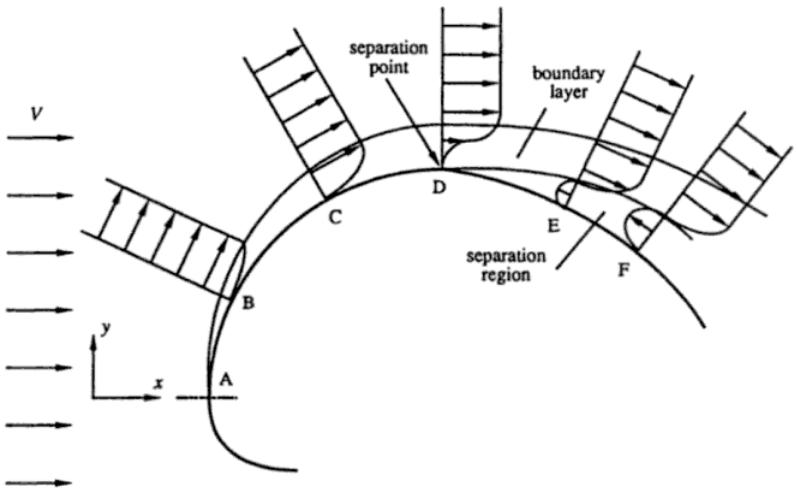

Figure 2.2: Flow over a curved plate [2]

transitions from laminar to turbulent. On passing point D there is a marked change in the velocity profile, where a steep (almost vertical) velocity profile has expanded to roughly 0.5δ. At this point the flow close to the surface has almost come to a complete stop, the boundary layer has grown significantly, and is losing its ability to remain attached to the surface. Between points D and E the flow has separated, forming a sheer layer that resulting in a area of low pressure between the surface and the boundary layer. At point E the velocity profile shows an adverse pressure gradient through the presence of a back flow, where $dP/dx > 0$. Separation produces a negative effect on both the lift and drag acting on the body.

2.1.3 Flow over a cylinder

At a low Reynolds number (Re $\lesssim 1$) a cylinder is affected by pressure and viscous drag, where it is completely enclosed by the fluid. As Reynolds number increases the fluid no longer remains fully attached, separating from the downstream face, leading to the formation of a separating region of adverse pressure and the periodic formation, and shedding of eddies. The nature of the flow across the cylinder has a direct effect on the total drag coefficient, as both the pressure and frictional drag can be of a significant value. At Re $\lesssim 10$ frictional drag is dominant and at high RE $5x10^3$ pressure drag is dominant. Figure 2.3 shows the effect that Reynolds number has on the drag coefficient over a cylinder. In general, the lover the Reynolds number the higher the drag coefficient. However, it should be noted that between a

Reynolds number of 10^3 and 10^5 there is an area of increased drag coefficient, at this point the flow in the boundary layer is laminar over the cylinder, with a turbulent separated flow producing a wide turbulent wake.

For the region of $10^5 \lesssim \mathrm{Re} \lesssim 10^6$ there is a sudden drop in C_D due to the laminar boundary layer becoming turbulent. This in turn moves the separation closer to the tail end of the cylinder reducing the wake and so reducing the pressure drag. This transitional phase lasts from about $2x10^5 \lesssim \mathrm{Re} \lesssim 2X10^6$ where C_D drops to a minimum, after this point it rises to its final turbulent point. [2], [29], [19]

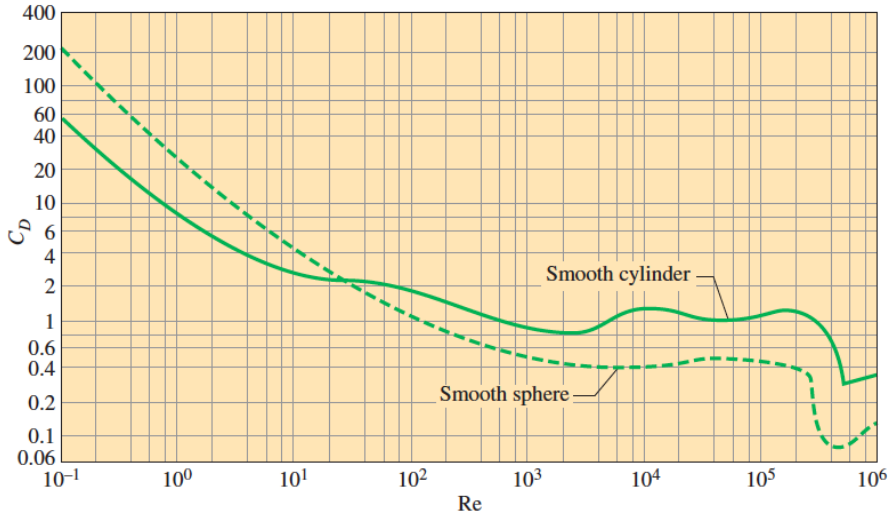

Figure 2.3: Effect of Reynolds number on drag coefficient over a smooth cylinder [2]

2.1.4 Flow over an Aerofoil

An aerofoil is a streamlined body, which benefits from a reduction in pressure drag due to a smaller wake compared to a bluff body. This reduction is at the cost of an increase in frictional drag due to an increase in surface area. Thus in order to optimise total drag reduction the sum of both forces must be calculated. Figure 2.4 shows that the length and thickness of a streamlined shape has a direct effect on the total drag produced. If the aerofoil is to rounded it will behave more like a cylinder suffering primarily with pressure drag, where as if it is too thin it will behave more like a flat plate and primarily experience large amounts of frictional drag. An optimum value for the ratio of length to thickness need to be established

depending on the requirements of the aerofoil.[2], [29]

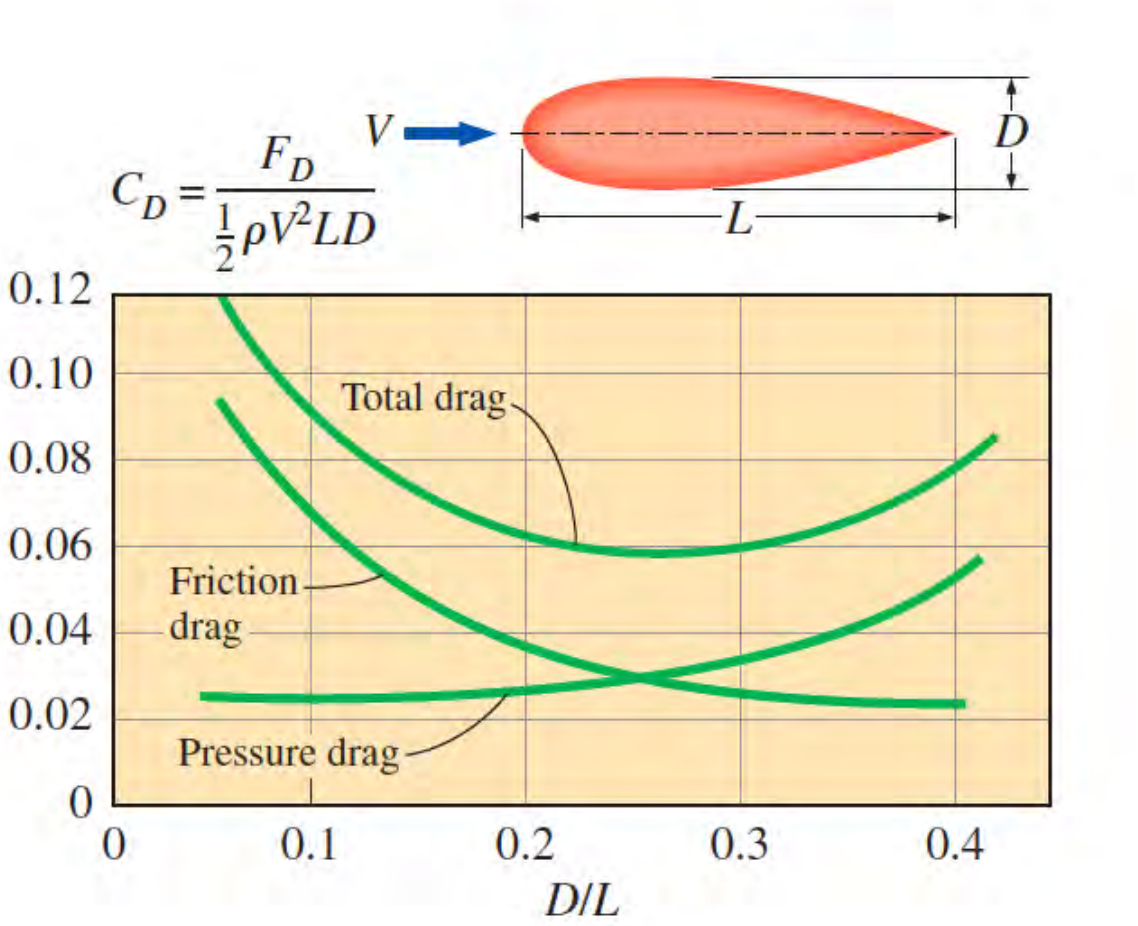

Figure 2.4: The effect of the ratio of thickness to chord length on total drag over an aerofoil [2]

2.1.4.1 Drag and lift forces

Lift is the net of the components of the pressure and wall shear forces acting normal to the flow. Drag is the force flowing fluid exerts on a body in the flow direction, figure 2.5 is a breakdown of the drag experienced by an aerofoil. [2]

$$C_L = F_L 1/2\rho U_\infty^2 A \tag{2.5}$$

For devices intended to produce lift the contribution of viscous effects to lift is ordinarily negligible due to streamlining, resulting in wall shear acting nearly perpendicular to lift as it is parallel to surface, so it can be taken that lift is the result of pressure distribution around

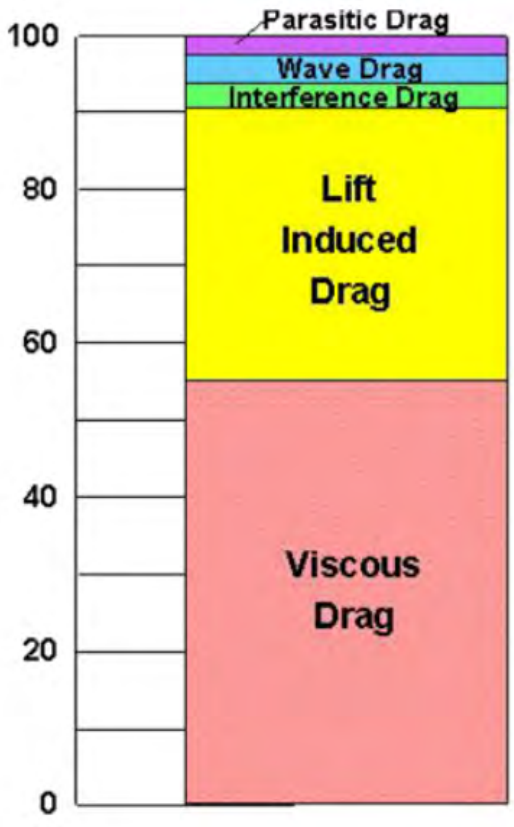

Figure 2.5: Example of total drag breakdown

the body. To maximise lift the average pressure must be minimised along the top side while maximise along the lower side. From Bernoulli's equation it is know that when velocity is high, pressure is low and vice versa. Bernoulli's can be used to determine the pressure across the surfaces. This would suggest that it is possible to ignore boundary layer separation in the estimation of the pressure distribution along the aerofoil, allowing a simple potential flow theory in which the net viscous forces along the aerofoil are zero.

Figure 2.6 shows the difference in lift between an symmetric and asymmetric aerofoil at zero angle of attack assuming *no* separation. The symmetrical aerofoil produces zero lift due to symmetry and the stagnation points being at the leading and trailing edges. The asymmetrical aerofoil at a slight angle of attack produces zero lift due to the initial stagnation point forming below the leading edge, and the rear stagnation point moving up along the upper surface. Experimentally this does not take place, as it is not possible for flow to turn 180^o around the trailing edge and still remain attached. The flow along the lower surface

separates and the flow along the top surface pushes the stagnation point down to the trailing edge. This results in the upper and lower flows meeting at this point, demonstrating that the lift generated by the wing is due to the pressure differential between the top and bottom surfaces. The flow along the top surface moves faster due to the clockwise offset of the stagnation point resulting in a clockwise circulation around the aerofoil, decreasing the velocity along the bottom surface.

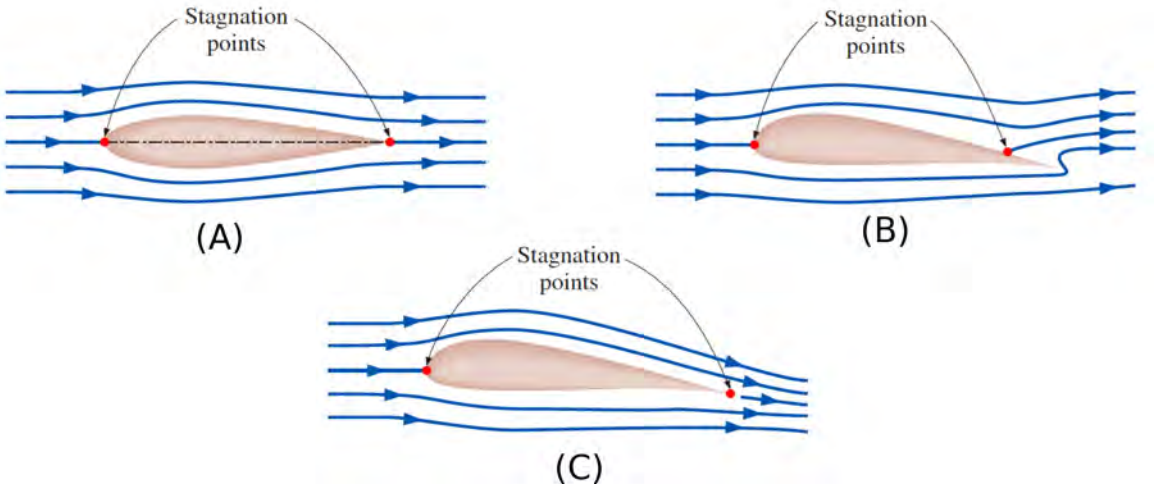

Figure 2.6: Irrotational and actual flow over an symmetric and asymmetric aerofoil: (A) irrotational flow over a symmetric aerofoil, (B)irrotational flow over an asymmetrical aerofoil, and (C) actual flow over an asymmetrical aerofoil [2].

In practical terms it is necessary when designing an aerofoil to produce maximum lift for minimal drag. A method to show how well an aerofoil preforms this is the lift-to-drag-ratio, which is equivalent to the ratio of lift to drag coefficients (C_L/C_D). This is obtained by either plotting for certain angles of attack the C_L against the C_D or by plotting the C_L/C_D versus the angle of attack as in 2.7(A). Using a NACA 64(1) a 412 aerofoil at an Re = $7x10^5$ we can see that as the angle of attach increases so the does the lift to drag ratio up to an order of 100, until stall is reached. Breaking lift and drag coefficients into separate components it is possible to see the effect that increasing angle of attack will have on them. The drag coefficient becomes very sensitive to variations in angle of attack, increasing at an exponential rate over certain angles such as in figure 2.7(B). Increasing drag required a larger energy input to overcome its retarding effect, while also increase structural loading. Figure 2.7(C) shows the difference in lift between a symmetrical and asymmetrical aerofoil. In both instances lift increases at

a similar rate, with stall being reached at similar angles of attack. Bellow a zero angle of attack there is no lift generated by the symmetrical aerofoil, but there is by the asymmetrical. This indicated that a well-designed aerofoil will produce a greater lift while at the same time reducing significantly the drag [2], [29].

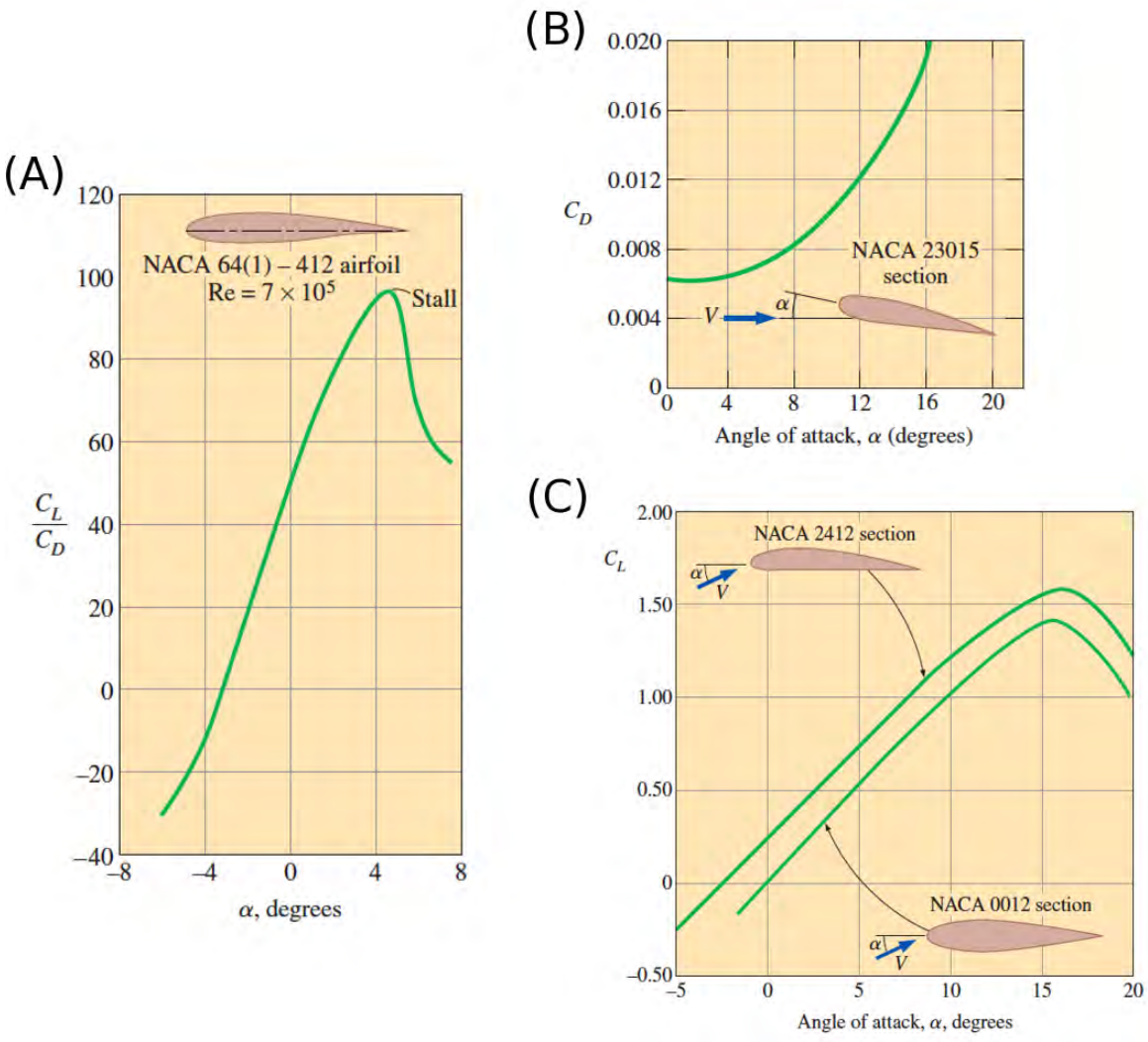

Figure 2.7: The effect of angle of attack on: (A) lift to drag ratio, (B)coefficient of drag and (C) lift coefficient for a symmetrical and asymmetrical aerofoil [2].

2.2 Flow Separation

Separation is a source of nuisance in the design and usage of aerofoils. At low speeds, the maximum lift is related directly to separation, with maximum lift taking place prior to

separation on well-developed high-lift devices. [30]

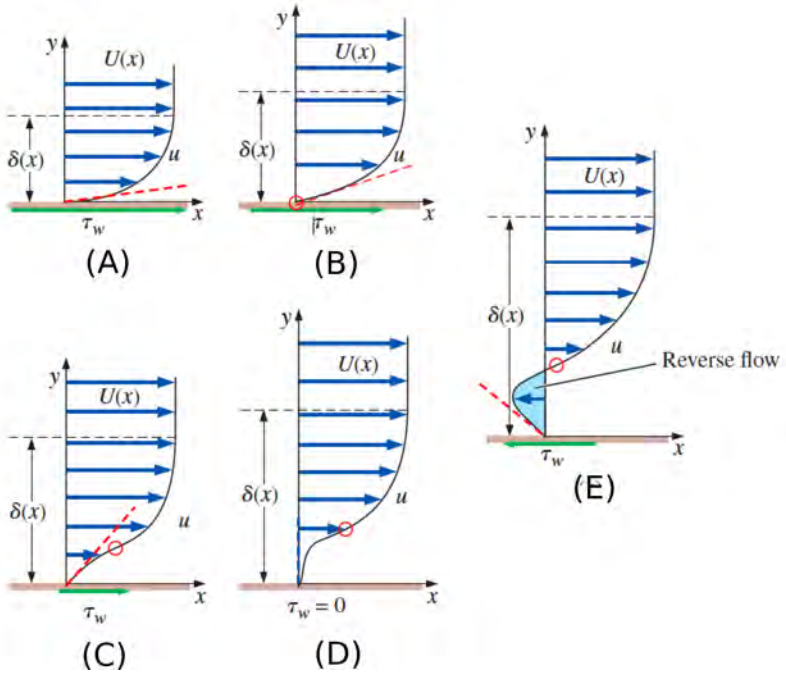

Figure 2.8: Boundary layer profiles shapes as a function of pressure gradients: (A) favourable, (B) Zero, (C) mild adverse, (D) critical adverse (point of separation), and (E) large adverse. Blue circle indicate inflection points and wall shear is given by τ_W [2].

When a flow passing over a body detaches from the surface producing a separated region of low pressure, recirculation and backflow occurs such as in figure 2.8(E). The larger the separated region the greater the pressure drag and wake produced. The wake region is felt downstream in the form of a reduced velocity compared to the upstream and surrounding flows. The separated region ends when both flow streams around the body reattach. To determine when separation will take place the pressure distribution along surface is initially examined. In the frontal area where the flow is accelerating, there is a favourable pressure gradient, and in the rear section where the flow decelerates, there is an adverse pressure gradient. If the pressure gradient (2.6) is large enough then it is likely that the boundary layer will separate. As such the boundary layer momentum equation given by White [31] of:

$$\frac{dP}{dx} = -\rho U_\infty \frac{dU_\infty}{dx} \tag{2.6}$$

Where U_∞ is free stream velocity, P is the pressure and x is the position along the chord.

Using the boundary layer momentum equation, we can learn a lot about the boundary layer velocity profiles.

$$U_\delta \frac{\delta U_\delta}{\delta x} + \nu_{delta} \frac{\delta U_\delta}{\delta y} = U_\infty \frac{dU_\infty}{dx} + \nu \frac{\delta^2 U_\delta}{\delta y^2} \tag{2.7}$$

Where U_δ is the flow velocity within the boundary layer, ν is the kinematic viscosity and y is the distance normal to the surface. Due to the no-slip condition the velocity at the wall is zero, now the left hand side of equation 2.7 is gone and the equation can be rewritten as:

$$\nu \frac{\delta^2 U_\delta}{\delta y^2}_{y=0} = U_\infty \frac{dU_\infty}{dx} = \frac{1}{\rho} \frac{dP}{dx} \tag{2.8}$$

Where ρ is density. During the favourable pressure gradient (figure 2.8(a)) dU_∞/dx is positive and so forms the above equation, the second derivative of U at the wall must be negative, as$(\delta^2 U_\delta/\delta y^2)_{(y=0)} < 0$. Knowing that $\delta^2 u/\delta y^2$ must remain negative as U_δ approaches U_∞, it is expected that the boundary layer will be rounded. In the zero pressure gradient condition (figure 2.8(B)) $(\delta^2 U_\delta/\delta y^2)_{(y=0)} = 0$. From this it is expected that U_δ will grow linearly with respect to distance from the wall. In an area of adverse pressure gradient (figure 2.8(C)), dU_δ/dx is negative and so $(\delta^2 U_\delta/\delta y^2)_{(y=0)} > 0$. Knowing that $\delta^2 u/\delta y^2$ must be negative as U_δ approaches U_∞ there must be an inflection point located somewhere along the velocity profile at which $\delta^2 U_\delta/\delta y^2 = 0$. The first derivation of U_δ with respect to y is directly proportional to τ_w ($\tau_w = \mu(dU_\delta/dy)_{y=0}$). τ_w is largest at favourable pressure gradients and lowest in adverse pressure gradients. This can be seen in figure 2.8, where the pressure gradient changes sign as the boundary layer grows. When the adverse pressure gradient is large enough, $((dy/dU_\delta)_{y=0} = 0)$, the flow is seen to separate[2].

Separation over an aerofoil usually takes place at an angle of attack of roughly 15^o. At this angle, flow can be totally separated from the top surface resulting in stall. A stalled aerofoils lift ability will be drastically reduced, resulting in a very unstable conditions. It should be noted that as the mean velocity profile of a turbulent flow is much fuller than that of a laminar flow, a larger adverse pressure gradient will be required in order for separation to take place.

2.3 Fluid mechanics of a synthetic jet emanating into quiescent fluid

An isolated synthetic jet is produced by the interaction of a train of vortices typically formed by periodic ejection of fluid through an orifice. The alternating ejection and suction of fluid across an orifice results in a zero net mass flux (ZNMF) flow. Due to the diaphragm imparting a force, the net average momentum imparted to the jet is non-zero. These attributes make synthetic jets unique in their ability to inject linear momentum into a flow without adding additional mass, as a result of the jet being synthesized from the surrounding fluid.
The synthetic jet's time-periodic reversal of flow results in the formation of a translating stagnation point forming downstream of the orifice along the centreline, confining the suction region to a narrow domain near the exit plane. The asymmetry between the omnidirectional suction and directional ejection leads to the establishment of a jet flow in the far-field.

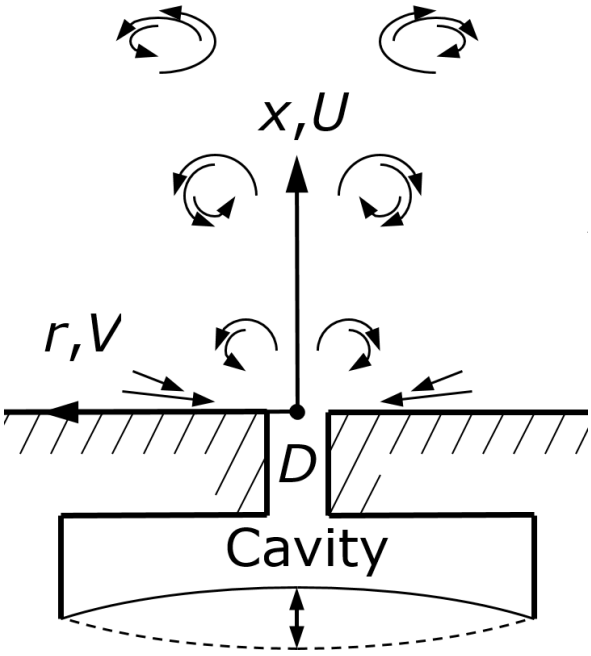

Figure 2.9: Formation of synthetic jet

The spatio-temporal evolution of a synthetic jet flow can be characterized into two domains, the near-field and far-field evolution. Synthetic jets can be formed from circular, rectangular (or differently shaped) orifices, resulting in a near-field flow field consisting of a train of either toroidal or more spanwise elongated (nearly two-dimensional) vortices. For

the sake of clarity, this section will focus mainly on synthetic jets formed from rectangular orifices with two-dimensional vortices. The near-field is dependent on time-periodic formation, detachment and advection of discrete vortices, that over time undergo a transition to turbulence. This transition begins a rapid increase of spanwise instabilities in the vortex, forming nominally spanwise-periodic counter-rotating streetwise vortex pairs that are wrapped around the main vortex core, leading to the vortex cores breaking down, losing cohesion and becoming indistinguishable from the background turbulent flow.

It is noted by Smith & Glezer [32] that transition of the vortex initiates at approximately the same time as the suction phase of the actuator commences. It is reckoned that this may be due to core instabilities linked with a velocity reversal and an associated negative pressure gradient near the orifice triggering the transition.

The synthetic jet is said to be in the far-field evolution, when the vortices have become indistinguishable from the main flow, and the synthetic jet now behaves much like that of a conventional two-dimensional jet, in that it has a fully developed self-similar turbulent flow. However, their behaviours are not exactly the same, for instance a synthetic jet's centre line velocity decreases more rapidly due to a faster spreading rate.

With regard to fluidic control the near-field evolution dictates how the synthetic jet will interact with a cross flow, as the interactions of the vortices with the near wall boundary layer is the means by which the jet is capable of modifying the hydrodynamic characteristics. For this reason, this report will be focused on the near-field evolution of the synthetic jets. [32], [33], [3], [34], [35]

2.3.1 Jet formation criterion

In order to determine the effects of a synthetic jet emanating into a boundary layer it makes sense to firstly understand the characteristics of a synthetic jet emanating into a quiescent fluid. The formation of a synthetic jet relies on the detachment of the formed vortex from the edge of the orifice. Sufficient momentum should be imparted to the forming vortex in

order for it to fully detach and propagate away from the orifice. If not, the formed vortex is re-ingested in the suction phase and no far-field jet is formed.

$$St = \sqrt{2\pi f D_O^2/\nu} \tag{2.9}$$

Holman *et al.* [34] highlights the two main methods used to estimate jet formation, a simple order-of-magnitude analysis such as proposed by Mittal *et al.* [36], which required the ratio of Re to Stokes number St^2 (St equation 2.9) must be greater than a threshold parameter (K) (Eq:2.10) or the slug-velocity-profile method described by Smith *et al.* [37] which relies on a minimum threshold value of L_0/D_O being exceeded. The selection of either method is heavily dependent on the type of actuator (e.g., surface roughness, geometry and actuation) and the compressibility of the fluid (i.e. air, water).

The selection and effects of these criterion has been a topic of discussion. Holman *et al.* [34] proposed a formation criterion based on the Strouhal number (Sr), Reynolds number (Re) and the Stokes number (St^2). Holman *et al.* [34] and Shuster *et al.* [3] concluded that in order for a synthetic jet to form it was necessary to achieve a L_0/D_O of greater than or equal to 0.5 and 3.14 for axisymmetric and two-dimensional synthetic jets respectively.

$$\frac{1}{Sr} = \frac{Re}{St^2} > K.\pi \tag{2.10}$$

Where K is:

$$K = \frac{32c^2(1+\varepsilon)^P}{k\pi^2} \tag{2.11}$$

Where k is the aspect ratio of the slot and ε is r_c/D_O.
Equation 2.11 is primarily dependent on the effects of orifice geometry. An increase of ε, a representation of the sharpness of the orifice lip, will result in an increase in power required to generate a jet, with little effect on the synthetic jet flow or initial vortices ([38]). A change in aspect ratio k will significantly affect the formation criterion threshold, in the region of an order of magnitude less for an axisymmetric jet as seen above. This has been dis-

cussed by Holman *et al.* [34], Smith *et al.* [37], David J. Nani & Smith [39], and Lee *et al.* [38]

In order for all calculations presented in this section to be in line with equations presented in the flow control chapter below, equation 2.10 needs to be put in terms of the dimensionless stroke length (L_0/D_O). The Strouhal number (Sr) is inversely proportional to the dimensionless stroke length, therefore equation 2.10 is now:

$$\frac{L_0}{D_O} > K.\pi \tag{2.12}$$

To clearly understand the formation of a synthetic jet it is convenient to take the flow within the cavity as being based on viscous, inertial and unsteady forces (unsteady being the uncertain effect such as the oscillating pressure field imposed by diaphragmatic action), and how they are influenced by formation criterion ([4]).

The Reynolds number (Re_{L_0/D_O}) determines the turbulent nature of the synthetic jet flow as it is the ratio of inertial forces to viscous forces. L_0/D_O determines if the vortex can overcome suction forces, it is the ratio of the inertia forces to the unsteady forces. And finally the Stokes number which represents the Stokes layer formed and its effect on vortex rollup strength, it is the ratio of unsteady forces to viscous forces. According to Holman *et al.* [34] a jet with a large Stokes number ($St \approx 1$) will have a slug like velocity profile. It should be noted that the Stokes number becomes less influential at high Reynolds numbers and when the orifice depth to diameter ratio is low.

2.3.1.1 Dimensionless stroke length

The import of the effect of modifying each formation criterion needs to be understood in depth, if a synthetic jet is to be used efficiently in fluidic control. The first parameter to be looked at is the dimensionless stroke length, defined as the ratio of stroke length L_0 to orifice diameter D_O. L_0/D_O is considered the most influential parameter in the formation in the near field [35], [34], [33], [8], [35], [40].

An axysmetric jet will form at an L_0/D_O of 3.14, however this is not a clearly defined

threshold. It was found by Shuster *et al.* [3] that even though the vortices where not ingested at this point they where also not advected at $L_0/D_O < 0.6$. This corresponds with the findings of both Zhou *et al.* [4] and Holman holman2005formation, where they found that when the Stokes number is too low a vortex will be unable to form properly. To best explain the effects of L_0/D_O the works of Shuster *et al.* [3] will be used, as the test conditions used were most similar to those used in this project (See chapeter 3).

At values of $L_0/D_O \leq 1$ vortex shape and propagation are significant effected by the suction phase. In figure 2.10 (A and D) it can be clearly seen that the formed vortex is being squashed during the suction phase and as such is unable to reach beyond x/D_O of 0.5. When the L_0/D_O is increased to 2 (Fig2.10B and E) and 3(Fig2.10C and F) the vortex is seen to be advected away form the orifice. In figure 2.10 the phase average results of an L_0/D_O of 2 and 3 are compared and it can be seen that the significant difference is in the distance the vortex has travelled from the orifice, suggesting that the propagation of the vortex scales with L_0 ([3], [32]). As the advection of a vortex scales with L_0, increasing L_0/D_O will increase the distance between propagated vortices. The interaction between vortices diminishes with distance until there is no interaction between vortex pairs, at this point a concomitant trailing jet indicates that a limiting factor has been reached. This is found this to be around $4 < L_0/D_O > 5$, [3], [8]. For heat transfer to an impinging synthetic jet, Persoons et al. (2011) found 4 flow regimes depending largely on the value of L_0/D_O.

With regards to flow control L_0/D_O will determine when the vortex will form in relation to the distance of the shear layer from the surface. It also determines the quantity of fluid expelled by the jet over each phase and as such will have an effect on the momentum flux of the jet. It is important not to confuse this with the quantity of expelled fluid rolled up into the vortex, determined by *Re* and *St*.

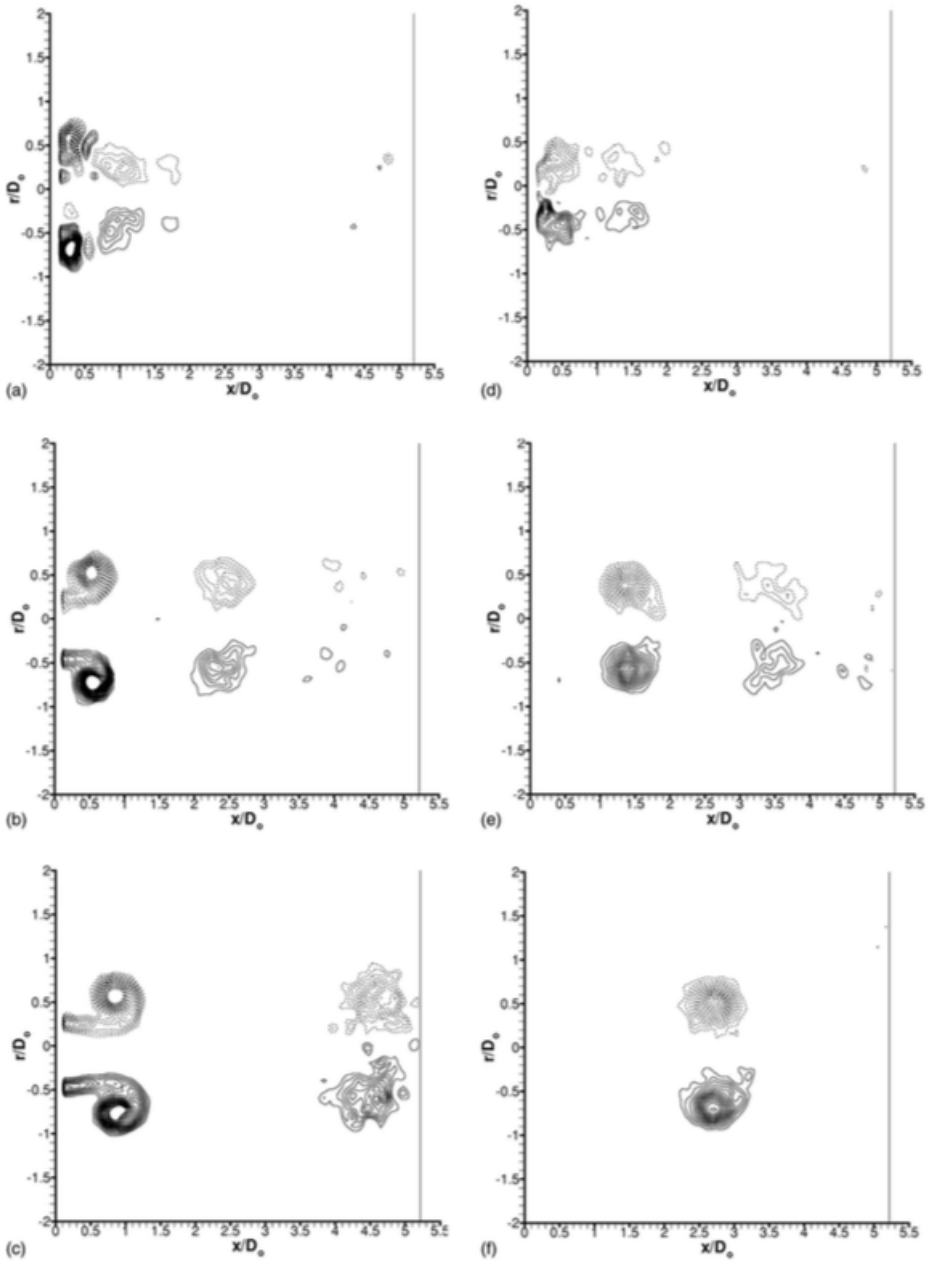

Figure 2.10: Phase-average, modification of L_0/D_O while maintaining a constant $\mathrm{Re}_{SJA} = 2500.When \mathrm{L}_0/D_O$ = 2 phase angle is C) $162^O D)342^O and when When \mathrm{L}_0/D_O$ = 3 phase angle is D) $162^O E)342^O of = 3$[3]

2.3.1.2 Effects Reynolds number and Stokes number on jet formation

The Reynolds number is usually attributed as being the main criterion characterizing the far-field evolution of a synthetic jet, however when looking at the near field in terms of fluidic control, the Reynolds number takes on significant importance, as it determines the structure of the jet in relation to turbulence and roll-up([32], [35], [8]).

$$Re_{I_O} = I_O/\mu h \tag{2.13}$$

Is the impulse per unit width of the jet (i.e., proportional to the momentum associated with the jet). Equation 2.13 gives the amount of momentum the jets is able to impart, which is stated by Shuster *et al.* [3] as being the most important characteristic of a synthetic jet in fluidic control.

$$Re_{L_0/D_O} = \frac{U_0 L_0}{\nu} \tag{2.14}$$

Another way to look at the Reynolds number is in terms of the dimensionless stroke length (L_0/D_O) as in equation 2.14([4]). This representation of Reynolds number is used to determine the flow regime of the produced vortex, and the effect of modifying the actuator parameters will have on the flow regime. For instance if L_0/D_O is kept constant and the velocity at the orifice is modified, a result such as in figure 2.11, would be expected, such that at each Reynolds number the state of the vortices changed, but without any signs of premature degradation of the vortices as *Re* increases. This supports the idea that the advected distance scales with L_0/D_O.

$$Re_{L_0} \sim \frac{L^2 St^2}{2\pi} = L^2 \frac{f D_O^2}{\nu} \sim \frac{\Gamma}{\nu} \tag{2.15}$$

From Equation 2.15 ([4]) the strength of a vortex is obtained (in the case of the slug method) through (Re_{L_0}) being approximately proportional to the non-dimensionalised integrated strength of a finite vortex (Γ/ν). In other terms *Re* will determine the total circulation ejected though the orifice in each expulsion phase. In figure 2.12 the relationship between Reynolds number and circulation is shown, where the increase of *Re* in B over A demonstrates a significant increase in the amount of fluid rolled into each vortex [8].

If a flow is assumed to be slug like, the use of L_0/D_O and *Re* should be sufficient to characterize the near-field evolution of a jet. This assumes that the changes made to the L_0 and the jet frequency f_{SJA} will have direct effect on jet formation (without effects such as compressibility)

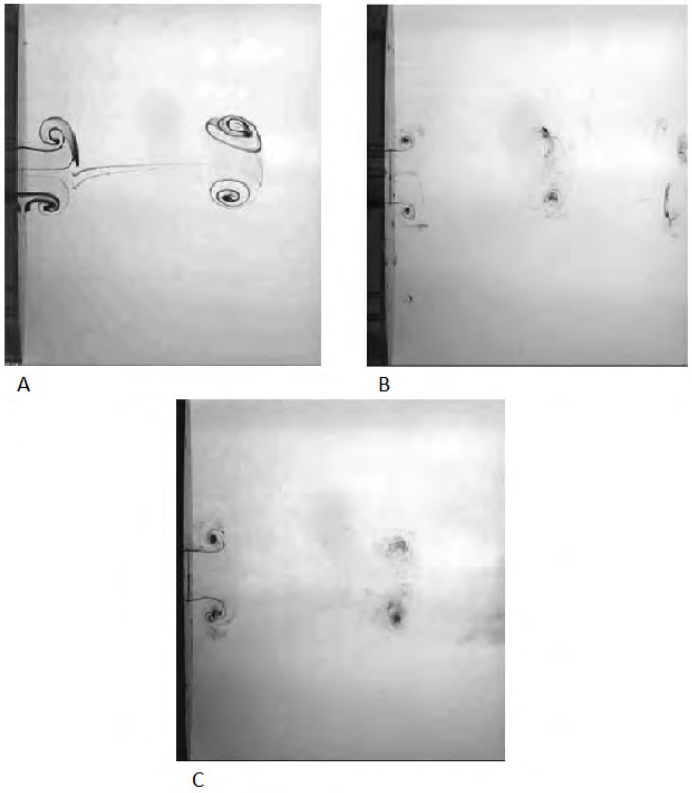

Figure 2.11: Synthetic jet transition from laminar to turbulent. $L_0/D_O = 3$ and Re_{SJA} A) 500 B) 2500 C) 4500 [3]

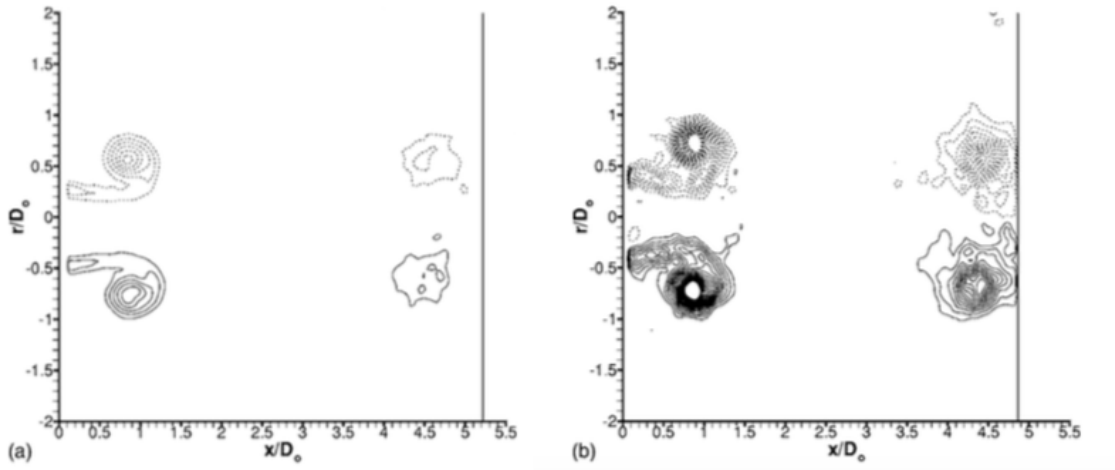

Figure 2.12: Phase-average azimuthal velocity contours, comparing vortex rings with constant L_0/D_O of 3 at A) $Re_{SJA} = 2500$ B) $Re_{U_O} = 10000$ [3]

The aforementioned formation criterion assumed the flow to be slug like, however this is not always the case as fluid compressibility in the actuator cavity can make it impractical to base Reynolds number on the values of stroke length and frequency imparted on the fluid by

the diaphragm, and apply incompressibility and continuity at the orifice to obtain a Reynolds number ([34]). In this case it is usually more appropriate to use an order-of-magnitude method, to determine a reliable value for *Re*. To obtain this value it is necessary to undertake the more difficult task of either directly measuring or indirectly estimating the exit velocity at the orifice. This can be achieved using reduced order (lumped parameter) analytical methods to determining a synthetic jet's operating conditions (*Re* and L_0/D_O) through a measurement of the cavity pressure, as proposed by Persoons & O Donovan [41].

When factors such as compressibility and orifice depth to width ratio become a significant factor, it is necessary to also take into account the effects of the Stokes number (*St*) on the formation of a synthetic jet. As mentioned previously *St* can be taken as a ratio of unsteady forces to viscous forces, making it sensitive to the compressibility of the fluid, the rigidity of the diaphragm, the polarity of the molecules and the orifice depth-to-diameter ratio (H_O/D_O). It should be noted that when H_O/D_O is too small then the flow in the orifice is unable to develop fully, weakening the influence of the Stokes length, due to the tendency of a potential core to form ([4])

St determines the thickness of the Stokes layer, which affects the strength of vortex rollup, as it affects the Stokes layer formed within the orifice. The larger the value of *St* the smaller the Stokes layer within the orifice. Zhou *et al.* [4] used an axisymmetric synthetic jet in air to show that formation could be prevented at an L_0/D_O of 3 (well above the formation of L_0/D_O of 1 criterion established by Holman *et al.* [34]) by adequately reducing *St*. This was done using two values of *St* while keeping an L_0/D_O of 3. The first value being an *St* of 2.32 (figure 2.13B) produced no jet at all and the second value of *St* of 5.68 (figure 2.13A) produced a jet, without vortex roll-up. In the *St* of 5.68 case the formations of wings can be seen however there is almost no entrainment of the surrounding fluid and there is little rotational motion visible, suggesting that the jet has not rolled up.

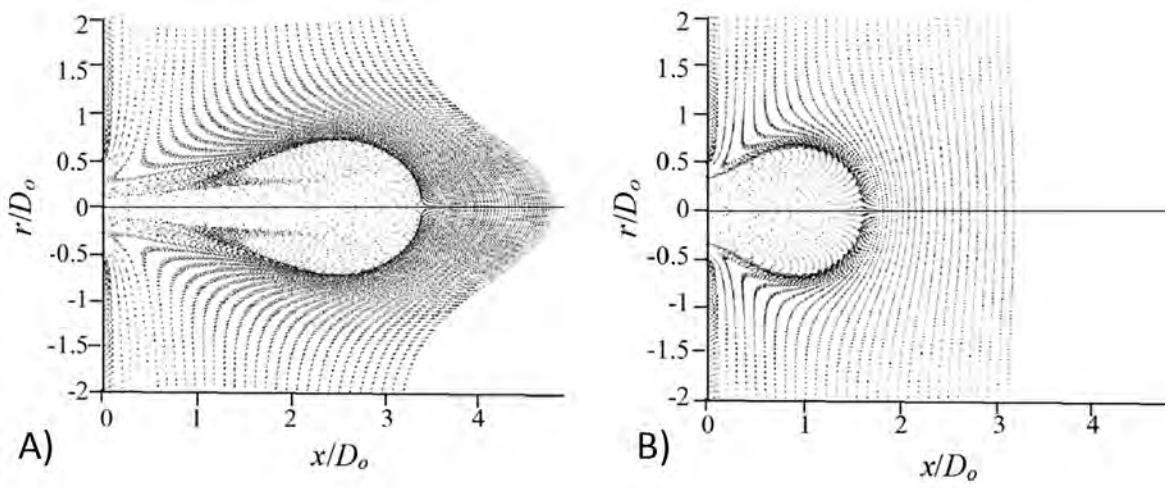

Figure 2.13: Velocity vectors for an axisymmetric synthetic jet at $L_{SJA} = 3$ when: A) St = 5.63 and B) St = 2.32 ([4])

Delay in formation is due primarily to the Stokes layer extending to the centre of the orifice, altering the velocity profile of the jet and forcing a large proportion of the flow to the centre of the orifice. This results in the maximum velocity being confined to the centreline of the orifices, producing a thick cylindrical vortex sheet, postponing vortex roll-up ([4]).

When the orifice flow is fully developed the Stokes layer thickness is dependent on St. Zhou *et al.* [4] found that at $St < 10$ the thickness of the Stokes layer extends to the centreline of the orifice, and at values of $St > 10$ the thickness of the Stokes layer reduces rapidly. In figure 2.14 it is seen that as St increases beyond 10 there is a exponential increase in D_O/δ_{St}.

$$\frac{\Omega D_O^2}{\nu} \sim \frac{L_0}{D_O} S^2 \frac{D_O}{\delta_{St}} \tag{2.16}$$

Where dimensionless vorticity ($\Omega.D_O^2./\nu$) is approximately proportional to the dimensionless stroke length (L_0/D_O), the Stokes number (St) and normalized thickness of the Stokes layer (D_O/δ_{St}). From this equation an increase in the St and consequently in D_O/δ_{St}, will significantly increase the strength of vortex rollup, at values of $St > 10$.

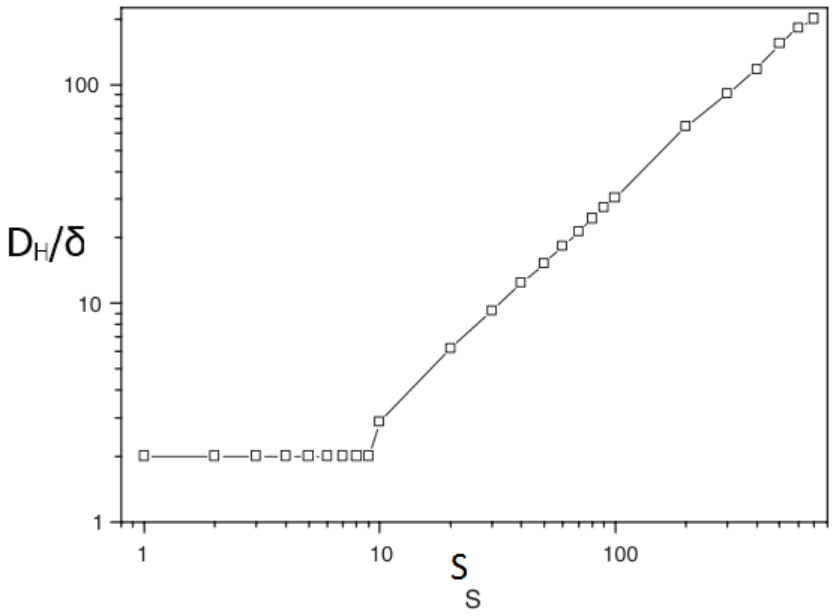

Figure 2.14: Effect of Stokes layer on D_O/δ_{St} [4]

In these conditions *Re* is not the only factor determining the quantity of fluid being rolled up within the vortices; *St* also has an influence. In equation 2.15 $Re_{L_0} \approx ((L^2.St^2)/(2.\pi))$, therefore *St* will affect Γ/ν and thus the amount of fluid that will be rolled up (Figure 2.15). Zhou *et al.* [4] showed that by using a constant *Re* and modifying *St*, the amount of fluid rolled up would change significantly. At *St* = 14.7 nearly all of expelled fluid was entrained within the vortices, and when *St* was reduced to 7.35 it was found that only a portion of the expelled fluid was entrained within the vortices.

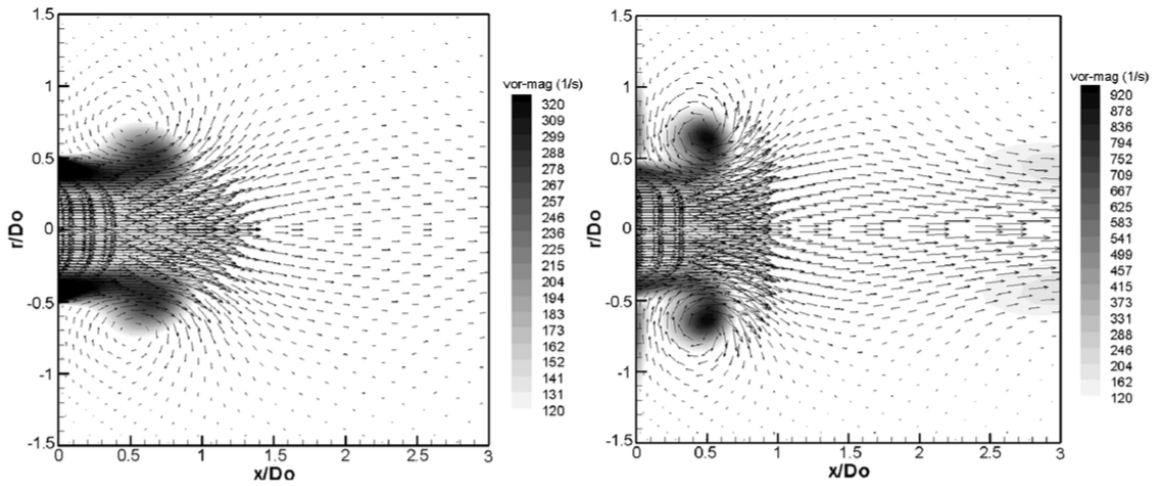

Figure 2.15: Effects of changing Stokes number from A) St = 7.35 $L_{SJA} = 4$ and B) St = 14.7 $L_{SJA} = 2$. While maintaining a constant $Re_{SJA} = 137$ [4]

2.4 Fluid mechanics of a synthetic jet emanating into a cross-flow

The use of active flow control is relatively new idea within fluid dynamics, providing the ability to alter on the fly the fluid dynamic properties of a body without the need to re-model the surface ([21]). Synthetic jets have become a very versatile method of achieving fluidic control for wall bounded and free-shear flows, reducing drag and increasing lift ([24]).

This section will be based on the interaction of an embedded synthetic jet actuator with a cross flow, looking at actuators with differing geometries and orientations, over a range of operating parameters.

2.4.1 Normalizing equations

In the previous section, the type of vortex produced was shown to be a direct result of the actuator conditions and parameters. In this section, the introduction of a cross-flow has a significant effect on the formation and advection of the vortices formed. With synthetic jet flow control, there are three basic types of vortices produced, hairpin, stretched and tilted vortices. These names depict the interaction of the vortex with the cross-flow and in particular the boundary layer. Vortex type directly effects the efficiency of a synthetic jet actuator in fluidic control. To determine the types of vortex being produced with regards to a cross flow the first parameter to be looked at is the dimensionless actuation Frequency (F^+) ([42], [43]. [43] [9], [8], [44], [45]).

$$F^+ = \frac{f_{act} L_C}{U_\infty} \tag{2.17}$$

Equation 2.17 can be rewritten to accommodate the orifice velocity such that is it:

$$F^+ = \frac{f_{act} D_O}{U_O} \frac{L_C}{D_O} \frac{U_O}{U_\infty} \tag{2.18}$$

As $Sr =_0 /(fD_O)$ and $L_0/D_O = 1/Sr$, Sr can be substituted into equation 2.18 to give:

$$F^{+} = \frac{L_0}{D_O}\frac{L_C}{D_O}\frac{U_O}{U_\infty} \tag{2.19}$$

2.19 is now broken down into 3 non-dimensionalised parameters to better understand the interactions: (I) Strouhal number(Sr), (II) a ratio of chord to orifice diameter, and (III) a velocity ratio(V_R).

$$Sr = \frac{fD_O}{U_0} \tag{2.20}$$

$$V_R = \frac{U_0}{U_\infty} \tag{2.21}$$

From this point on V_R will be used to characterise the type of vortex produced and a Reynolds number based on the dimensionless stroke length (Re_J) will be used to determine the strength of the vortices produced.

2.4.2 Axisymmetric synthetic Jet actuator

In the previous section 2.3 it was seen that as L_0 and f_{SJA} where changed in a quiescent flow, there was a direct effect (strength, circulation, distance of propagation etc.) on the formed vortex. Crook *et al.* [5] found using dye visualisations that the shape of the vortex rings leaving the synthetic jet was dependant on the ratio of jet velocity to free-stream velocity (V_R). In figure 2.16 a slight increase in tilting of the vortex is seen for the high L_0 case, with little or no stretching as the free-stream velocity (U_∞) increases. At a low L_0 as U_∞ increase the vortex becomes highly asymmetrical as it is stretched and tilted, in the lower V_R the vortices are streak like and remain attached to the surface. This was further investigated by Jabbal & Zhong [9], Jabbal & Zhong [45], Zhong *et al.* [43], Zhang & Zhong *et al.* [8], Zhong *et al.* [44], Crook *et al.* [5], and Glazer *et al.* [46],into the detail of the effect of the free-stream on the symmetry of the synthetic jet and thus its effect on the boundary layer. Upon the vortex interacting with the cross-flow it is no longer seen to be a simple symmetrical jet as seen in figure 2.9 instead the jets are now characterised based on their primary V_R:

- (A) when the V_R is low a highly stretched and tilted vortex that remains attached to the wall called a hairpin vortex is produced,

- (B) when the V_R is at an intermediate value a highly stretched an tilted vortex that separates from the wall called a stretched vortex ring is produced, and
- (C) a high V_R produces a jet that only undergoes slight tilting and no stretching called a tilted vortex ring (Fig2.17.)

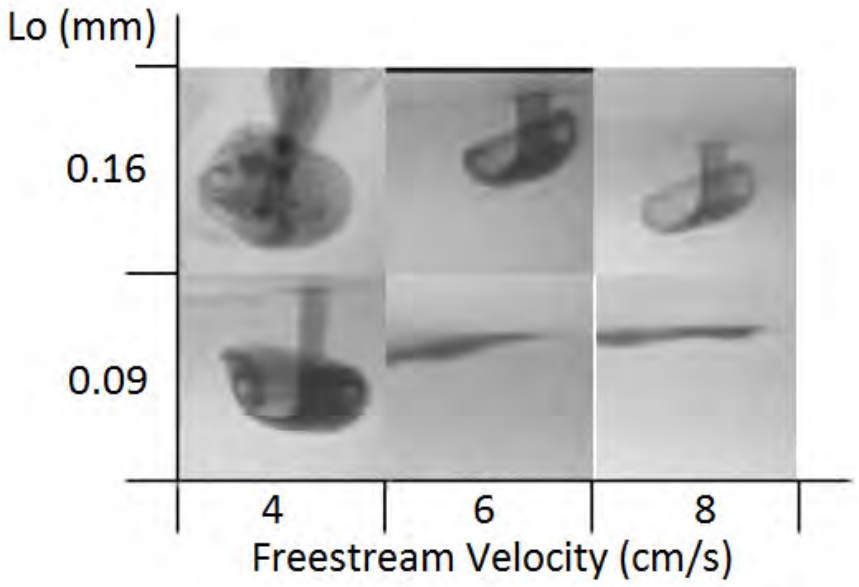

Figure 2.16: Effect of cross-flow and L_{SJA} at constant f of 2Hz on synthetic jet [5].

The reason for the asymmetry is due to the influence of the cross-flow (taken to have a clockwise vorticity) on the clockwise (CW) and counter clockwise (CCW) vortices components of the synthetic jet. In simple terms as the counter-rotating vortices come in contact with the cross-flow, the CCW vortex if it is able to overcome CW cross-flow is weakened, while the CW vortex is energised. An example of the growth of the CW vortex is shown by Amitay & Glezer [7] through smoke visualisation in figure 2.18, where the CW vortex grows to roughly half the thickness of the aerofoil. This interaction is explained in more detail below in section 2.4.3.

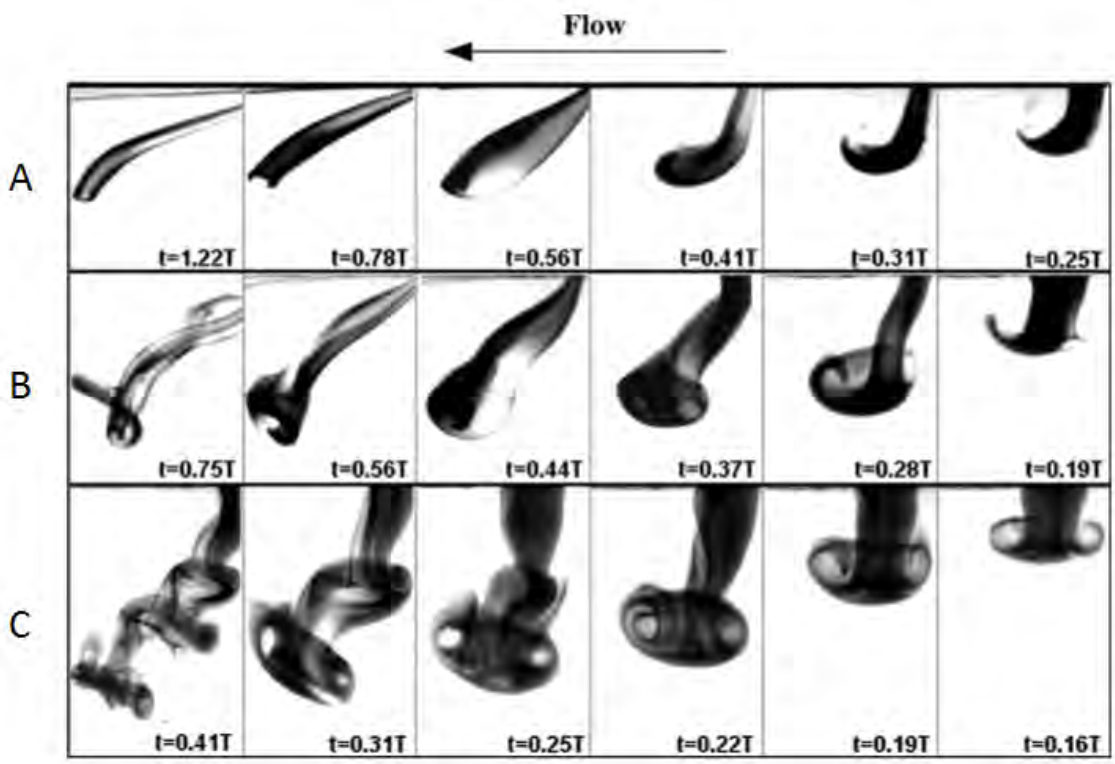

Figure 2.17: Synthetic jet formation and roll up in a cross-flow: (A) hairpin vortices, (B) stretched vortices and (C) Tilted vortices [6]

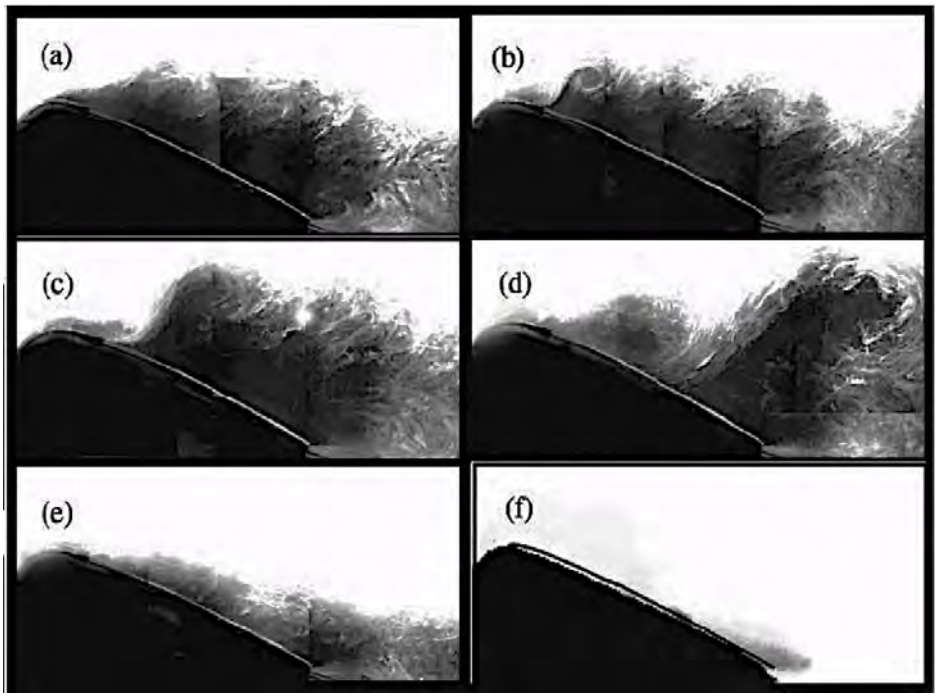

Figure 2.18: Phase-averaged images during the reattachment process for $\alpha = 17.5°$, $= 60^o$, and $Sr = 10$. $\delta t = 0$ (a), 8 (b), 18 (c), 24 (d), 33 (e) and 125 (f). [7]

Zhong *et al.* [43] summarised the effects the three types of vortices and their basic interactions with the boundary layer. A low Re_J and V_R produces a hairpin vortex, which is highly stretched and remains attached to the wall and will not penetrate the boundary layer. An intermediate Re_J and V_R produces a stretched vortex, which still undergoes significant stretching and tilting. Unlike the hairpin vortex, it will eventually pass through the boundary layer where it will no longer have a significant effect. A high Re_J and V_R produces a tilted vortex, which undergoes little or no stretching or tilting and quickly passes through the boundary layer, resulting in a minimal effect on the near wall flow.

Jabbal & Zhong [6] gives an insight into the near wall effects of a synthetic jet in a laminar boundary layer using stereoscopic dye visualisation and surface liquid crystal, their main concentration being placed on hairpin and stretched vortices, as a tilted vortex abruptly penetrates the boundary layer resulting in poor flow control for high energy consumption. For the hairpin vortex it was seen that there are two types, a hairpin vertex that produces longitudinal secondary counter-rotating vortices and hairpin vortex without secondary longitudinal vortices, found to be at the lower and higher range of V_R and Re for hairpin vortices respectively (figure 2.19).

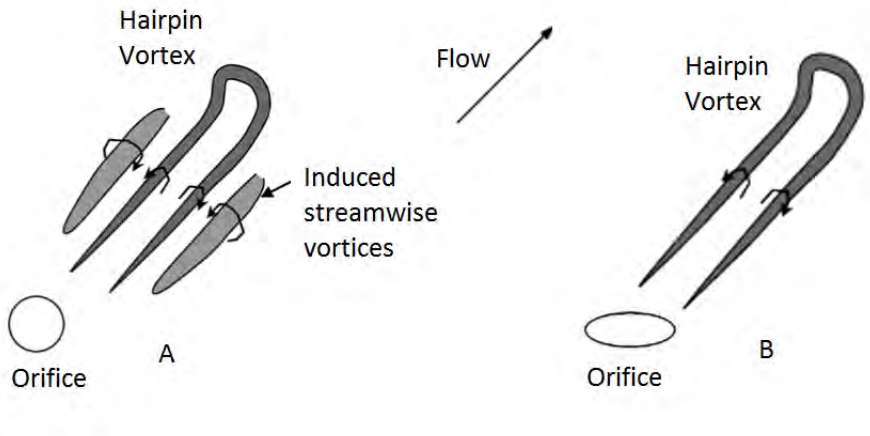

Figure 2.19: The structures of a hairpin vortex A) with induced streetwise vortices and B) without being produced by an axisymmetric synthetic jet [8]

It can be seen in figure 2.20A. that at a $V_R = 0.14$ ($Re_L = 46$ and $L_0/D_O = 1.4$) a hairpin vortex is formed straight out of the orifice and remains within the near wall region of the

boundary layer. The degree of stretching of the counter rotating vortex indicates that the level of shear in the boundary layer has a strong influence on the vortex. Either side of the counter-rotating legs a secondary (or longitudinal) vortex pair formed due to the fluid outboard of the vortex being sucked inward. In these conditions the vortex is dominated by the suction stroke, as the counter-rotating legs stretch back to the orifice.

Fig.2.20B. shows that when $V_R = 0.14$ ($Re_L = 46$ and $L_0/D_O = 1.4$) is increased the vortex is now advected from the to orifice and due to the increase in Re_L, this vortex is then able to break free from the wall and penetrates the boundary layer more deeply, without passing through. The presence of the longitudinal vortices has disappeared.

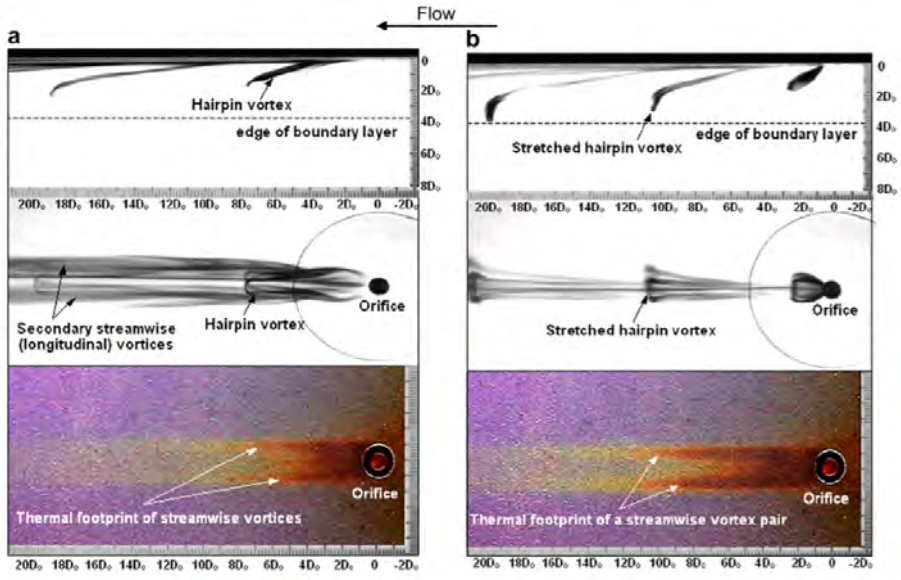

Figure 2.20: Stereoscopic dye and surface liquid crystal images of a synthetic jet at (a) $V_R = 0.14$, $Re_{SJA} = 46$, $L_0/D_O = 1.4$, (b) $V_R = 0.19$, $Re_{SJA} = 89$, $L_0/D_O = 1.9$, [6]

Figure 2.21B. shows a stretched vortex being formed and advected at a $V_R = 0.27$($Re_L = 182$ and $L_0/D_O = 2.7$). The structure of the vortex produced has a similar shape to that of the hairpins described by Jabbal & Zhong [6], but they differ in two distinct ways that are attributed to an increase in Re_L and L_0/D_O. With an increase of L_0/D_O the legs of the vortex no longer remain attached to the orifice or the wall, indicating the suction phase no longer has a significant effect on formation. Increasing Re_L results in an increase in the strength of vorticity which is seen by the prominent vortical structure present at the head of the vortices.

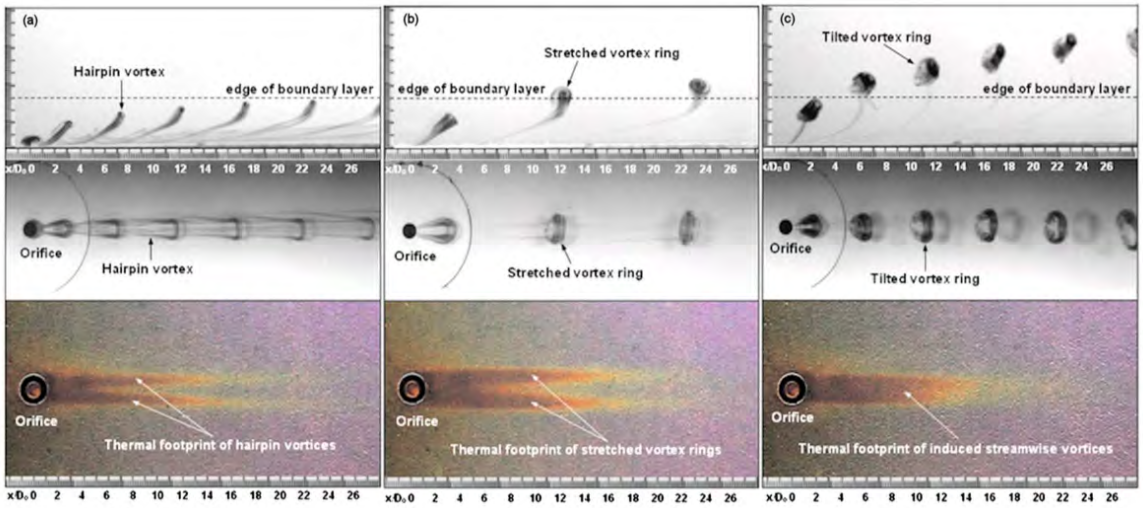

Figure 2.21: Flow visualization and thermal footprints of: A) Hairpin vortices, B) Stretched vortices, and C) Tilted vortices. [9]

These effects coupled with the increase of V_R results in a steeper trajectory leading to the vortex becoming embedded within the boundary layer and eventually penetrating through. This is shown in detail by Jabbal & Zhong [9], using PIV they are able to show how the vortex effects the flow in the surrounding area.

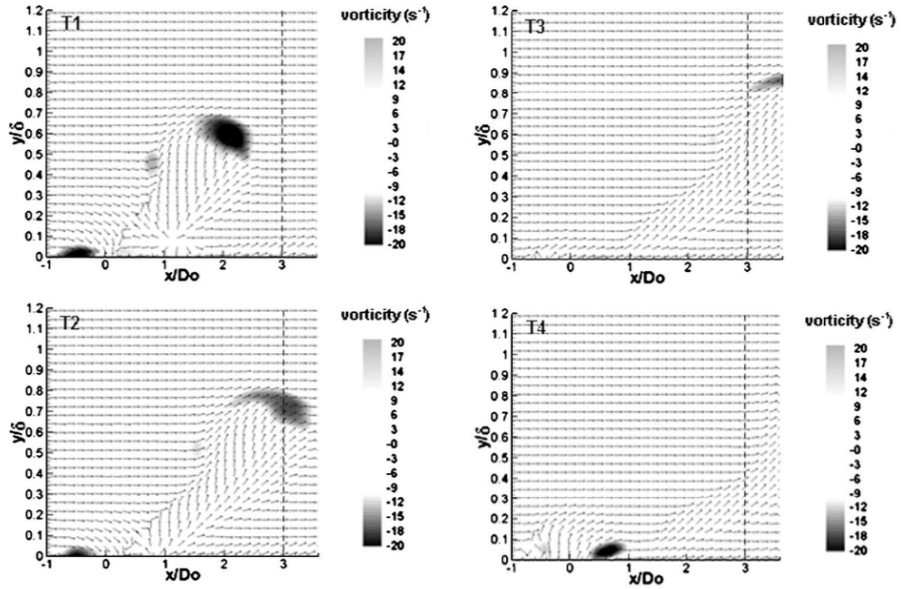

Figure 2.22: Phase average PIV of the boundary layer velocity profile of a stretched vortex ring at the jet centreline. $T1$ = near maximum suction $T2$ = a time after maximum suction $T3$ = just after blowing phase begins $T4$ = near maximum blowing. [9]

Figure 2.22 shows the growth and evolution of a two-dimensional stretched vortex as it is advected downstream. In $T4$ where the jet is at roughly maximum blowing a CW vortex is clearly seen, whereas there is only a faint trace of a CCW vortex. The CCW vortex has sufficient strength to overcome the vorticity of the boundary layer which helps to create a greater upwash, increasing the amount of CCW tilting to the jet, as can be seen in figure 2.21B. This added tilt changes the trajectory of the jet so that it is able to, with the aid of the extra vortical strength, becomes embedded in the shear layer before breaking through (fig2.23)([6], [9])

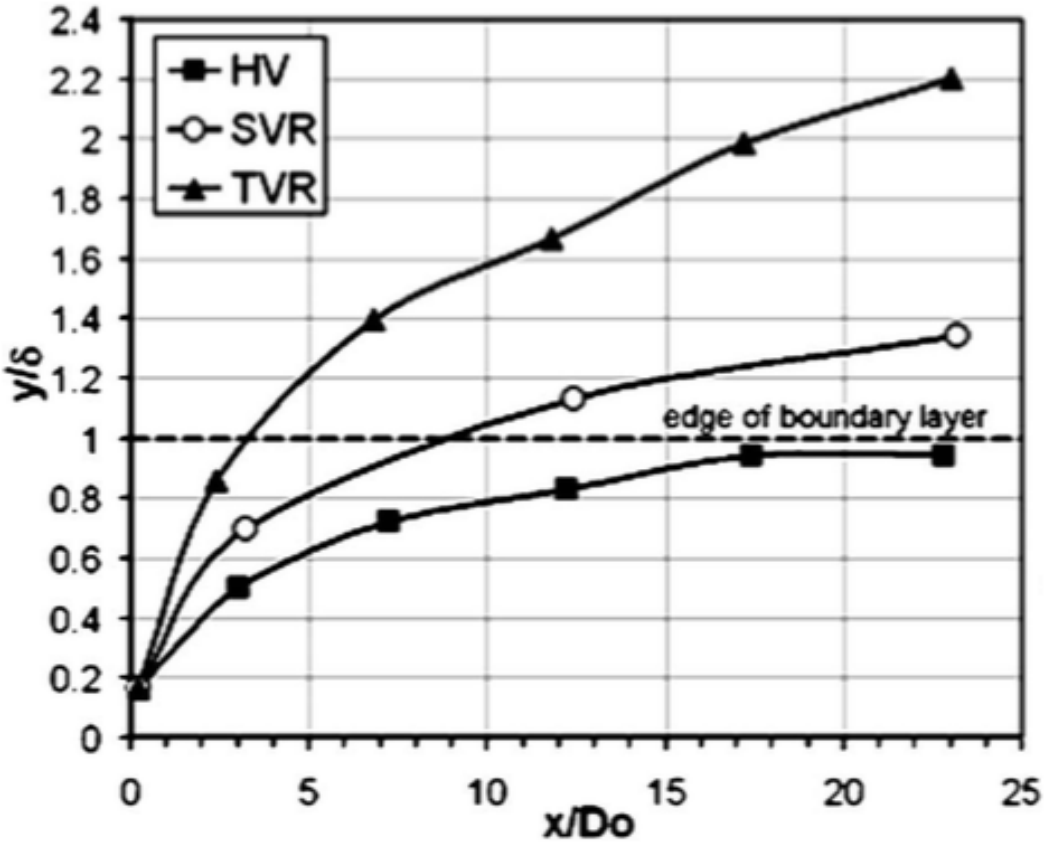

Figure 2.23: Trajectory of synthetic jets in the boundary layer: HV = hairpin vortex, SVR = stretched vortex ring, and TVR = tilted vortex rings. [9]

The Tilted vortex is the final main vortex to be looked at, it differs significant from the previous two cases, looking more like a traditional synthetic jet formed in a quiescent flow and only undergoing a slight amount of tilting and stretching (Fig. 2.17C). The strength of the vortex produced by a high L_0/D_O and Re_L, produces a vortex capable of overcoming the

boundary layer vorticity and breaking through the shear layer without being significantly affected. Previously it was discussed in the findings of Shuster *et al.* [3] that when L_0/D_O increased sufficiently (to around L_0/D_O of between 4 and 5, which is supported by Jabbal & Zhong [6] where it was found to occur at an $L_0/D_O > 4$) there is a limiting factor at which successive vortices no longer interact with one another, thus creating a secondary shedding vortex (Fig2.24). These secondary vortices mix the high momentum fluid with the low momentum fluid energising the flow. This effect can be seen in results such as those by Zhang & Zhong [8], where depending on the L_0/D_O separation prevention doesn't take place or is significantly reduced, when the jet structure has initially transitioned to a tilted vortex, but as L_0/D_O is increased the separation prevention is recovered. [9]

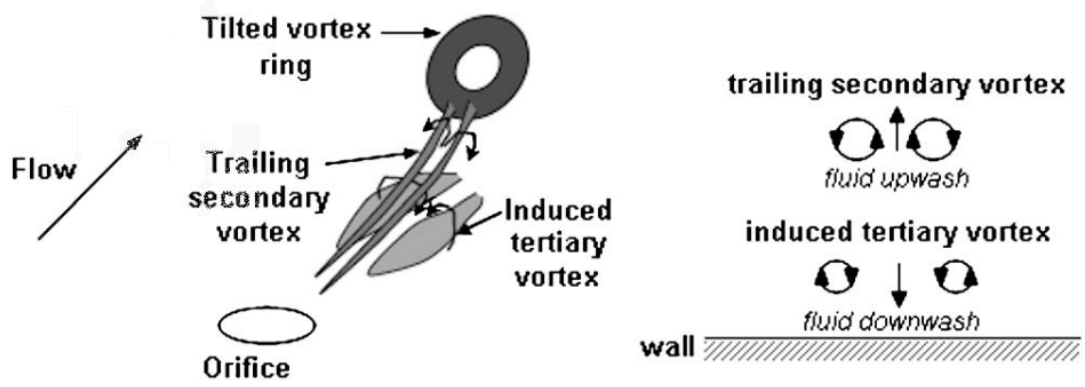

Figure 2.24: Secondary and tertiary vortical structures produced by tilted vortex [9]

Jabbal & Zhong [9] showed that stretched vortex rings offer greater potential for flow separation control compared to the other vortices in terms of the following (I) higher net enhancement of wall shear stress, (II) greater streamwise persistency of wall shear stress, and (III) lower spatial rms wall shear stress.

Zhong *et al.* [44] and Jabbal & Zhong [9] found experimentally that the most effective separation prevention will be given by a stretched vortex, due the fact that it is able to break through the boundary layer, but does not make its way thought until it has travelled a significant distance downstream. during the time in which the vortex is in the shear layer, it energises the flow by taking fluid from the free stream and mixing it into the reversed flow and visa versa. ([45], [46])

2.4.3 Finite synthetic jet issued into a cross flow

The use of vortices issued from an axisymmetric (round) synthetic jet was used to determine the basic interaction of a jet with a cross flow, in this section the concentration will be on the interaction of a cross-flow with a finite span (rectangular) synthetic jet.

Unlike an axisymmetric synthetic jet, the orifice orientation to the direction of flow will have a significant effect on the manner in which the jet interacts with the mean flow, it will not always be possible to have the orifice angled parallel or perpendicular to the flow (e.g., a finite span jet embedded in an unswept or swept wing). Smith [11] looked at how a finite jet reacts to a flow when it is in a streamwise (parallel to flow) and a spanwise(normal to flow) orientation.

In the streamwise orientation it was found that the jet effect was dominated by spanwise longitudinal counter-rotating vortices. The jet penetrated the into the boundary layer compared to that of the spanwise orientation which at the same V_R only penetrated to a maximum of 0.8δ. [11] theorised that the array of longitudinal jets work together as one jet, due to an off centre actuation of the central streamwise jet in an array. However, it was also noted that the off centre nature of the velocity profiles would suggest an external starving the centre actuator of fluid. Streamwise orientated synthetic jets are limited by the need of significantly more actuators to cover the same area as that of a streamwise synthetic jet.

Bridges [10] looked into the effect of the orientation of the jet to the cross-flow, taking an orientation from streamwise (0^o) to a 10^o and 20^o offset angle, whilst keeping all other conditions fixed. A streamwise orientation produced a pair of weak counter rotating vortices that penetrated the boundary layer, where as the 10^o and 20^o offsets produced a vortex that was tilted to one side and only penetrating 0.6δ and 0.5δ respectively. Interestingly the phase-average results of the 20^o deflection suggest the formation of a horseshoe vortex (Fig2.25 A.). This was as a result of rapid and sudden turning of the jet structure after formation, producing a fluid obstacle, causing a blockage within the boundary layer, whose

quickly closing wake produces the horseshoe vortex enhancing mixing of high momentum fluid with the low momentum near wall flow (Fig2.25B.). At a low V_R the effectiveness of a synthetic jet in separation prevention was negligible for the streamwise jet, but the offsets would produce a level of separation control.

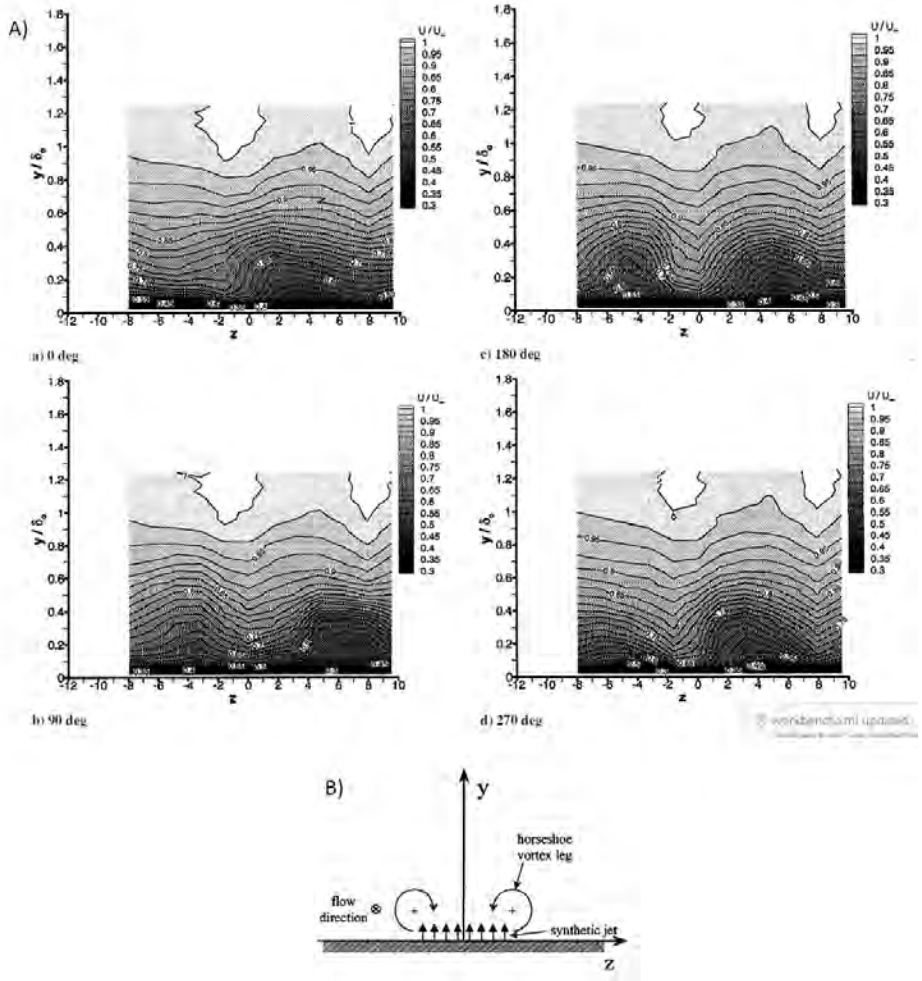

Figure 2.25: Phase average of a synthetic jet turned 20° off streamwise orientation in a cross-flow [10]

A spanwise jet naturally has a significantly larger area of effect on the cross-flow when compared to that of the streamwise and offset jets, potentially reducing the amount of actuators required. When Bridges *et al.* [10] offset the actuators a significant change in the interaction with the boundary layer was observed. The streamwise jet was seen to produce a symmetrical counter rotating vortex pair, as was also seen by Smith [11], and a degree of tilting of the vortex produced from the offset actuators. The reason for this tilt is elucidated when the interaction of a spanwise synthetic jet is looked at in detail. As was seen previously

in Fig2.18 there is an interesting interaction between the longitudinal vortex pair and the cross flow, where the downstream vortex is seen to grow significantly until it has a diameter of roughly half the aerofoil thickness, and the upstream vortex is seen to rapidly shrink and eventually break down ([7]).

Early work by Smith [11] showed that the high aspect ratio rectangular vortex produced by the synthetic jet would quickly deform as it was advected down stream. This is clearly shown when looking at the downstream monotonically increasing velocity profiles in figure 2.26. The V_R of the near wall flow at each Z value is staggered suggesting that the vortex has deformed, agreeing with the findings of Elimelech *et al.* [12] in figure 2.27, where the vortex is seen to warp along its length.

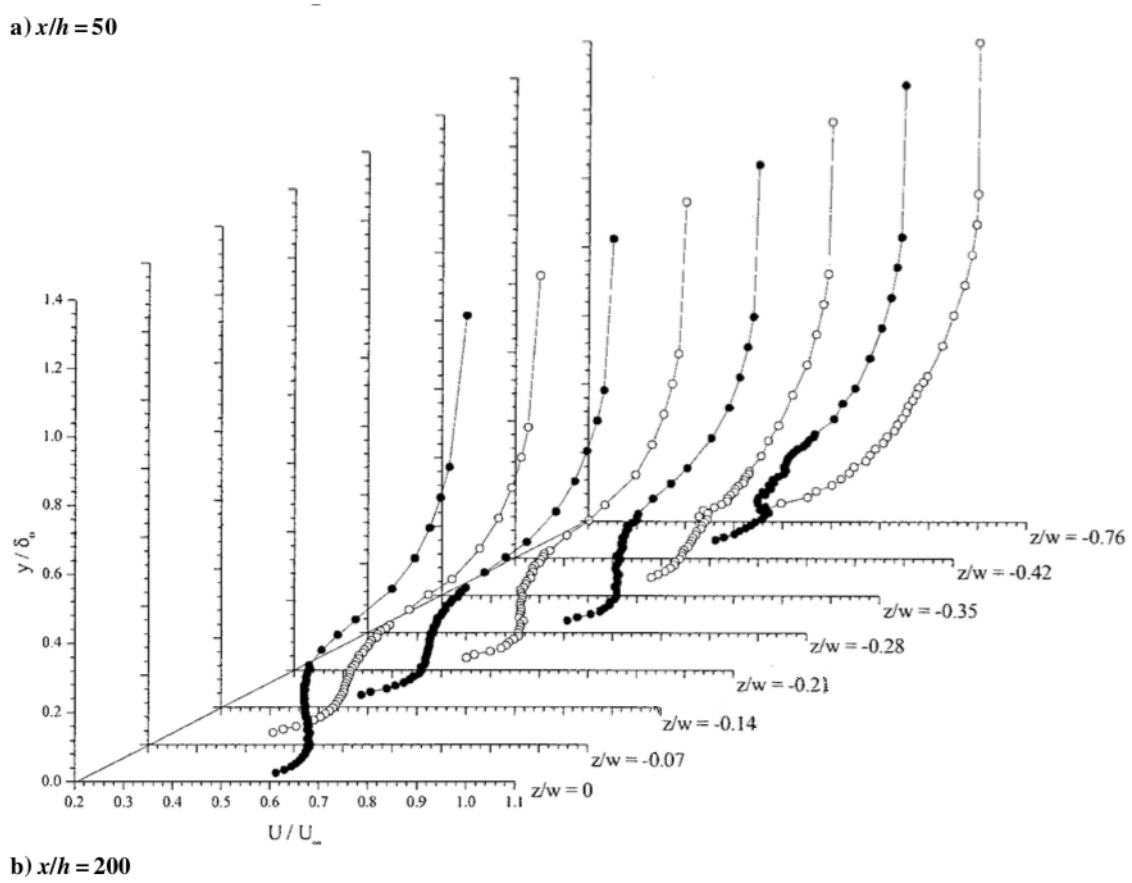

Figure 2.26: Spanwise variation in the mean streamwise velocity profile at $x/h = 200$ downstream of a spanwise actuator [11]

.

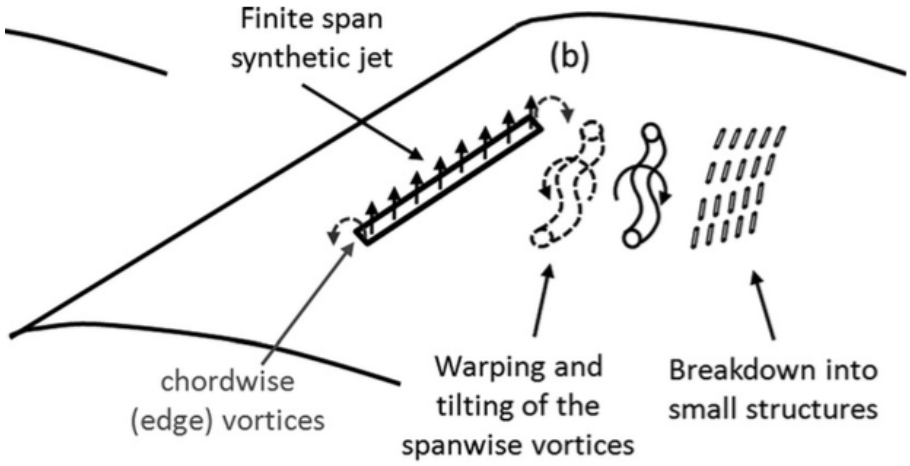

Figure 2.27: Phase average synthetic jet structures [12]

To better understand the interactions between a finite span vortex and a boundary layer, the initial structure of the vortex and the velocity ratios (V_R) of low, intermediate and high will be used to characterise the structures of the jet as it is advected downstream.
A spanwise finite span rectangular orifice produces a vortex that can be broken down into, a CCW and CW rotational longitudinal vortices and shorter counters-rotating streamwise vortices. This injection of fluid creates a blockage in the boundary layer, leading to two significant effect on the structure of the synthetic jet as it is advected downstream. Firstly the cross flow is forced to either go over the top or around the sides and consequently an area of low pressure is created in the lee of the vortex. This according to Sahni [13] results in a:

- reduction in velocity upstream of the jet, but a higher velocity downstream,
- a thickening of the boundary layer and,
- the production of organised streamwise orientated secondary structures (Fig 2.28).

These effects are seen to increase with an increase in V_R, due to the increase in size and strength of the vortex. Sahni [13] found that the two-dimensional flow spanning 95% and 60% of the span of the orifice for the low and high V_R respectively. As was the case with an with the axisymmetric vortex the level of penetration into the cross flow increase with V_R.

These effects are best seen in figure 2.28 where the structure of the jet grown in the normal to the wall as it narrows in the spanwise direction. The narrowing can be accounted primarily for by several reasons:

- Increased blockage causes a channelling effect, as more fluid is forced around the jet and a larger area of negative pressure is produced in the lee of the jet,
- the stronger streamwise vortices have an effect on a larger percentage of the spanwise vortices, while being channelled inwards by the flow,
- the interaction of the spanwise vortices with the cross flow leading them to become separated from the near wall of the boundary layer as they break down and lose cohesion (Fig2.27.).

Figure 2.29 shows the phase average two-dimensional interaction of the streamwise vortices with the cross flow over a range of velocity ratio's, where it can be seen that a finite span synthetic jet is similar to that of the axisymmetric synthetic jet in that it is possible to characterise the jets into 3 distinctive categories: (A) a low V_R where the vortex remains in the near wall of the boundary layer, (similar to that of a hairpin vortex), (B) an intermediate V_R where the vortex displays the characteristic's of both the low and high velocity ratio, where the vortex lifts from the surface penetrating deeper into the boundary layer (similar to that of a stretched vortex) and, (C) a high V_R where the jet is detaches from the surface nearer to the orifice and penetrates much deeper into the boundary layer (similar to a tilted vortex).

Sahni [13] demonstrated that the interaction between the counter rotating spanwise vortices and the boundary layer significantly affects how the jet forms and behaves downstream of the orifice. At a low V_R the CCW vortex is not able to overcome the CW vorticity of the boundary flow, and so the periodic actuation of the produces a CW dominated wave like undulation.

Interestingly as the V_R is increased enough to allow the synthetic jets CCW vortex to overcome the boundary layer flow, the CCW vortex roles over the CW vortex due to momentum imparted by the cross flow on the vortex. In the intermediate V_R it can be seen at the phase of 240^o the CCW vortex collides with the CW vortex splitting it. When moving from phase

300^o to 120^o the downstream section of the split CW vortex is completely diffused, the CCW and upstream CW vortex section are significantly weakened.

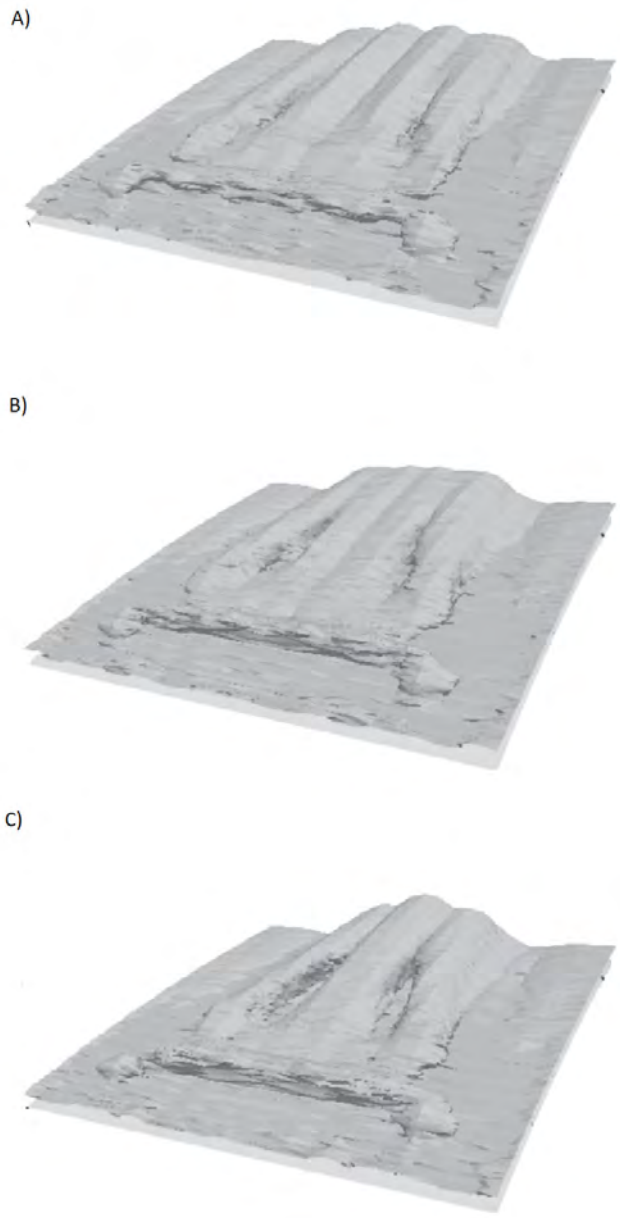

Figure 2.28: Shape of finite synthetic jet at: A) low ($V_R = 0.4$), B) medium ($V_R = 0.8$) and C) high ($V_R = 1.2$) velocity ratio [13]

When the jet is actuated to produce a high V_R the CCW vortex rolls over and past the CW vortex completely without being significantly weakened, lodging between successive CW vortices. At a phase of 240^o the upwash produced by the CCW vortex causes the downstream

CW vortex to separated from the surface at roughly $x/h = 12$.

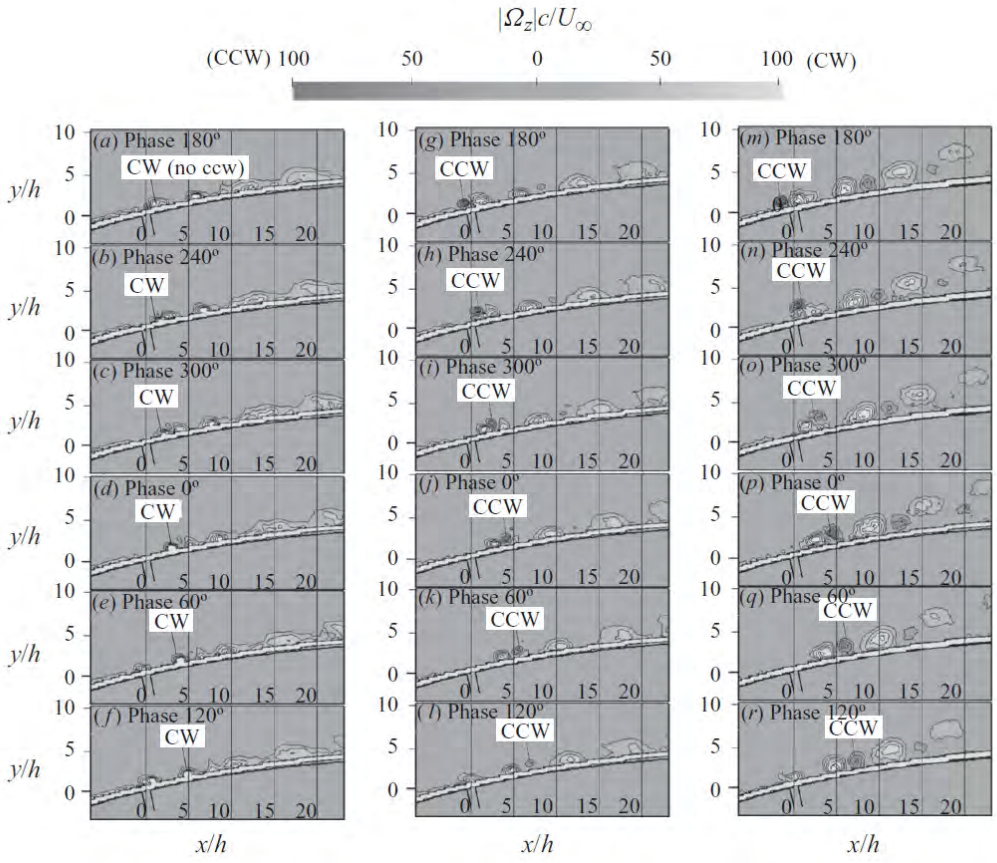

Figure 2.29: Phase average spanwise vorticity at a low (0.4), medium (0.8) and high $(1.2)V_R$ [13]

The interaction of the synthetic jet with a cross flow and the subsequent structures formed will allow the actuator to be used for fluidic control whether it is separation prevention or virtual aerodynamic shaping.

2.4.4 Fluid flow control over a cylinder

Circular cylinders have a poorly preforming hydrodynamic profile commonplace in many structures, such as offshore wind and tidal turbines that result in high structural loading due to increased levels of drag. These high structural loads result in a significant increase capital cost and added difficulty in the placing of structures. One of the biggest issues encountered by offshore technologies is securing structures to the seafloor, which is made more difficult when foundation size must be increased to accommodate the extra loading. As such a simple

means to mitigate drag forces is essential in reducing capital cost and making offshore structures more commercially viable. Synthetic jets can present a potential technology to control the hydrodynamic forces acting on the cylinder, though the exploitation of the interaction between the synthetic jet and the embedded flow ([14] [47]).

It was found by Amitay *et al.* [47], Niam *et al.* [48], Fujisawa & Takeda [15], Feng & Wang [49], and Tensi *et al.* [26] that an optimised synthetic jet actuator can significantly reduce drag (up to 30%). This is a level of drag reduction comparable to the use of a physical structures, such as the use of duel detached splitter plates by Hwang & Yang [50] to reduce drag by 38.6%. Drag reduction is achieved through the formation of a recirculation region directly behind the cylinder, by the interaction of the synthetic jet with the embedded flow. This recirculation region can act like a virtual profile, displacing local streamlines well outside the undisturbed boundary layer, and having a global effect on circulation around the cylinder. The ability of a synthetic jet to alter the flow around the cylinder, allows the SJA to modify the lift and drag forces acting on the cylinder. The ability of the SJA to modify the lift and drag forces is primarily dependant on the cylinder Reynolds number, velocity ratio, jet momentum coefficient and azimuthal location.

When the cylinder Reynolds number is set to produce a laminar boundary layer it was found that when V_R was kept constant and the jet angle was altered from a low jet angle (facing into the cross-flow) to a high jet angle (facing upstream), lift was reduced to a point of reversal. This is shown in n figure 2.30, where it was noted by Amitay *et al.* [47], that in the range of $45^o < \alpha_{SJA} < 120^o$, as the differential between the the base pressure of the forced and unforced sides of the cylinder increases (lift increased), drag reduction is increased. This indicated that as drag is reduced the levels of lift are increased, this was also found by Niam *et al.* [48]. Amitay *et al.* [14] further illustrated this in figure 2.31, where it is seen that as pressure drag is reduced, lift is increased. However, Fujisawa & Takeda [15] found that this is not always the case, as in certain circumstances lift could be modified without any alteration of drag, most likely due to the formation of a low pressure region around the orifice. It was observed by Bera *et al.* [51] that when the cylinder Re increased to produce a turbulent boundary layer that an increase in drag would also result in an increase in lift. This was also

shown by Fujisawa & Takeda [15].

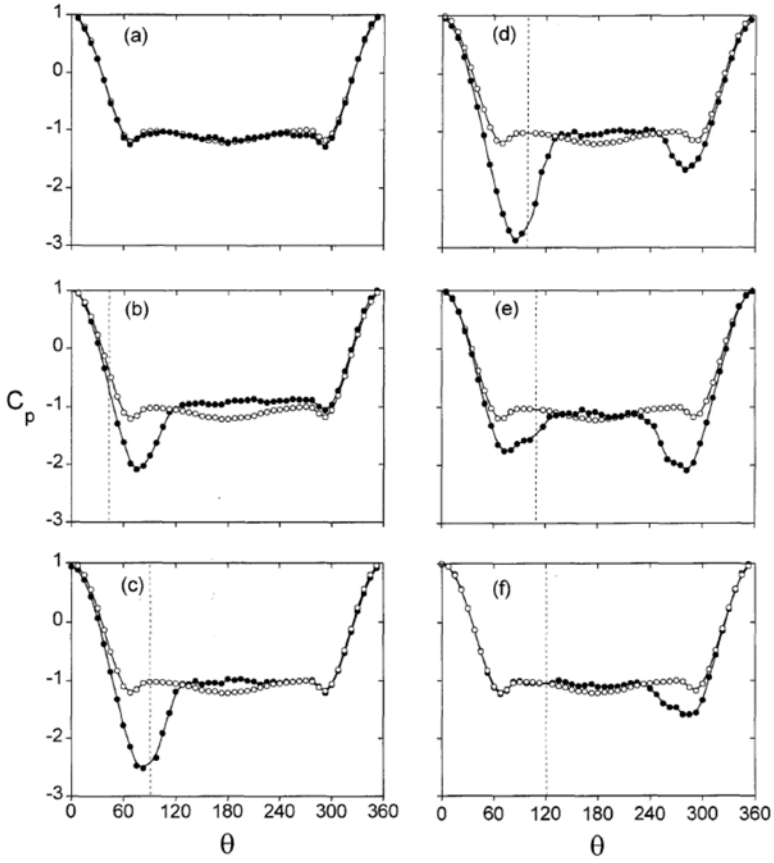

Figure 2.30: Azimuthal variations of C_p (Σ) at $Re_{SJA} = 75,500$ between the jet angles $45^\circ < \alpha < 120^o$. Unforced (empty circules) and forced (dark circles). The dashed lines indicate jet angle ([14])

Niam *et al.* [48] looked at the location of the synthetic jet in relation to the point of separation. Their work found that the optimum location for their jet setup was around 102^o, but tripping of transition would take place earlier for jet angles less than 90^o. It was found by Tensi *et al.* [26] that an SJA placed in the vicinity of, or upstream of the separation, would improve the efficiency of the jet. Feng & Wang [49] found that at high jet angles (close to 180^o) separation could be delayed by an increase in the suction duty cycle, which enabled the suction cycle to be altered and for the exit velocity to be enhanced. These findings differed from Fujisawa & Takeda [15] who established it to be at around 90^o. This descrepency is due

to the selection of an optimum jet angle at sub-critical Re being problematic as it is difficult to establish a location of separation due to the cyclical motion of the shedding vortices that are sensitive to changes in Re. Niam *et al.* [48] noted that at an angle greater than this optimum (some where around 100^o) would require a larger input from the jet in order to produce a similar result.

In figure 2.31 It is seen that the largest drag reduction value takes place at 100^o, with a sudden plummet in drag levels. Amitay *et al.* [14] suggest that this sudden drop may be due to the reorientation of the recirculating flow regions induced by the jets relative to the cross-flow. Amitay *et al.* [14] and Amitay *et al.* [47] discuses the *virtual surface* produced by jet forcing, capable of displacing local streamlines well outside of the undisturbed boundary layer, thus altering the aerodynamic forces acting on the circular cylinder on a scale of one to two orders of magnitude larger than the characteristic scales of the jets themselves. The virtual surface they observed was formed by the creation of a closed recirculation zone in the lee of the cylinder. Fujisawa & Takeda [15] found through PIV that the shape and velocity fluctuation of these zones directly impacted the lift and drag forces experienced by the circular cylinder. They demonstrated experimentally as shown in figure 2.32 I)(a), that actuation resulted in the down-stream elongation of the of the recirculation region (form and X/D of 1.5 to 4) a reduction in the width of the cylinder wake, and the lengthening of the high-velocity regions either side of the cylinder, indicating acceleration of the side-flow by the influence of the velocity deficit in the wake. In figure 2.32 II)(a) it can be seen that there is a strong suppression of velocity fluctuation by actuation, indicating that drag reduction can be achieved though actuation modifying the mean-velocity distribution and reducing the velocity fluctuations in the wake. Figure 2.32 III) shows the removal of the recirculation region near the cylinder (Fig. 2.32 III) (b)), instead it produces a recirculation region near the down-stream separating shear layer. This results in a mean reversal-flow being formed behind the cylinder, indicating a more uniform velocity distribution in the cylinder wake, resulting in a smaller turbulent kinetic energy behind the cylinder.

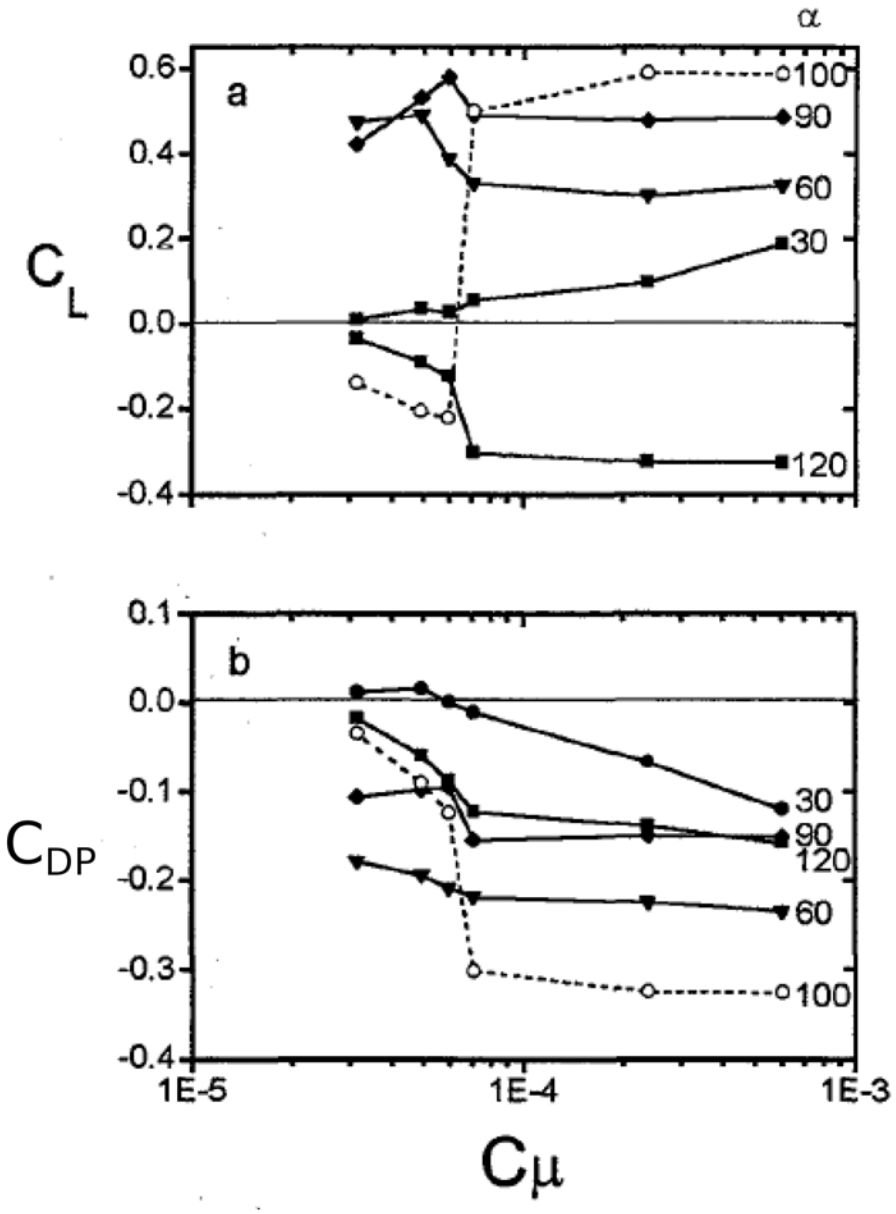

Figure 2.31: Variations of C_L and C_{DP} with C_ν between the jet angles $30^o < \alpha < 120^o$ ([14])

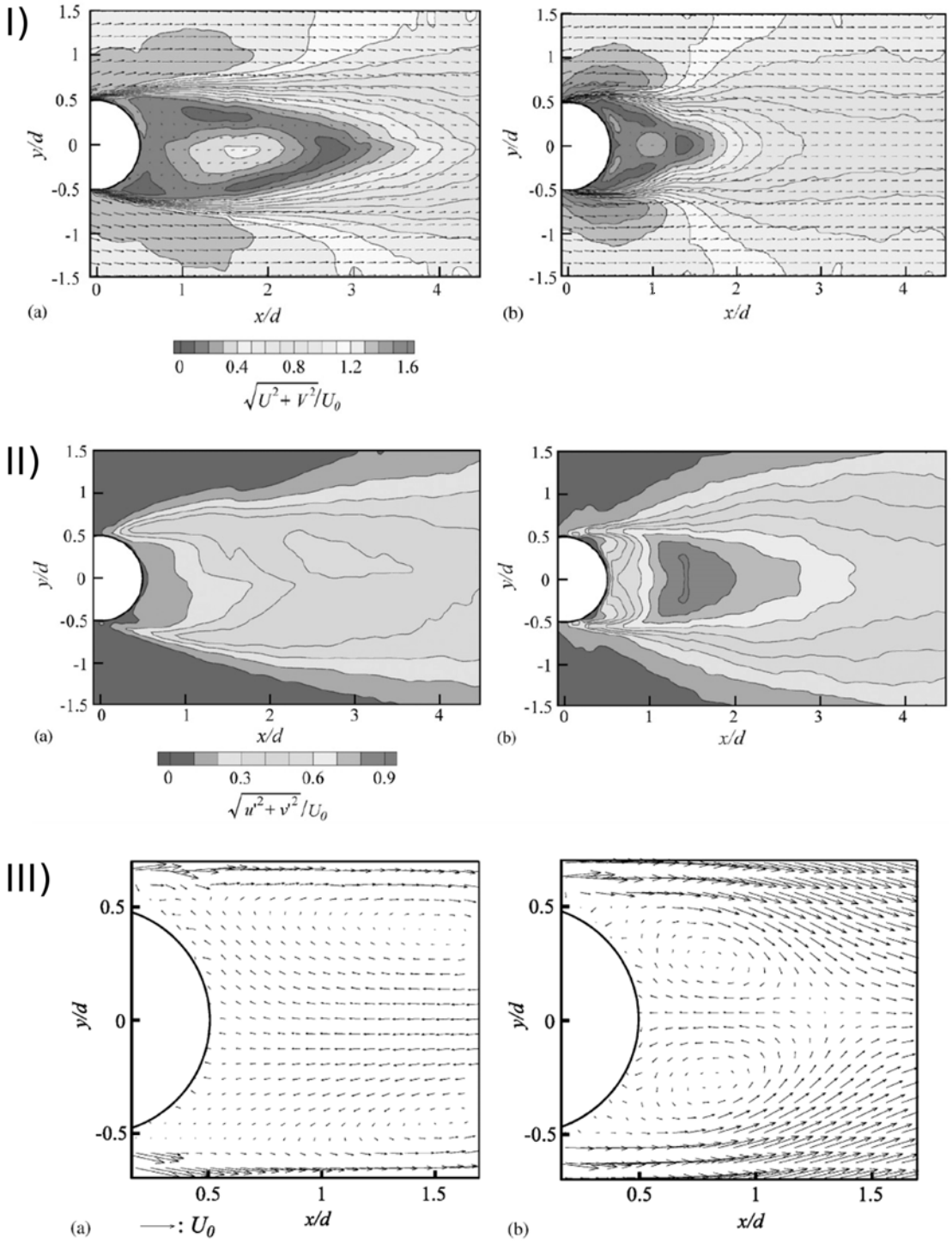

Figure 2.32: 50mm cylinder in a 2.6m/s cross-flow, with an orifice angle of 90^o. Where I) velocity vectors and contours of velocity magnitude, II)countours of velocity fluctuation, and III) close-up view of velocity vectors in near-wake region. In all cases (a) is optimum acoustic control and (b) is without control [15]

2.5 Conclusion of the literature review

This literature reviews focused on building an understanding of how a synthetic jet actuator behaves in quiescent fluid, a cross flow and how it alters the fluid flow over a body. It was found that a synthetic jet could delay separation reducing the wake size, reducing drag forces by up to 30%. In the case of a synthetic jet located on one side of the cylinder it was found that as drag was reduced lift was increased ([48] [14] [15]). If was found that drag reduction ability of a synthetic jet could be fine tuned by altering the velocity ratio and circumferential location of the jet. This lead to optimum jet angles being established that differed depending on cylinder Reynolds number. Amitay *et al.* [14] & *et al.* [47] discussed the formation of a virtual surface in the lea of the cylinder and Fujisawa & Takeda fujisawa2003flow where able to show these structures using particle image velocimetry.

After reviewing the literature review it was found that even there is little work on:

1. producing a simple test method of mapping a synthetic jets effects on drag levels on a cylinder in cross flow over a large range of values, though direct force measurement,

2. using PIV equipment to produce high speed and high definition flow visualisation to give a detailed interaction of the interaction and effects of the vortices produced by the synthetic jet actuator on the boundary layer, shear layer and cylinder wake, form drag reduction to drag increase, and to show the basic structures of the virtual profiles.

3. Using particle image velocimetry to show the effect of an synthetic jet actuator on the cylinder wake in terms of average velocity, average turbulence intensity, and average voracity. Allowing the shape of the virtual profiles to be determined, the strength of wake shear layers and the effect these structures have on the flow around the cylinder.

Chapter 3

Experimental Apparatus

3.1 Introduction

The experimental setup for this project was an ambitious feet, requiring the designing and building of a fully functional, purpose built water tunnel to allow for high quality flow visualisation (FV) and particle image velocimetry (PIV) to be performed on the effect of a synthetic jet on separation. All parts of the water tunnel were custom built for this project, with a modular setup to allow for future improvements. For this reason the experimental setup section is quite extensive, but still only represents a portion of the setup required to produce the final product.

3.2 Closed circuit water tunnel test facility

In order to be able to accurately test the abilities of a synthetic jet to prevent separation over a stalled body, FV, PIV, and strain gauges where used to determine the effect the synthetic jet has on the flow over the cylinder and its effect on lift and drag. In order to produce the best quality results, water was used, due to its benefits when working with FV and PIV (such as more uniformly suspended particles and ease of controlling particle density). Water also increases the strain effects on the strain gauges resulting in simpler system for recording the lift and drag forces.

In order to work with water it was necessary to design and build a fully functional and purpose built modular closed loop water tunnel. The initial designs where based on the designs for a wind tunnel (as the literature was more available). The tunnel was given some basic rules set out by Gordon & Mohammed [16] and mehta & Bradshaw [52] to governing the layout and design.

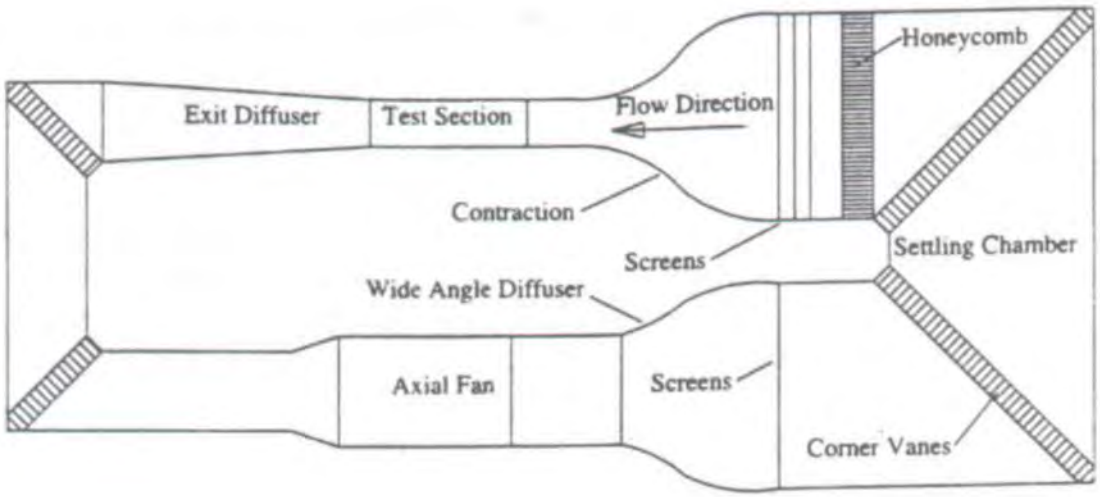

Figure 3.1: Basic layout of a wind tunnel [16]

The rules lay out the basic parts of the water tunnel required to produce a test section with sufficiently low turbulence intensity. (I) An open or closed circuit tunnel, (II) a well designed contraction and diffuser either end of the test section, (III) correctly designed test section, (IV) effective turning of the flow, (V) Turbulence reduction and, (VI) appropriate drive system.

3.2.1 Water tunnel layout

The layout of the water tunnel is shown in figure 3.2 below. It is a closed circuit design, meaning it has a well designed pressure recovery return flow (e.g. the fluid is not being deposited into an open channel). A closed loop benefits in that not all pressure is eventually lost, the careful reduction of pressure through flow control measures produces less turbulence and maintains a more developed flow. It also means that the system responds very quickly to user input for pumping power, reducing settling time.

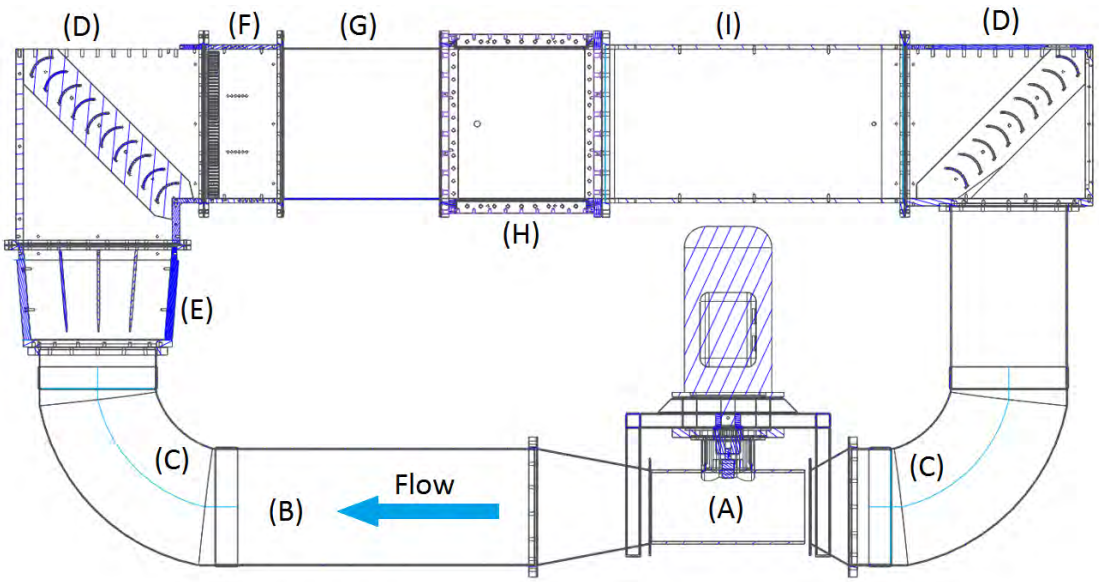

Figure 3.2: Cross sectional cut through of water tunnel

Starting from the drive system figure 3.2(A) has a pipe of a smaller diameter in order to accommodate the factory sized propellers. This requires a diffuser to allow the flow to expand more gradually into the larger diameter long horizontal pipe 3.2(B). The increase in diameter reduces wall effects on the flow and and reduces the mean velocity, which coupled with the length reduces the turbulence caused by the rotors.

At each corner of the rig there are 90° turns, at the bottom they are cylindrical (figure 3.2(C).) and the top mitre bends (figure 3.2D).). The mitre bends require turning vanes in order to aid the flow around the corner, reducing turbulence and pressure losses.

Figure 3.2(E) is the cylindrical to rectangular diffuser, a change from circular to rectangular is due to the test section needing to be a rectangular shape to facilitate PIV tests. This diffuser is designed to allow the flow to transition with as little turbulence increase as is possible. The settling chamber 3.2(F) is the last point of turbulence reduction prior to the test section. In a traditional system a settling chamber would have a honeycomb and screens, however due to the nature of water it was found that a screen would most likely be detrimental to flow control as it would most likely flex or pulse in the flow resulting in adding of turbulence and an negatively affecting the velocity profile[53].

3.2.2 Test section

In designing a water tunnel the test section (Fig. 3.2(H).) is the most important part, it influences the design of the entire system. In the design of the test section it is desired that the maximum speed and size possible will be achieved, and as these are opposing criterion a compromise must be reached.

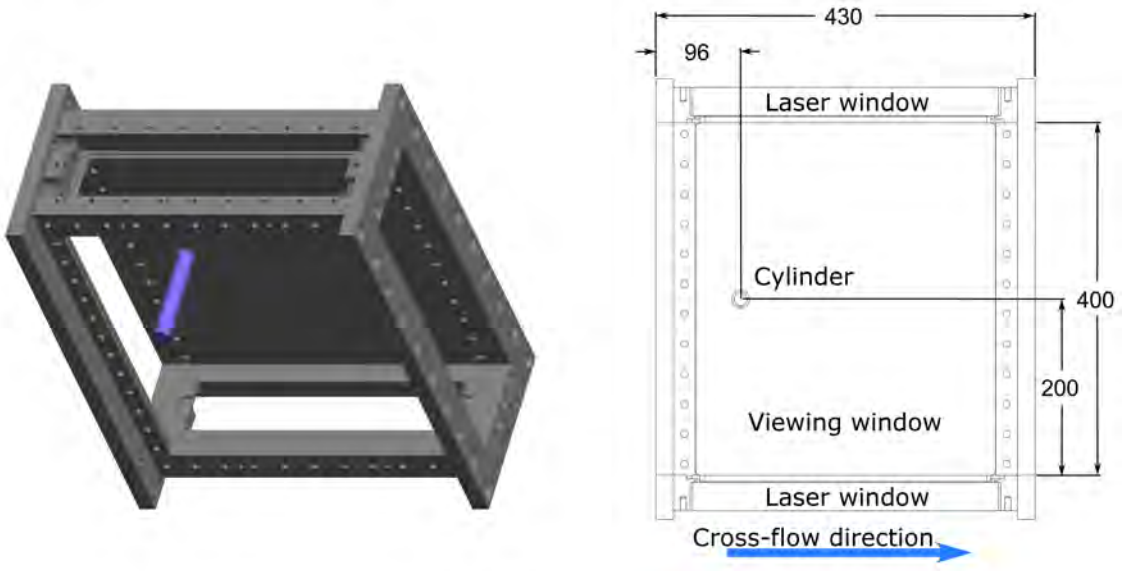

Figure 3.3: Test section corresponding to figure 3.2 (H)

The sizing was based on the use a 20mm diameter cylinder. This led to a height of 400mm to prevent any wall interference at high angles of attack, and a length of 400mm, 3.3 times the width (Rae *et al.* [54] suggest width to length ration of two or greater when the wake of the model is of concern). The width of the test section was chosen based on the use of a 40mm wide finite span synthetic jet. Rae *et al.* [54] suggests a span of no more than 0.8 of the width.

The flow rate of the test section was based on the Reynolds number over a 60mm aerofoil or a 20mm diameter cylinder. At the expected maximum velocity achievable with the selected dimensions this will allow for a Reynolds number of $8.16x10^5$. As can be seen in figure 3.4 at this Reynolds number, separation over a cylinder will have taken place.

The test section required an intricate design to accommodate the test required. It consists of a shell that holds a large viewing window and a large mounting window at each side, that can be interchanged. It has two large laser sheet ports to allow for two-dimensional streamwise sheets to be positioned at different streamwise and spanwise locations and it must also be water and air tight at the highest velocities experienced in the water tunnel.

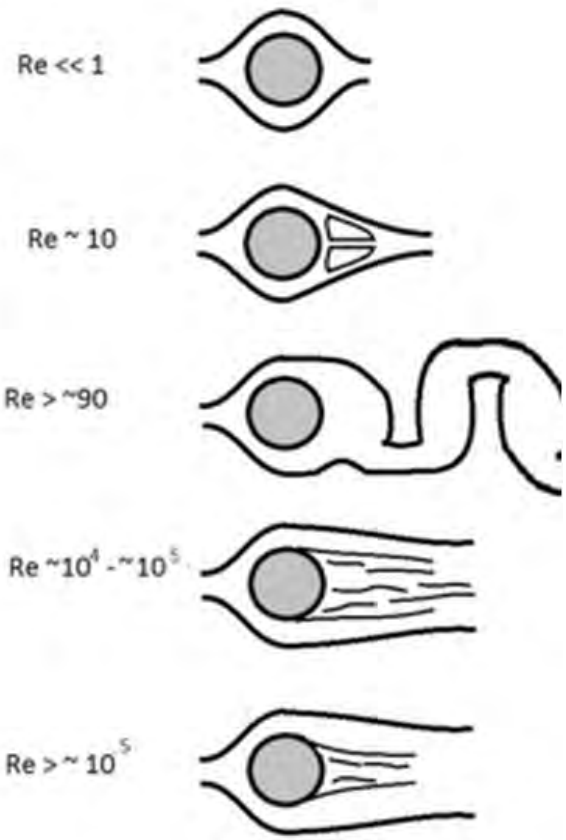

Figure 3.4: Effect of Reynolds number on flow over a cylinder

3.2.3 Contractions

The main contraction (Fig. 3.2(G).) takes the flow from the settling chamber to the test section while increasing the average speed. When contracting the flow the side wall geometry needs to allow the flow speed to increase while maintaining a uniform velocity profile. The flow exiting the chamber needs to have a uniform velocity profile, as it cannot be left to settle

as any settling time will increase the wall effects and thus affect the velocity profile.

Figure 3.5: Internal view of contraction as seen in figure 3.2 (G)

3.2.4 Diffusers

The performance of the diffuser (Fig. 3.2(I)) is estimated by relating the geometry and inlet flow conditions of the diffuser to a number of standard diffuser geometries with a defined inlet flow condition [17]. A diffuser should be designed to be at or below an optimum design line (as show in figure 3.7), if it the diffuser is to maintain flow stability, be effective at reducing energy loss in the system and produce a uniform velocity profile.

For a diffuser to work the offset of the wall angle must not exceed 6°, if this value is exceeded then significant flow separation will take place, thus rendering the diffuser ineffective [17]. Due to facilities available to this project the diffuser was required to be as short as possible resulting in an increased offset wall angle of 9.9°. The length of the diffuser

(N) is $0.8m$.

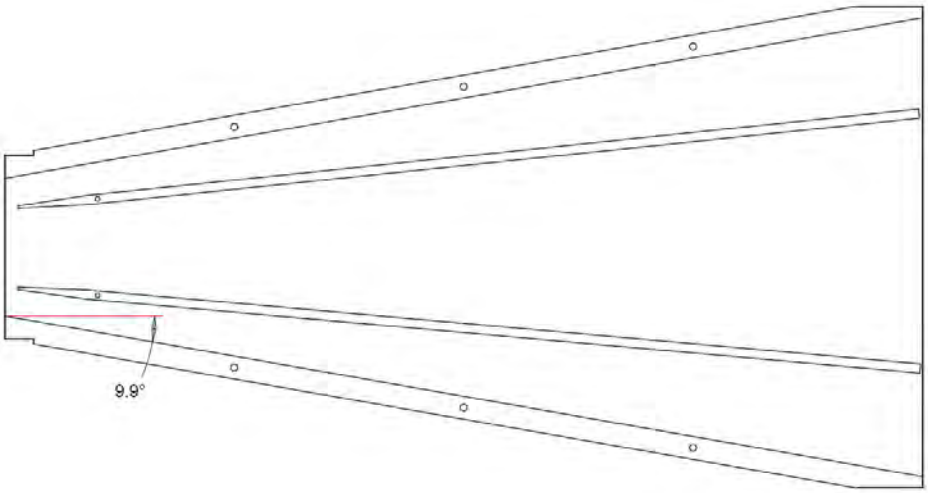

Figure 3.6: Basic layout of a diffuser

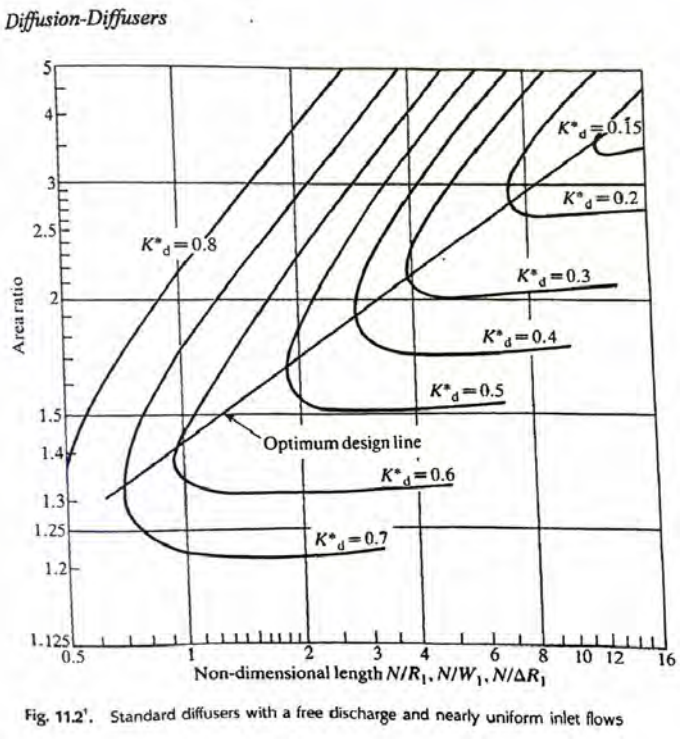

Figure 3.7: Standard diffuser with a free discharge and a nearly uniform inlet flow[17].

To conform with figure 3.7 the length is converted into a dimensionless length (N/W_1), where W_1 is the inlet width of the diffuser (0.12m.), giving a dimensionless length of 3.3. The area ratio is a ratio of the inlet area A_in to outlet area A_out, in this case an area ratio

of 3.3 is required. When these values are imputed into figure 3.7, a value well above the optimum design line is given. As the area ratio is fixed, the length is the only geometry that can be changed, however the length would need to be increased to approximately 1.8m. This was not possible due to space and machining constraints. This necessitated using a more complex system of adding vanes.

The addition of vanes can increase the wall offset angle to 25° when 3 vanes are used and 20° for two [17]. For this thesis 2 vanes were used as the increased reduction produced by a third vane on the loss coefficient was not significant enough to merit the possible uncertainties in the setup of an extra vane (Fig. 3.8).

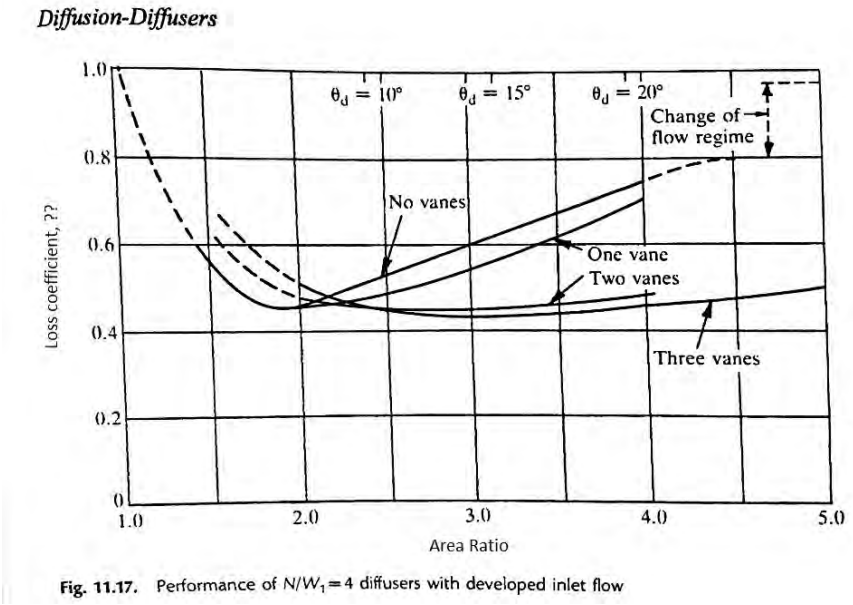

Figure 3.8: Basic layout of a diffuser with vanes

According to Miller [17] Reynolds number will have a complex effect on the diffuser, especially if there is a smooth contraction a short distance upstream such as on this rig, as this contraction produces a boundary layer at the inlet. This causes a larger loss coefficient in narrow optimally designed diffusers. This supports the selection of a wider angle diffuser as the effects of Reynolds number are minimised.

3.2.5 Propulsion

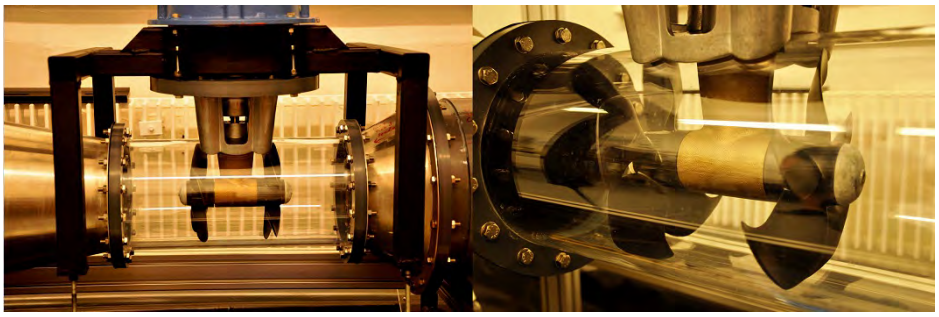

Figure 3.9: Photographs of the axial flow pump installed on the water tunnel (corresponding to A in Fig. 3.2

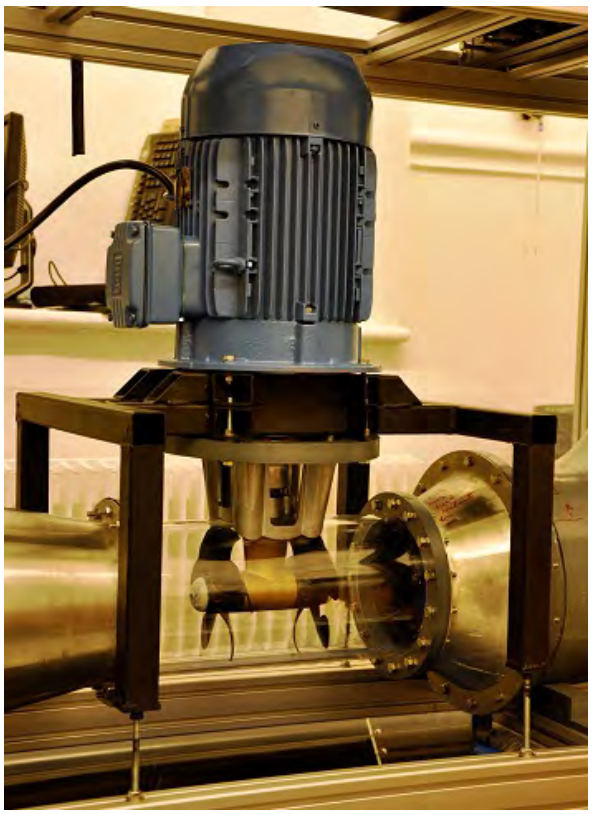

Figure 3.10: axial flow pump

The propulsion system in the water tunnel sets the maximum free stream velocity possible in the test section. The propulsion system for the water tunnel can be broken down into three parts, a 50Hz 5.5KW (6.3KW overdrive) electric motor, dual 0.185m diameter bow thruster rotors, capable of producing 180N of thrust at 3000RPM, and a 0.195m diameter pipe section. As this propulsion system is not standard, there is no pump power curve.

In order to determine the flow rates that would be possible from this pump an initial velocity was required. As a simple point of reference the entire system was looked at as a only the pump section working in and open channel allowing the assumption that there was no pressure recovered. This gives the lowest maximum velocity that could be expected. This velocity was found using:

$$U_\infty = \sqrt{\frac{T}{(\rho \pi D_H^2/4)}} \tag{3.1}$$

From this it is possible to get the flow rate:

$$Q_{pump} = \frac{U_{pump} \pi D_H^2}{4} \tag{3.2}$$

Using these equations it was found that the maximum rate of flow would be $0.17 m^3/s$, which equates to a test section velocity of 3.564 m/s. This is not a true representation of the flow in the water tunnel as there will be a certain amount of pressure recovery.

3.2.6 Pressure loss

To adequately set up testing it is necessary to determine the expected free steam velocity range that would be available in the test section. As the flow has to go though several diffusers, contractions, bends and flow straighteners (resulting in a significant pressure drop), the pressure drop attributed to each part had to be calculated to give a total pressure loss experience by the flow. Equation 3.3 is used to estimate the total pressure loss (ΔP) in each section:

$$\Delta P = P_{dyn} K_d \tag{3.3}$$

Where the dynamic pressure (P_{dyn}) is given in equation3.4 and the loss coefficient (K_d) from Miller [17] is given in equation3.5. For the more complex parts such as the diffusers and contraction, K_d was found using empirical date supplied by Miller [17]. This empirical data is used to give a good approximation of the pressure losses, as a full CFD simulation would be overly complex and with the number of unknowns could not be guaranteed to give

a good result.

$$P_{dyn} = \frac{\rho U_\infty}{2} \tag{3.4}$$

$$K_d = \frac{4 f_r L}{D_H} \tag{3.5}$$

When all of the pressure losses are calculated, it is possible to determine the individual parts responsible for the greatest amount of pressure loss. This can be seen in figure 3.12, where the pressure losses of over two different configurations are shown at a pump flow rate of $0.17 m^2/s$. These configurations are the pressure losses with; A) all flow control devices in place ($\Delta P = 5,156 Pa$) and B) and no flow controls ($\Delta P = 7,873 Pa$). A reduction in pressure loss of 42% can be achieved by implementing all flow controls. This reduction in pressure loss results in an increase in the rate of flow from the propulsion system.

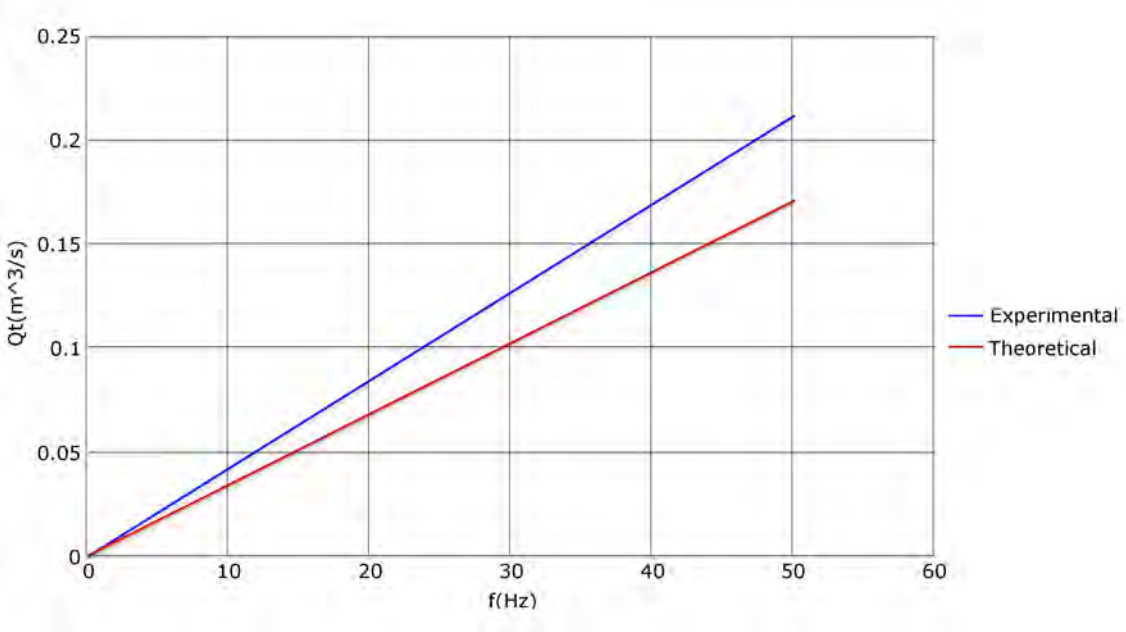

Figure 3.11: Theoretical no pressure recovery and experimental flow rates

From experimental data the flow velocity in the test section was measured from 0.2Hz to 18Hz in increments of 0.2Hz over the majority of that range. This data showed that the flow speed increased linearly as was expected from theoretical results (figure 3.11). The experimental flow (extrapolated beyond 18Hz) rate being greater than the theoretical value

confirms that the recovery of pressure has increased the maximum velocities that can be produced by the propulsion system.

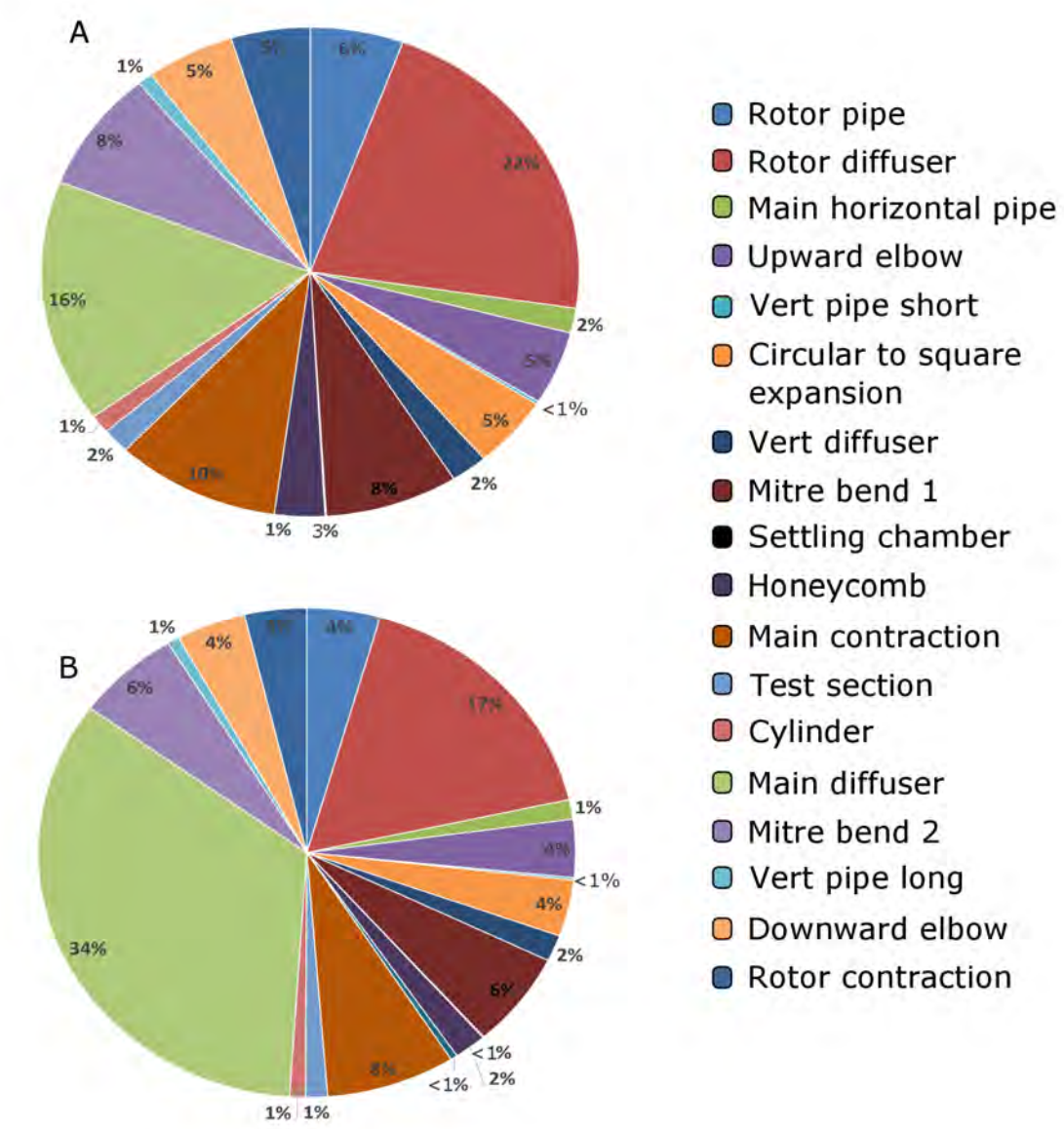

Figure 3.12: Pressure loss across the water tunnel when: A) flow conditioning present and B) no flow conditioning present

Figure 3.13 shows the expected pressure losses in the system at the 4 different conditions already mentioned, and using the interpolated experimental results, a rudimentary power curve has been established to give an expected flow velocity for a given pressure loss. This power curve makes it possible to approximately determine the velocities that will be achieved by improving flow controllers. Improving the flow controllers does not only improve

the efficiency of the pump but also reduces the turbulence intensity in the flow, which is preeminent in producing good PIV results in a water tunnel.

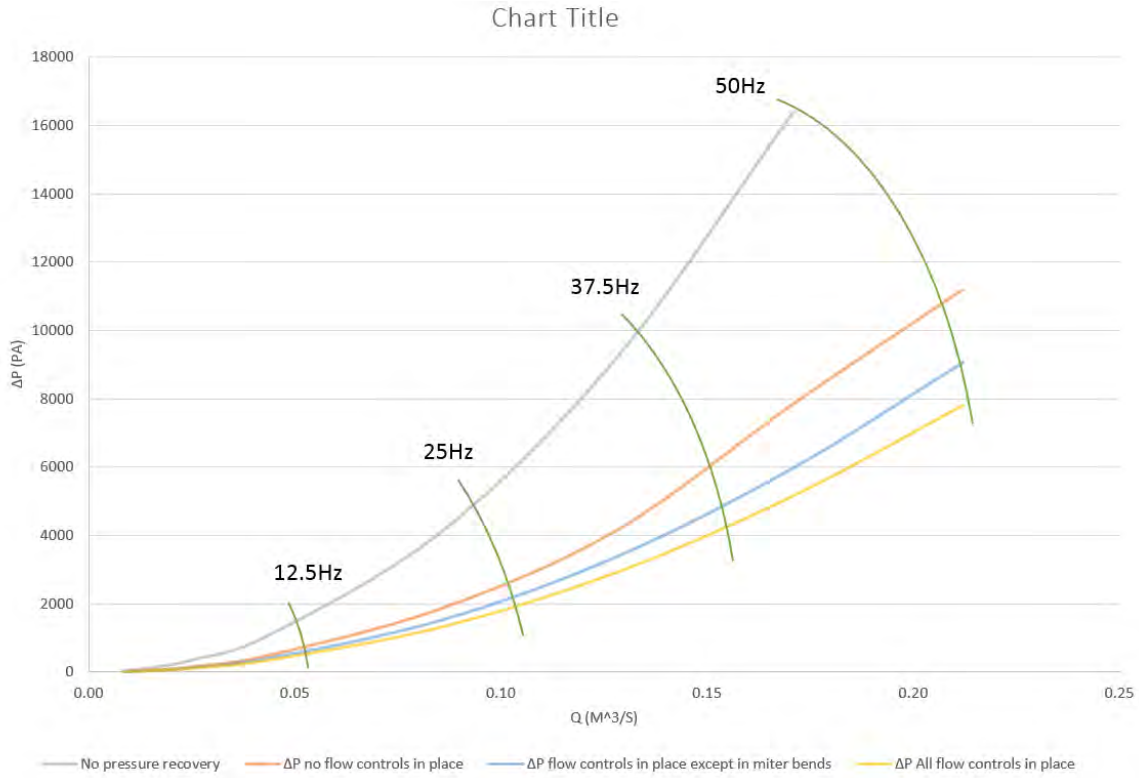

Figure 3.13: Water tunnel pressure losses

3.2.7 Frame

The water tunnel frame is made from 40×40mm and 40×80mm box profile aluminium, it is designed to be load bearing, practical (for camera and laser) and also aesthetic.
As the water tunnel contain $0.7m^3$ of water, weighs approximately 1000Kg, and capable of reaching a velocity in the test section of about 4.2m/s, a secure frame is necessary. The frame design in figure 3.14 was chosen as it would spread the weight out over the 3m length of the tunnel producing a pressure of approximately $3.3KN/m^3$, and would provide sufficient lateral stability for any effects caused by high flow rates.

Figure 3.14: Water tunnel frame

3.3 Turbulence intensity reduction

In the design of the water tunnel the primary goal is to produce a flow in the test section that is as near as possible to a parallel steady flow, with uniform speed through([54]). In the design of this tunnel the turbulent reducers looked at are:

- Honeycombs and screens.
- Diffuser and turning vanes.
- A well defined contraction.

3.3.1 Honeycombs and screens

In this water tunnel a honeycomb was selected to provide the main turbulence reduction. They effectively reduce cross flow velocity, swirls, turbulence length scales, mean flow gradients and lateral turbulent components ([55], [56]). They have a lesser effect in reducing

longitudinal components of turbulence (or mean-velocity variation or axial turbulence) in comparison to wire mesh screen. For this reason, it is commonly accepted that a honeycomb is best at primarily straightening the flow, reducing the lateral components in the main flow and breaking down the lager eddies in the main flow [55].

Honeycombs force the main body of water to flow in one axial direction, producing a more uniform velocity gradient. In order to optimise the efficiency, the cell shape, size, length and positioning must be selected carefully.

In turbulence suppression it is normal to have a series of honeycombs and screens placed in the settling chamber. When devices are placed in series the decay rate must be taken into account, if the devices are place to closely an undue effect can occur, increasing turbulence and pressure losses [55]. In the case of a honeycomb, this turbulence usually takes 10 cell diameters to dissipate, approximately 75mm in this case[57].

A single honeycomb was used as it would provide sufficient flow controls, based on the manner in which water acts on flow conditioners and the geometries of the water tunnel. The settling chamber has a length, after the honeycomb of 170mm, which wouldn't allow for the addition of a second flow conditioner without increasing the length of the settling chamber, as the flow entering the contraction must have as smooth a velocity profile as is possible. Lumley & McMahon [53] found that a higher Reynolds number in the cell leads to better turbulence reduction. Lumley & McMahon [53] also found that the use of screens in water results in significant pressure losses and excess loading, producing pulsing or singing in the flow. This would result in an increase in the downstream turbulence to that of the upstream.

It was found numerically that for the flow conditions expected in the water tunnel that a single honeycomb with a thickness of 35mm and a hexagonal cell diameter of 7.5mm placed at the entrance to the settling chamber could reduce turbulence in the test section to as low as 0.3%, within acceptable limits for PIV testing.

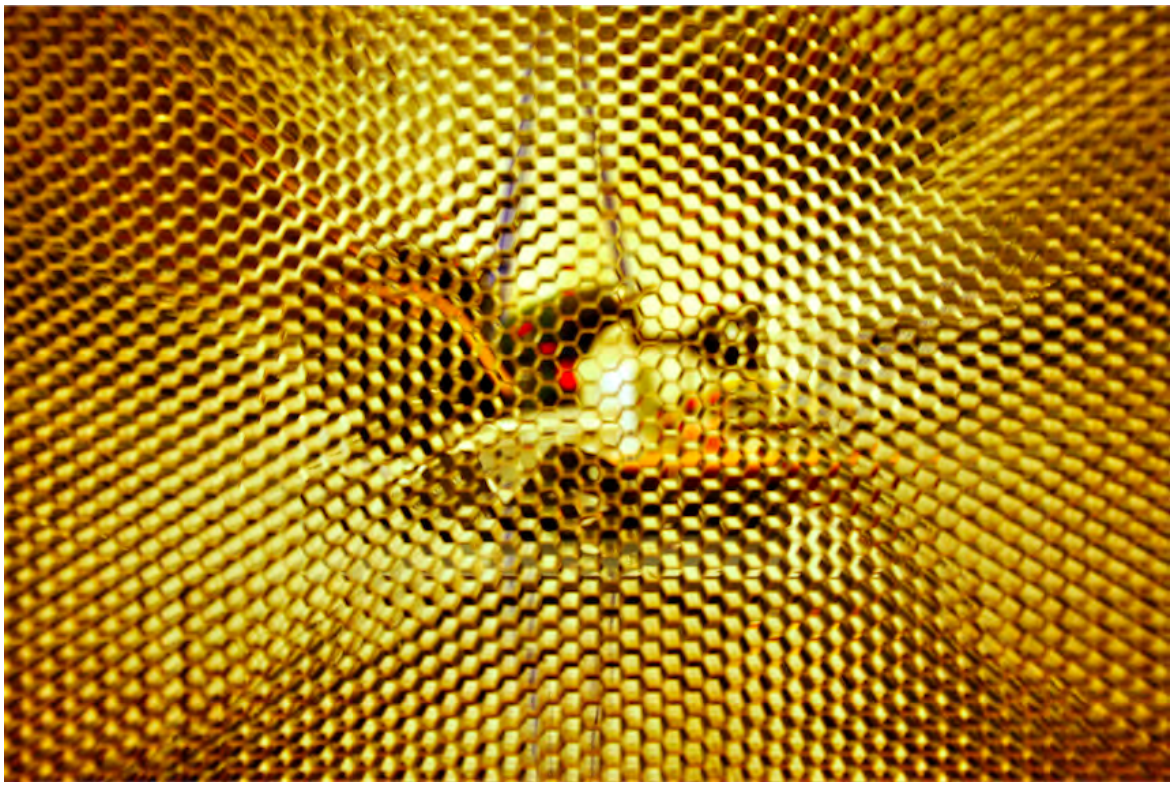

Figure 3.15: Honeycomb

3.3.2 Turning vanes in mitre bends

The use of 90 deg mitre bends in the upper corners gives rise to several problems with regards to flow stability, turbulence and the velocity profile. Flow around a sharp turn leads to the central core of fluid going straight into the wall normal to the flow, resulting in some of the flow being reversed producing a vortex pair [58], this instability created within the flow will have a detrimental knock-on effect on the flow quality in the test section [59], [60], [54].

If guide vanes are not used, then more emphasis needs to be put on the flow conditioners in the settling chamber to sufficiently reduce these instabilities. This would result in a significantly larger pressure drop [59]. Miller [17] found that the use of turning vanes allows the Mitre bend to act similarly to a bend with a circular cross section. The guide vanes are used to prevent large pressure losses and to help maintain a straighter flow, the shapes of the turning vanes can vary form simple semi-circular vanes to highly cambered aerofoils [54], in this thesis it was not possible to produce the latter due to budget restrictions. The mitre

bends used instead where of a simple design thin semi-circular vanes presented by Miller [17], where Johl *et al.* [61] found that with the right setup good results could be obtained form simple vanes.

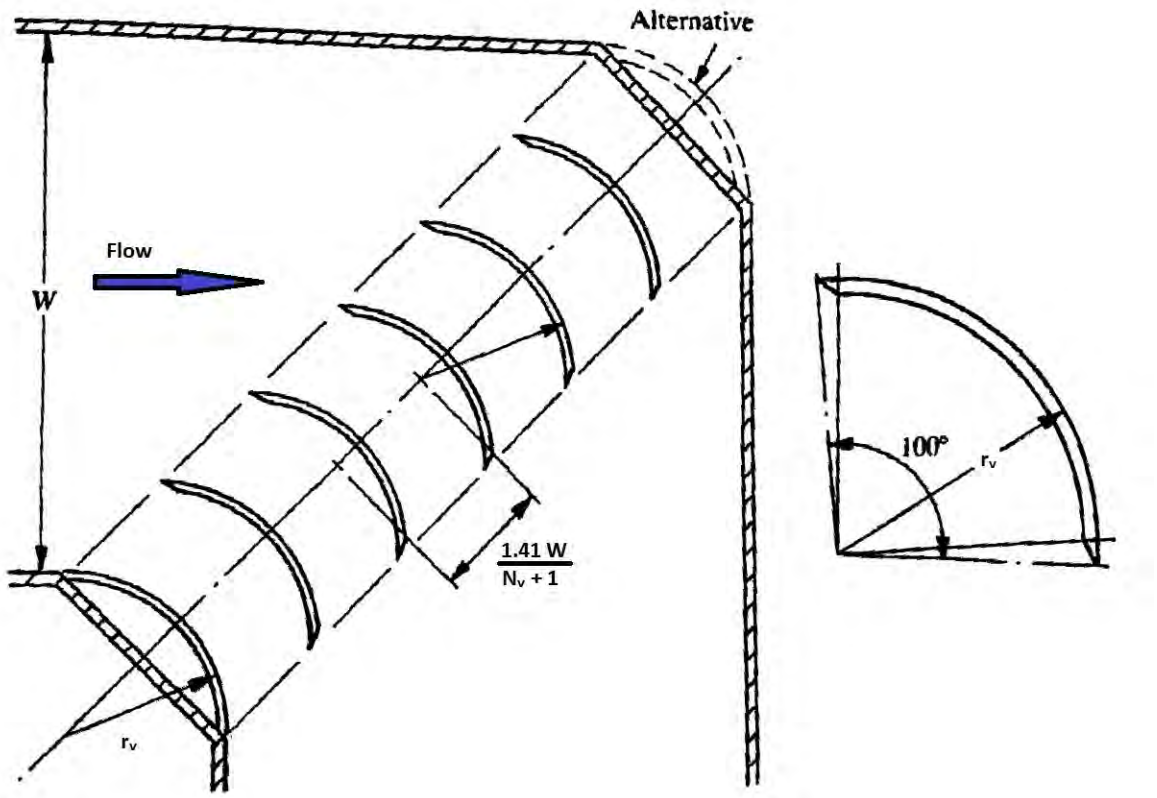

Figure 3.16: Geometry of turning vanes [17]

The number of vanes used is determined by:

$$N_v = \frac{1.8W_v}{r_v} - 1 \tag{3.6}$$

Where N_v is the number of vanes, W_v is the width and r_v is the vane radius of curvature (r_v is based on W). For this project it was found that the optimum umber of vanes was 13 spaced at 40mm apart. This configuration can be seen in figure 3.17.

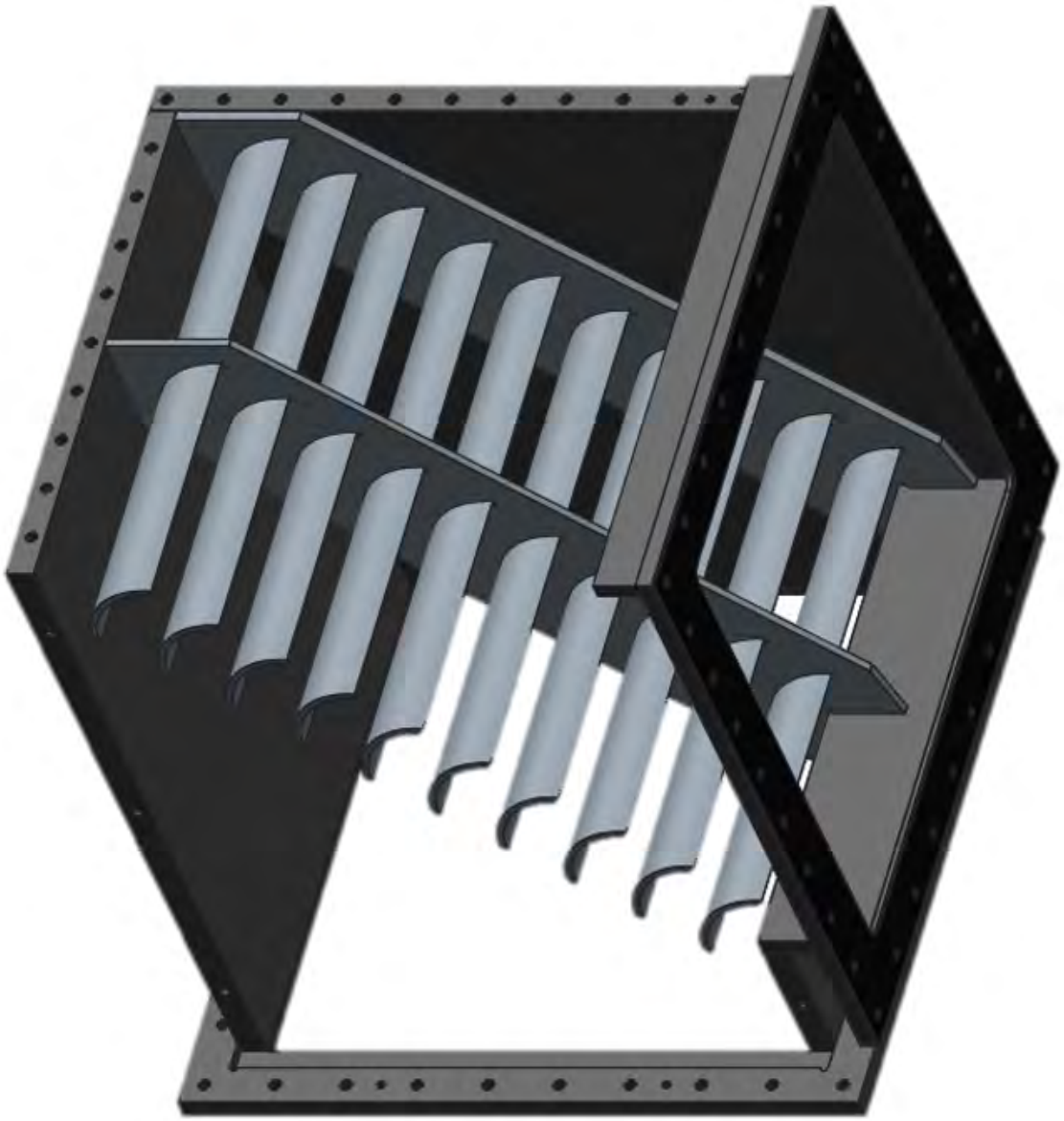

Figure 3.17: Setup of turning vanes in mitre bend

3.4 Test section layout

In order to get the most effective test results from the water tunnel a good deal of time was spent on the test setup within the test section. To achieve this several goals were identified; (a) the system had to allow for easy PIV setup and allow for a broad range of tests where the tests had to be repeatable, (b) the setup had to give a lift and drag reading and (c) a synthetic jet actuator that the frequency and stroke length could be changed as required.

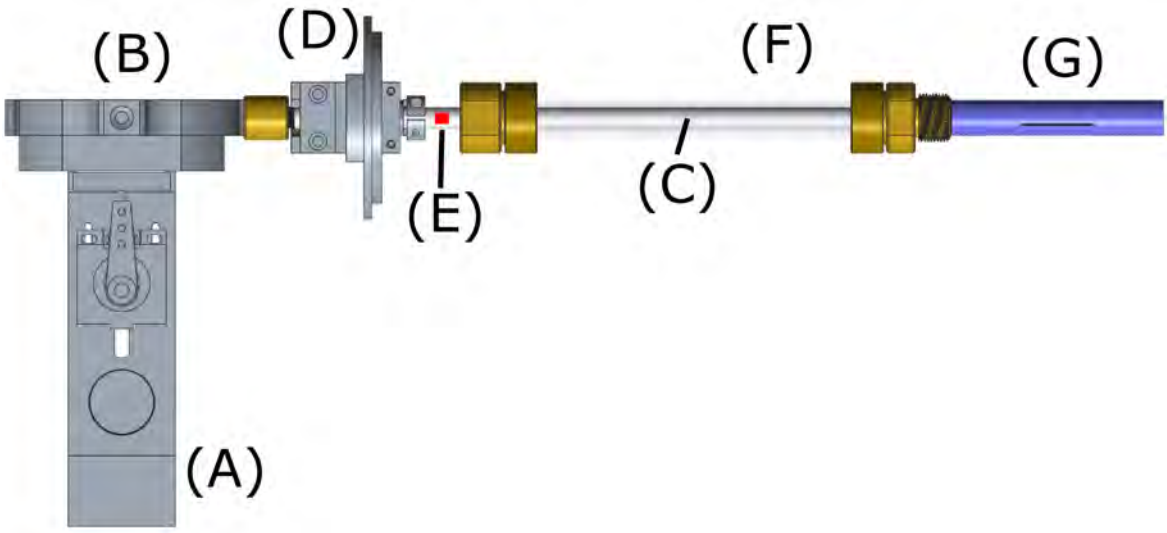

Figure 3.18: Test section test piece setup

Figure 3.18 details the layout of the testing mount and synthetic jet actuator where: (A) is the synthetic jet actuator, (B) is the jet cavity containing a bleed valve to remove any air, (C) is the sting arm, (D) clamp and Vernier scales, (E) are the strain gauges, (F) is the insertion chamber and (G) is the cylinder with a finite synthetic jet orifice slit.

3.4.1 Synthetic jet actuator setup

The synthetic jet actuator is the heart of the project and so it functionality is pivotal. The original test using speakers proved to be ineffective due to the large forces required to push the water through the orifice. So in order to overcome these forces, a piston drive system shown in figure 3.19 was used. This was in keeping with the idea of the system being kept simple. Piston drive systems have a reciprocal motion, which even though its not sinusoidal, the small eccentricity results in no significant difference.

Figure 3.20 I shows the full synthetic jet actuator and figure 3.20 II shows the cross-section of the cylinder. During the suction phase fluid from the test section is drawn thought the jet orifice (Fig. 3.20 I.a) by the jet pump (Fig. 3.20 I.b) via the hollow sting arm (Fig. 3.20 I.c), to a pump chamber (Fig. 3.20 I.d). This process is reversed during the ejection phase, resulting in a vortex rolling up around the edges of the jet orifice (Fig. 3.20 II). This side is known as the forced side of the cylinder.

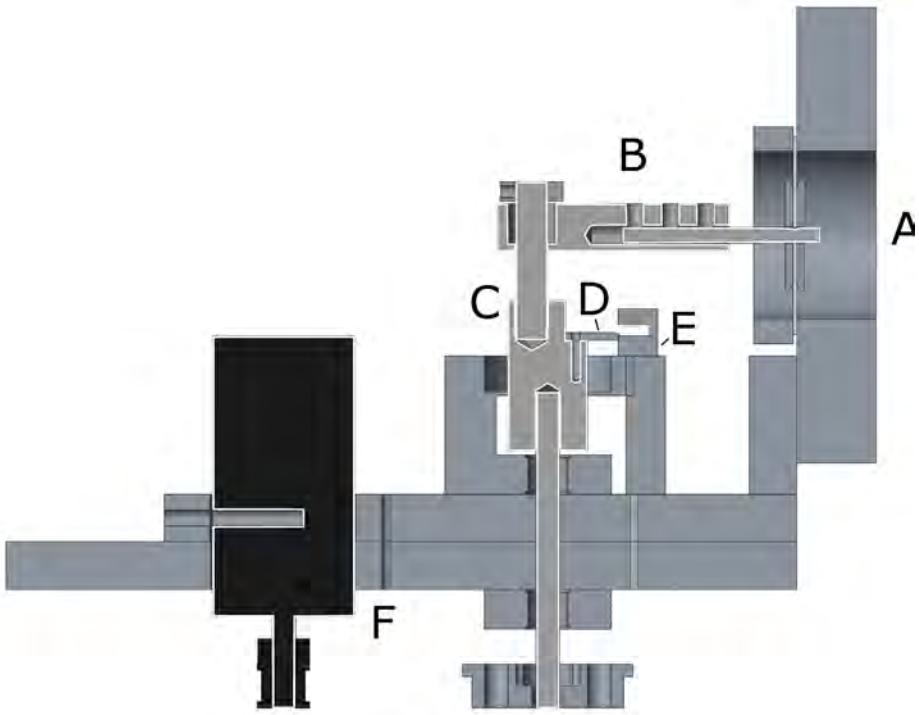

Figure 3.19: Synthetic jet actuator drive, where 1) is the piston, 2) is the piston arm, 3) is the crank, 4) is the splitter, 5) is the light-gate, and 6) it the continues frequency motor and gear drive

Figure 3.19 is a schematic of the SJA pump and the main SJA chamber. Fluid is drawn in and expelled from the SJA by the movement of the diaphragm and piston head (Fig. 3.19 A). The Piston head imparts the majority of the force on the fluid, with the diaphragm being primarily for sealing. The stroke length of the SJA is determined by the eccentricity of the crank (Fig. 3.19 C). The eccentricity of the crank is given by the piston being mounted to a rod that has an offset of either 0.125mm or 0.25mm form the centreline to give a 0.25mm or 0.5mm stroke length. The SJA is powered by a continuous frequency drive motor (Fig. 3.19 F), that is connected to the crank via a drive shaft and a gearing mechanism. The gearing mechanism is designed to allow the pump to operate under minimal torque conditions over the range of jet frequencies selected for this thesis (1Hz < f_{SJA} < 12Hz), to give a smoother actuation. As the SJA is driven by a rotational crank the motion is not strictly sinusoidal, but is reciprocal. However, for this project it was not considered an issue do to the small stroke lengths used. This system allowed for a maximum frequency of 25Hz, which was significantly more that the max test velocity of 12Hz. This drive system allows for the frequency to be changed by altering the voltage into the motor and the stroke length to be modified by changing out the crank.

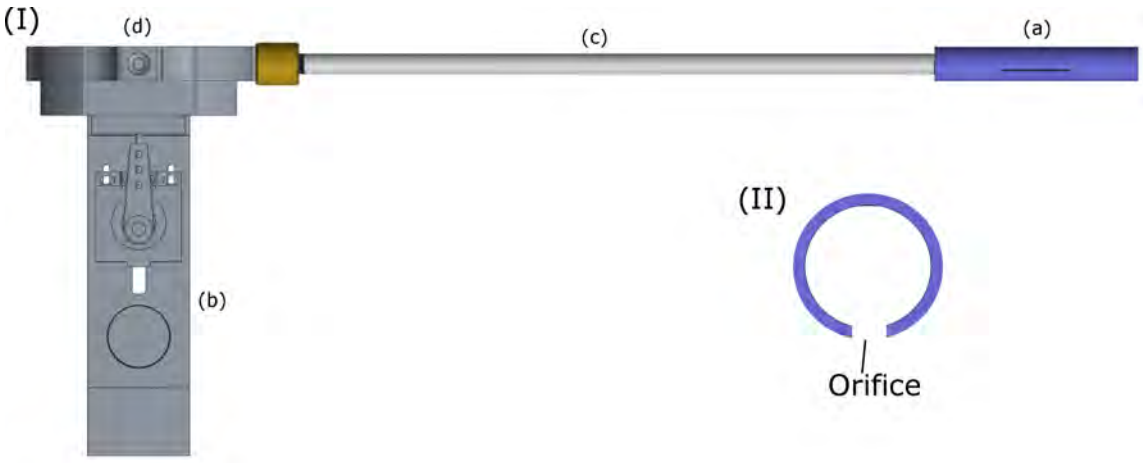

Figure 3.20: Synthetic jet actuator drive I and the cross-section of cylinder II, where: I(a) is the cylinder, I(b) is the SJA drive, I(c) is the Sting arm, and I(d) is the pumping chamber

As the synthetic jet actuator is driven by a piston with a head area of A_{SJA}, and a displacement (or stroke length L_{SJA}) that is responsible for sucking and ejects fluid through an orifice of a different area A_O, it is required that the relationship between these values and the commonly held values for synthetic jets are understood. Firstly, converting piston displacement into dimensionless stroke length:

$$L_0/D_O = \frac{A_{SJA}}{A_O}\frac{L_SJA}{D_O}k_{SJA} \tag{3.7}$$

Where D_O is the hydraulic diameter of the synthetic jet orifice, k_{SJA} is the usable membrane of the piston (see section 4.5).

The velocity ratio (V_R) is determined by the stroke length and the synthetic jet actuation frequency f_{SJA}. V_R is given by:

$$V_R = \frac{U_O}{U_\infty} \tag{3.8}$$

Where U_O is the average orifice expulsion velocity, which is given by:

$$U_O = \frac{Q_{SJA}}{A_O}\pi \tag{3.9}$$

Where Q_{SJA} is the volumetric flow rate of the SJA.

$$Q_{SJA} = L_0 k_{SJA} A_{SJA} \omega \tag{3.10}$$

Where ω is the angular frequency of the SJA.

$$\omega = f_{SJA} 2\pi \tag{3.11}$$

3.4.2 Drag and lift force measurements

Incorporating drag and lift sensors in the experiments allows for direct force measurements of the drag and lift caused by the synthetic jet in the cross flow to be measured and recorded.

Figure 3.21: Cylinder with embedded synthetic jet, and test section sting arm

Figure 3.21 shows the cylinder test piece, its sting arm and the disassembled view of its connecting port. figure 3.21*A* works using the brass sections to form a water proof seal around the clear acrylic tube. The brass fitting on the far right connects directly to the test section wall and the brass fitting to the far left had a small gasket that allows the sting arm (figure 3.21*B*) to enter, rotate and deflect slightly while maintain a waterproof seal.

The brass and acrylic section which fill with water from the main body of the water tunnel, has an internal diameter significantly greater than the sting arm. The strain gauges are placed on the sting arm just outside the gasket (on the dry side). This design is key to the drag and lift measurements, as the distance the connecting port spans from the test section allows for greater bending of the sting arm, thus allowing a better reading in the strain gauges. If the strain gauges were to be placed closer to the cylinder, the strain reading would be significantly less and the stiffness of the sting arm would need to be reduced, increasing flexibility. This would make sealing more difficult. The strain gauges are placed at 90^o offsets so that when the system was at its 0^o position the strain gauges are located at 0^o, 90^o 180^o and 270^o. Calibrations where done to give exact lift and drag force when the system was taken out of the 0^o position as the forces would not longer be acting directly on the horizontal and vertical planes. When the stain gauges are calibrated it is imperative that the clamping position of the sting must remain the same and that the tension on it must not change.

The initial deign (figure 3.22 A) required the clamp to be loosened so that the part could be rotated and then re-tightened. This immediately led to problems in replicability and over an arc of about 45^o a significant change in results with slight differences in tightening was seen. The most likely cause being that the sting arm is not perfectly round. This led to a full rethink of the part.

Figure 3.22 B is the final design for the clamp and as can be seen immediately it is significantly more complex than the original. An exploded view in figure 3.23 shows the parts more clearly. In this version the sting is held in place by the clamp (figure 3.23B). This clamp is then placed into a bearing (figure 3.23C.) that sits in the mounting block(figure 3.23A). This allows the test piece to be rotated freely without any tilt or positional offset that would have a detrimental effect on the strain calibrations. Figure 3.23D shows the clamping section that locks the clamp in place when the desired angle is reached. Figure 3.23E shows the vernier scales used to set the pitch angle of the test piece with a resolution of 0.1^o. The parts in figure 3.23F are to attach the vernier scales to the clamp(3.23A.)

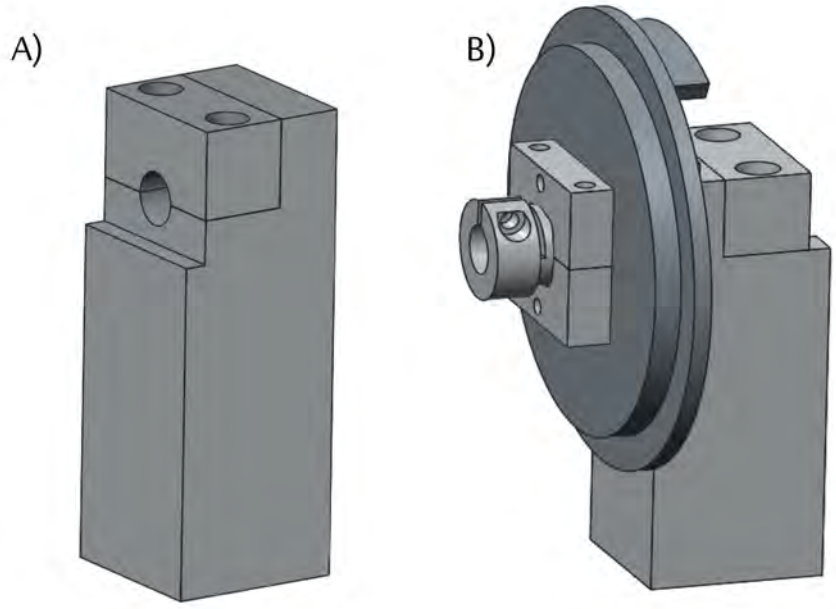

Figure 3.22: Sting arm clamp, where A) is the initial sting arm clamp, and B) is the updated sting arm arm clamp

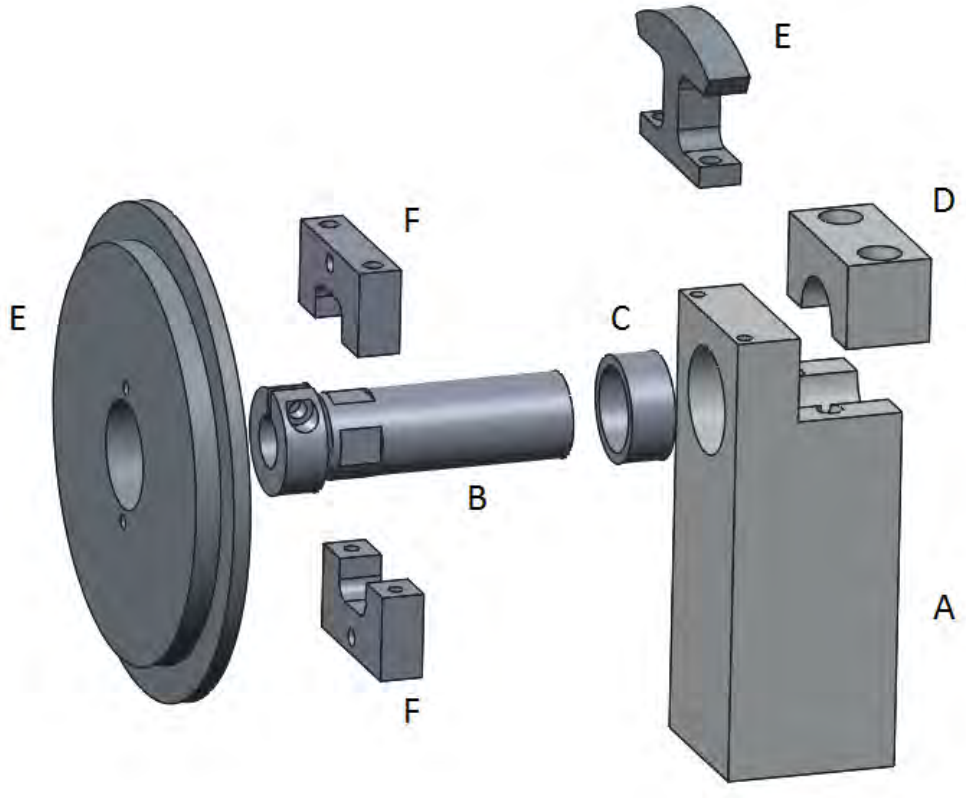

Figure 3.23: Exploded view of sting arm clamp

3.4.2.1 Calibrating strain gauges

The strain gauges were calibrated by clamping the sting in place in a vertical orientation and a pulley system was connected to eliminate any effects caused by the self weight of the bar. The tests where conducted by rotating the bar at the angles of 0^o, 90^o, 180^o and 270^o (the same as the orientation of the strain gauges). Incremental readings from 0N to 20N where taken to establish strain on the material. The results of this testing is shown in figure 3.24, where the strain is seen to change in a linearly fashion for each loading case. At the zero load case for each set of strain gauges it can be seen that there is a slight difference in the zero strain value, this is most likely due to the manner of clamping, which may have resulted from a slightly different level of tightening of clamp. It should be noted that the levels of strain in both graphs are different, this is due to the amount of strain that registers between the pair of gauges on the wheatstone bridge. However, this is not a problem as the graph is still linear.

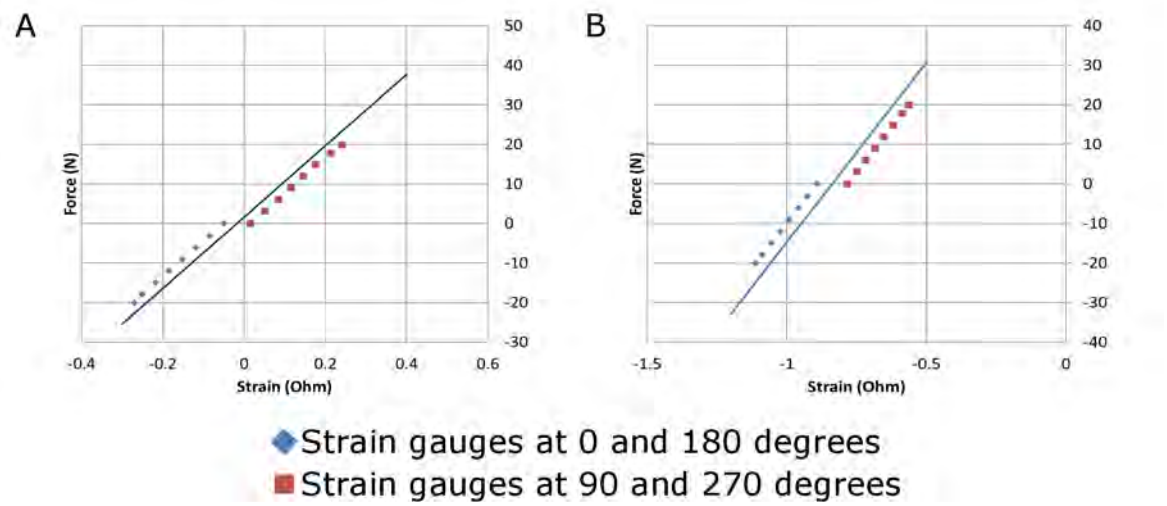

Figure 3.24: Strain gauge calibrations. A the strain gauges placed at A 0 and 180 degrees and B the strain gauges placed at 90 and 270 degrees

Tests will not always be carried out at the four angles shown previously, and so several random angles where also chosen and it was found that there was a maximum discrepancy of 4% between experimental and expected results.

3.4.3 Accommodating particle image velocimetry testing

In order to be able to get the most out of the testing, the test section needs to be able to accommodate the required need of PIV. This is seen by the use of an acrylic viewing window to the front and large laser ports in the top and bottom vertical walls. The large horizontal windows serve two main functions: I) providing a large area so that the laser can be used to take two dimensional PIV data measurement planes from the centreline of the synthetic jet outwards, similar to the setup used by Sahni *et al.* [13], and II) to allow access to the internals of the test section to allow for calibration of the PIV camera and the laser sheets, without needing to drain the water tunnel.

Figure 3.25: PIV laser illuminating the test section

3.4.4 Cylinder test piece

The test piece is a 20mm diameter cylinder with a span of 119mm. The cylinder contains a single spanwise rectangular orifice located around the centre with a length of 40mm, a width of 1mm and a depth of 2mm. The diameter was selected based on the Reynolds number that

can be achieved, shown in table3.1

Table 3.1: Reynolds number of cylinder at various test section flow velocities

Test section Flow Velocity *(m/s)*	Re_{cyl}
0.178	3.56×10^3
0.356	7.13×10^3
0.535	1.07×10^4
0.891	1.78×10^4
1.782	3.56×10^4
2.673	5.35×10^4
3.564	7.13×10^4
4.420	8.84×10^4

3.5 Construction and material selection of the water tunnel

3.5.1 Materials

For the water tunnel the main material used for the body was PVC, which gives the water tunnel is distinct grey colour. Polyvinyl chloride (PVC) was chosen due to its strength, lack of reactivity to water, low cost and its easy to work with. It was used for all sections apart from the parts that required complex geometries and parts where internal viewing ports were required. Stainless steel was used in the main contraction (figure 3.5) to achieve the precise curvature required to channel flow into the test section, it was also used in conical contraction and diffuser on either side of the pump.

Acrylic was used to create the viewing windows on the test section and the pipe around the propellers, it was also used for the laser light windows in the test section. The choice of Acrylic was due to its ready availability, cost, and it has a refractive index that is closer to water than glass.

The most exotic material used in the water tunnel is in the honeycomb made from stainless steel $SMO254$, this is a non-magnetic austenitic stainless steel containing a high molybdenum

content to prevent pitting and corrosion in hostile marine conditions. It was only possible to use this due to a company supplying it gratis.

3.5.2 Bonding

In the early stage of the project when the basic layout of the water tunnel had be configured and a few possible materials had been selected. the biggest issue was bonding the materials, in such a way as to be cost effective, water tight and strong enough to withstand the significant forces that would be produced by the circulating water and possible thermal expansion. For this thesis Loctite 9466 was used for bonding due to both its high tensile strength and its viscosity, which allowed for it to fill all gaps, thus preventing any leakage.

3.6 Conclusion of the experimental apparatus

This chapter outlines the design and construction of the water tunnel facilities to be used to test the effects an embedded synthetic jet actuator has on the forces excreted on a cylinder by a cross flow. It shows in detail the steps taken to improve and optimise the water tunnel, and the development of the testing equipment from scratch; such as the sting arm assembly to allow for direct forces readings to be taken, while allowing the circumferential position of the jet orifice to be changed, and fluid to be piped thought to the piston pump at the same time. From initial test it was found that the the pump produced more then sufficient levels of thrust, and that the strain gauges would more than adequate for the testing required. The flow condition and turbulence intensity in the test section and the and the synthetic jet actuator orifice velocity still needs to be determined experimentally.

Chapter 4

Experimental Analysis and Uncertainty

This chapter provides more details about the experimental analysis techniques used in this thesis. Section 4.1 discusses the particle image velocimetry measurements. Section 4.2 discusses how flow visualisation was set up. Section 4.3 details and discusses the experimental uncertainties involved in the testing. Section 4.4 characterises the fluid flow in the test section and over the cylinder. Section 4.6 details the main conclusions of this chapter.

4.1 Particle image velocimetry (PIV)

PIV has become a useful tool in modern fluid dynamics, due to it being a non-invasive method of measuring whole field velocity profiles, allowing for an improved understanding of unsteady flow phenomenon in experimental analysis. It is often used in conjunction with CFD to build detailed flow structures for unsteady flows such as a synthetic jet re-attaching a separated flow ([13]). This is achieved through PIV being able to spatially resolve measurements of the instantaneous flow velocity field over a short time allowing the detection of large and small scale spatial structures in the flow velocity field *et al.* [18]. The baseline knowledge of PIV in this section is primarily based on Raffel *et al.* [18] and Westerweel [62].

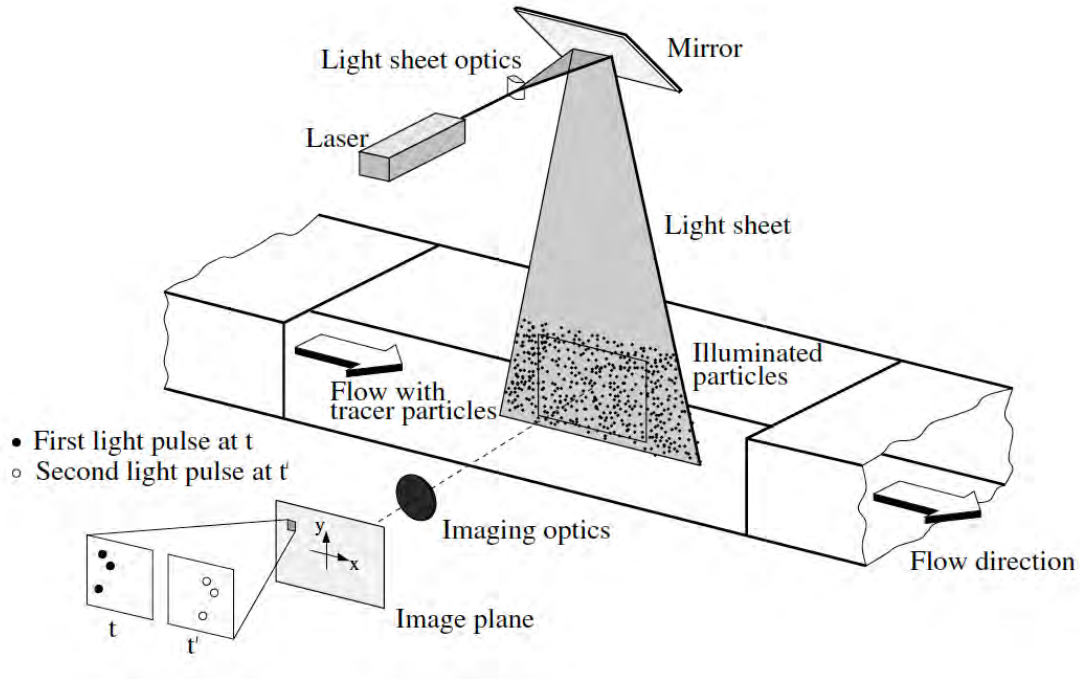

Figure 4.1: Basic layout of a PIV system [18]

An experimental PIV system is shown in figure 4.1. It is usually comprised of a laser to produce a light sheet that illuminates neutrally buoyant tracer particles suspended in the fluid and a high speed camera that records the particle displacement across the two-dimensional plane.([18])

4.1.1 Seeding particles

It is necessary to select an appropriate particle size in order to obtain good quality PIV, as the particles must be small enough to be able to follow the flow closely, but large enough that they produce a sufficient level of illumination. The diameter of a spherical seeding particle dictates its ability to scatter light, and the contrast of the PIV recording is directly proportional to the scattered light power. As such the selection of a larger diameter particle can offset the required laser power. When the particle diameter (D_p) is larger than the incident light (Γ), the Mie scatter theory dictates that the light intensity from particle reflection is proportional to the square of the particle diameter. The quantity of light scattered is dependent on the polarization and observation angle, with the optimum observation angle being normal to the

light sheet. In this current study water is the testing medium. The refractive index of water is significantly more than air. This results in the light scattering ability of particles in air being at least one order of magnitude greater for the same particle size, as such a larger particle is required in water. This can be accomplished as the density matching of particles with water is more easily accomplished. According to Westerweel [62] if particles are capable of following exactly the fluid motion, without interfering with each other or the fluid properties, then they are considered to be ideal. In PIV the fluid velocity is obtained indirectly via the displacement Δ_P(X;t',t") of the tracer particle in a finite time interval $\Delta t = t''t'$ *et al.* [18], such that:

$$\Delta_P(X;t',t'') = \int_{t'}^{t''} U_P[X(t),t]dt \tag{4.1}$$

Where the tracer particle velocity is given by U_P[X(t)]. For an ideal tracer particle, velocity is equal to local fluid velocity V(X,t). In a practical situation this can only be approximated, and so Δ_p leads to an approximation of V within a finite error ε:

$$||DpD_P \bullet \Delta t|| < \varepsilon \tag{4.2}$$

If the spatial and temporal scales of the flow are large with respect to the spatial resolution and the exposure time delay, then the associated error is often negligible.

The density of tracer particles in the flow is separated into three categories; low, medium and high density (figure 4.2), where a homogeneous distribution of medium density is preferred for high quality PIV. In low density the particle distribution is too large and the number of particles are too low to properly determine the flow structures or velocities, however it can be used to determine flow evolution. In the high density case there are too many particles to determine the displacement of individual particles. The medium density is the desired density for PIV. According to Raffel *et al.* [18] a homogeneous distribution of medium density is desired for high quality PIV recordings in order to obtain optimal evaluation, as it allows for tracking of each particle over a small distance, giving a high resolution and thus allowing the flow structures and velocities to be determined.

The particle size will effect the amount of illumination and how well it follows the flow, for instance large particles will be more illuminated but will not follow the flow as well as small particles.

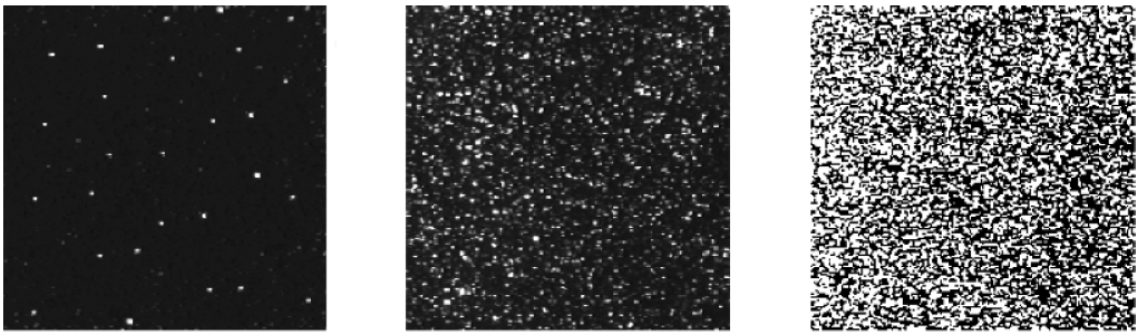

Figure 4.2: Particle density: A) low density, B) medium density and C) high density [18]

For the current study, 20μm polyamide seeding particles with a density of $1,030$Kg/m^3, which is close to that of water (999.1Kg/m^3 at 15^OC) are used. The process of seeding the water tunnel begins with adding approximately $10000mm^3$ of seeding particles into a beaker, then just adding enough alcohol to suspend the particles. The beaker was filled with 500ml of distilled water and stirred with a magnetic stirrer. Stirring took place for around 20 minutes and particles where let settle for 40 minutes. Particle density was established through trial and error. 200ml's of suspended seeding particles were added to the water tunnel using a syringe.

4.1.2 Light source

Lasers are commonly used in PIV due to their ability to emit monochromatic light with a high energy density, which can be formed into a sheet by passing it thought a series of optical lenses. Normally a double pulsed ND:YAG laser would be used for high speed PIV. However, as the one available to our research group was out of commission during the main PIV and FV tests carried out in this thesis a continuous wave laser was used instead. A continuous

wave laser (CW_L) constantly illuminates the particles, and the time between pulses is instead given by the camera exposure time and the timing between pulses is given by the camera frequency (Hz). The use of a CW_L resulted in the maximum recordable flow velocity being reduced. This was due to a peak power of the laser not being sufficiently large enough for the shutter speed to be increased to prevent streaking beyond a flow velocity of 0.6m/s. It was found by Meehan *et al.* [63] that a CW_L laser would be adequate for PIV provided flow velocity was not large enough to cause image streaking.

4.1.3 Setup and calibration of the laser's and camera

In all imaging based tests, a high-speed camera with a complementary metaloxide semiconductor (CMOS) sensor with an active pixel sensor was used. This camera converts charges accumulated by the photodiode into a voltage, which is then amplified inside each pixel. This signal is additionally processed in sequential rows and columns. The camera is also equipped with a highly parallel readout electronic storage device. The combination of these factors allow the camera to achieve a recording rate of several thousand hertz without significant error ([18]). The CMOS camera used was a double-framed Photron Fastcam SA1 (1024x1024px, 12 bit, 5400Hz maximum recording rate), with a 50mm (sigma 50mm, f/1.4) and 105mm(sigma 105mm, f/2.8) lens for FV and PIV respectively.
For the initial characterization of the water tunnel, the light source was produced by a Quantronix Darwin-Duo Nd:YLF twin cavity pulsed laser capable of producing 15mJ at 1000Hz, with a wavelength of 527nm. For the PIV and the FV a ST-II-N-532 1W Continuous wave laser, with a wavelength of 532nm was used.

For the Characterization test of the water tunnel a concave lens of $f = -10$mm was used, for the velocity ratio tests a f $= -20$mm lens was used. The sheet thickness had a thickness of 0.2mm.

For all tests, a laser sheet was set up below the test section, producing an upwards light sheet that was located at the centre of the cylinder span and was aligned parallel to to the flow. To ensure that the light sheet was vertical and parallel to the flow paper sheets that had been cut and marked where placed at the top and bottom light windows. These sheets

allowed for the vertical alignment and to ensure the sheet was parallel to the flow. The light sheet was focused using a flat plate with an illumined strip that could be immersed into the test section to align with the cylinder. The camera was positioned normal to the light sheet and was calibrated using a precision machined twin level calibration target (2mm step between levels, with dots spaced equally in a 10mm grid) that was placed in the test section and aligned with the laser sheet. As the camera and the laser sheet are separated by three different mediums (air, Perspex, and water), an optical distortion will be caused by refraction. However, provided that the calibration is based on a view plane in one medium, then optical distortion can be ignored ([64]). As the test section had a flat viewing window and the camera was positioned normal to the laser plane and window, a *define scale, no image distortion* was selected in the calibration setup in DaVis 7.2. Calibration was completed by focusing the camera on the particles, then placing the face of calibration target into the light sheet, so that it is illuminated such as in figure 4.3. Two dots are selected in figure 4.3, this allows Davis to convert the pixel displacement into a distance. The CMOS sensor is affected by noise from electrical and thermal factors. With the thermal effect producing electron-holes that cannot be separated form the photoelectric effect. This results in an effect called the *dark count* that makes it impossible to distinguish the weak particle images from noise. This effect remains constant at a given temperature and exposure, as such this can be accounted for by subtracting a constant bias voltage at a charge to charge voltage converter, through taking a dark image ([18]). As the dark count is sensitive to both temperature and time, it is necessary to regularly calibrate the camera to mitigate its effect.

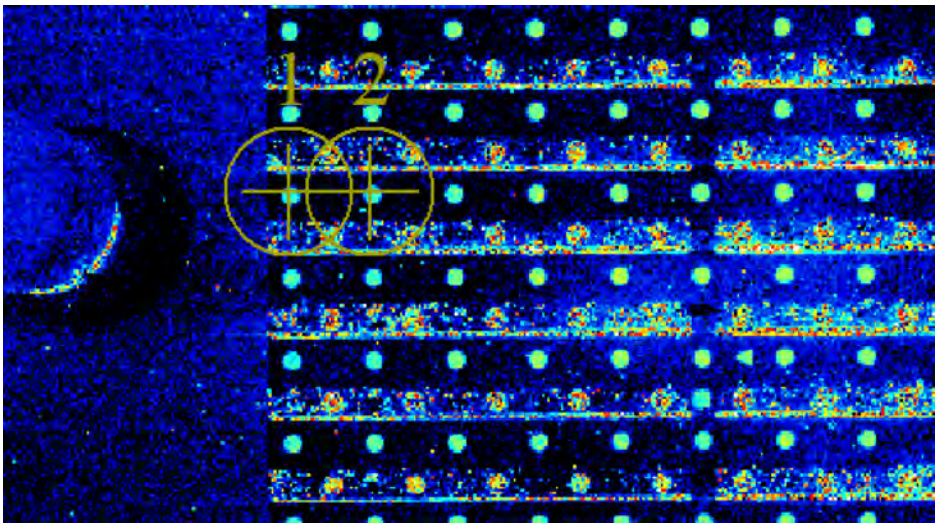

Figure 4.3: Calibration setup form DaVis

4.1.4 Cross-correlation

In order to obtain quantitative two dimensional vector fields, the particle images need to be systematically interrogated. This is achieved through splitting PIV images into interrogation windows as in figure 4.1. The interrogation windows determine the spatial resolution of the measurement, thus measuring the distance travelled by a particle in the time Δt. The interrogation windows can be set to have either no overlap or a percentage of overlap and can be given a variety of shapes (rectangular for this thesis). The overlap and shape will determine the spatial resolution. The particles are traced using correlation. This is usually either auto-correlation or cross-correlation. Auto-correlation of a single exposure intensity field results in a single peak being formed. Cross-correlation makes use of a doubly-exposed intensity field that results in the production of a large central peak, with two smaller symmetric side peaks. Due to the formation of these symmetrical peaks, if the particle displacement is insufficient then the central peak can be slightly overlapped by the smaller peaks. This results in the measurable velocities being limited, which can be problematic when there is a high dynamic velocity range between the minimum and maximum resolvable particle displacement ([65]). As a result of these issues and the advent of high speed cameras and ND:YAG lasers, images are normally single exposed and a cross-correlation analysis is used. Two images separated by a time Δt, have a cross-correlation procedure performed on them. According to Westerweel [62] this results in a cross-correlation with a dominant peak that shifts with the particle shift.

This pixel shift of the particle is then converted by Davis into a velocity.

4.1.5 Experimental vector processing

Figure 4.4 shows a raw PIV image. From this image it can be seen that the image produced using a continuos wave laser at 1W, allows for sufficient illumination of a particles without large surface reflection. It can be seen that above the cylinder there is a shadowed region where laser light cannot access. In PIV it is difficult to achieve readings close to the surface of an object due to reflections and in areas of low light, and to prevent error in vector analysis it was necessary to mask these areas off ([18]). It can be seen form figure 4.4 B that there is a sufficient seeding density per interrogation window, more than 10 particles per interrogation window ([66]).

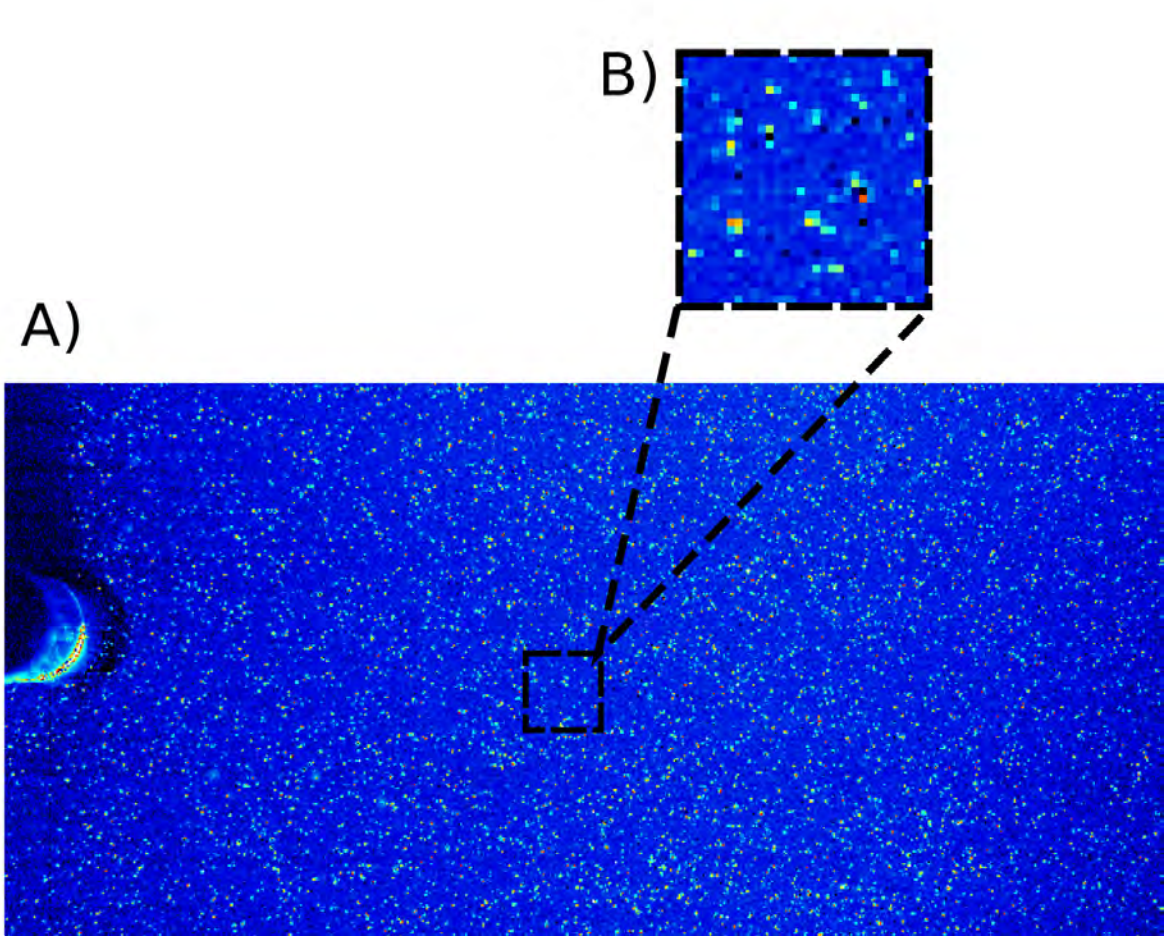

Figure 4.4: Raw PIV image, where A) shows the seeding density, and B) shows the particles per interrogation area

The Raw images in figure 4.4 had PIV algorithms applied that used multi-pass correlations and Gaussian sub-pixel fitting to decrease the interrogation window from 64 x 64 to 32 x 32. The was done in three parts, one pass for the larger window size and two passes for the smaller, with all pass's having an overlap of 75%.

4.1.6 Particle Flow behaviour

The Stokes number characterizes the behaviour of a particle suspended in a fluid, and is defined as the ratio of the characteristic time of a seeding particle to a characteristic time of the flow. Stokes number is given by:

$$St = \frac{{}_pU_\infty}{L_D} \tag{4.3}$$

Where t_{Part} is the particle relaxation time, and L_D is characteristic diameter of the cylinder in the flow. The relaxation time is given by:

$$\tau_p = \frac{d_p^2(\rho_p - \rho_f)}{18\mu} \tag{4.4}$$

Where d_p^2 is the particle diameter, and ρ_p is the particle density and ρ_f is the fluid density.

The relaxation time is a useful measurement of the tendency of a particle to attain velocity equilibrium with the fluid. Particles suspended in water allows for an easier matching of particle density to that of the fluid density. In this case the water at a temperature of 15^oC has a density of $999Kg/m^3$, and the polyamide seeding particles have a density of $1030Kg/m^3$. This closely matched densities result in a short relaxation time of 0.619μm, which gives a small Stokes number of 0.000097, far less than 0.1 given by Tropea *et al.* [67]. This means that the particles not only follow the fluid closely, but they will also have an error of less than 1% on tracing accuracy. [[68], [18]]

4.2 Experimental flow visualisation

For flow visualisation, the most important aspect of setup was the selection of the shutter speed (ms) and the recording rate (Hz) of the camera, as they dictated the length of streaking

of the particles and the particle displacement respectively. The selection of the shutter speed was of significant importance as it dictated the length of streak lines, thus allowing for the identification of flow structures. If the shutter speed was set to a value that was too fast, then it would result in slower structures being lost and if it was set too slow than smaller structures would be shown but larger objects would be lost and images would suffer from noise as off plain motion would be seen. In the selection of shutter speed, consideration had to be taken to allow for the same shutter speed to be used over the range of 4Hz < f_{SJA} < 11Hz. Through trial and error, the shutter speed of 1.1ms and a recording rate of 100Hz was selected as it gave the best visualisation of flow structures with minimal noise, producing the best analysis of the effects an SJA has on the wake. For each test 1000 images were taken to give a minimum of around 9 images per period and sufficient time to determine if the flow structures remained constant.

4.3 Experimental uncertainty

4.3.1 Strain gauge-based drag and lift force measurement

For these experiments $360,000$ strain readings were recorded at a sample rate of 2000Hz for 180seconds. Prior to testing the flow was allowed to develop for three minutes before test where take. An uncertainty analysis of experimental measurements is necessary results to be used to their fullest ([69]). As such these experiments are to be carried out to give a confidence level of 95%. Absolute uncertainty on the strain reading is given by

$$\Delta_\varepsilon = \frac{1.96 \times \sigma_\varepsilon}{\sqrt{N_{samp}}} \tag{4.5}$$

where σ_ε is the standard deviation on the strain measurement, N_{samp} is the total number of (assumed to be independent) samples.

And the relative uncertainty on the strain reading is

$$\delta_\varepsilon = \frac{\delta_\varepsilon}{\varepsilon_{avg}} = \frac{1.96 \times \sigma_\varepsilon}{\varepsilon_{avg}\sqrt{N_{samp}}} \tag{4.6}$$

Where σ_ε is the average strain value.

As the sample rate is very high compared to the natural shedding frequency (3.2Hz), the samples could not be said to be properly independent of each other. As samples are not independent, the number of samples N_{samp} in the above expressions need to be corrected as follows:

$$N_{samp,independent} = N_{samp}\frac{f_{flow}}{f_{samp}} \tag{4.7}$$

where f_{flow} is a characteristic frequency in the flow field and it is 3.2Hz for a flow velocity of 0.312m/s. This approach gives a conservative estimate of the number of independent samples, and thus lead to a conservative estimate of the uncertainty margis, given by:

$$\Delta_\varepsilon = \frac{1.96 \times \sigma_\varepsilon}{\sqrt{N_{samp,independent}}} \tag{4.8}$$

and

$$\delta_\varepsilon = \frac{1.96 \times \sigma_\varepsilon}{\varepsilon_{avg}\sqrt{N_{samp,independent}}} \tag{4.9}$$

For these tests the jet angle of 140^o, with an L_0/D_O of 0.5 and a V_R of 0.69 was chosen.

This gave a conservative absolute uncertainty (Δ_ε) of 0.0023 and 0.0044 for drag and lift respectively, at a 95% level of confidence. This gave a relative uncertainty (δ_ε) of 4.9% and 7% for drag and lift respectively, for strain readings at a 95% level of confidence.

Table 4.1: Strain gauges-based uncertainty values

Quantity	Absolute uncertainty		Relative uncertainty	
Drag force	0.0023	N	4.9	%
lift force	0.0044	N	7	%

4.3.2 Synthetic jet operating conditions

The rotational frequency of the synthetic jet actuator was obtained using a light-gate sensor and an in-house developed LabVIEW program. The program used an NI9401 digital 8 channel input mounted on a NI cDAQ-9178 chassis to give the time between high-pulses generated as a breaker attached to the drive shaft passed through the light-gate. LabVIEW

then converted this signal into a frequency reading. The PIV system was triggered by the high-pulse produced by the light gate. It was determined experimentally that the frequency readings could deviate to a maximum of ± 0.1Hz.

As the SJA drive is operated using a piston and a diaphragm, there will most likely be a small amount of uncertainty in the stroke length. Uncertainty of drive shaft eccentricity = 0.25 ± 0.02 mm and the use of a diaphragm in the piston could result in an uncertainty in the diameter of piston area = 42 ± 0.5 mm. This would translate to a 2.5 ± 0.14 dimensionless stroke length, assuming that the fluid and piping connections between the actuator and the orifice are incompressible.

4.3.3 Uncertainty in particle image velocimetry

Persoon *et al.* [70] found that significant improvements to the phase-averaged and turbulence intensity results could be obtained from PIV using a constant value to estimate the displacement value ($\sigma = 0.1$ pixels). Stanislas *et al.* [71] found that the use of a 0.1 pixel displacement remains a reasonable estimate for best practice laboratory setup as. In order for this technique to work for time-resolved flows such as in this study, a method to determine local uncertainty $\Delta s = \sqrt{\varepsilon_s^2 + \beta_s^2}$ is needed. Previously it was only possible to obtain a rough estimate of the expected error for average measurements, when there was a specific flow condition and image quality achieved. An *uncertainty surface* was determined using the four-Dimensional uncertainty response by Timmins *et al.* [72]. This was based on the parameters of particle density, particle image diameter, shear, and displacement). The particle displacement for velocity fields were compared by Wilson and Smith [73] for a known rectangular jet flow. From their analysis of uncertainty, it was seen that elevated turbulence levels would result from large particle images, insufficient seeding density, and flow gradients. Xue *et al.* [74] hypothesized that the uncertainty of an individual measurement could be obtained from the quality correlation quantifiable from the signal to noise ratio metrics calculated from the PIV correlation plane. A method of measuring error bounds to a confidence interval for a specific individual measurement that holds regardless of flow condition and image quality was developed by Charonko and Vlachos [75]. They found that there was a strong

correlation between the observed error and the correlation peak ratio. Sciacchhiatano *et al.* [76] presented a method based on super resolution PIV to estimate uncertainty and bias error, relying on statistical analysis of particle disparity vector field from the residual distance between pairs matched images. This approach was validated using Mont Carlo analysis that used artificial particle images and experimental PIV data, using a pyramid technique from their earlier work ([77]) as a point of reference. The work of Persoons [78] used a multiple-pulse-separation PIV technique to enhance the measurable turbulence intensity and signal to noise ratio throughout the flow fields, in particular the entrainment region and outer shell layer.

4.3.4 Experimental particle image velocimetry

For the PIV test (and test using the PIV equipment) conducted this is a level of uncertainty in the pixel displacement. This pixel displacement (Δpx) analysed as a $\pm$ pixel displacement will result in a $\pm$ velocity offset. Therefore, it was necessary to determine if this offset was to an acceptable level. This was obtained using the following equation:

$$\frac{\pm 0.1\, x\, \Delta px}{\Delta t} \tag{4.10}$$

The velocity offsets were looked at for the worst-case scenarios (highest recoding frequency) for the Far field PIV, the PIV at the jet orifice and for the flow visualization as this was also using the PIV system. It was found that the far field PIV gave a maximum particle velocity uncertainty of ± 0.006m/s, PIV at the jet orifice had a maximum error of ± 0.0024. It was found that flow visualisation could have a potential particle displacement of ± 0.0018m to that seen in the image. As such the PIV and FV error for the optical scaling selected was acceptable for the tests conducted.

Table 4.2: Uncertanty values for flow visualisation and PIV

Quantity	Absolute uncertainty	
flow vis	± 0.0018	mm
PIV velocity (far field)	± 0.0024	m/s
PIV velocity (near field)	± 0.006	m/s

4.4 Characterization of flow in the test section

Baseline analysis was carried out using PIV to characterize the flow in the water-tunnel with a 20mm diameter cylinder, spanning the width of the test section, located on a central plane 100mm into the test section at vertical centre. Tests were conducted based on the frequency of the turbine, starting form 2Hz and were increased in increments of 0.2Hz up to 15.6Hz with additional readings of 16Hz and 18Hz also taken. This translated to a test section velocity ranging from a minimum of 0.1m/s to a maximum of 0.99m/s.

The tests where conducted using a high-repetition rate pulsed laser (Quantronix Darwin-Duo double-pulsed Nd:YLF laser, 527nm, 15mJ at 2 kHz, 120ns pulse width) and a Photron Fastcam SA1 CMOS high-speed camera (10242 pixels, 5.4 kHz, 12 bit). A times-resolved double-frame pulse separation based on a particle displacement of roughly $8-10$ pixels per double frame cross-correlation. The tracer particles have a mean diameter of approximately 10μm with a particle images of 2 pixels in diameter ([78]). A limitation of viewing of around 0.5mm from the surface of the cylinder was seen due to reflections of the laser off the surface and a shadowing effect caused by the cylinder.

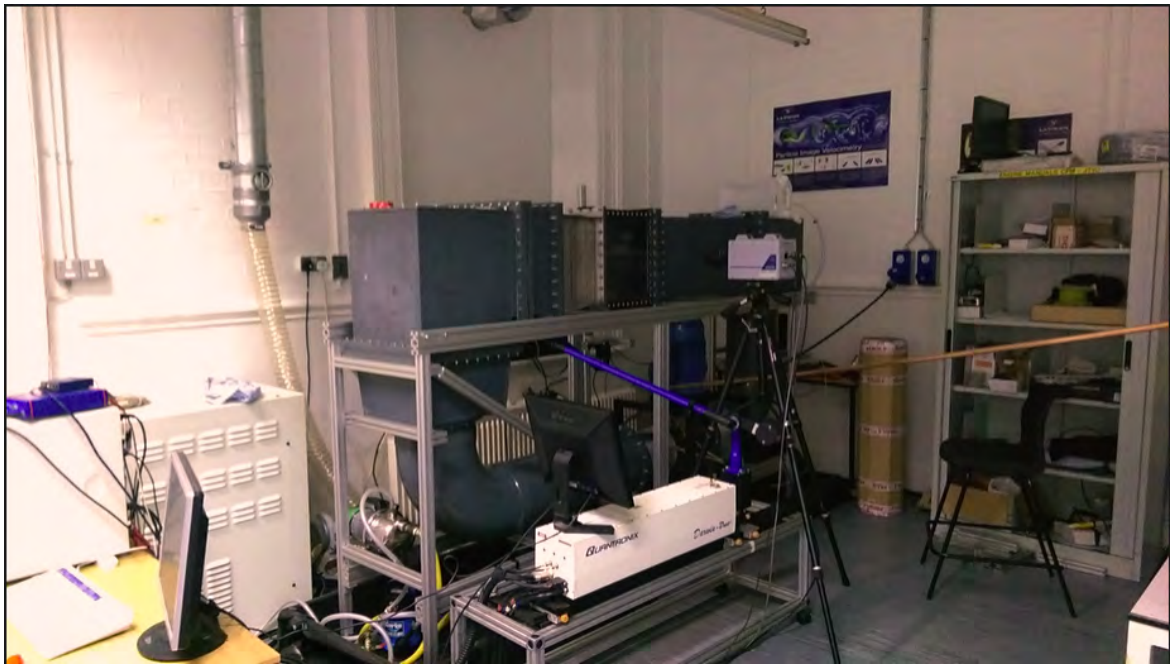

Figure 4.5: Water tunnel set up for testing

4.4.1 Analysis of test section characterisation results

Analysis was carried out to characterise the flow over the cylinder and the mean flow in the test section.

In figure 4.6 a slight offset can be seen in the cylinder wake, with the flow tending to be slightly more clockwise around the cylinder. This offset is due to the imperfections in the turning of the flow at the mitre bends, producing an asymmetrical velocity profile, with a slightly faster flow over the top half. As such PIV test where conducted to determine the turbulence intensity and cross stream non-uniformity, where non-uniformity is = $(U_{o,max} - U_{o,max})/U_{o,mean}$. The span-wise non-uniformity was based on Morel [79] as it was not possible to perform span-wise PIV on the test section. For a crossflow velocity of 1m/s the results were as follows:

Table 4.3: Characterisation of test section flow quality at a cross-flow of 1m/s

Turbulence intensity	$< 1\%$
Cross stream non-uniformity	1.5%
spanwise non-uniformity	max 7% ([79]

4.4.2 Analysis of flow over the cylinder

The flow over the cylinder was analysed over a range of flow velocities to visualise the baseline effects of increasing Reynolds number on flow separation and the cylinder wake structures.

These baseline test were carried out to allow an easy comparison of the effects of the synthetic jet on the flow structures around the cylinder.

4.4.2.1 Problems with flow

Figure 4.6 is a comparison of the velocity streamline for a Reynolds number of 2.2×10^3 (Figure 4.6A) and 2×10^4 (Figure 4.6B). In both instances the cylinder wakes have different separated regions, with the recirculation region in the low Reynolds number ($2.2x10^3$) case being situated between $1.5D$ (cylinder diameters) and $4D$ downstream, whereas the recirculation region is attached to the cylinder for the high Reynolds number ($2.2x10^3$) flow regime and spans to about $2.5D$ downstream.

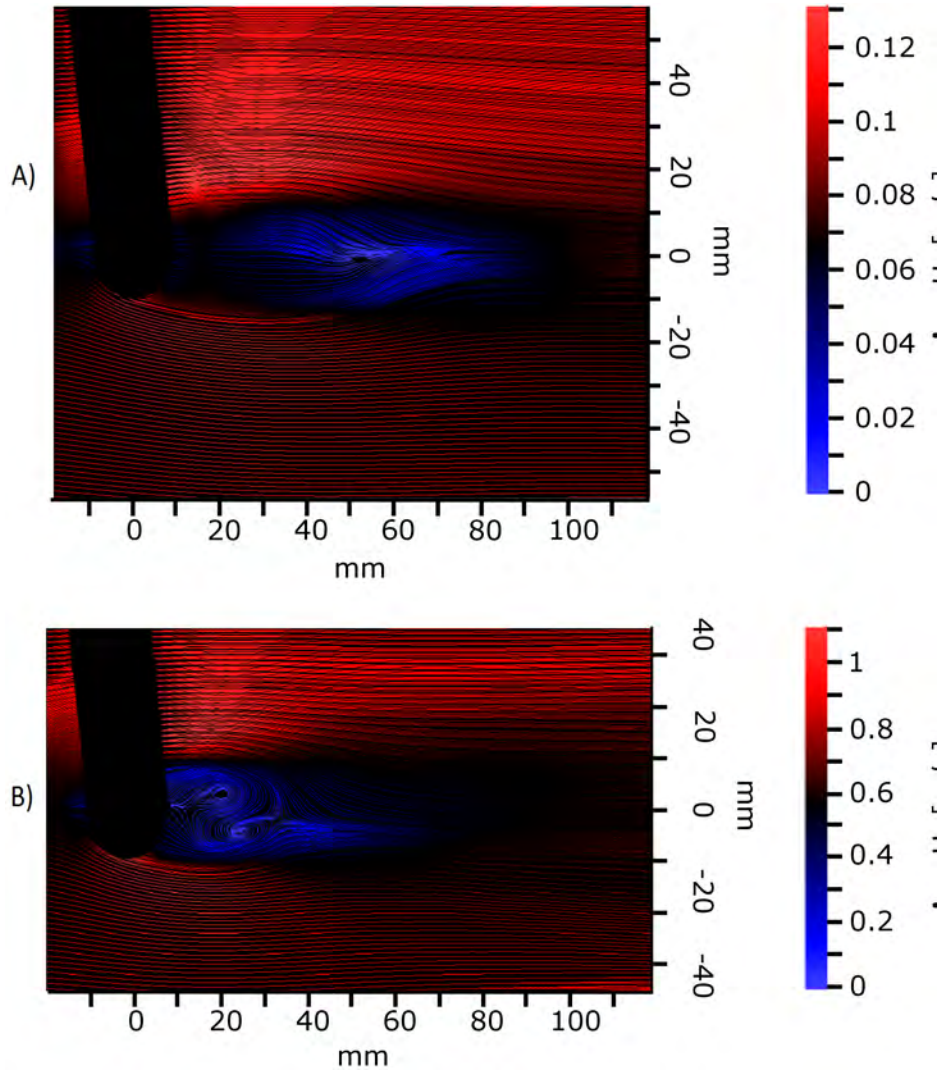

Figure 4.6: Average velocity streamlines over a cylinder with a Reynolds number of: A) 2.2×10^3 and B) 2×10^4

4.4.2.2 Cylinder flow regimes

Flow regime tests examined a range of Reynolds numbers from $2.2x10^3$ to $2x10^4$ using PIV. The Range of Reynolds numbers was selected as it spanned the subcritical flow regime where the length of eddy formation and transition in the wake changes significantly, giving a good range of tests. Zdravkovich1 [19] breaks the subcritical flow regime down into three sub-flow regimens of lower ($350<Re<1 \times 10^3 2 \times 10^3$), intermediate ($1-2x10^3<Re<2x10^4-4x10^4$) and upper ($2-4 \times 10^4<Re<1 \times 10^5 2 \times 10^5$). This range allows for the observation of the flow regimes transitioning over the cylinder from the lower to intermediate and intermediate to higher flow regime, whilst also giving results at the well developed intermediate regime

(figure 4.7B.). The effects of Reynolds number on the flow around the cylinder and the wake can be seen in figure 4.7 and figure 4.8 respectively.

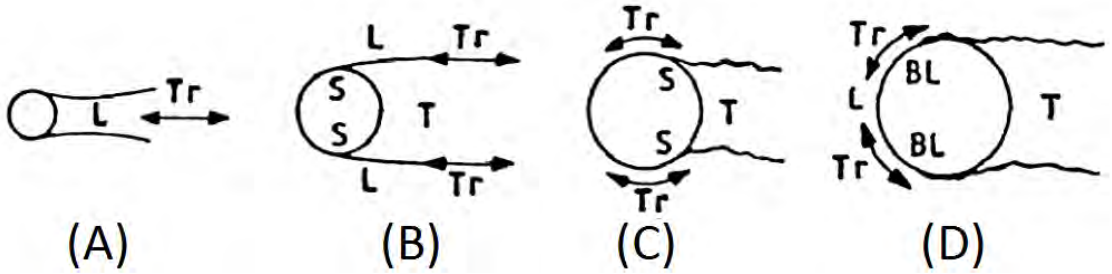

Figure 4.7: The transitions in the disturbed regions: (A)Transition in wake state of flow($220 < Re_{cyl} < 400$), (B) subcritical flow state($400 < Re_{cyl} < 2 \times 10^5$), (C)($2 \times 10^5 < Re_{cyl} < 3 \times 10^6$ - 6×10^6) (D)($Re_{cyl} > 3 \times 10^6$ - 6×10^6) are different stages of the critical flow state. Where BL is the boundary layer, L is laminar, T is turbulent, Tr is transitional and S is separated [19]

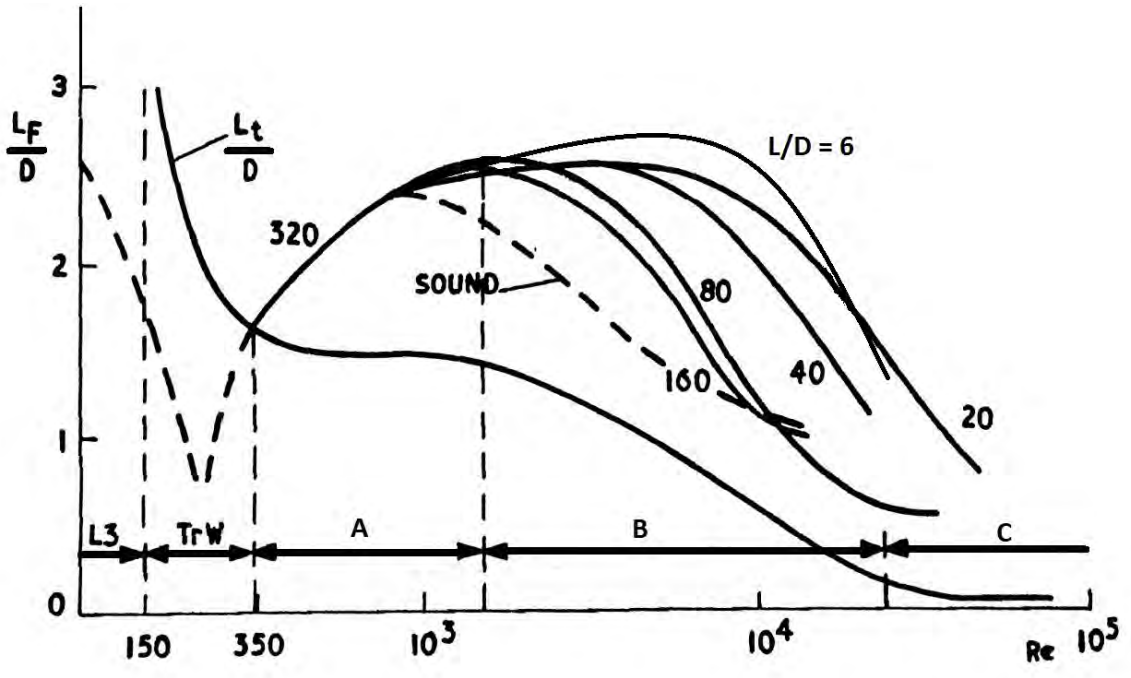

Figure 4.8: Length of translation (L_t) and formation regions (L_f) in terms of Reynolds number where the subcritical flow regimes are: A) low, B) intermediate and C) upper. [19]

When comparing figure 4.7 and figure 4.8 to the experimental results in figure 4.9 similar trends can be seen. In figure 4.9A the length of the laminar and transitional arm is seen to be significantly larger than that of figure 4.9B. This is explained more in section 4.4.2.3

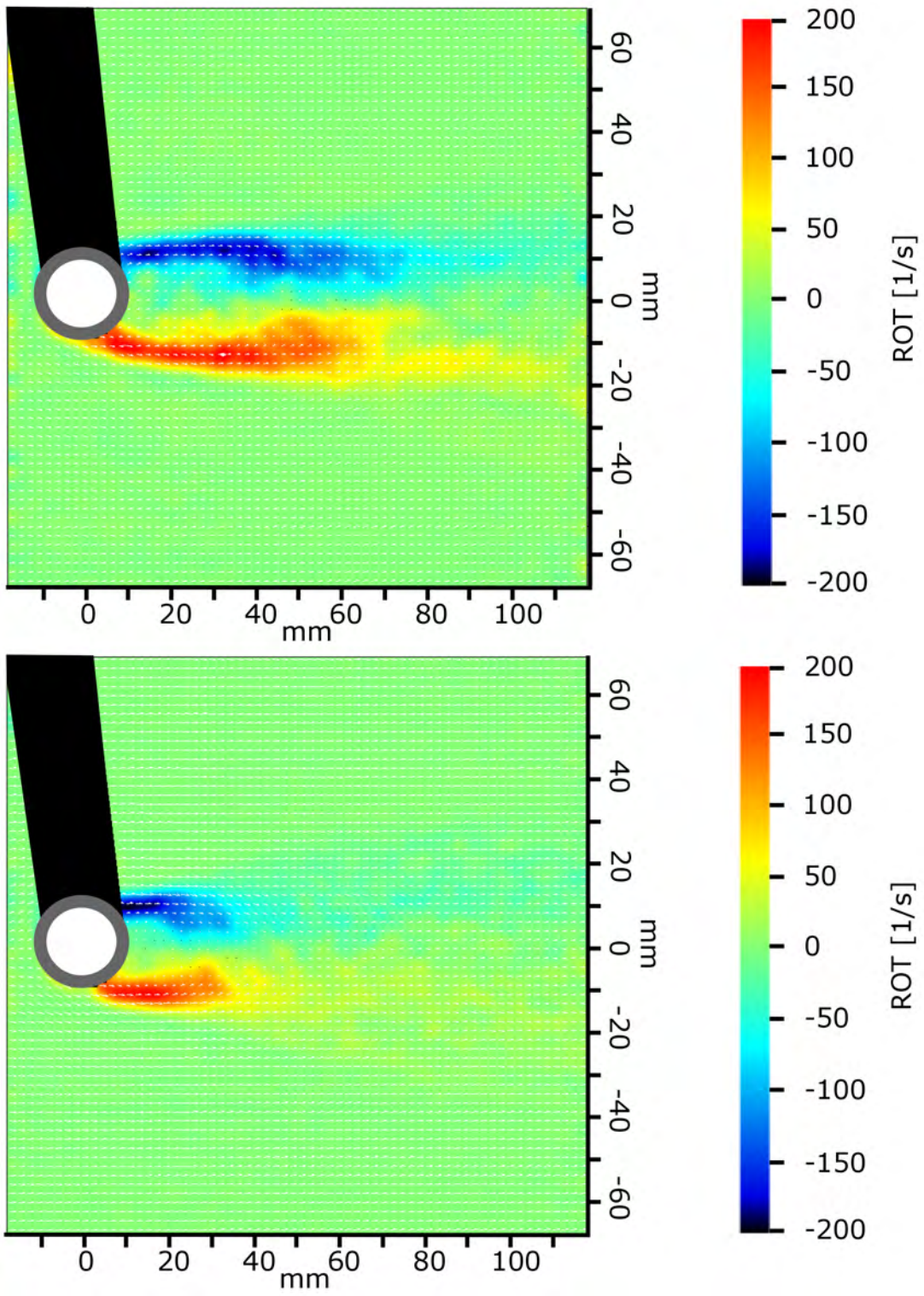

Figure 4.9: Effect of Reynolds number on the free stream shear layer formation, when $Re_{cyl}isA$)2.2 $\times 10^3$ and B) 2×10^4

The results in figure 4.8 agree well with that of figure 4.9. An increased rate of thickening

of the shear layer with an increase in Reynolds number, shown by a maximum thickness being reached at an x/D of roughly 1.5 and 0.5 for the low and high Reynolds numbers respectively. This agreement of the PIV with well established results shows that the experimental results are of good quality and reliable.

Knowing that the PIV data is of good quality it was then possible to use the intermediate results to give an area ratio of L/D of 6 in figure 4.8. This line shows a higher value of formation length of eddies in the wake with a sharp drop thereafter, which would seem to be correct as it follows similar trends to the area ratios as they decrease from 80 to 20. The results in figure 4.10 show a reduction in the length of the transition wake, with an increase in the eddy formation region, prior to its rapid reduction and straightening as seen in figure 4.9B.

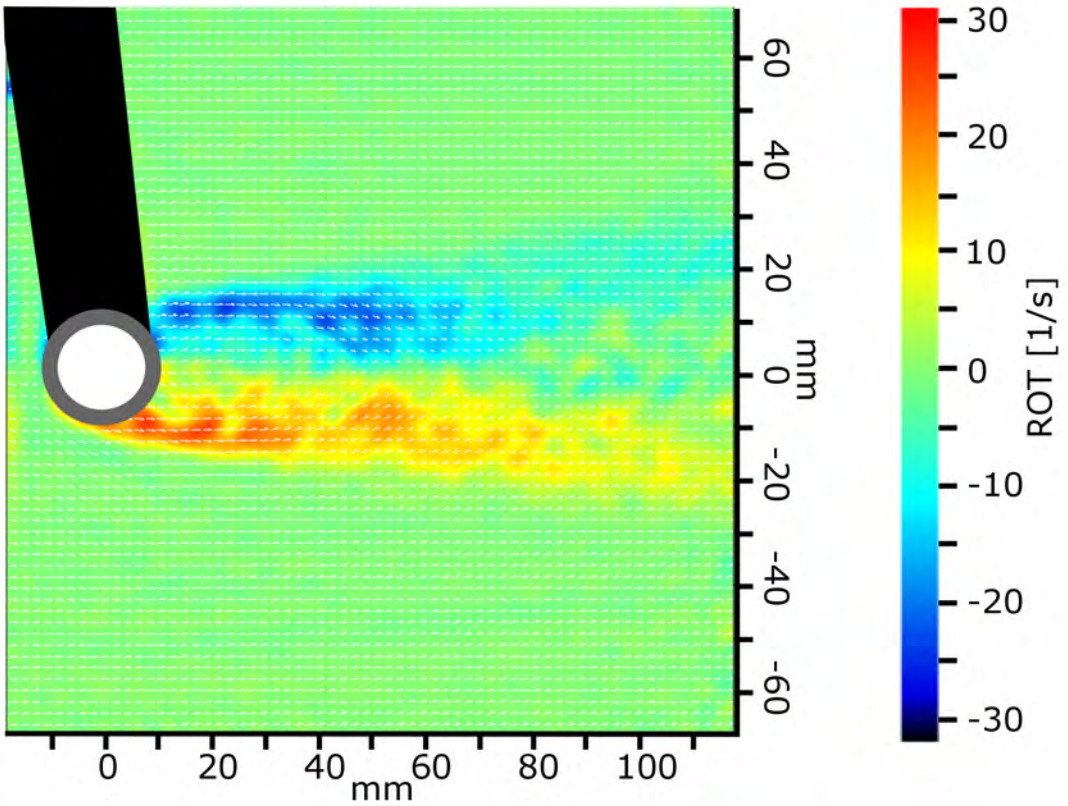

Figure 4.10: Effect of Reynolds number on the free stream shear layer formation, when $\mathrm{Re}_{cyl} is 1.1 \times 10^4$

4.4.2.3 Effect of flow regime on drag

As the eddy formation region decreases there is a negative effect on the pressure at the downstream side of the cylinder resulting in an increase in the coefficient of drag[19]. This is shown in figure 4.11, where a reduction in the coefficient of pressure (C_p) is related to a reduction in eddy formation region (L_F). It is possible to see that there will be an increase in drag when comparing the separated regions in figure 4.12A & B. The transition of the area of negative pressure from a distance down-stream face of the cylinder to being attached to the downstream face of cylinder will result in a larger pressure differential between the upstream and downstream sides thus resulting in an increase in the coefficient of pressure, resulting in an increase in drag ([19]).

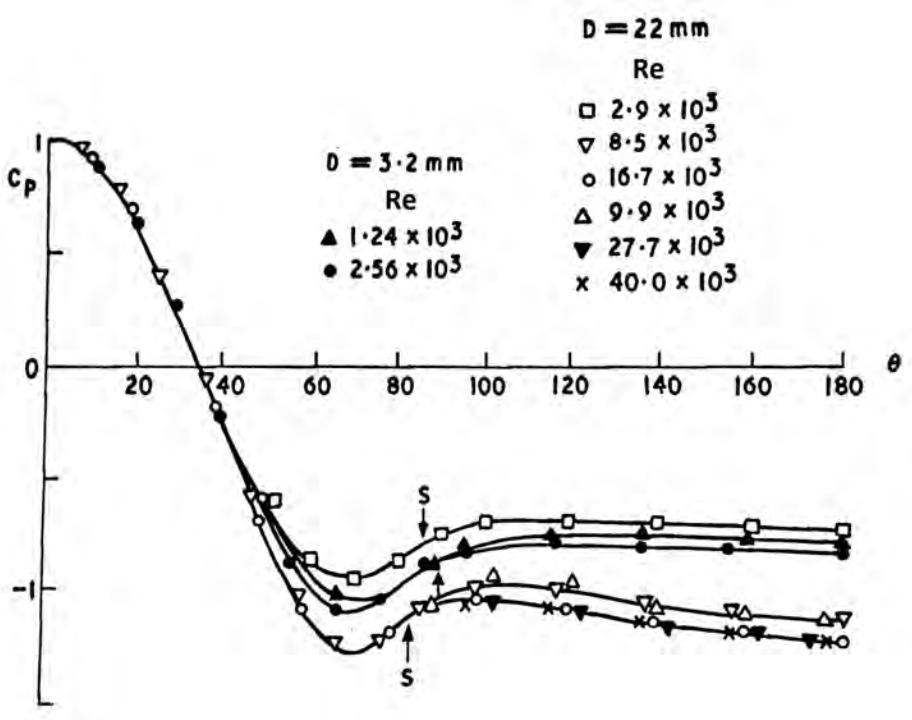

Figure 4.11: Effect of Reynolds number on drag for a cylinders of 3.2mm and 22mm dimeters[19].

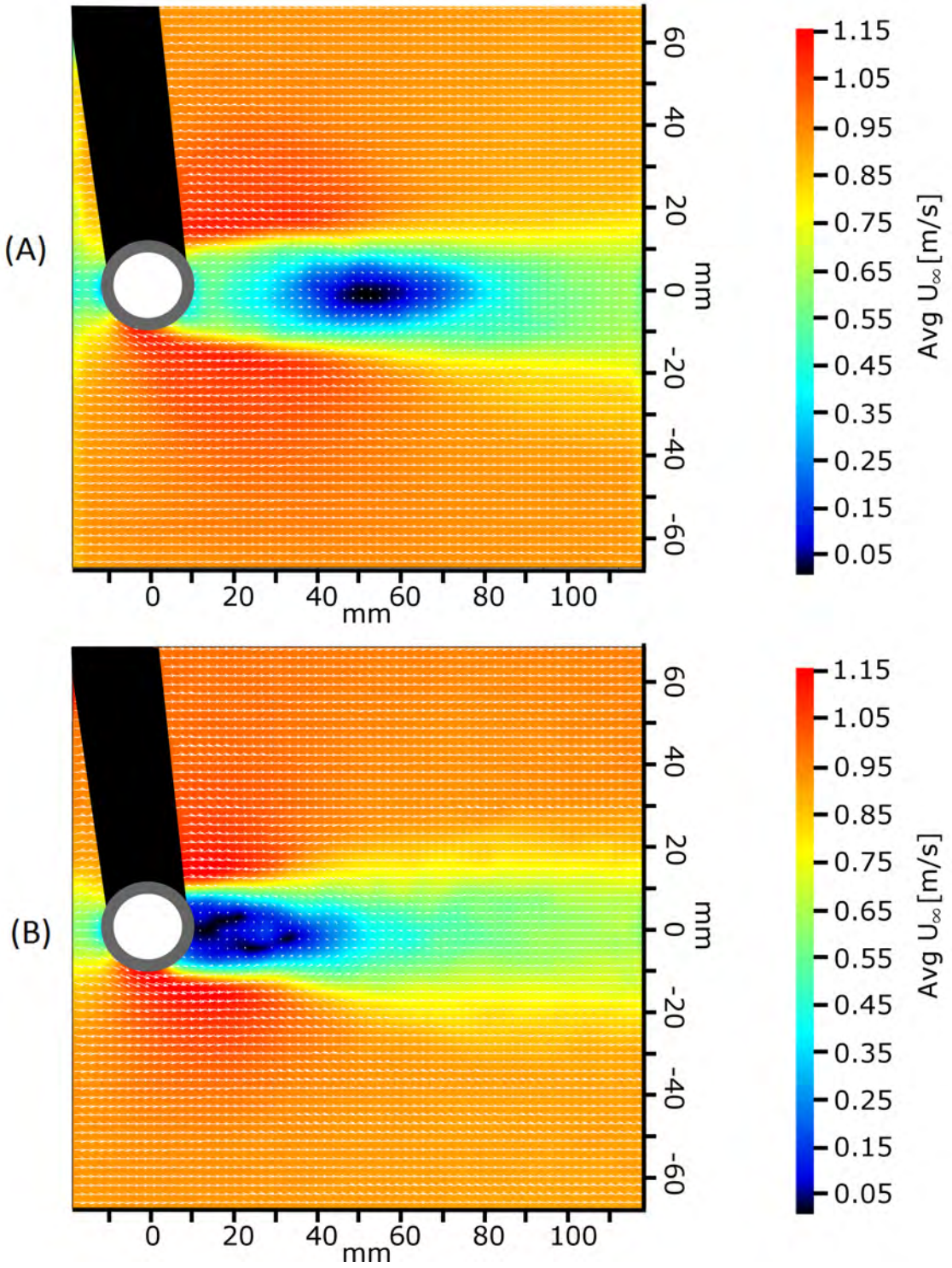

Figure 4.12: Effect of Reynolds number on the average flow velocity over a 20mm cylinder when Reynolds number is: (A) 2.2×10^3 and (B) 2×20^4

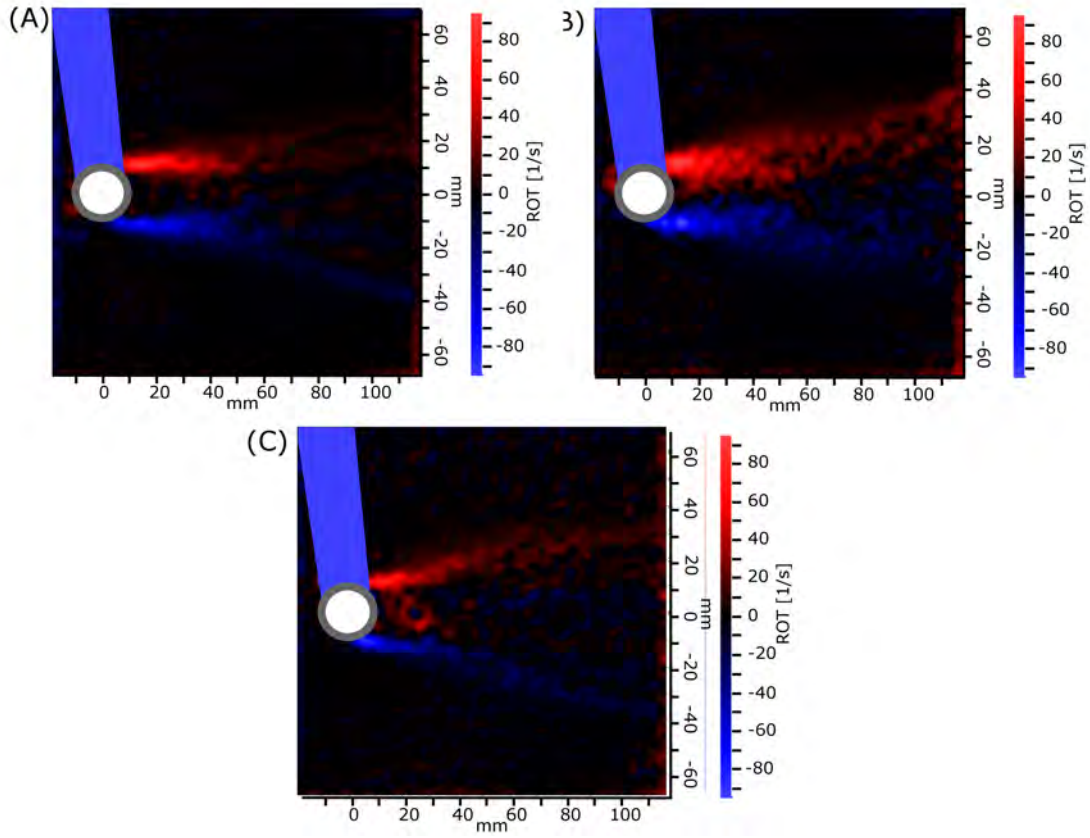

Figure 4.13: Effect of Reynolds number on the free stream shear layer formation, when Re_{cyl} is 1.1×10^4

4.5 Establishing a velocity ratio

The velocity ratio (V_R) was determined though analytical and experimental means. In order to establish a velocity ratio it is necessary to know both the cross-flow velocity (U_∞) and the average ejection velocity form the orifice (U_O) as such PIV was used to give an actual cross flow velocity and an approximation of the maximum ejection velocity. The analytical method assumes the fluid is incompressible ([8]) and that the usable area of the diaphragm is less than 100%. As the diaphragm was made using solid washers occupying around 75% of the diaphragm area, it was take that the percentage of usable area (k_{SJA}) would be an value less than this due to factors such as, diaphragm flexibility, fastening structures, and the step caused by the washer's thickness. As such, PIV was necessary to approximate the usable area of the diaphragm.

PIV was performed using the CW_L laser at a power of 1W, using an $f = -20$mm cylindrical lens. The camera was equipped using an 80mm extension tube and a 105mm lens at an aperture of 2.8, to give a viewing window of 4.5×5mm as is seen in figure 4.14A & B. The test were conducted over a range of recording rates from 240Hz to 2880Hz , depending on the SJA frequency and stroke length. In order to prevent streaking and to allow for ease of testing a shutter speed of 0.2ms, based on the maximum velocity was selected for all tests.

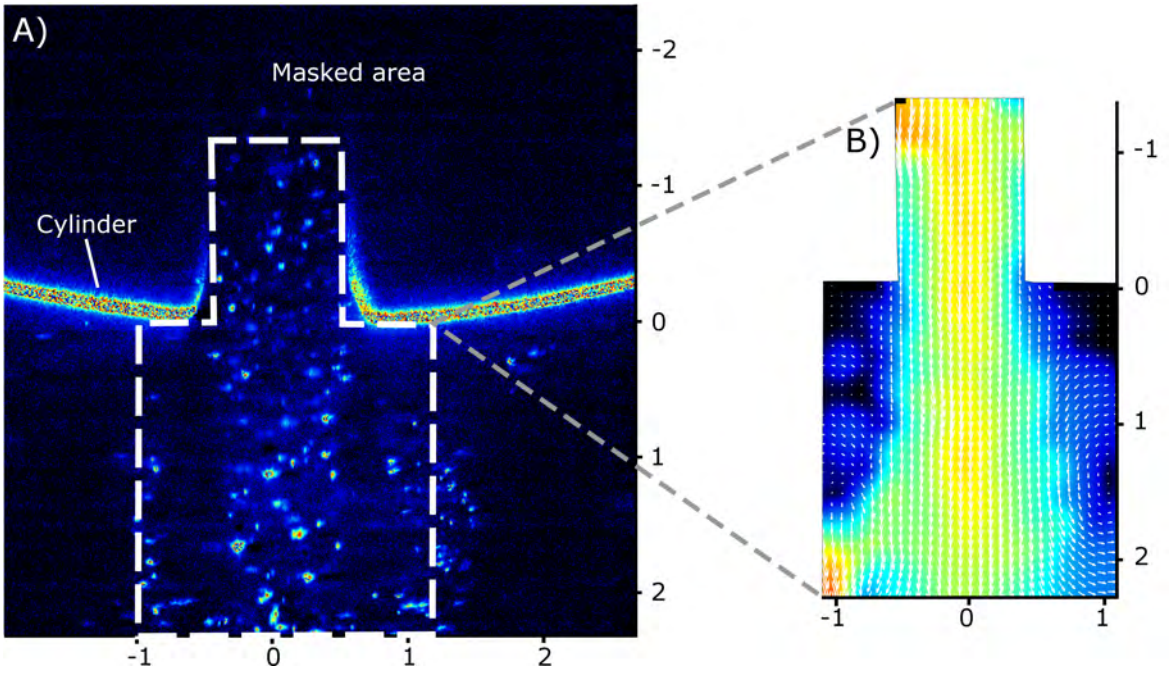

Figure 4.14: A) Raw image of the ejection phase of a SJA at 6Hz for a dimensionless stroke length of 0.5, and B) PIV of the masked of section of raw image

Figure 4.15 shows a typical image form the ejection phase of the SJA where the vortex has fully formed. PIV was taken for the jet frequencies of 4, 6, 8, and 10Hz for the L_0/D_O's of 0.25 and 0.5 (It should be noted to prevent confusion that for this thesis the dimensionless stroke length and the stroke length have the same numerical value). Test were conducted to give a minimum of 20 jet cycles, with 240 images per period, giving 120 images per ejection stroke.

In order to get sufficient illumination PIV particles were injected into the actuator so that a sufficient quantity of particulates would be present during the ejection phase. As a

result of this it was difficult to predict the actual average velocity over the ejection phase as there would typically be a lack of particles during the initial $20-30$ images, followed by a large spike as a sufficient density of seeding particles were ejected. As these tests were conducted at such a small scale, and seeding particle density was variable between each ejection phase, the results where used to estimate the average maximum ejection velocity. The average orifice ejection velocity is obtained using:

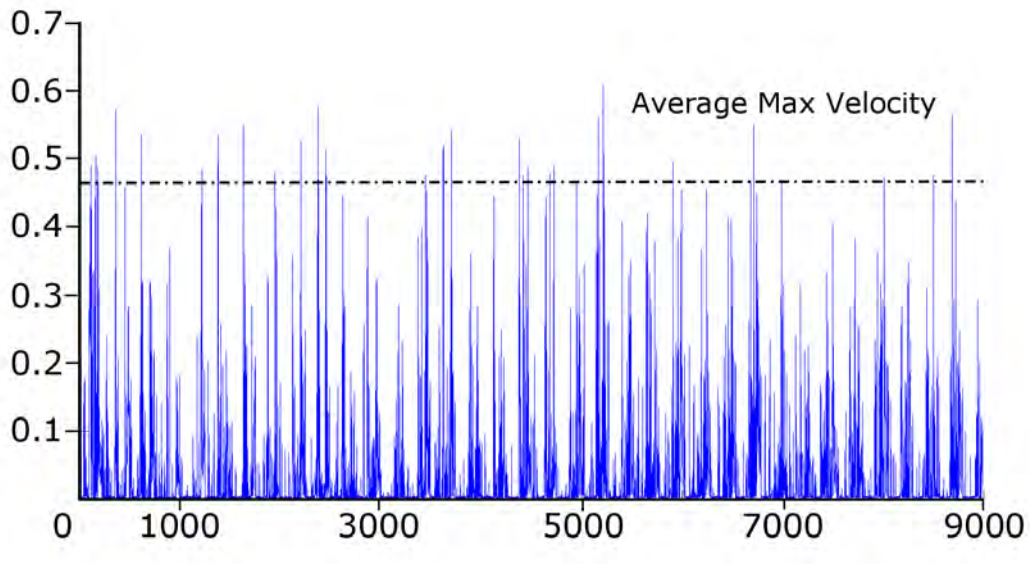

Figure 4.15: Velocity profile for a SJA actuating at 8Hz with an dimensionless stroke length of 0.5

$$\overline{U}_O = \frac{Q_{SJA}/A_O}{\pi} \tag{4.11}$$

Where $\overline{U}_O$ is the average orifice ejection velocity, A_O is the area of the orifice, and Q_{SJA} is the volumetric flow rate of the SJA and is obtained using:

$$Q_{SJA} = L_{SJA}\omega A_{SJA} k_{SJA} \tag{4.12}$$

Where L_{SJA} is the stroke length (diaphragm displacement), ω is the angular frequency, A_{SJA} is the area of the SJA diaphragm, and k_{SJA} is the usable area of the diaphragm.

It was found that a k_{SJA} value of 55% for the numerical solution corresponded well with the values obtained for the average maximum ejection velocity from the experimental PIV

tests. When the k_{SJA} value was applied to the analytical solutions it was found that the tests in this thesis were conducted over a range of $0.03 < V_R < 0.75$, as is shown in table 4.4.

Table 4.4: Velocity ratio and $\mathrm{Re}_{SJA} for all tests$

L_0/D_O	0.25		0.5	
f_{SJA}	Re_O	V_R	Re_O	V_R
1	59.5	0.03	119.1	.1
2	119.1	0.06	238.2	.13
3	178.6	0.09	357.3	.19
4	238.2	0.13	476.4	.25
5	297.7	0.16	595.5	.31
6	357.3	0.19	714.6	.38
7	416.8	0.22	833.7	.44
8	476.4	0.25	952.8	.50
9	535.9	0.28	1071	.56
10	595.5	0.31	1190.9	.63
11	655.0	0.34	1310	.69
12	714.6	0.38	1429.1	.75

4.6 Conclusion of experimental analysis and uncertainty

This project project was undertaken on a limited budget, which meant parts could only be made once. Even so the values obtained for the water tunnel where to an acceptable level. It would be expected that with more financial means in the future that the water tunnel would be updated and improved.

4.6.1 Limiting factors to testing

With a construction of a water-tunnel as ambitious as this, several issues arose due to a mixture of the following factors: limited budget, breakdown of lab equipment and time. As such the issues that bound the scope of testing are laid out here:

- Due to the construction of the SJA piping system and diaphragm a maximum value of 15Hz was achieved prior to degradation in the structure of the Vortices produced. For this reason, it was decided that test would be conducted up to 12Hz. The most likely cause for degradation was thought to be due to the inability of the silicone diaphragm membrane to cope with the pressures produced at 15Hz and above.

- Originally there had been three L_{SJA}'s chosen, with an additional stoke of 1mm used. However during initial tests it was found that a significant amount of thrust was produced by the jet in comparison to the force generated by the cross flow. This meant that it was not possible to obtain accurate results of the interaction of the SJA on lift and drag. However when L_{SJA} was reduced to 0.5mm, test showed thrust values (a maximum of 0.01 N) had no significant bearing on results.

- Originally tests were to be conducted using a doubled pulsed ND:YAG laser, for high speed PIV. However as testing was about to commence the laser system failed, requiring it to be sent away for repair and a continuous wave laser used in its place. This resulted in a maximum velocity cap of 0.6m/s, as was explained in section 4.1.2

Chapter 5

Synthetic Jet Actuated Cylinder in Cross-Flow: Effect on Drag and Lift Force

5.1 Aims

The aims of these tests were to determine how an embedded synthetic jet alters drag (F_D) and lift (F_L) forces acting on a cylinder by altering orifice angle (α_{SJA}), velocity ratio (V_R), and dimensionless stroke length (L_0/D_O) through the alteration of the synthetic jet actuator Stroke length (L_{SJA}) and the frequency (f_{SJA}). This was achieved through strain readings taken using four strain gauges positioned around a cylindrical sting arm at 90 degree offsets at a distance of 320mm form the centre of the cylinder, as laid out in section3.4.2.

5.2 Introduction to force measurement

As this thesis is concerned with fluidic control via a SJA embedded within a cylinder, it is necessary to be able to determine the direct effect the embedded SJA has on the lift and drag forces acting on a cylinder in a cross flow. This was achieved by recording strain taken at a rate of $2,000$Hz over two separate plains. These tests were broken in to 600 average points consisting of $2,000$ readings each, this gave a clear average effect of a SJA on lift and drag.

The goal of these tests were to produce graphs establishing how an SJA would alter lift and drag as the parameters of L_{SJA}, f_{SJA}, and α_{SJA} were altered, in order to optimize its usage. Testing was spit into two main categories:

- L_{SJA} = 0.5mm ($L_0/D_O = 5$)
- L_{SJA} = 0.25mm; ($L_0/D_O = 2.5$)

Test conditions for both of the jet stroke lengths where performed using the same values of α_{SJA} and f_{SJA}. These parameters were selected to build a *map of how the SJA affects* the lift and drag over a range of f_{SJA}'s at a variety of orifice angles relative to the boundary layer, such that the jet is located at the frontal and rear stagnation points, pre-separation, during and post-separation. To the author's knowledge there is little (or no) literature on the effects of a rectangular orifice synthetic jet on lift and drag alteration over 180^o, when comparing two dimensionless stroke lengths over the same range of jet frequencies.

5.3 Test setup and procedure

A test setup procedure was established prior to testing to ensure that the tests were conducted to a high standard and consistency to produce accurate and repeatable results.
This was achieved using the following steps:

1. The first step was to run the motor and the SJA for several minutes to ensure any bubbles that may have formed in the tank or cylinder over time are dislodged.
2. Cylinder was cleaned to ensure smoothness and rotated to the desired angle and the tank was left until the fluid had settled.
3. Using a specifically designed Davis code (that converted strain readings into lift and drag), lift and drag forces where zeroed to remove any issues caused by gravitation and sagging affects on the sting arm. A test was then run to asses if the tank was sufficiently settled or if it the system required rezeroing.
4. The tanks was then run for 3 minutes to allow flow to settle around the cylinder, after which a three-minute recording was taken with the SJA turned off. This was to determine no-jet lift and drag conditions.

5. After this the SJA was turned on and allowed to settle for 1 minute before another three-minute test was conducted to determine the lift and drag conditions due to actuation. Two more tests were conducted at the next values of f_{SJA}, followed by the SJA being turned off and a second no-jet condition being recorded.

6. Steps 4 and 5 were repeated, with the exception of the second no-jet condition being used as the first no-jet reading for the next batch.

7. Steps 4 to 6 were repeated until all values of f_{SJA} were tested. This batch system allows for an average no-jet condition to be established between batches of f_{SJA} improving the accuracy of test data collected.

8. These values where then laid out in a table to show the percentage difference.

9. Two values where chosen, usually due to their level of effect on drag (outliers or the most extreme changes) to be re-tested for every α_{SJA} set. If the results of these tests were within 2% of the original values then the tests were accepted, if not the test set was repeated. The value of 2% was chosen based on the level of accuracy obtainable from the equipment used.

5.4 Test range

As stated earlier the test where conducted at different L_{SJA}'s, f_{SJA}'s, and α_{SJA}'s to give an understanding of the effects an SJA has over a broad range, optimizing it abilities. The range of test conditions is laid out in table5.1 below.

Table 5.1: Experimental parameters for Lift and Drag measurements

L_{SJA}	0.5						0.25							mm
α_{SJA}	0	80	90	100	110	120	130	140	180	Degrees				
f_{SJA}	0	1	2	3	4	5	6	7	8	9	10	11	12	mm

Each test was taken over a duration of 180 seconds, with a recording rate of $2,000$Hz giving a total of $360,000$ strain readings per strain gauge pair. To make reading of values more convenient to interpret and to give an average trend of force values, the $360,000$ readings where broken down into 600 average points, each consecutive of 600 force values.

5.5 Strain results

Results from tests show excellent fluid control is achieved through the use of a SJA embedded in a cylinder. A total drag modification of approximately 50% was achieved, based on the SJA being able to achieve a maximum drag increase of approximately 30% and a maximum drag reduction of approximately 20% from the no-jet condition.

5.5.1 Baseline drag acting on a cylinder

The baseline test were to characterise the stain gauges against literature to ensure that the results obtained from testing are correct and to give a proper baseline result from which to base the effects that the SJA has on the lift and drag forces acting on the cylinder. The coefficient of drag is worked out using:

$$C_D = F_D 1/2 \rho U_\infty^2 A \tag{5.1}$$

With a cross-flow velocity of 0.312m/s (Re_{cyl} = 5.62$x10^3$) an average drag force (F_D) of 0.11N is obtained. This gives a coefficient of drag of 0.95. This value agrees well with Yunus & Jhn [2], who give a C_D of 1 for a cylinder with a Re of approximately 5$x10^3$

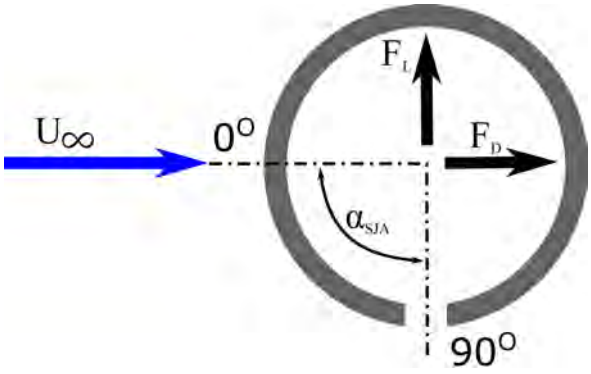

Figure 5.1: Schematic of synthetic jet embedded in cylinder

5.5.2 Overview of the effects of synthetic jet actuator on Drag

The primary concern of this Thesis is in the investigation of drag modification achieved by the interaction of the SJA with the boundary layer, shear layer and wake produced by a cylinder. As such the primary focus will be on drag.

Figure 5.1 shows the setup for the strain test, the PIV and flow visualisation test. The angle of zero degrees is taken to be the jet orifice facing directly into the cross-flow.

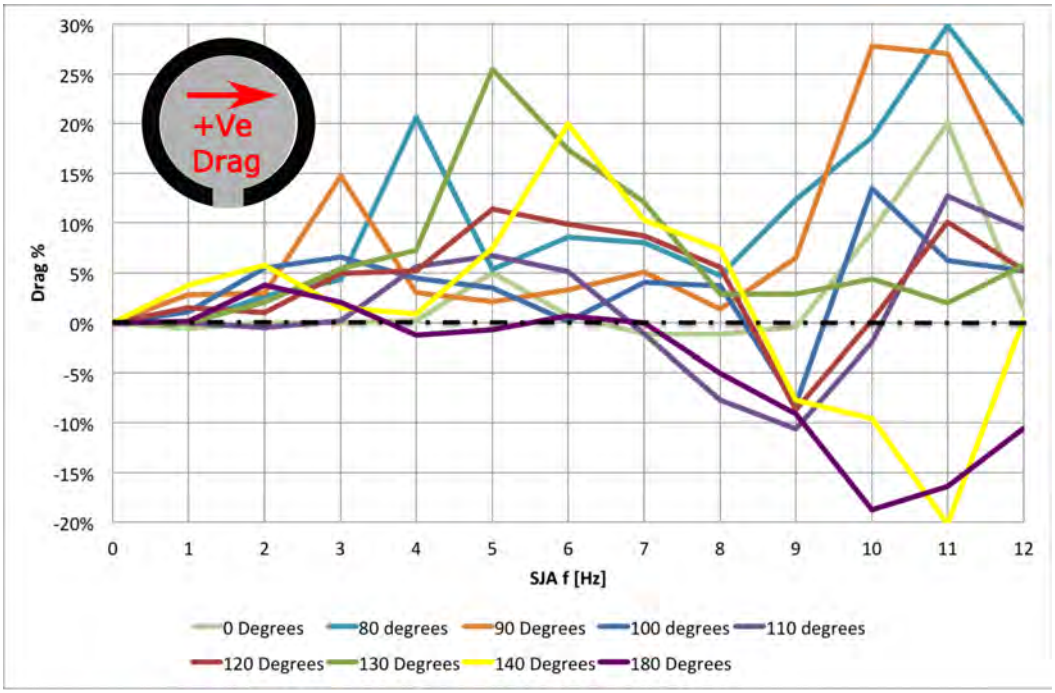

Figure 5.2: Effect of synthetic jet actuator on drag from α_{SJA} of 0° to 180° at L_{SJA} of 0.5mm when f_{SJA} goes from 0Hz to 12Hz

Figures5.2 and .5.3 show the overall drag effects produced by the SJA using the 0.5mm and 0.25mm L_{SJA} respectively. It is clear that a change in stroke length produces different effects, in particular with regards to magnitude and the degree of change in trend lines over small ranges of frequencies. The points that stand out the most are as follows:

- the maximum drag reached by the 0.5mm jet stroke length is significantly higher than that of the 0.25mm jet stroke length, with a maximum drag value of 30% (L_0/D_O = 0.5mm) compared to 18% (L_0/D_O = 0.25mm). Conversely the differences in drag reduction are less dramatic with a -20% and -15% for 0.5mm and 0.25mm respectively.

- The highest drag level of 30% occurs at 80°, when L_0/D_O is 5 (L_{SJA} = 0.5mm) and V_R is 0.69 (f_{SJA} = 11Hz).

- At low f_{SJA} large spikes in drag take place for only the 0.5mm stroke length.

- In both cases the majority of large scale drag modification for nearly all angles takes place after 8Hz.

- Trends in drag effects are seen throughout the f_{SJA} range tested. These trends are seen in two major ways:

    1. over certain ranges of frequencies there are distinctive changes in drag characteristics taking place, such as in figure 5.2 with a sudden spike in drag in between 3Hz (V_R = 0.19) and 6Hz(V_R = 0.38) and a splitting of drag characteristics from 8Hz(V_R = 0.5) to 12Hz(V_R = 0.75). Similar effects are seen in figure 5.3 with a splitting of drag characteristics between angles from 2Hz(V_R = 0.06) to 6Hz(V_R = 0.19). Between 7Hz(V_R = 0.22) and 12Hz(V_R = 0.38) this splitting continues at a greater magnitude. These trends appear to be dependent on a mixture of V_R, L_0/D_O, and orifice angles, this is covered in more detail in section5.6.1 below.
    2. Similarities in drag affects are seen between certain angles, where the SJA has a similar influence on drag between closely related angles. These angles are laid out in tables 5.2 & 5.3.

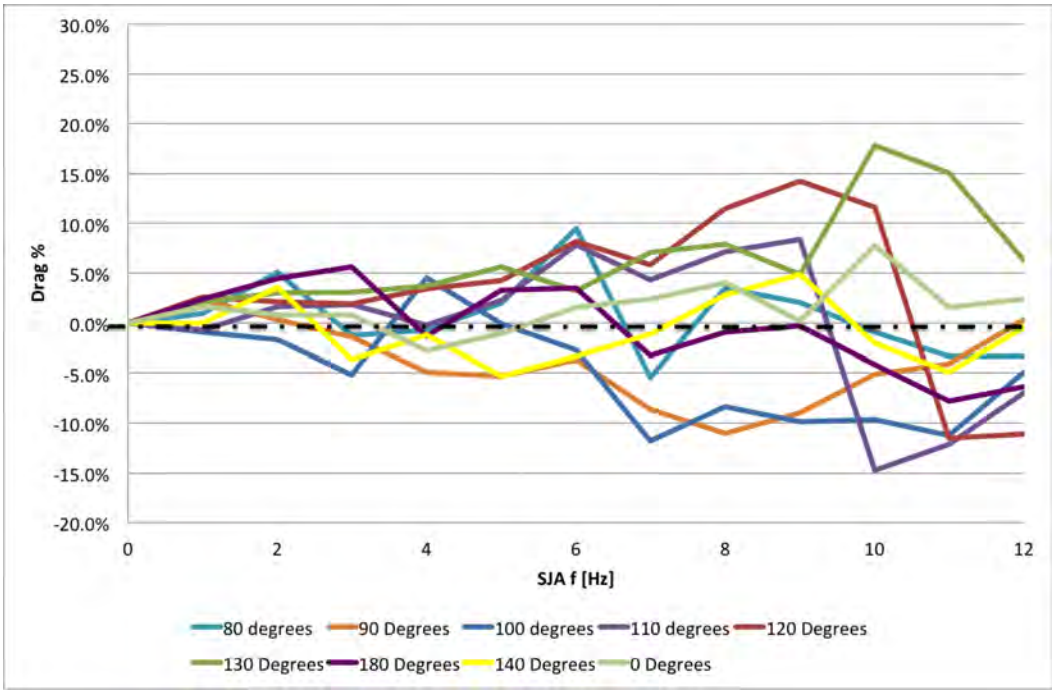

Figure 5.3: Effect of synthetic jet actuator on drag from α_{SJA} of 0° to 180° at L_{SJA} of 0.25mm when f_{SJA} goes from 0Hz to 12Hz

5.5.3 Analysis of drag effects when L_0/D_O is 0.25

This section is concerned with the examination of drag effects produced by the SJA when the synthetic jet stroke length (L_{SJA}) is 0.25mm (L_0/D_O) and a V_R range of 0.03 to 0.38. Tests results are separated based on angles as laid out in the table5.2 below.

Table 5.2: Drag Angle Sets for L_0/D_O of 0.25

L_{SJA}	Graph 1	Graph 2	Graph 3
0.25	$0°, 80°, 90°$	$90°, 100°, 110°, 120°, 130°$	$130°, 140°, 180°$

5.5.3.1 Drag effects when the jet angles are at $0°$, $80°$, and $90°$.

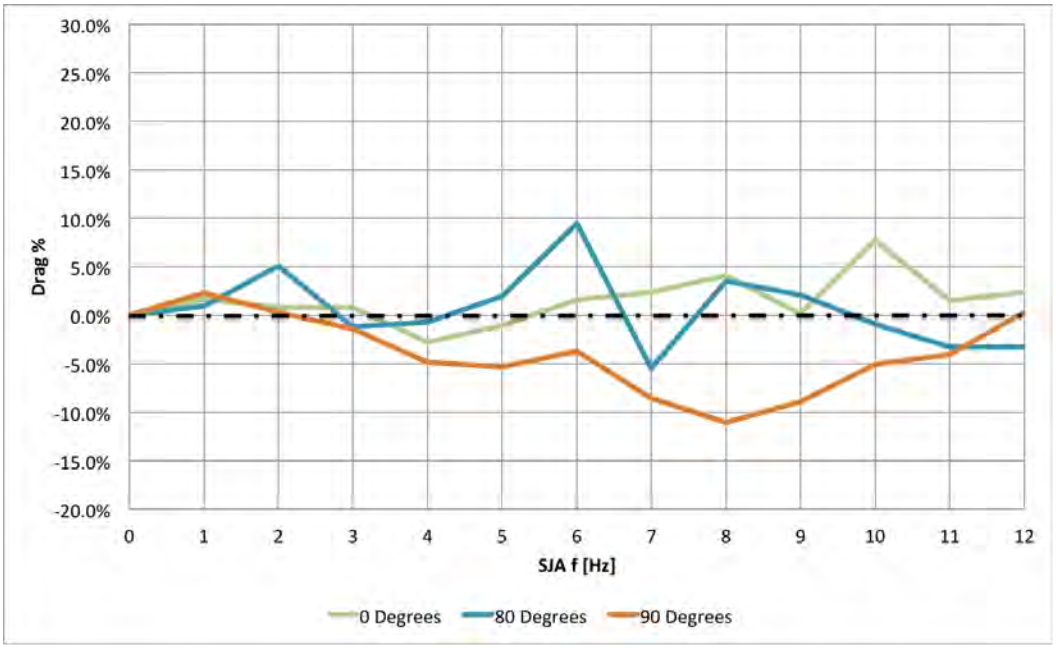

Figure 5.4: Effect of synthetic jet actuator on drag at L_{SJA} of 0.25mm when α_{SJA} are at 0°, 80°, and 90°

In figure 5.4 the jet angles of 0°, 80°, and 90° are examined. Three distinct drag trends are present, which is expected to take place as the three jet angles lay in different flow conditions of: the front stagnation point (0°), well within the pre-separation zone(80^o), and around the separation point(90°).

Looking firstly at α_{SJA} of 0° (fig5.4 light green) it can be seen that there is no significant drag reduction achieved, only a small short lived drop in drag of -3% from the no-jet. This

is followed by a gradual 7% gain in drag as f_{SJA} transitions from 4Hz (V_R = 0.13) to 8Hz (V_R = 0.25). At 9Hz V_R = 0.28) there is a loss in drag modification, which is followed by an 8% gain in drag at 10Hz (V_R = 0.31).

An α_{SJA} of 80° (fig5.4 light blue) produces the most unstable trend of the group and of all jet angles with an L_0/D_O of 0.25, transitioning from a spike in drag gain to loss of modification to gain, to drag reduction and an increase again, followed by a gradual drag reduction. The most prominent of these spikes takes place between 5Hz (V_R = 0.16) and 8Hz (V_R = 0.25), where a drag increase of 7% occurs when f_{SJA} is increased by 1Hzfrom 5Hz (V_R = 0.16) to 6Hz (V_R = 0.19). This is followed by a sudden drop in drag of 14% over an increase of 1Hz, taking drag from 9% to -5%. This drop is followed by another increase in drag of 9% as the frequency increase form 7Hz(V_R = 0.22) to 8Hz(V_R = 0.25). Another lesser spike takes place over single hertz at 2Hz(V_R = 0.06) where drag increases to 5%.

α_{SJA} 90° (fig5.4 light orange) presents the first case with a consistent reduction in drag over the majority of the frequency bands tested. Apart from a small drag increase of 2% at 1Hz (V_R = 0.03), drag reduction begins at some point between 2Hz (V_R = 0.06) and 3Hz (V_R = 0.09), and remains below the no-jet condition. Between 3Hz (V_R = 0.09) and 4Hz (V_R = 0.13) a drag reduction of 4% takes place followed by a near levelling out prior to a small drag increase of roughly 1% at 5Hz (V_R = 0.16). This is then preceded by a further drop in drag of around 7% to -11% drag at 7Hz (V_R = 0.22). Beyond this point the drag reduction diminishes relatively linearly to -5% at 10Hz (V_R = 0.31).

5.5.3.2 Drag effects when the jet angles are set to 90°, 100°, 110°, 120°, and 130°.

Figure 5.5 examines the jet angles of 90°, 100°, 110°, 120°, and 130°. Unlike in figure 5.4 these angles can be split into two groups based on their similarities in characteristic drag affects:

- **Group A**: Predominant Drag decrease - 90° and 100°
- **Group B**: Predominant Drag increase with a potential for significant drag reduction -

110°, 120° and 130°

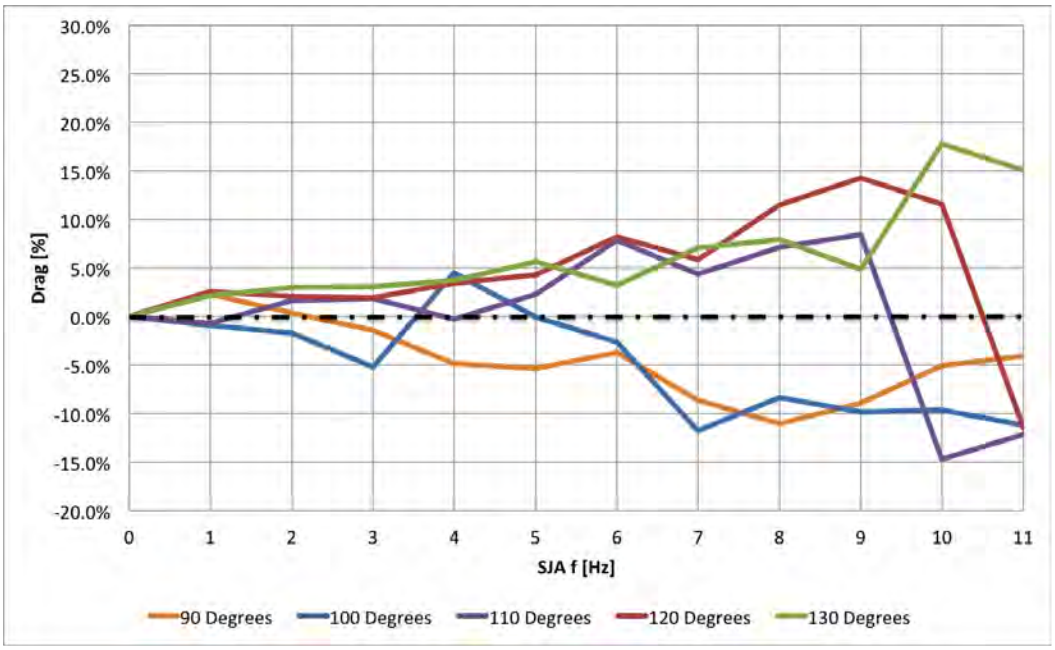

Figure 5.5: Effect of synthetic jet actuator on drag at L_{SJA} of 0.25mm when α_{SJA} is 90°, 100°, 110°, 120°, and 130°

In both instances the profiles show a similar affect on drag alteration, with *group B* having almost identical results for 110°(fig5.5, Purple line) and 120°(fig5.5, Red line), with an earlier drop off in drag after 9Hz (V_R = 0.28) for 110°, compared to the 10Hz (V_R = 0.31) drop off for 120°. 130°(fig5.5, Green line) show a similar profile to the others until 9Hz (V_R = 0.28), where an increase of drag is produced. *Group A*'s profiles shows similar characteristic trends, however two significant points of deviation are present:

1. Between 3Hz (V_R = 0.09) to 6Hz (V_R = 0.19), 100° has a sudden spike in drag from 3Hz (V_R = 0.09) to 4Hz (V_R = 0.13), that is not present in the 90° case.

2. When the two profiles separate from one another between 9Hz (V_R = 0.28) and 10Hz (V_R = 0.31), with a degradation in drag reduction experienced only by the 90° jet angle.

Having looked at the profiles in general terms, a more detail analysis will be done of *group A*. α_{SJA} of 100° (fig5.5, Blue line) will be discussed initially, keeping the breakdown chronological, and as 90° has already been examined previously. The most prominent feature of 100° is that is flip-flops from drag reduction to an increase in drag and back to drag

reduction form the no-jet. This culminates in a change of drag around 25%, over only a 4Hz range from 3Hz (V_R = 0.09) to 7Hz (V_R = 0.22). This initiates when a gradual reduction in drag up to 3Hz (V_R = 0.09) abruptly changes to a gain in drag of about 9%, from -5% to 4% over a single hertz. This is preceded by a sharp drop to drag reduction at 5Hz (V_R = 0.16). This drag reduction continues until 6Hz (V_R = 0.19), where it then has its most pronounced drop of 9%, from -3% at 5Hz to -12% at 7Hz (V_R = 0.22). After this drag stabilises, where it remains at around -10%. *Group A* produces the most consistent drag reduction, spanning a relatively large range of f_{SJA}'s from 7Hz (V_R = 0.22) to 11Hz (V_R = 0.34) with an average drag reduction over this range of -10%.

For the jet angles of *Group B*, all three angles follow a very similar trend up to 9Hz (V_R = 0.28), with a gradual increase in drag for all (except for at 1Hz (V_R = 0.03) and 4Hz (V_R = 0.13) for 110°). It can be seen that between 6Hz(V_R = 0.19) and 11Hz (V_R = 0.34) for the 110° and 120° cases, the profiles are very similar with slight differences in the amount of drag produced by each. This is even seen with both taking a sudden plummet in drag, offset by 1Hz. In the 120° case this drop in drag to -15% results in the largest drag reduction for L_{SJA} of 0.25mm (see fig5.3).

Up until 9Hz (V_R = 0.28), 130° has a similar profile to that of the rest of *group B*, with a slight difference presenting at 7Hz (V_R = 0.22) where 130° experiences a slight dip in drag. After 9Hz (V_R = 0.28) 130° profile changes significantly, when it only experiences sudden gain in drag from 9Hz (V_R = 0.28) to 10Hz (V_R = 0.31). At 10Hz (V_R = 0.31) α_{SJA} 130° reaching its maximum drag gain attained of 18% (for any angle tested at L_{SJA} of 0.25mm).

5.5.3.3 Drag effects when the jet angles are set to 130°, 140°, and 180°

In figure 5.6 it is seen that there is little commonality between the profile trends of the three angles of 130°, 140°, and 180°. It is expected that 180^o would be different as it's angles is so different, thus any vortices produced would be emanating into significantly different conditions to that of the 130° and 140° cases. From figure 5.5 it was seen that there where

similarities in profiles from 110° to 130°. However, these similarities are not present when transitioning from 130° to 140°, where both profiles behave differently.

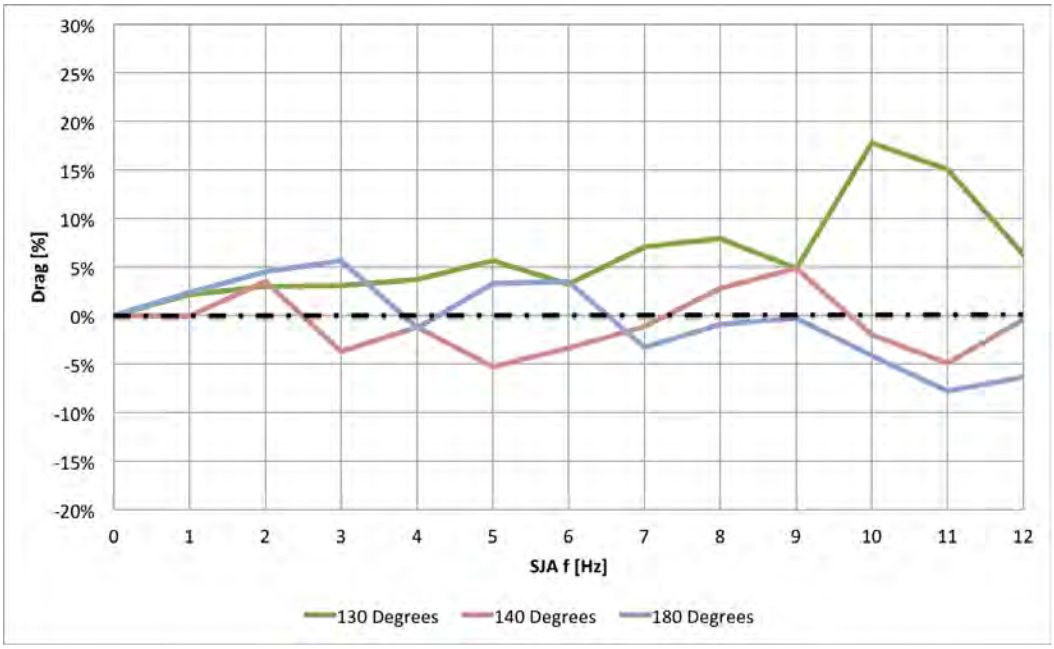

Figure 5.6: Effect of synthetic jet actuator on drag at L_{SJA} of 0.25mm when α_{SJA} is 130°, 140°, and 180°

An α_{SJA} of 140° (fig5.6 pink line) does not provide much fluidic control in comparison to previous angles with a maximum drag reduction and drag increase of -5% and 5% achieved respectively. No-jet effect takes place until a small drag increase of 4% at 2Hz ($V_R = 0.06$), followed by a seesawing motion of drag reduction from 3Hz ($V_R = 0.09$) until the maximum drag reduction of -5% at 6Hz ($V_R = 0.19$). A steady increase of drag from 5Hz ($V_R = 0.16$) to 9Hz ($V_R = 0.28$) results in the maximum drag of 5% prior to a drop off to -5% at 11Hz ($V_R = 0.34$).

The jet angle of 180% (fig5.6 Blue line) has little impact on fluidic control, lacking consistency between jet frequencies. The initial profile trends towards an increase in drag up to 3Hz ($V_R = 0.09$), when a loss of drag modification takes place, followed by a resurgence in drag at 5Hz ($V_R = 0.16$) that remains constant till it drops off again after 7Hz ($V_R = 0.22$). Beyond this point little drag modification takes place until a brief reduction in drag of -8% is seen at 11Hz ($V_R = 0.34$).

5.5.4 Analysis of drag effects at an L_{SJA} of 0.5mm

As in the previous section5.5.3, the concern in this section is the examination of drag effects produced by a synthetic jet with a L_0/D_O is 0.5 (L_{SJA} = 0.25mm) over a range of f_{SJA} from 1Hz to 12Hz (V_R of 0.6 to 0.75). The test results will be separated into graphs based on angles as laid out in the table5.3 below.

Table 5.3: Drag Angle Sets for L_0/D_O of 0.5

L_{SJA}	Graph 1	Graph 2	Graph 3
0.5	$0°, 80°, 90°$	$90°, 100°, 110°, 120°$	$130°, 140°, 180°$

5.5.4.1 Drag effects when the jet angles are set to 0°, 80°, and 90°.

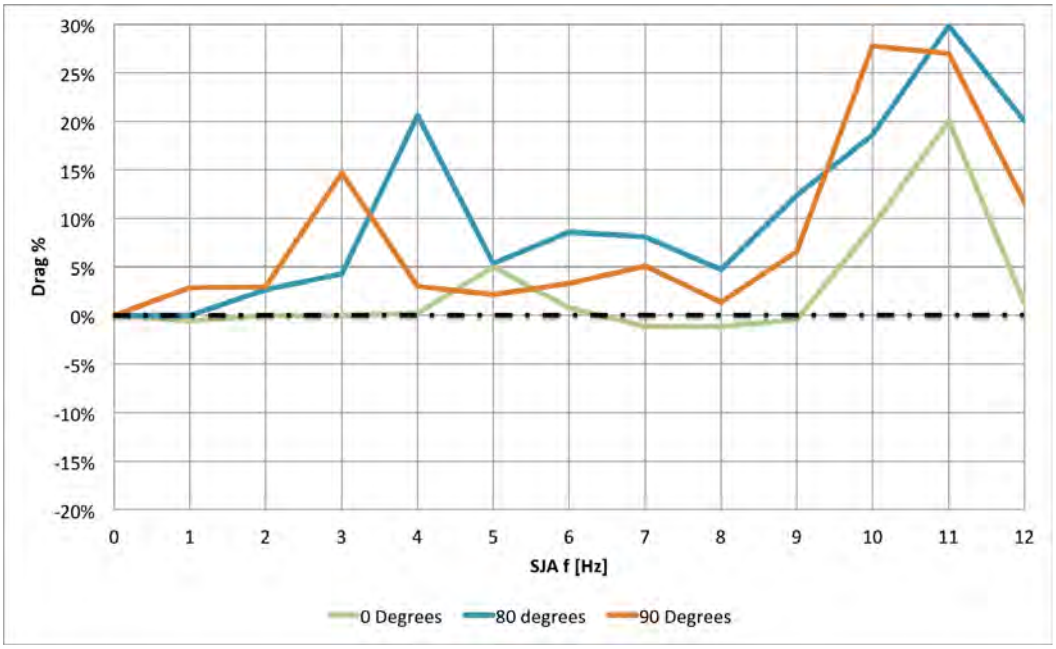

Figure 5.7: Effect of synthetic jet actuator on drag at L_{SJA} of 0.5mm when α_{SJA} is 0°, 80°, and 90°

Results in figure 5.7 show that the profiles undergo substantial spikes in drag. These areas of drag gain take place at similar V_R (f_{SJA}) for all the Jet angles, with the magnitude of drag gain being the primary difference. In all three angles a similar profile is apparent. This also takes place with the 0°(fig5.7, light green line), with a difference in drag gain at 5Hz(V_R =

0.31) of 5%, compared to a 21% at 4Hz ($V_R = 0.25$) for 80°(fig5.7, light blue line).
for the majority of the SJA frequencies tested 0^o has no effect on the drag, with only three frequencies displaying any significant effect. At 5Hz ($V_R = 0.31$) there is a small drag increase of 5%, that dissipates by 6Hz ($V_R = 0.38$). Drag experiences a near linear growth form 9Hz ($V_R = 0.56$) to 11Hz ($V_R = 0.69$), where it reaches a drag value of 20%, the highest drag value experienced buy any jet angle for an L_{SJA} of 0.25mm.

To best describe 80° and 90° they are placed together into *group C*.

- **Group C** Large spikes in drag.

Even though 0° displays very similar characteristics it is not placed in this group due to its large difference in α_{SJA}, and its small drag gain at 5Hz ($V_R = 0.31$). In both cases drag grows gradually until the first spike is reached, with it taking place 1Hz earlier for 90^o and having a less of a drag effect. A difference in magnitude is maintained as they undergo minor drag changes to 7Hz ($V_R = 0.44$), at which point both experience a drop in drag of $2-3\%$ before both undergo a large increase in drag of roughly 25%. Again 90° reaches its maximum drag value (28%) 1Hz prior to 80°, which again reaches higher maximum drag value of 30% (highest value experienced across all tests). A levelling off of drag is seen from 10Hz ($V_R = 0.63$) to 11Hz ($V_R = 0.69$) for the 90° jet angle. This is followed by a drop-off in drag effects at 12Hz ($V_R = 0.75$) for both jet angles.

5.5.4.2 Drag effects when the jet angles are set to 100°, 110°, and 120°.

In figure 5.8 close similarities in the general trend between the three profiles is seen, and as such they are designated as *group D*.

- Predominantly drag increase with sudden short lived drag reduction.

Group D's most prominent feature is sudden spike in drag reduction at between 8Hz ($V_R = 0.5$) and 9Hz ($V_R = 0.56$), where drag is reduced to between -9% and -11% before it shoots back up to 13% over one to two hertz. For the three peaks it is noticed that the 100° case has its largest peak offset by one hertz earlier than the others.

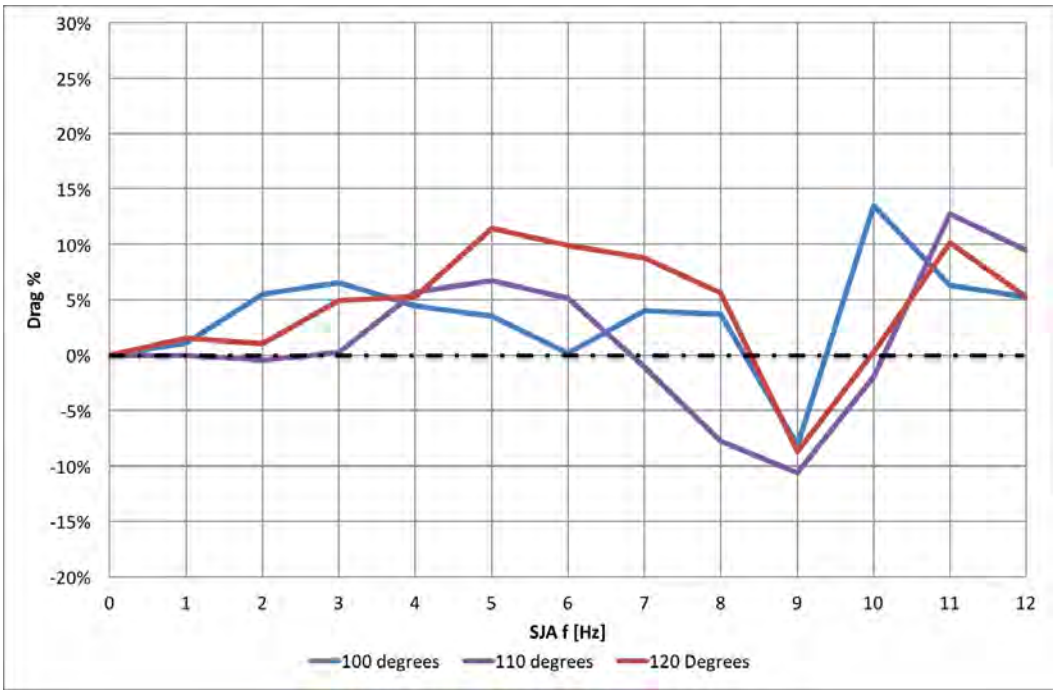

Figure 5.8: Effect of synthetic jet actuator on drag at L_{SJA} of 0.5mm when α_{SJA} is 100°, 110°, and 120°

Prior to 8Hz (V_R = 0.5) the profiles are less similar with just a single crossover at 4Hz (V_R = 0.25) for all profiles. 120° has a steady drag increase up to 5Hz (V_R = 0.31) at which starts to reduce, prior a large drop at 8Hz (V_R = 0.5). This drop is the same as the 100° case. Interestingly 120° and 110° both undergo a drop in drag after 5Hz (V_R = 0.31), 110° has a larger drop after 6Hz (V_R = 0.38), due to this earlier drop 110° maintains a high drag reduction for a longer period of time.

5.5.4.3 Drag effects when the jet angles are set to 130°, 140°, and 180°.

Figure 5.9 looks at 130° (green line), 140° (yellow line), and 180° (purple line). The general profiles of 130° and 140° are similar except for the sudden drag reduction experienced by 140° and can be grouped into *group E* due to their similarities and closely related angles.

- **Group E** Large drag increase followed by a large drag reduction.

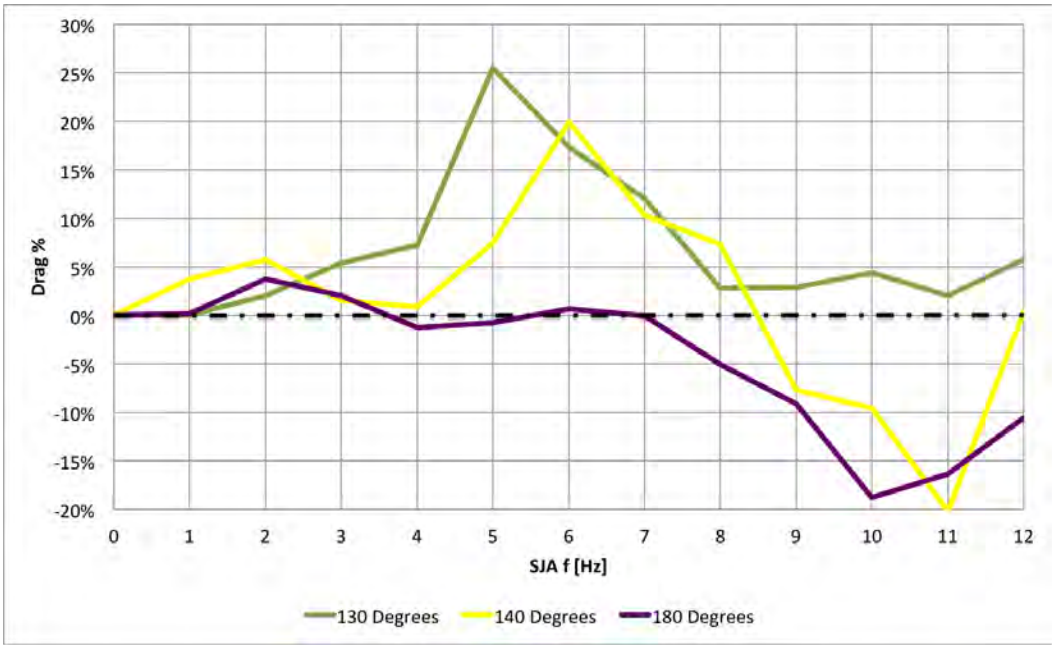

Figure 5.9: Effect of synthetic jet actuator on drag at L_{SJA} of 0.5mm when α_{SJA} is 130°, 140°, and 180°

Initially there are similarities in group E's profiles, this is seen in figure 5.9, beginning with an area of low levels of drag modification, followed by a significant spike in drag levels over two to three hertz. These spikes result in peak drag forces of 25% and 20% for the 130° and 140° jet angles respectively. As with *group D*(fig5.8) there is an offset in the point of maximum drag of one hertz between the peaks, with a difference in magnitude.
These spikes disappear as quickly as they formed, 8Hz (V_R = 0.5)after this point that the two profiles differ. After the spike 130° returns to a low lever of drag up to 12Hz (V_R = 0.75), whereas the 140° case continues on its downward trajectory. This trajectory results in α_{SJA} undergoing a 45% transition from of 25% drag at 6Hz (V_R = 0.38) to a drag reduction of -20% at 11Hz (V_R = 0.69), producing the lowest level of drag across all tests conducted. This is followed by a gain in drag at 12Hz (V_R = 0.75)

The final angle to be looked at was α_{SJA} of 180°. 0Hz to 7Hz yield little or no drag effects. However, after 7Hz a steep drag reduction from 0% to -19% at 10Hz occurs. This is followed by a gradual increase in drag to -11% at 12Hz.

5.5.5 Effects of an synthetic jet actuator on Lift

As mentioned previously (Sec. 5.5.2 drag analysis was the primary concern of this thesis, and as a result of having lowered cross-flow velocity to accommodate available equipment (see section 4.6.1), it was decided that the values obtained for lift would be taken as quantitative measures. As such the trend lines of lift were used to determine the direction of lift produced. Figures 5.10 and 5.11 below show the lift for the L_{SJA} of 0.5mm and 0.25mm respectively.

5.5.5.1 Overview of lift effects

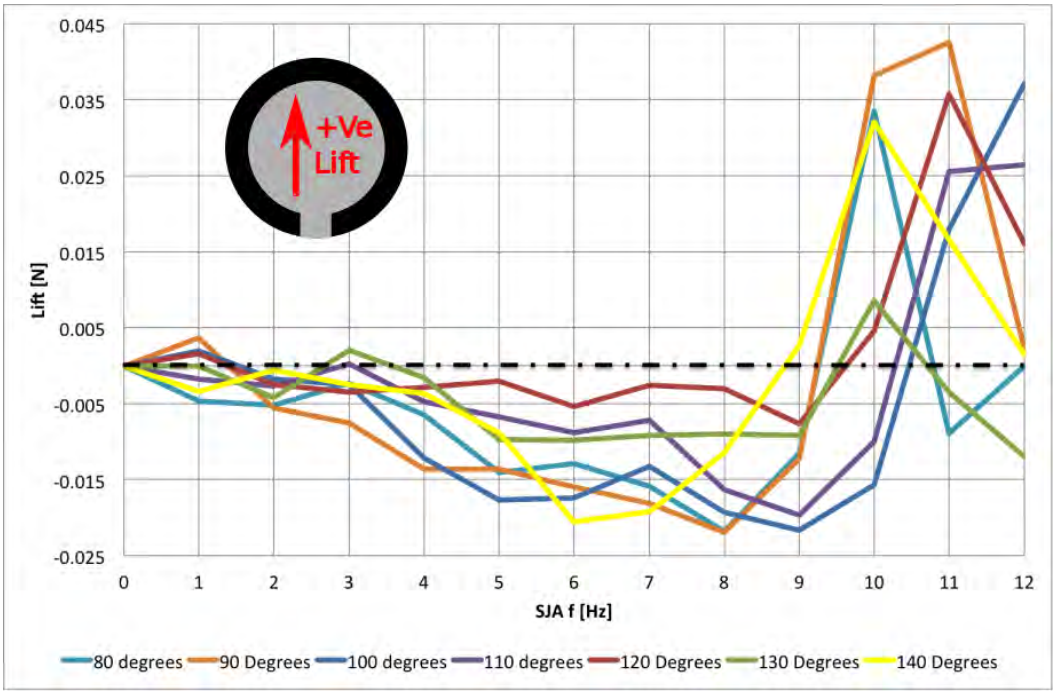

Figure 5.10: Effect of synthetic jet actuator on lift at L_{SJA} of 0.5mm when α_{SJA} ranges from 80° to 140°

For both $L'_{SJA}s$ (L_0/D_O) there are similarities in the profiles of their respective angles, with a predominant downward lift (In the direction of the orifice, fig5.10) for the profiles of all angles. For L_{SJA} of 0.25mm (fig5.11), the trend of the profiles it towards a negative lift, with a small resurgence towards no-jet at 12Hz ($V_R = 0.38$). The exception to this is the 140° jet angle, as it has an initial jagged profile transitioning from negative to positive and back to negative over the first half of the frequency band. The profile remains unsteady in comparison

to other angles.

The primary difference between the two jet stroke length occurs after 9Hz where they differ significantly, with an abrupt change from negative to positive lift for the 0.5mm jet stroke length. For 0.5mm stroke length the highest levels of positive lift are recorded for all the angles between 10Hz (V_R = 0.63) and 12Hz (V_R = 0.75), with the exception of the magnitude of maximum positive lift experienced for 130° being less.

When comparing the effects an SJA has on lift to drag, several trends can be identified. Looking at Group D (see table5.5, and figure 5.8), where the similarities between the drag of the jet angles looked at is also present for the same angles for lift in figure 5.12.

For both lift and drag the SJA takes an effect on the profiles at around 3Hz and 4Hz. Again at 7Hz to 9Hz there is sudden change in the lift and drag conditions, in this case with a reversal from negative lift to positive lift starting from 9Hz. During this range drag goes from drag reduction to an increase from the no-jet case.

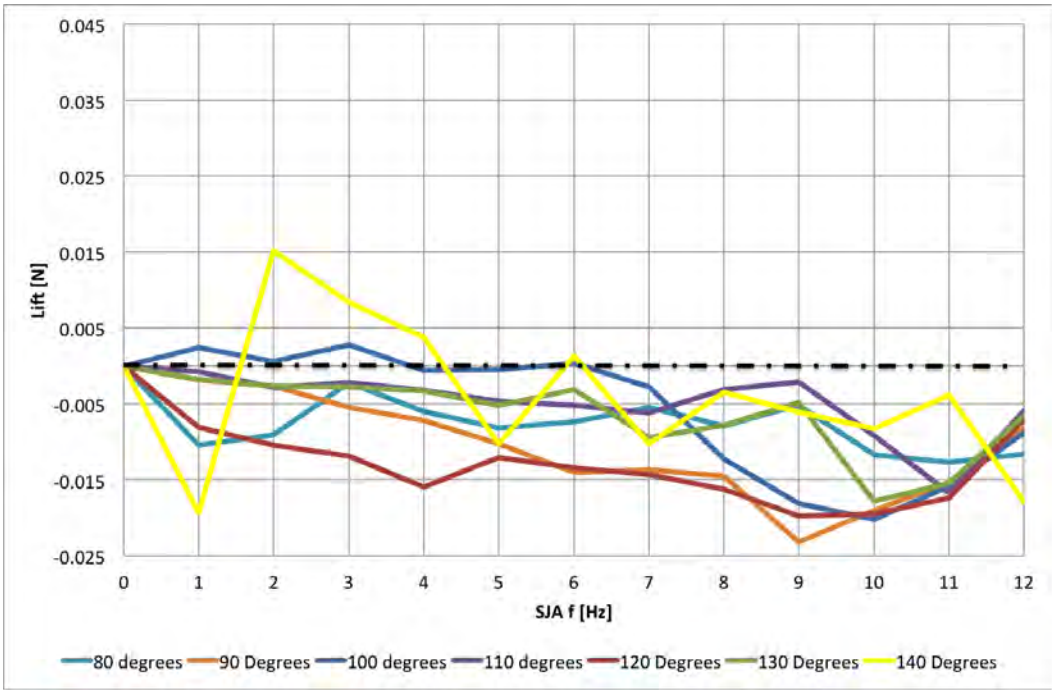

Figure 5.11: Effect of synthetic jet actuator on lift at L_{SJA} of 0.25mm when α_{SJA} ranges from 80° to 140°

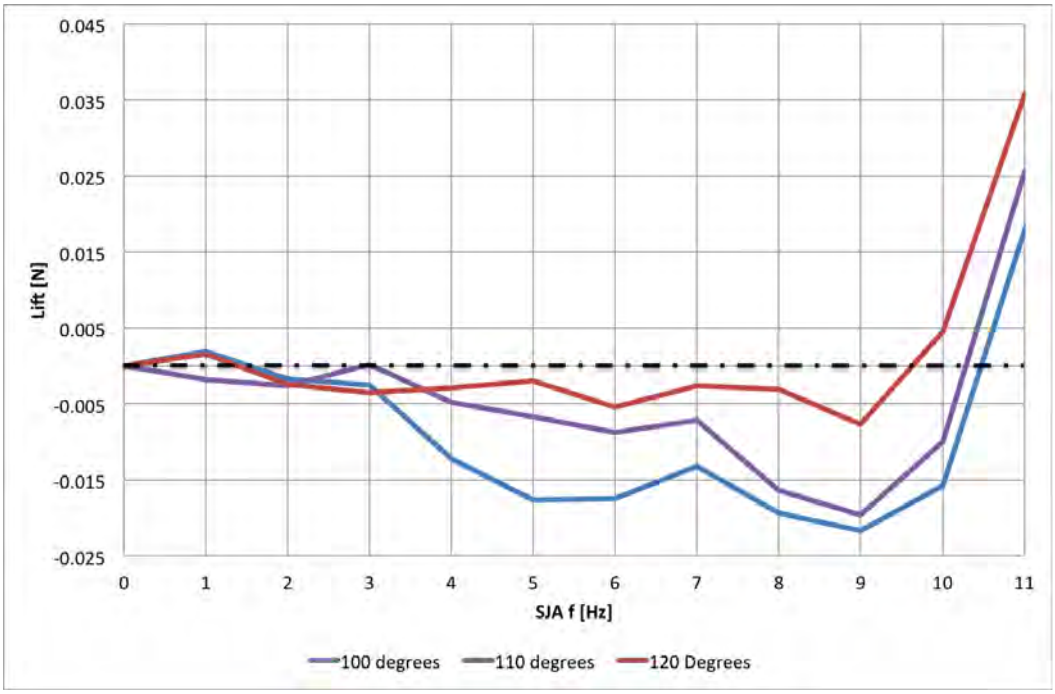

Figure 5.12: Effect of synthetic jet actuator on lift at L_{SJA} of 0.5mm when α_{SJA} is 100°, 110°, and 120°

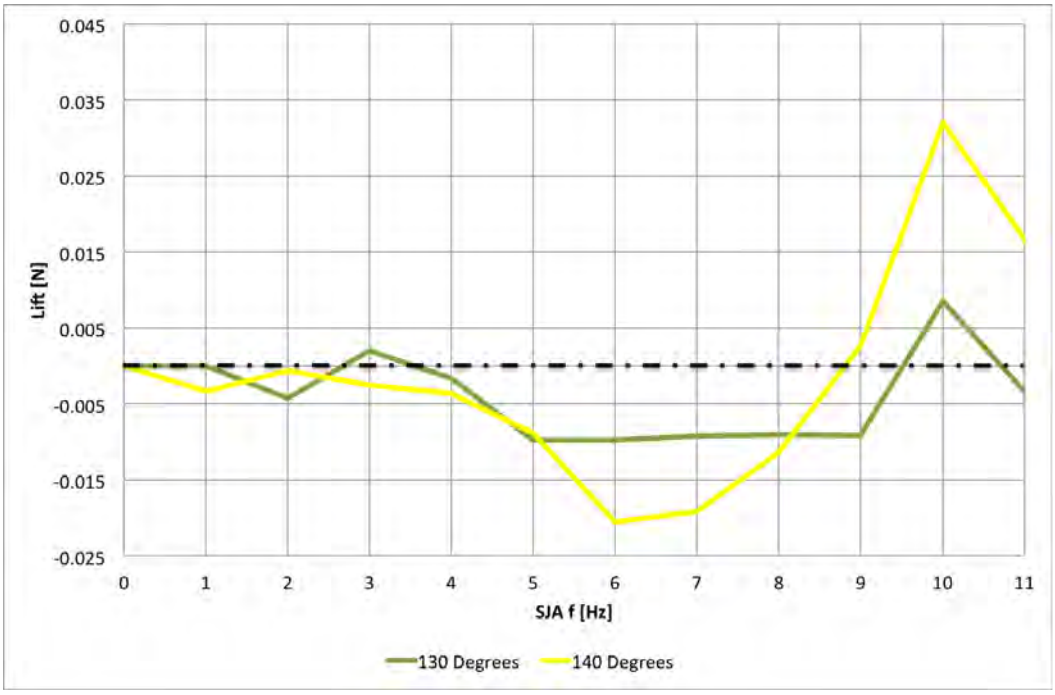

Figure 5.13: Effect of synthetic jet actuator on lift at L_{SJA} of 0.5mm when α_{SJA} is 130°, and 140°

Figure 5.13 shows the lift conditions corresponding to group E. When looking at the lift profiles produced for these jet angles distinctive similarities can be seen, with both profile

behaving similarly but with a difference of magnitude. When these values are compared to the drag effects for the same angles in figure 5.9, it is seen that a significant increase in drag occurs after 4Hz. A striking comparison is seen then comparing drag and lift for 140° with drag going form its highest level at 6Hz to the lowest at 11Hz (V_R = 0.), while at the same time lift going from its maximum negative lift at 6Hz (V_R = 0.) to its maximum positive lift at 10Hz(V_R = 0.), with similar profile slopes. It can also be seen that even though lift for 130° changes its values.

5.6 Discussion of force measurements

5.6.1 Flow Regimes

From section5.5 it was seen that as f_{SJA} is increased from 1Hz to 12Hz, drag and lift deviate from the no-jet conditions based on their individual operating parameters. However, it was also seen that certain angles could be grouped based on their similar drag characteristics5.5. When looking at figure 5.14, the drag response across the range of jet frequencies shows a similar characteristic in the magnitude of change from the no-jet condition. These bands of activity will be referred to as *areas of effect* and are laid out in table5.4 below.

Table 5.4: Flow regimes from SJA modification

Flow regimes	
I	Low level of deviation from no-jet drag levels
-	Only small changes in drag are seen
II	Intermediate level of deviation from no-jet drag levels
-	Both drag reduction and increase
III	High level of deviation from no-jet drag levels
III.a	Pimarily drag increase
III.b	Both drag reduction and increase

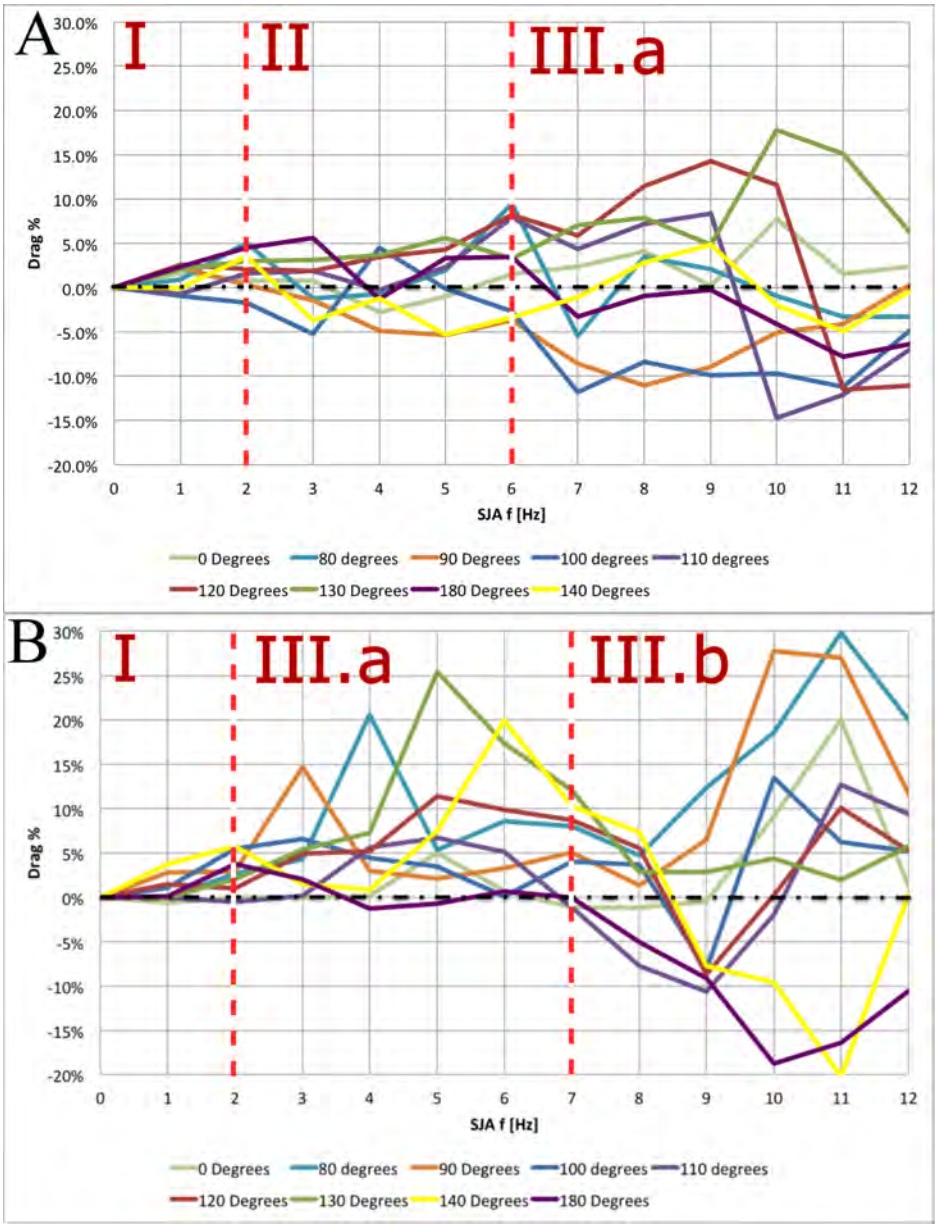

Figure 5.14: Flow regimes across the range of jet frequencies at the jet stroke lengths of: A) 0.25mm and B) 0.5mm.

For both jet stroke lengths prior to 2Hz, there is little drag alteration or variation between the jet angles, and as such they are categorised as *flow regime I*. It should be noted that there is no significant difference in this regime between the magnitude of drag alteration between the jet stroke lengths. Even though dimensionless stroke lengths (L_O/D_0) of 2.5 and 5 are produced by the SJA of L_{SJA} 0.25mm and 0.5mm respectively, formation of a jet does not take place. The reason for this lack of formation is due to the low Reynolds number (Re) and Stokes numbers (St) associated with low V_R. From figures 5.15 and 5.16 it can be seen that

below 2Hz an L_{SJA} of 0.5mm has an Re of 238.2 and a St of 6.9. [4] demonstrated that when St is low, even if the formation criterion is met, jet formation may be prevented or may be present but without vortex rollup. The general trend of gradual drag increase would support a lack of toroidal formation, as the jet will cause a blockage in angles prior to separation, and an effect on the wake in the post separation angles. 180^o does not alter drag, which is probably due to it being to far from the shear layers of the wake to cause significant effects.

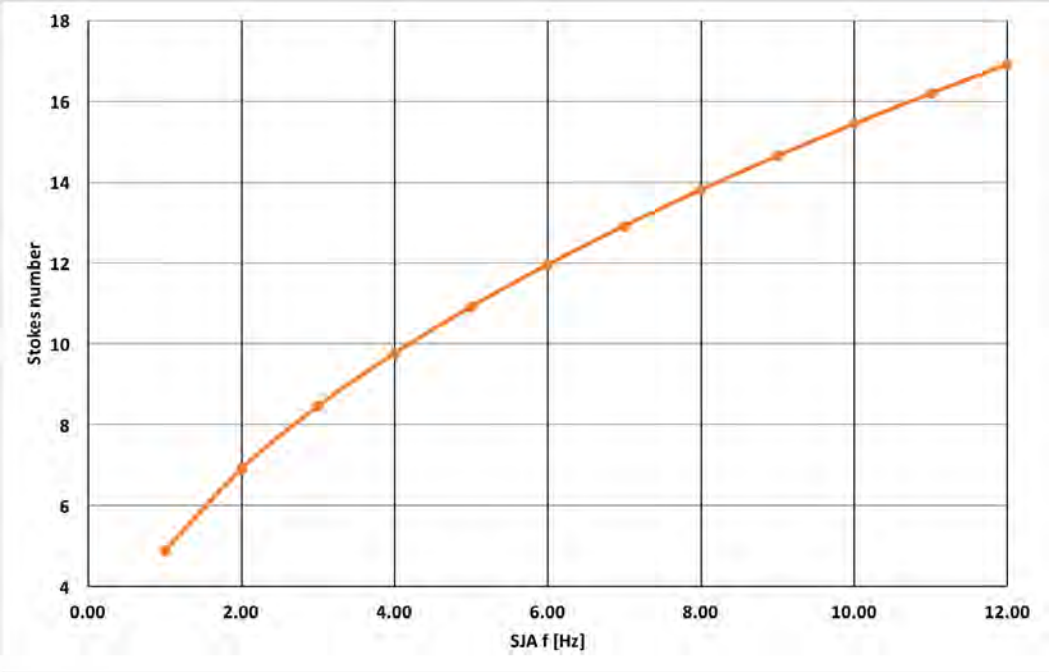

Figure 5.15: Stoke number across the range of jet frequencies tested

For L_{SJA} 0.5mm large spikes take place between 3Hz (V_R = 0.19) and 6Hz (V_R = 0.38), this area is designated *flow regime III.a*. The point of the spike is different for each jet angle, with some angles not presenting an increase. For the pre-separation angles it is seen that the drag gain is tripped earlier at 3Hz (V_R = 0.19) for the 90° jet angle, compared to 4Hz (V_R = 0.25) for 80°. At 3Hz (V_R = 0.19) St is 8.5, meaning that effects caused by stokes layer are minimized resulting in higher chance of rollup taking place. This combined with an increase in Re to 357.3, will produce a stronger jet. 90° is located such that it is normal to the cross-flow and close to the point of separation. This proximity to the separation point allows the jet to move the separation point upstream, while producing a obstruction that causes a bulge in the cross-flow, increasing the level of drag. As 80° is facing into the cross-flow, it

has to overcome a larger force before it can cause an effect, resulting in it requiring a larger frequency to cause a disruption.

The next two spikes at 5Hz (V_R = 0.31) and 6Hz (V_R = 0.38) for 130^o and 140^o respectively take place in very different conditions to that of the previous two. In this situation, the vortices have greater vortical strength and an area of negative pressure to develop more fully. It should be noted that there is a small spike at 5Hz for 120° and no spikes for 100° and 110^o. This would suggest that there is a transition between the pre-stall angles to the post-stall, indicating a different jet interaction is causing the drag spikes. To understand what is going on in this section more testing will be needed.

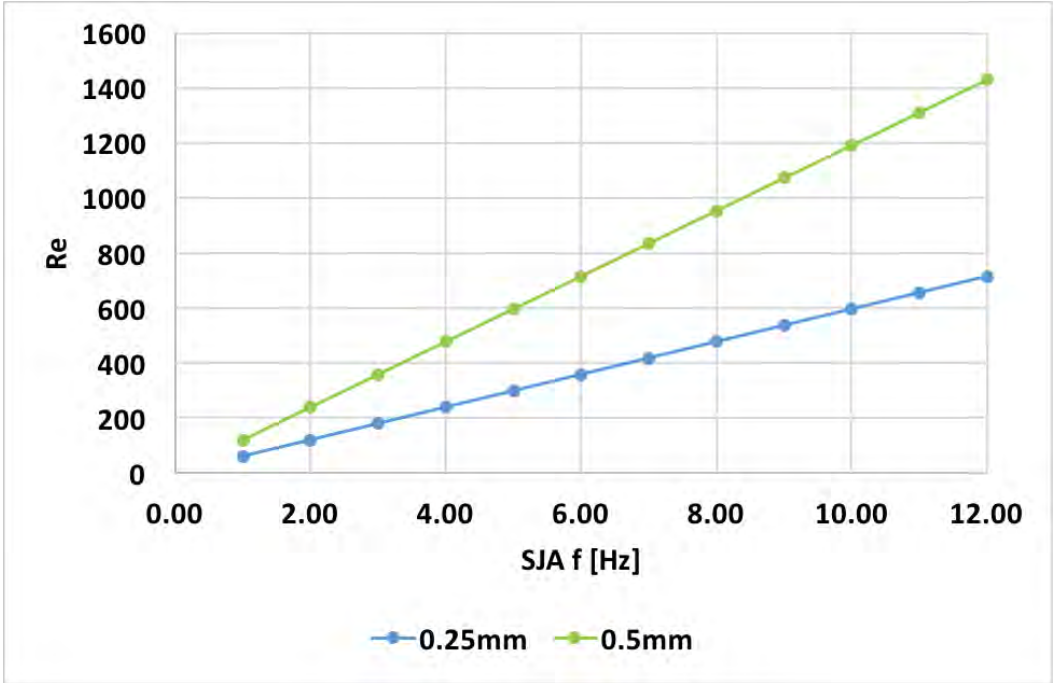

Figure 5.16: Reynolds number, where green line is $L_{SJA} = 0.25$mm and orange line is $L_{SJA} = 0.5$mm

In figure 5.14, At 6Hz (V_R = 0.19) and 7Hz (V_R = 0.44) for the 0.25mm and 0.5mm stroke lengths respectively have entered into the *flow regime III.b*, both jet stroke lengths undergo a significant change that leads to their largest drag alterations. Again as V_R (f_{SJA}) is increased, so too is the quantity of fluid rolled up and vortical strength, this in turn increases the ability of the vortex to develop and to overcome the effects of the cross-flow and shear layer. This in combination with the difference in stroke (change in distance between vortices, V_R,

Re, and quantity of fluid expelled) produces the differences in drag over the same frequencies.

Flow regime III.b for L_{SJA} 0.5mm shows profiles with steep drag effects, that reach a peak before dropping off again. Whereas L_{SJA} of 0.25mm undergoes a sharp short drag alteration before leveling off for a short period prior to large drag modification again.
To best describe how different stroke lengths and V_R alter the effect an SJA has on drag, the angle effects will be looked at within *flow regime III*. The most striking difference between the stroke lengths presents when looking at 90°, where they produce opposite effects, and at 80° and 140°, where only one stroke produces a significant impact on drag.

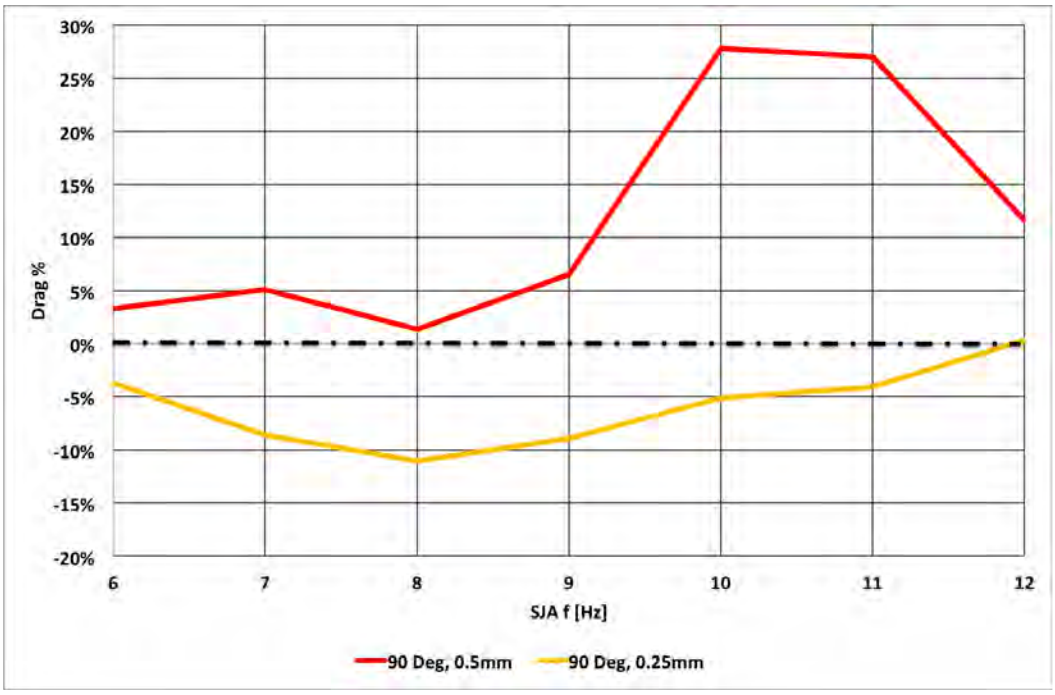

Figure 5.17: Drag effects for both stroke lengths at α_{sja} of 90°

From figure 5.17, the difference between the α_{SJA} of 90° for the L_{SJA} of 0.5mm (red line) and 0.25mm (orange line) can be seen. Firstly 90° is normal to the cross-flow, it is the point prior to flow having to go around the object to remain attached, and it is located around the separation point.

If we initially consider the V_R, we know that halving the the Stroke length while maintaining the α_{SJA} and f_{SJA} will result in the V_R being halved. Between 6Hz to 12Hz, V_R goes from 0.19 - 0.38 and 0.38 - 0.75 for L_0/D_O 0.25 and 0.5 respectively. This means that the forma-

tion of the counter rotating vortical components of the vortex will be significantly different, particularly in regards to the CW vortex (when the cross-flow vorticity is CCW). When V_R is low, as in a jet stroke length of 0.25mm a CW vortex is unable to form, resulting in only a CCW vortex being formed. The CCW vortex remains attached to the surface as it travels downstream, resulting in the separation point moving downstream, imparting turbulence into the shear layer and wake. While not causing the boundary layer to be deformed significantly, reducing the wake structures, while adding turbulence to the shear layer and so reducing drag. It would also explain why as V_R starts to approach the higher value of 0.38 the level of drag begins to increase towards the no-jet drag value as the CCW vortex is strong enough to negatively deform the boundary layer.

In the case of the higher V_R produced by the 0.5mm stroke, a CW vortex is able to partially form. The CW vortex produces a blockage, forcing the cross-flow around it, resulting in separation taking place earlier, increasing the wake size. As V_R increase the CW vortex is better able to overcome the CCW vorticity of the boundary layer. It also shelters the CCW vortex allowing it to cause a larger effect on the boundary layer as it propagates diagonally away from the cylinder, increasing the footprint of the cylinder, thus increasing drag. After 11Hz (V_R = 0.69) a drop-off in drag occurs, this is as a result of the vortex being strong enough to punch through the boundary layer, without causing a significant blockage. This is shown by the drop-off in drag modification as V_R nears 0.75, as the vortices are more capable of breaking through the boundary layer. It should also be noted that a doubling of stroke length also doubles the distance between each vortex and doubles the quantity of fluid expelled, which would also account for the large difference between the strokes.

A similar effect is seen to take place one hertz later for 80°, as a result of the CW vortex needing more strength to overcome the boundary layer vorticity.

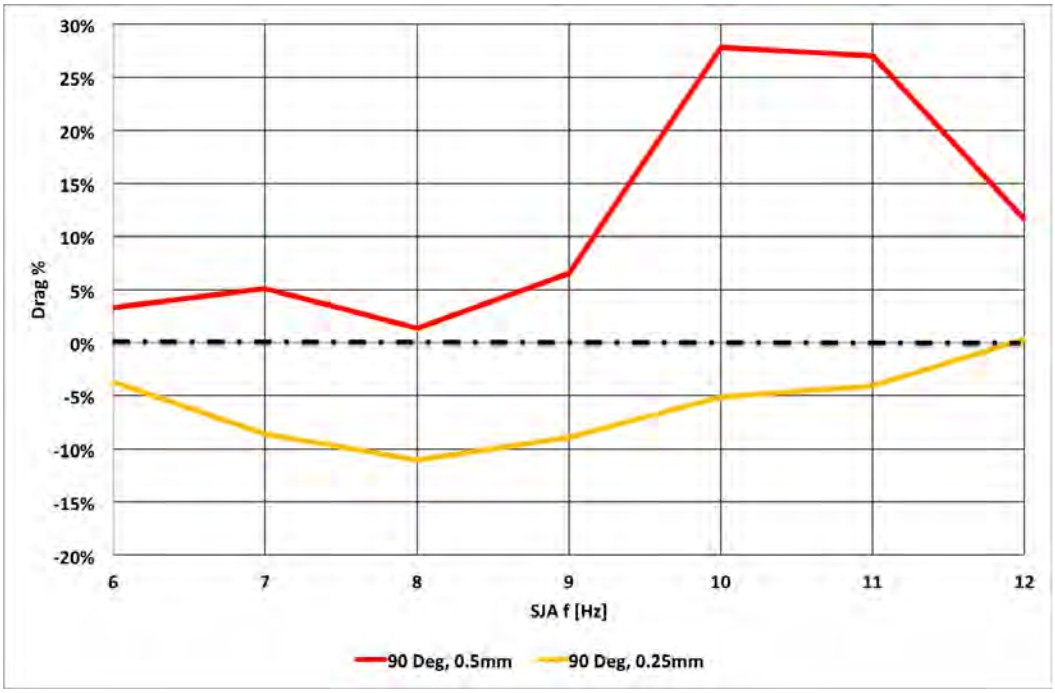

Figure 5.18: Drag effects for both stroke lengths at α_{sja} of 140°

Looking at *flow regime III* (6 – 12Hz) for the 140° in figure 5.18, it can be seen that the 0.5mm stroke length causes a sharp drop in drag, followed by a near return to no-jet conditions. The 0.25mm stroke has a drag gain from 6Hz (V_R = 0.19) to 9Hz (V_R = 0.28) followed by a small loss, prior to a gain again nearing the no-jet condition.

Like with the 90° jet angle, V_R and L_{SJA} determine how vortices emanating from the SJA orifice interact with the wake and the shear layer. Unlike the pre-stall cases, the orifice is located well beyond the separation point. This allows more space for both the CW and CCW components of the vortex to develop before interacting with the shear layer, and allowing it to mix and energises the low-pressure fluid in the wake. Increasing the V_R increases the distance the vortex can travel before beginning to lose cohesion, giving it more strength when interacting with a distant boundary layer. Increasing L_{SJA} while maintaining f_{SJA} will increase the quantity of fluid ejected and the orifice velocity, increasing the strength of the vortices interacting with the shear layer and wake fluid. Increasing the jet stroke will also increase the strength of the suction phase, which may draw the point of separation towards the orifice, as fluid is primarily sucked in from the sides of the SJA orifice (see fig2.9).
From figure 5.3 it is seen that as the orifice rotates from 100° to 120° there is no real difference

in the magnitude or location of the maximum drag reduction, and it taking place earlier than for 140°. This suggests that as vortical strength increases beyond this point, the vortices disrupt the wake structure negatively, and cause a blockage, resulting in a large increase in drag. The maximum drag reduction points associated with the post stall angles are primarily due to a combination of three factors:

1. The suction phase of the SJA pulling the point of separation downstream along the cylinder to the orifice. Shrinking the wake width reducing drag.

2. The vortex interacting with the shear layer tripping turbulence at a lower Re.

3. The vortices energizing the wake through vortical motion, tripping turbulence in the shear layer and through pulling high velocity fluid from the cross-flow into the wake

The SJA interactions mimic the effect of increasing the Re over the cylinder, as seen in figure 4.7C and D. This allows the SJA to alter the flow conditions such that they behave like that of a cylinder with a higher Re. This results in a reduction in drag as is seen in figure 2.3. A higher drag reduction for the 140° jet angel is due to the SJA pulling the boundary layer further downstream. At the same time as the orifice is more tilted, the jet comes out at greater angle to the shear layer, allowing for a large more turbulent vortex to interact and remain within the wake, this produces a large amount of energizing of the wake. To better understand this further testing must be conducted.

For the post stall angles of the 0.25mm stroke length (100°, 110°, 120°, and 140°), a similar interaction between the shear layer and vortices takes place, but to a lesser degree due to the V_R and L_{SJA} being smaller (see fig5.5). This is seen with a growth in drag before a sudden plummet, that is not followed by the complete loss of drag reduction that the 0.5mm stoke length produced.

Table 5.5: Grouping of related angles

Groups	A	B	C	D	E
L_{SJA}	0.25mm	0.25mm	0.25mm	0.5mm	0.5mm
α_{SJA}	90°, 100°	110°, 120°, 130°	80°, 90°	100°, 110°, 120°	130°, 140°

5.6.2 Conclusion of force measurements

In this section it is seen that the orifice location (α_{SJA}, V_R and dimensionless stroke length(L_O/D_0), determine how the synthetic jet alters the flow conditions around the cylinder, resulting in fluidic control. Increasing the jet stroke length while maintaining f_{SJA} and α_{SJA}, results in a large quantity of fluid being expelled at a higher orifice velocity and an increase in the distance between vortices. Increasing V_R while maintaining L_{SJA} and α_{SJA}, produces a vortex with a larger percentage of entrained ejected fluid and higher vorticity is formed. The type of drag modification achieved by the SJA is dependent on whether the orifice is located in the pre-stall or post-stall region.

When the jet was located in the pre-stall regions of $0^o, 80^o$, and 90^o, the 0.5mm stroke length only caused an increase in drag, while the 0.25mm stroke length can produce a significant reduction in drag, even at similar velocity ratio's. This is as a result of the vortices having a different L_O/D_0 while having the same Stoke number, resulting in a difference in formation strength. This difference is particularly important in the formation of the CW vortex, as this is responsible for causing a blockage and allowing separation of the CCW vortex form the surface of the cylinder. If the CW vortex is unable to form ($L_{SJA} = 0.5$mm) then the CCW vortex will remain attached to the surface of the cylinder, introducing turbulence to the boundary layer, shear layer and wake.

In the post stall zone, both stroke lengths produce an increase and decrease in drag from the no-jet condition, with the largest loss and gain of drag presenting for the 0.5mm stroke lengths. In this case the stoke length is important in determining the strength of the vortex and suction phase. This is seen in the 0.25mm stroke length with drag reduction generally not taking place until a higher jet frequency, compared to the 0.5mm stroke length which achieves a high level of drag reduction for a very narrow range, before a sudden gain in drag. The exception to this being the 140^o jet angle as the vortex can be stronger before negatively effecting drag, as a result of hitting the shear layer at a greater angle.

From these results, it was found that a synthetic jet actuator is capable of causing a

significant alteration of flow conditions around the cylinder over a small range of frequencies, with a significant difference presenting between the two dimensionless stroke lengths. These results also show a complex interaction is taking place between the SJA and the shear layer, to gain a better understanding of this further testing using *flow visualization* (7) and *PIV* (7) was undertaken in the following chapters. Where Flow visualization was able to show how the vortices produced by the SJA effected the wake structure thought altering flow conditions such as, the suppression of natural shedding vortices and the entrainment of high energy cross-flow into the cylinder wake, resulting in a reduction in drag (6.4.4.3). And with PIV allowing for the identification of possible wake structures responsible for the levels of drag reduction (7.5).

Chapter 6

Synthetic Jet Actuated Cylinder in Cross-Flow: Flow Visualisation in the Wake and Jet Formation Region

6.1 Aims

The aim of this section is to better understand the interaction of the Synthetic jet's vortices with the shear-layer and the mechanism that cause the drag modifications seen in section 5. This method of visual investigation is qualitative unlike the quantitative measurements that will be taken later by PIV.

Flow visualization will allow for a detailed examination of how vortices are formed at the orifice and how they interact with the cross flow and the boundary layer, giving a better understanding of the mechanisms in play that allow the SJA to modify the lift and drag on a cylinder in such a divers manner.

6.2 Introduction to flow visualisation

Flow visualization (FV) is used to show the physical interaction of the SJ with the boundary layer, shear-layer and wake structures of the fluid passing over a cylinder. The pervious

section gave detailed analysis on the effects an SJA has on the drag modification. However, it does not show the mechanisms involved in achieving these drag modifications. As such FV is a natural step forward, as it will give a qualitative understanding of the mechanisms. FV is more beneficial at initial stage of investigation in comparison to PIV as it does not have as complex or as sensitive a setup and time consuming post-processing is not required. Another benefit is that what is being seen is a physical unprocessed interaction, thus giving a means to assure PIV results are correct.

In this case, FV was achieved using a PIV system, where shutter speeds and recording rate were altered to produce a streaking of PIV particles to give a visual representation of the fluid.

Table 6.1: Setup differences between FV and PIV

Test type	FV	PIV
Camera Position	Normal to Flow	
Laser Power [W]	0.55	1
lens [mm]	50	105
Aperture	2.8	2.8
Recording rate [Hz]	100	185
Sutter Speed [ms]	1.1	0.25
Measurment Duration [sec]	100	50
Viewing window Size [mm]	125X85	225X200

6.3 Test setup and procedure

Test where set up to show the fluid prior to reaching the cylinder and the maximum amount of wake structure by means of illumination by a $1W$ CW laser sheet with a focal length of $f = -6$. A double framed Photron Fastcam SA1 camera was positioned to normal to test section to give a viewing window of 125mm $\times 85mm$.

The water was seeded with $20\mu m$ polyamide spherical seeding particles. These particles show up on the camera as individual dots of reflected light as seen in figure 6.1 A.

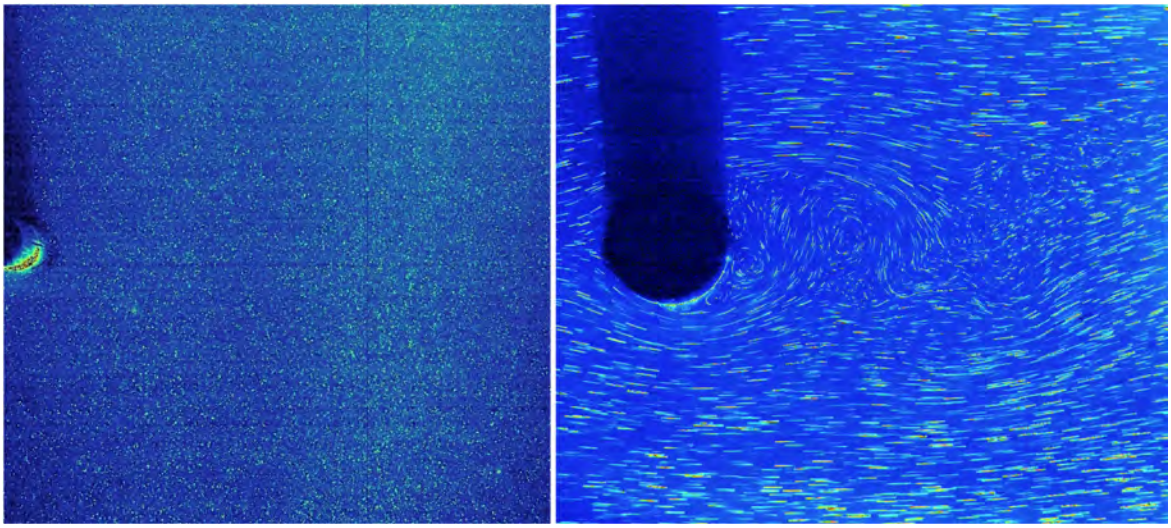

Figure 6.1: Comparison of PIV imaging to flow visualisation, where A) is PIV, and B) is FV

In figure 6.1 A it is impossible to determine the particle motion, or the physical structures without post processing. In order to show physical structures, the aperture, shutter speed, frame rate, and laser light intensity are altered to cause the particles to streak Figure 6.1 B.

Using this method the $2D$ physical structures of of the wake and the synthetic jet can easily be seen, allowing for a detailed analysis of the mechanisms responsible for the changes in drag and lift from chapter 5.
To achieve this level of streaking a 105mm lens with a 50mm extension tube, set to an aperture of 2.8mm. The camera was set to a recording frequency of 100Hz and a shutter speed of 1.1ms. This setup results in large streaking for higher velocities and solid dots for points that are not moving, this shows qualitatively how fast the fluid particle are moving.

6.4 Results of flow visualisation tests

From chapter5 a map of the effects of a SJA on the lift and drag of a cylinder in a cross flow, this map allowed for a selection of points to be looked at in more detail. The points where selected based on being areas of high modification, to understand how changing V_R alters drag modification, and due to their similarities to other points. The points selected are laid out in table7.1 below.

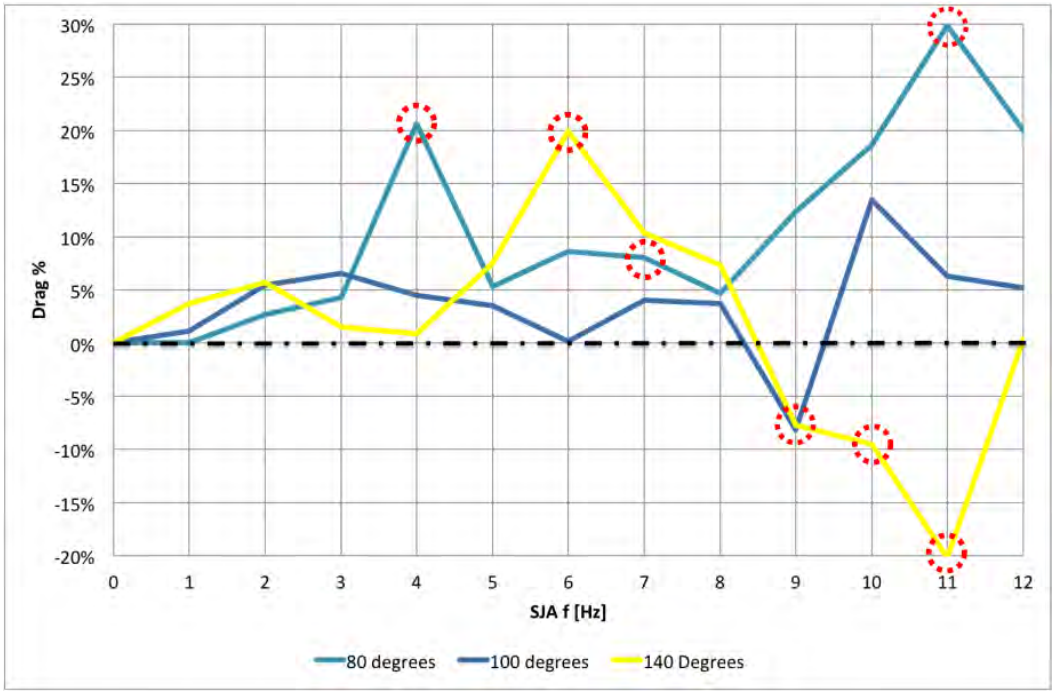

Figure 6.2: Drag angles used for flow visualization for the SJA stroke length of 0.5mm, with points of interest highlighted with red circles

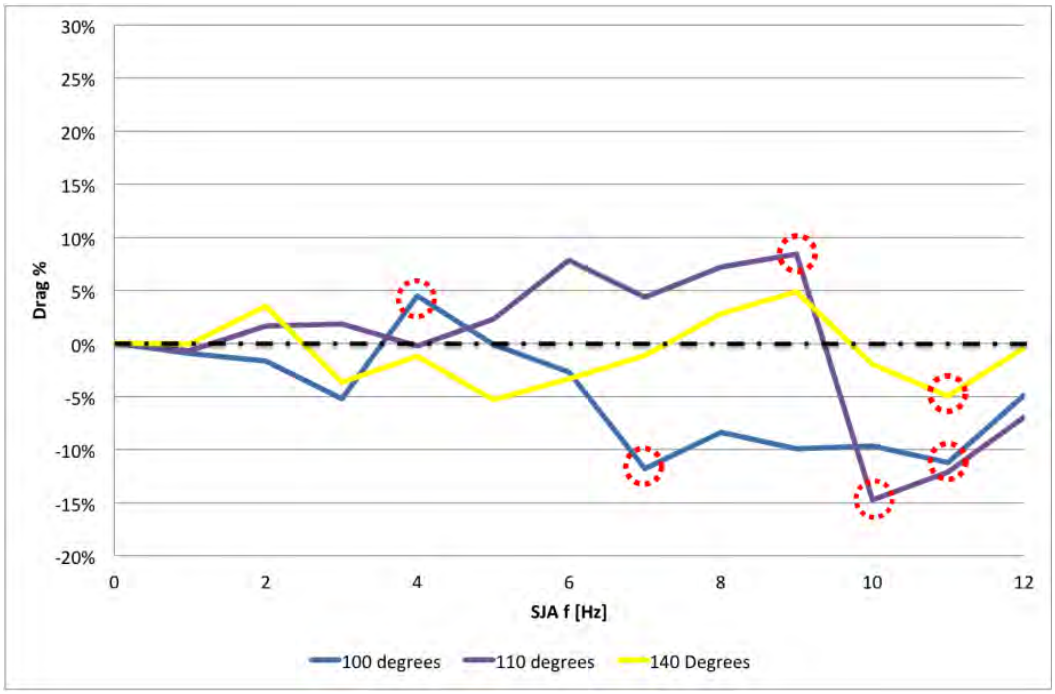

Figure 6.3: Drag angles used for flow visualization for the SJA stroke length of 0.25mm, with points of interest highlighted with red circles

Table 6.2: Flow visualisation results looked at

Modification	No-jet	Drag increase	Drag reduction				—
α_{SJA}	NA	80	100		110	140	Degrees
L_0/D_O	NA	0.5	0.25			0.5	—
f_{SJA}	0	6	8	9	10	140	Hz
V_R	0	0.	0.	0.	0.	0.	—

6.4.1 Flow over a cylinder without synthetic jet activity

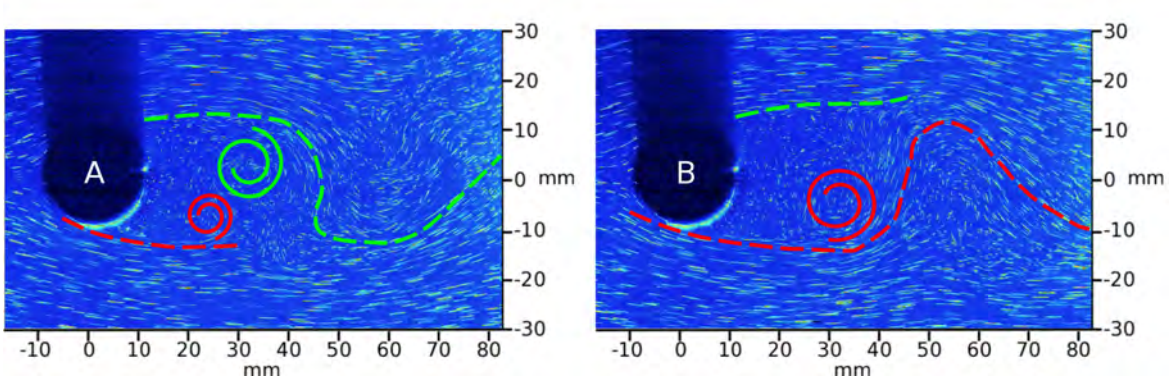

Figure 6.4: Wake structures when L_{SJA} is 0.5mm, α_{SJA} is 140°, and f_{SJA} is 9Hz where: A) periodic shedding of vortices, and B) vortices breaking down into turbulence. Red = CCW vorticity and Green = CW vorticity

In the no-jet condition and the cross-flow is able to travel over the cylinder naturally, with large periodic eddies forming in the wake of the cylinder, starting around 10mm down-stream after an area of no flow. This can be seen in figure 6.4 A with the formation of a CW vortex (green spiral) from the top surface of the cylinder that grows to around the diameter of the cylinder before breaking down. This is followed by the formation of a CCW vortex (red spiral) from the bottom surface, that behaves in the same way, shown in figure 6.4 B. These vortices produce a defined periodic oscillations in the wake, shown by the Orange (CW shear-layer) and yellow (CCW shear-layer) lines.

6.4.2 SJA at high stroke length after the separation point (L_0/D_O = 0.5, $\alpha_{SJA} = 140°$)

The 0.5mm stroke length (L_0/D_O = 0.5) at an α_{SJA} of 140° setup was selected due to it's uniqueness in producing high levels of drag modification, for both drag increase (20%) and

in particular drag reduction (-20%) from the no-jet levels.

6.4.2.1 Mid frequency 9Hz, corresponding to drag reduction

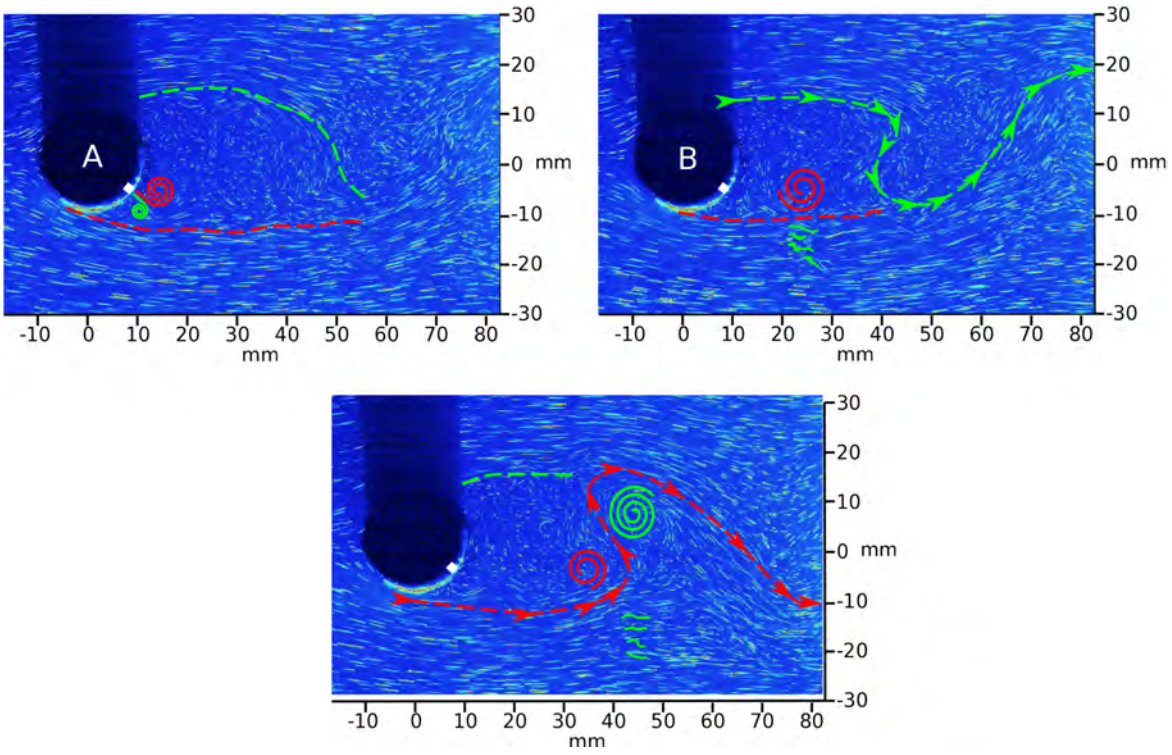

Figure 6.5: Wake structures when L_{SJA} is 0.5mm, α_{SJA} is 140°, and f_{SJA} is 9Hz where: A) Jet formation, B) near-field effects of CCW vortex, and C) far-field effects of vortices. Red = CCW vorticity and Green = CW vorticity

From figure 6.5 A it can be seen that a full vortex is produced at 9Hz (V_R = 0.56) that can be broken down into it's $2D$ components of both a clockwise(CW) and counter-clockwise(CCW) vortex. The CW vortex interacts with the CCW shear-layer just after formation, resulting in it slowing down and reduce in size prior to punching though the shear-layer(fig. 6.5 A). After breaking through the shear-layer the CW vortex's down-stream velocity increases as it quickly loses its vortical structure, continuing down-stream in the cross-flow as turbulence (6.5 B and C as green squiggles). The CCW vortex interacts with the shear-layer slightly after the CW vortex and its velocity and vorticity are energised by the CCW vorticity of the wake. This results in the vortex growing rapidly as it travels down-stream (6.5 B), before it dissipating at around 35mm down-stream of orifice (6.5 C).

Looking at the wake structure as a whole, the wake oscillate at around 45mm down-stream of the cylinder, causing fluid from the cross-flow above the cylinder to be pulled though the wake (6.5 B), and visa-versa (6.5 C. Small CW vortices shed off the upper surface of the cylinder, where they grow gradually in size, until they interact with the the CCW vortices produced by the SJA ((6.5 C). As these vortices are staggered, the CCW SJA vortex is able to impart vortical momentum onto the CW vortex resulting in a sudden growth. This mechanism seems to be responsible for the location and scale of the oscillation in the wake as the vortices pull fluid from the cross flow into the wake.

6.4.2.2 High frequency 10Hz, corresponding to drag reduction

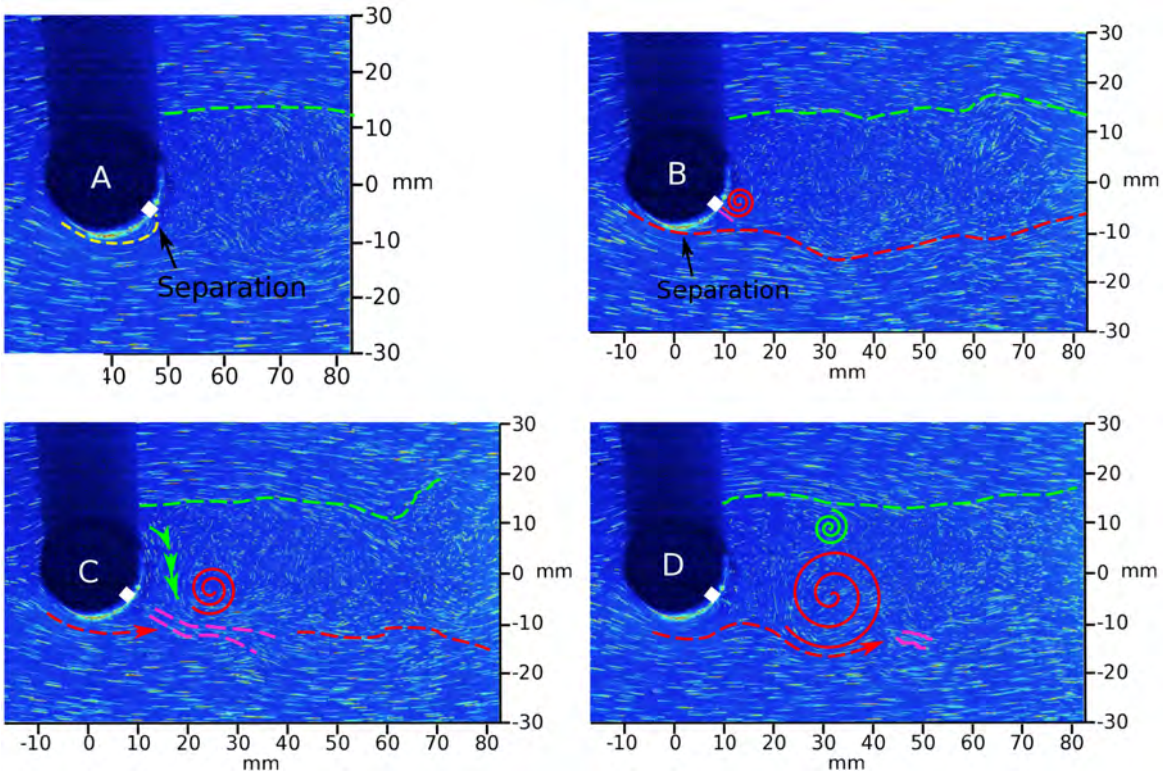

Figure 6.6: Wake structures when L_{SJA} is 0.5mm, α_{SJA} is 140°, and f_{SJA} is 10Hz where: A)down-stream movement of separation point, B) formation of CCW vortex, C) effect of slug on shear-layer, and D) far-field effect of SJA on wake. Red = CCW vorticity and Green = CW vorticity

Increasing frequency by 1Hz, from 9Hz (V_R = 0.56) to 10Hz (V_R = 0.63) notably changes the interaction of the SJA with the shear-layer. During the suction phase of the SJA cycle the boundary layer is sucked down-stream to the mouth of the orifice, prevent a CW vortex

from forming as seen in figure 6.6 A. Figure 6.6 B shows that at 10Hz (V_R = 0.63) there is no formation of a coherent CW vortex, only a CCW vortex forms. A slug of fluid shown in purple is forced out normal to the orifice, interacting with and disrupting the shear-layer. This result in separation being pushed further upstream along the cylinder(fig. reffig: Wake structures when SJA is at 10Hz 140deg C).

In figure 6.6 C the slug of fluid breaks through the shear-layer as the CCW vortex grows gradually as a it entrains fluid from the surrounding wake and from fluid pulled down form the upper region of the cylinder wake, causing the vortex to grow to around a 10mm diameter, at roughly 15mm down-stream of the cylinder.

In figure 6.6 D as the slug of fluid travels down-stream away form the cylinder the shear-layer collapses back in behind, allowing it to energizing the CCW vortex. This results in exponential growth to roughly the same diameter as the cylinder at around 30mm down-stream from the cylinder. The vortex shortly thereafter coalesces with the smaller CW vortex shed from the upper surface, after which it loses cohesion, breaking down into turbulence. It should also be noted that the wake structure is a more streamlined shape than that of the 9Hz.

6.4.2.3 High frequency 11Hz, corresponding to drag reduction

When the SJA frequency was further increased to 11Hz (V_R = 0.69) its produced an effect similar to a mix of the 9Hz (V_R = 0.56) and 10Hz (V_R = 0.63) condition. In figure 6.7 A it can be seen that the suction phase of the SJA pulls the boundary layer inwards, significantly delaying separation. However, a small area before the orifice of no flow is present bounded by the shear-layer. In figure 6.7 B the CW vortex is able to overcome the shear-layer vorticity, unlike the 10Hz (V_R = 0.63) case, due to this area of negative pressure and increased vortical strength. The increased strength of the CW vortex and the zone of negative pressure at 9Hz (V_R = 0.56) (6.5 A), its initial velocity is not slowed significantly compared to the CCW vortex. This results in the CW vortex shadowing the CCW vortex, preventing it from growing rapidly; reducing the influence the shear-layer has on its trajectory.

In figure 6.7 C it is seen that due to the suction phase pulling the boundary layer down-

stream the CW vortex breaks through the shear-layer shortly after separating from the orifice and in figure 6.7 D It can bee seen that the CW vortex is unable to overcome the effects of the cross flow, dissipating quickly into turbulence roughly 15mm down-stream form the cylinder, where it continues down-stream as turbulence (fig. 6.7 E).
As a result of the shadowing on the CCW vortex by the CW vortex, the CCW vortex is not energized by the shear-layer as it is forming reducing its degree of grow as it moves down-stream. In figure 6.7 E the shear-layer cuts between the turbulence of the CW vortex and the CCW vortex. This results in the CCW vortex embedding partially in the shear-layer causing mixing between the cross-flow and wake. At the same time a regular shedding of CW vortices from the top surface is seen. They do not interact directly with the CCW vortices until around 30mm down-stream. A channel of return flow in the centre of the wake forms between the counter rotating vortices. As these vortices move down-stream they briefly interact as they the trailing CCW vortex collides with the leading CCW vortex causing them to break down into turbulence at round 60mm down-stream. The shape of the wake behind the cylinder at 11Hz (V_R = 0.69) is more streamlined than 9Hz (V_R = 0.56) or 10Hz (V_R = 0.63).

From strain readings of 140° (fig. 6.2) it was seen that a change in f_{SJA} (V_R) from the higher values to the mid range values results in a flip in drag effects from reduction to production. At 6Hz (V_R = 0.38) the wake structures are significantly different with large wake oscillations caused by the periodic shedding of large vortices form the top and bottom of the cylinder. This results in a wake structure of roughly 50mm at around 60mm down-stream of the cylinder (dashed black lines figure 6.8 A), unlike the streamlined wake of the previous setups.

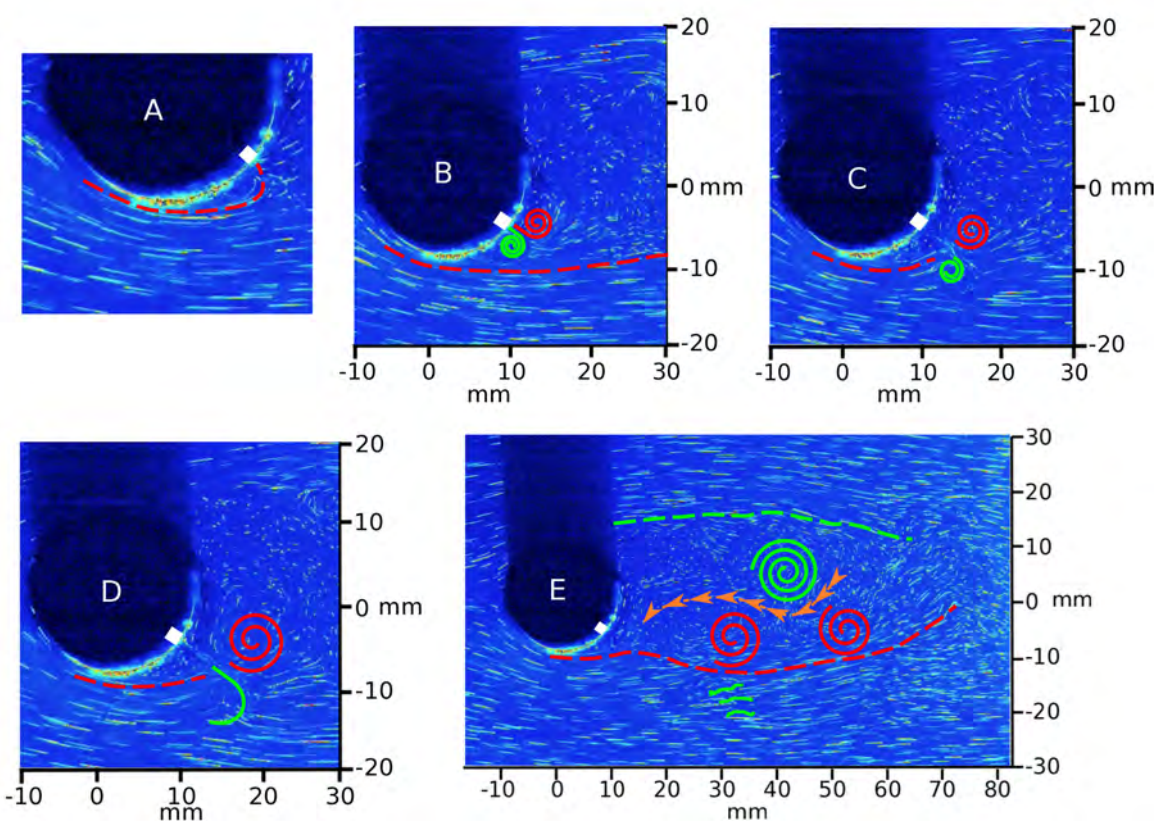

Figure 6.7: Wake structures when L_{SJA} is 0.5mm, α_{SJA} is 140°, and f_{SJA} is 11Hz where: A) downstream pull of separation point, B) formation of SJA vortex, C) CW vortex punching through shear layer, D) shear layer breaking down CW vortex, and E) wake structures. Red = CCW vorticity, Green = CW vorticity, and Orange = backflow

6.4.2.4 Low frequency 6Hz, corresponding to drag increase

Prior to the ejection phase, the separation point is moved upstream along the cylinder resulting in a large area of separation as shown in yellow in figure 6.8 A. This allows the formation of a full vortex from the orifice. The CW component of the vortex dissociates upon interaction with the shear-layer, causing the shear-layer to collapse into the wake. In figure 6.8 B. The shear-layer imparts its CCW vorticity on the CCW vortex resulting in a significant growth. During this time, another vortex is produced by the SJA, however as is shown in figure 6.8 C, the shear-layer prevents the CW vortex from forming and the small CCW vortex it absorbed by the larger CCW vortex, adding mass. At this point the CW vortex shed from the top surface begins to dissipate into turbulence.

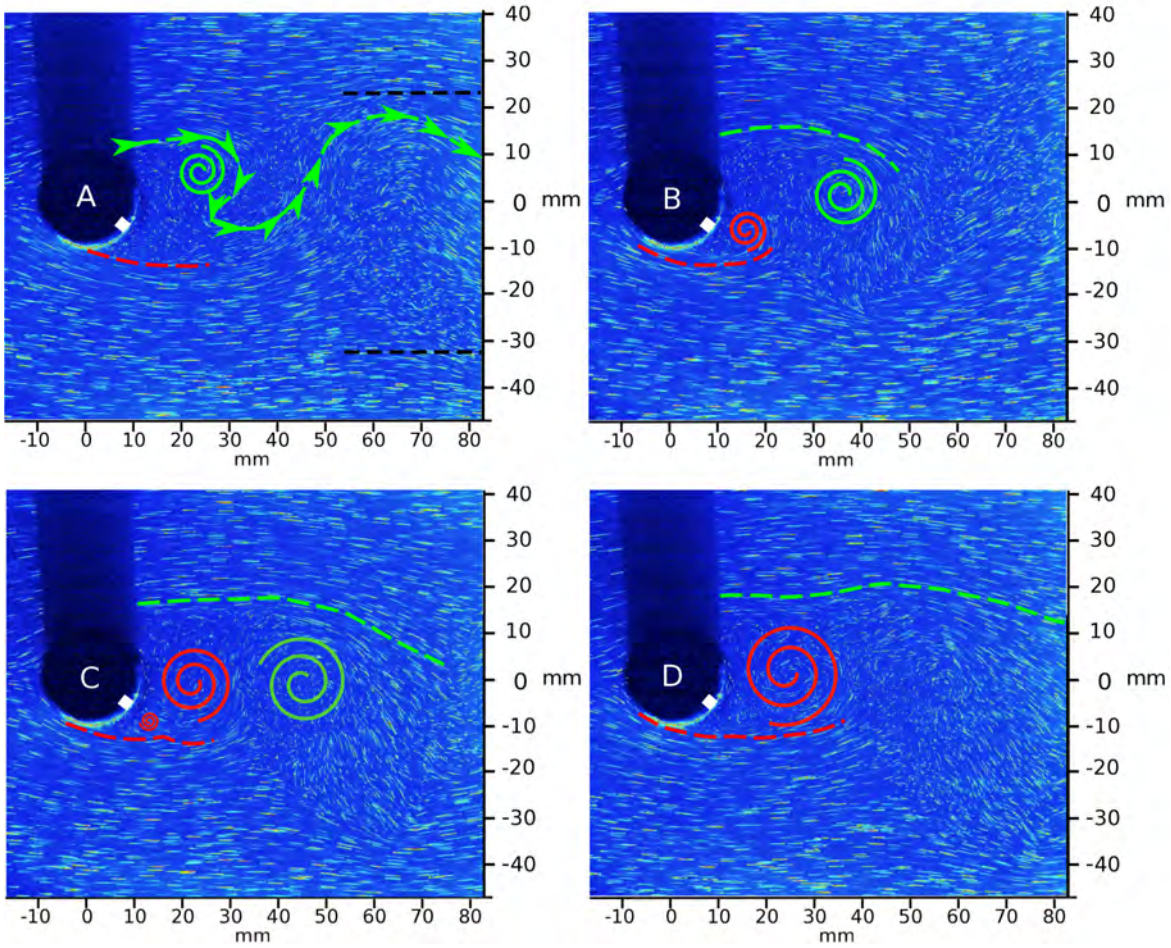

Figure 6.8: Wake structures when L_{SJA} is 0.5mm, α_{SJA} is 140°, and f_{SJA} is 6Hz where: A) end of suction phase, B) SJA CCW formed, C) trailing SJA vortex formed and D) ingestion on trailing vortex. Red = CCW vorticity and Green = CW vorticity

In figure 6.8 D the CCW vortex has grow to roughly the diameter of the the of the cylinder at around 10mm down-stream of the cylinder pulling fluid from the cross-flow through the wake producing another oscillation. After this point the CCW vortex dissipates as another CW vortex sheds from the top surface of the cylinder.

6.4.3 SJA at high stroke length before the separation point (L_0/D_O = 0.5, α_{SJA} = 80°)

Unlike with the previous jet angle of 140°, an α_{SJA} of 80° never reduces drag, instead it produces two large drag peaks 6.2. As such the jet frequencies of 4Hz (V_R = 0.25), 8Hz (V_R = 0.5), and 11Hz (V_R = 0.69) will be looked at. 8Hz (V_R = 0.5) was chosen due to its low level

of drag increase compared to the high peaks either side of it, to give a better understanding of why drag does not remain constantly high between the two peaks.

6.4.3.1 Low frequency 4Hz, corresponding to drag increase

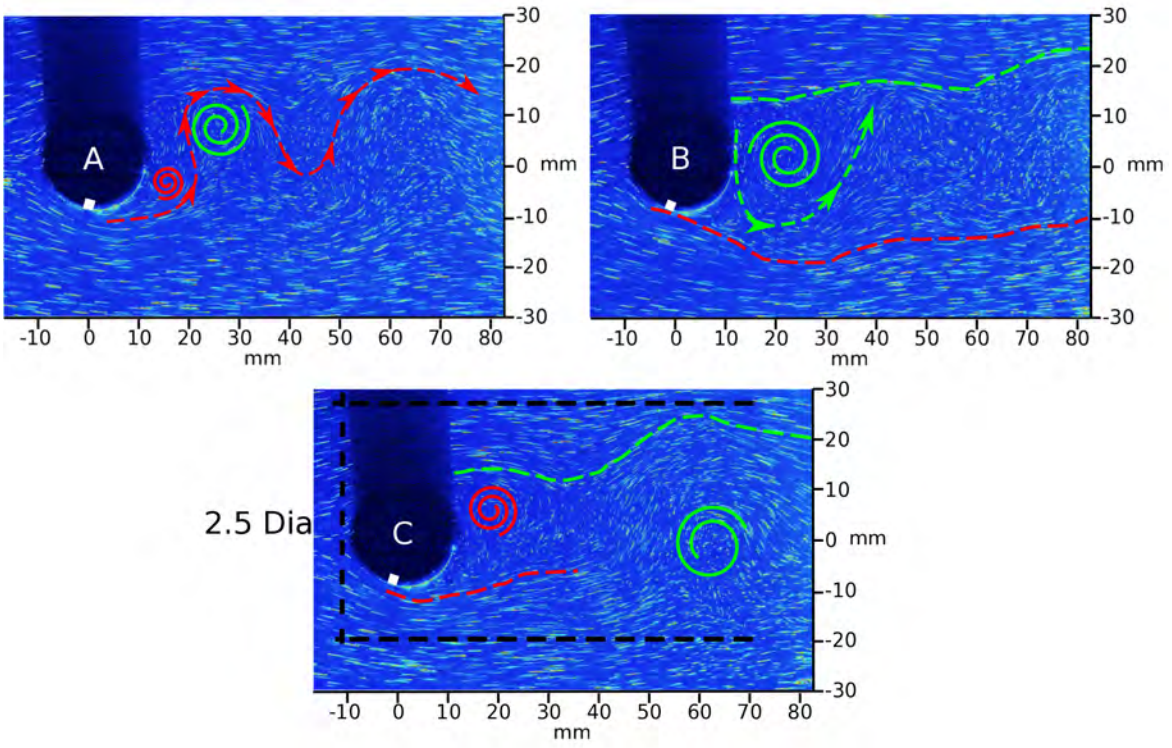

Figure 6.9: Wake structures when L_{SJA} is 0.5mm, α_{SJA} is 80°, and f_{SJA} is 4Hz where: A) large wake oscillation forming behind cylinder, B) shedding of large CW vortex, and C) far-field wake structure. Red = CCW vorticity and Green = CW vorticity

In figure 6.9 there are significant oscillations in the wake, forming directly behind the cylinder. 4Hz (V_R = 0.25) behaves similarly to 6Hz (V_R = 0.38) for a jet angle of 140° in that the SJA causes the separation point to move up and down-stream between the suction and ejection phase, resulting in formation of the large oscillations. In figure 6.9 A only a CCW vortex is formed, this vortex remains attached and travels along the lower surface of the cylinder until it separates at approximately 170° (the back of the cylinder). After separating the vortex's CCW vorticity causes fluid to be channelled downwards between the cylinder and the vortex, this fluid blocks the motion of the shear-layer forcing it to go around, resulting in a bulging of the wake as seen in figure 6.9 B and C, with the red spiral for the CCW vortex and orange

line for the channelled fluid. Swelling results in the wake having a larger width than cylinder diameter. In both figure 6.9 A and B, a large level of turbulence is present. In figure 6.9 C, a CW vortex is shown at around 2.5 cylinder diameters down-stream causing a large oscillation, widening the wake to around 2.5 cylinder diameters (Red bars), with high levels of turbulence.

6.4.3.2 High frequency 11Hz, corresponding to drag increase

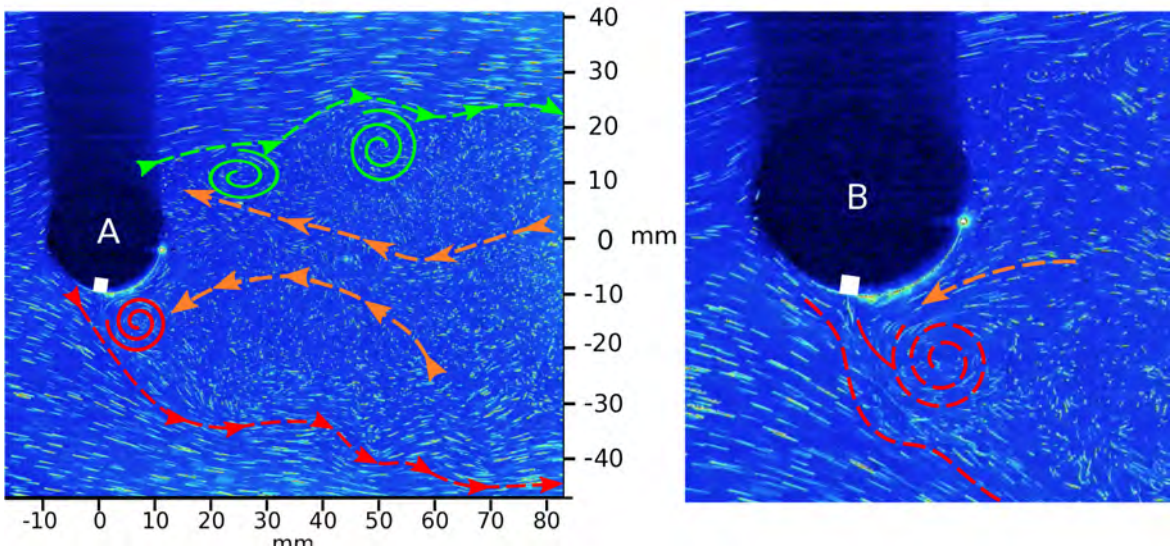

Figure 6.10: Wake structures when L_{SJA} is 0.5mm, α_{SJA} is 80°, and f_{SJA} is 11Hz where: A) wake structure produced by the SJA, B) close up of the CCW vortex produced by the SJA. Red = CCW vorticity, Green = CW vorticity, and Orange = backflow

When α_{SJA} is set to 11Hz (V_R = 0.69) it produced the largest recoding of drag in chapter5, the reason for this high level of drag is instantly apparent when looking at the wake structures and separation points in figure 6.10. In figure 6.10 A the red (CCW vorticity) and green (CW vorticity) dashed lines show the boundaries of the wake produced by the SJA. The wake structure has a width of about 3.5 cylinder diameters, with significant growth seen to both sides of the cylinder. In the central core of the wake, there is a return flow indicated in orange. The core is energized and fed by the vortices produced by the SJA, and by vortices shed from the top surface of the cylinder.

The reason the SJA causes such a large widening of the wake is shown in figure 6.10 B, where the SJA causes a blockage at the orifice, resulting in separation taking place nearly vertically. Only a CCW vortex is formed at the orifice, growing exponentially as it is energized by both

the CCW shear-layer and the flow from the central core. The CCW vortex quickly breaks down into turbulence as it travels along the wake, pulling the fluid from the central core.

6.4.3.3 Mid frequency 8Hz, corresponding to drag increase

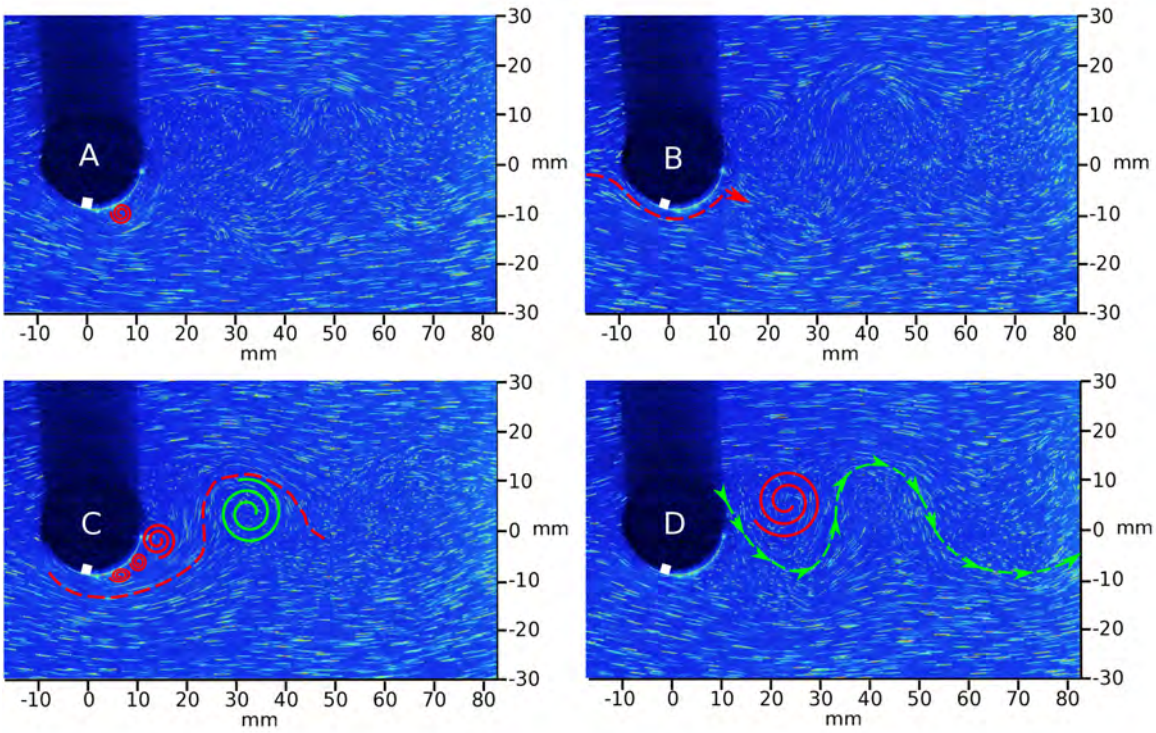

Figure 6.11: Wake structures when L_{SJA} is 0.5mm, α_{SJA} is 80°, and f_{SJA} is 8Hz where: A)formation of CCW vortex from SJA, B) separation point, C) formation of 3 CCW during ejection phase of SJA, and D) oscillations caused by CCW traveling downstream. Red = CCW vorticity and Green = CW vorticity

When f_{SJA} is set to 8Hz (V_R = 0.5), again only a CCW vortex is produced from the orifice by the SJA (fig. 6.11 A). The CCW vortex produces a small blockage forcing the cross flow to go around, resulting in a swelling in the wake, that continues down-stream with the vortex. Unlike the previous cases as the vortex separates from the surface removing the blockage the boundary layer collapses and travels down-stream along the surface of the cylinder to approximately 160° shown in figure 6.11 B (yellow line). As the SJA begins to force fluid out of the orifice, it trips separation in the boundary layer resulting in the formation of three

CCW vortices in a row as seen in figure 6.11 C, where the first two vortices are produced by shedding over the forming vortex, and the third vortex being the CCW vortex produced by the SJA. These vortices coalesce expanding significantly as they move into the centre of the wake, before dissipating about 20mm down-stream from the cylinder. As with the other jet frequencies looked at for α_{SJA} the wake starts to oscillate fully across the wake directly behind the cylinder as seen in figure 6.11 D.

6.4.4 SJA at low stroke length at around the separation point (L_0/D_O = 0.25, α_{SJA} = 100°)

6.4.4.1 Low frequency 4Hz, corresponding to drag increase

In Figure 6.12 A, a CW vortex periodically sheds from the top surface of the cylinder. At the same time the separation point moves down-stream along the cylinder compared to that of figure 6.12 C. The SJA is unable to form a CW vortex due to being overcome by the CCW vorticity of the shear-layer. As fluid is ejected from the orifice, it obstructs the flow resulting in several small CCW vortices being shed from the obstruction it produces, that quickly breakdown. In figure 6.12 B the CCW vortex produced by the SJA travels down-stream, remaining attached to the surface of the cylinder until around 170°, separating and traveling diagonally into the wake as indicated by the red arrow. In figure 6.12 C another CW vortex is shed from the top surface. This vortex roles up the CCW vortex and travels down-stream producing an oscillation that circulates around the CW vortex as shown by the orange line in figure 6.12 A.

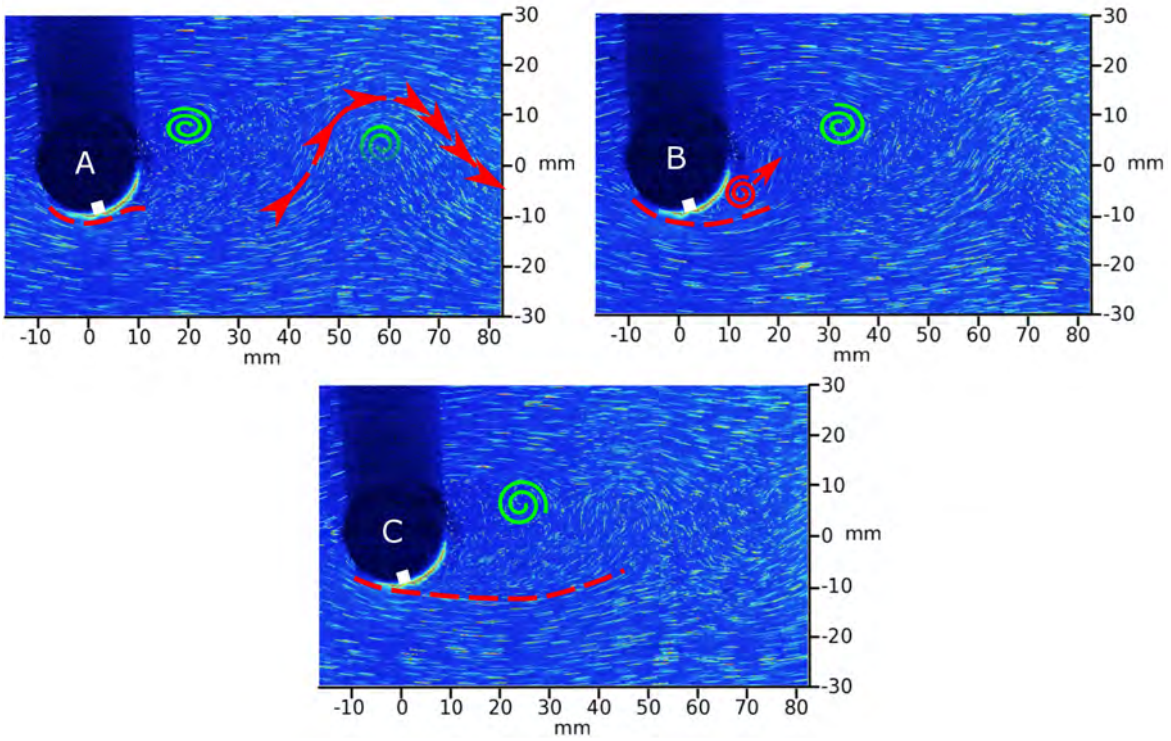

Figure 6.12: Wake structures when L_{SJA} is 0.25mm, α_{SJA} is 100°, and f_{SJA} is 4Hz where: A) suction phase of SJA, and B) down-stream advection of attached CCW vortex, and C) CCW vortex rolled up by CW vortex. Red = CCW vorticity and Green = CW vorticity

6.4.4.2 Mid frequency 8Hz, corresponding to drag decrease

From figure 6.13, the wake is seen to undergo 3 transition:

1. In figure 6.13 A the wake is smooth, with no oscillation's seen. With only small vortices, that do not role up until around 25mm down-stream of the cylinder. An area of stagnant flow is seen behind the cylinder.

2. In figure 6.13 B The counter vorticity of the vortices produces a backflow through the centreline, this backflow energizes the vortices allowing them to grow significantly compared to the previous.

3. In figure 6.13 C As the vortices grow in size and strength, oscillations take place at around 50mm down-stream of the cylinder. The vortices grow larger, cutting off the backflow, preventing vortices from growing, and the process repeated.

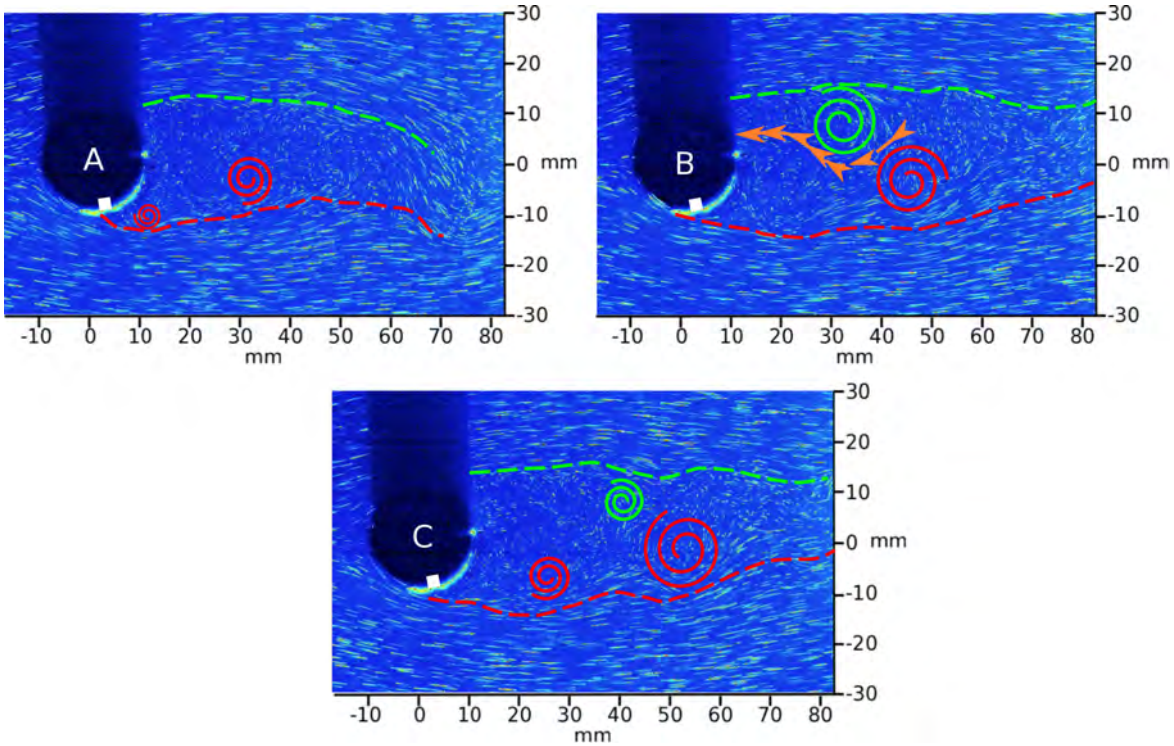

Figure 6.13: Wake structures when L_{SJA} is 0.25mm, α_{SJA} is 100°, and f_{SJA} is 8Hz where: A) smooth wake without oscillations, B) wake becoming unstable as vortices grow and return flow forms, and C) vortices collapse return flow and turbulence shed. Red = CCW vorticity, Green = CW vorticity, and Orange = backflow

6.4.4.3 Mid frequency 9Hz, corresponding to drag decrease

When the SJA operates at 9Hz (V_R = 0.28) the separation point again undergoes only a small amount of movement (fig. 6.14 A and B , only moving when the CCW vortex is produced by the SJA as shown in figure 6.14 B. This CCW vortex remains attached to the surface as it grows, causing a bulging of the shear-layer. This results in a collapse of the boundary layer behind the CCW vortex as it reaches the back of the cylinder. The faster trailing fluid breaks down the CCW vortex into turbulence as shown in figure 6.14 C. However, before the vortex breaks down fully it vorticity draws fluid form the cross-flow into the wake, energizing the wake represented by the red arrowed lines. The fluid travels diagonally through the wake, and can be seen to move down-stream (fig. 6.14 C, fig. 6.14 A, and then fig. 6.14 B) until it is re-energized by the next CCW vortex.

This results in a distinctive upward vectoring of the wake structure. The flow effects caused be the SJA prevents the formation of any significant CW vortices from forming from the top

surface. The small CW vortices are broken down when they come in contact with the fluid forced into the wake by the CCW vortices. This results in a hydrodynamically shaped wake structure behind the cylinder.

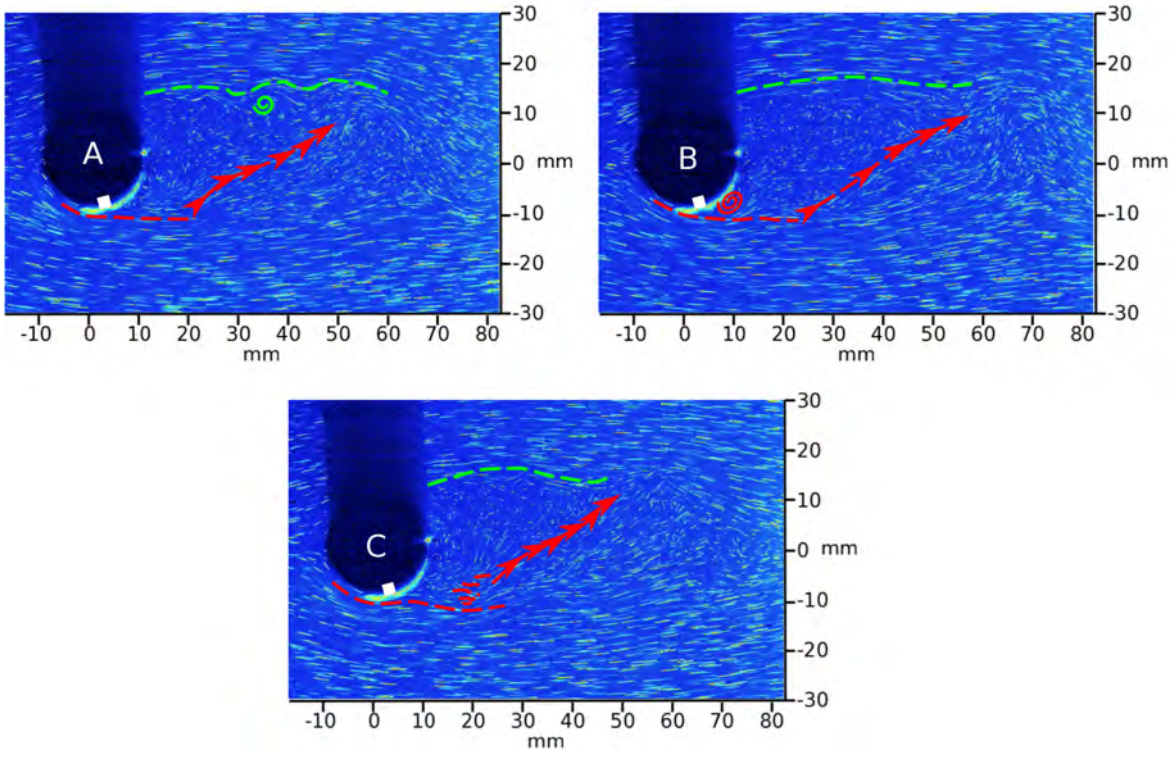

Figure 6.14: Wake structures when L_{SJA} is 0.25mm, α_{SJA} is 100°, and f_{SJA} is 9Hz where: A) suction phase of SJA, B) formation of CCW vortex, and C) interaction of CCW with shear layer. Red = CCW vorticity and Green = CW vorticity

6.4.5 SJA at low stroke length after the separation point ($L_0/D_O = 0.25$, $\alpha_{SJA} = 110°$)

The 110° jet angle was chosen due to its sudden drop from a drag value of around 8% at 9Hz ($V_R = 0.28$), to -15% at 10Hz ($V_R = 0.31$) from the no-jet drag values over only 1Hz.

6.4.5.1 Mid frequency 9Hz, corresponding to drag increase

From figure 6.15 it is seen that at 9Hz the wake behaves similarly to the previous cases of drag increase, with large vortices being shed naturally or produced by the SJA. This in

conjunction with the presence of large and early oscillations within the wake.

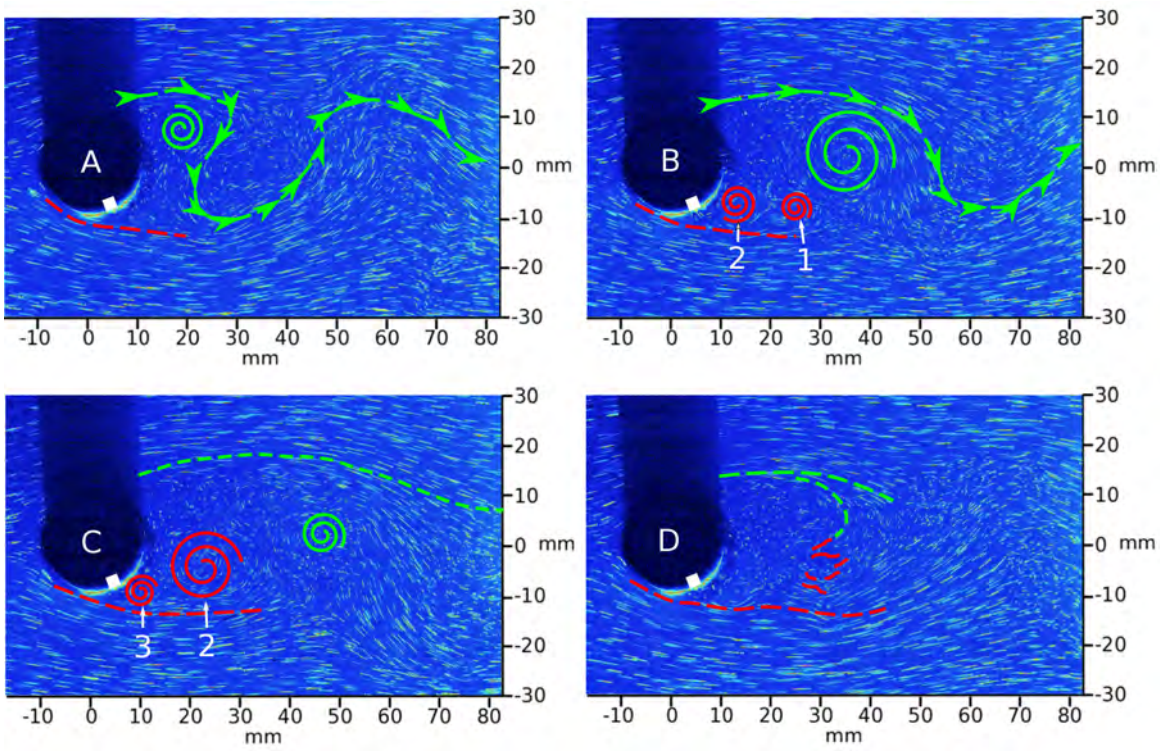

Figure 6.15: Wake structures when L_{SJA} is 0.25mm, α_{SJA} is 110°, and f_{SJA} is 9Hz where: A) shedding of a CW vortex from the top of the cylinder, B) formation of two CCW vortices from two SJA cycles, C) formation of a third CCW vortex due to another SJA cycle, and D) Breakdown of CCW vortices into turbulence. Red = CCW vorticity and Green = CW vorticity

In figure 6.15 A as a CW vortex sheds from the top surface of the cylinder, an area of low-pressure forms around the orifice allowing the formation of a CCW vortex. During the ejection phases, an SJA CW vortex is unable to overcome the CCW vorticity of the shear-layer. In figure 6.15 B the CW vortex shed form the cylinder moves down-stream, growing to roughly the size of the cylinder. During this time the SJA undergoes two cycles, where the initially formed CCW vortex (fig. 6.15 B.1) travels down-stream at a faster rate than the CW vortex, catching up to the CW vortex and is slowed down, this allows the CCW vortex to be broken down and rolled-up by the trailing CCW vortex(fig. 6.15 B.2). In figure 6.15 C as the second CCW vortex travels down-stream, a third CCW vortex (Fig. 6.15 C.3) is produced by a third cycle of the SJA, this CCW vortex collides with, and is rolled-up by the former (Fig. 6.15 C.2) due to added down-stream velocity from increased contact with the shear-layer. In figure 6.15 D the CCW vorticity of the large CCW vortex pulls fluid down

from the upper wake (this results in the formation of a CW vortex as seen in fig. 6.15 A), this fluid breaks down the CCW vortex into turbulence.

6.4.5.2 High frequency 10Hz, corresponding to drag decrease

From figure 6.16 it can be seen that the wake structure closely resembles that of figure 6.14, with the SJA preventing both the formation of large vortices and the advection of any vortices down-stream.

In figure 6.16 A prior to the start of the ejection phase, a strong attachment can be seen, with separation taking place down-stream at around 130^o. Upon the formation, the CCW vortex remains attached and an area of low pressure forms in the lea of the CCW vortex(figure 6.16 B). As was seen in with the 9Hz ($V_R = 0.28$) jet frequency at 100° and a stroke length of 0.25mm in figure 6.14 C the area of low pressure is seen to collapse. This results in the breaking down of the vortex into turbulence as seen in figure 6.16 A (shown with squiggly red lines).

No CW vortex is formed from the top surface of the cylinder. Again as with the 9Hz ($V_R = 0.28$) jet frequency at 100° and a stroke length of 0.25mm, fluid from the cross-flow is drawn into the wake, traveling diagonally through the wake. From Figure 6.14 A to 6.14 C this column of fluid stretches, tilts, and moves down-stream. However, in this case an increase in the strength of the vortex pulls a large quantity of fluid into to the wake, with a larger area of influence. This addition of fluid prevents any CW vortices from forming, producing a smooth wake profile that undergoes only minor changes in shape.

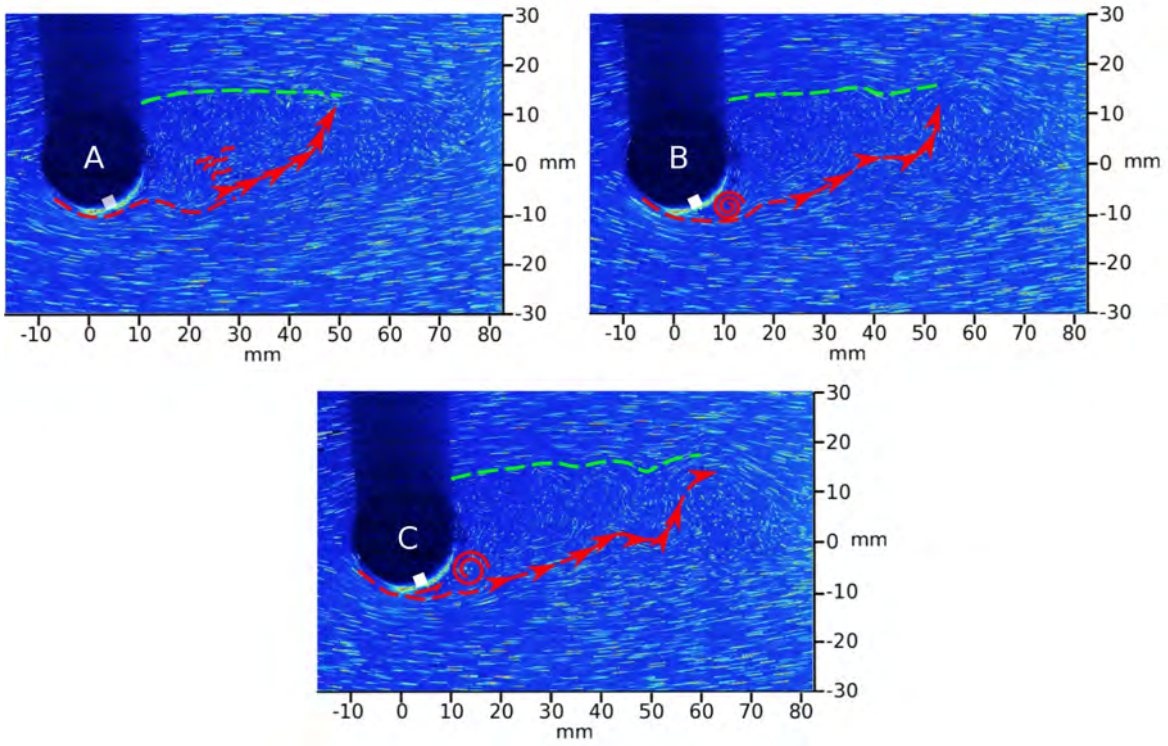

Figure 6.16: Wake structures when L_{SJA} is 0.25mm, α_{SJA} is 110°, and f_{SJA} is 10Hz where: A) suction phase, B) formation of a CCW vortex from the SJA, and C) interaction of the CCW with the shear layer. Red = CCW vorticity and Green = CW vorticity

6.4.6 SJA at low stroke length after the separation point (L_0/D_O = 0.25, α_{SJA} = 140°)

6.4.6.1 High frequency 11Hz, corresponding to drag decrease

This was chosen due to it producing a drag reduction similar to that of L_{SJA} of 0.5mm at α_{SJA} of 140° with a $_{SJA}$ of 11Hz, with a different magnitude.

From figure 6.17 it can be seen that the SJA behaves in a similar manner to that of the 0.5mm L_{SJA} case as shown in figures6.5 to 6.7.

The first significant difference between reducing L_{SJA} from 0.5mm to 0.25mm is shown in figure 6.17 A, during the suction phase of the SJA, where the actuator no longer pulls the separation point down-stream, instead it remains more or less fixed. This leaves an area of

low pressure, allowing both the CW and CCW vortex components to form. The CW vortex comes in contact with the shear-layer during formation(figure 6.17 B), breaking through the shear-layer as it is broken down and moves down-stream as turbulence (show with green lines). This causes a shadowing that prevents the cross-flow from influencing the CCW vortex, resulting in a CCW vortex growing without moving down-stream(figure 6.17 C). This vortex is fed by new pulses from the SJA and keeps growing until the CW vortex travels down-stream pulling the CCW vortex behind it(figure 6.17 D), until it breaks down and thy cycle starts again.

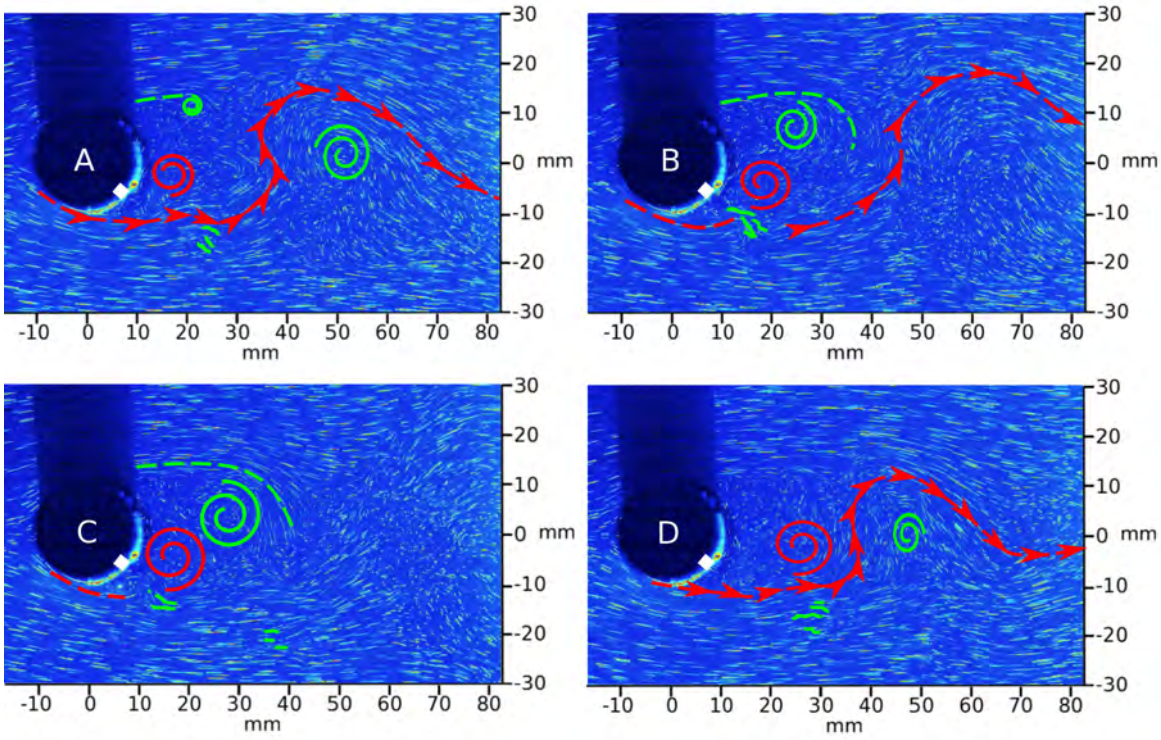

Figure 6.17: Wake structures when L_{SJA} is 0.25mm, α_{SJA} is 140°, and f_{SJA} is 11Hz where: A) suction phase of SJA, B) interaction of SJA CW vortex with shear layer, C) separation of CCW vortex from cylinder surface, and D) far field vortical interaction. Red = CCW vorticity and Green = CW vorticity

6.4.7 SJA at high stroke length after the separation point ($L_0/D_O = 0.5$, α_{SJA} = 110°)

6.4.7.1 Mid frequency 8Hz, corresponding to drag decrease

In figure 6.18 a smooth almost hydrodynamic wake structure is seen without oscillations and only small vortices that brake down into turbulence shortly after formation. Prior to the ejection phase, the boundary layer separation is at its furthest point down-stream in figure 6.18 A. As fluid is ejected from the orifice, it causes a swelling in the boundary layer, as only a CCW vortex is formed as shown in figure 6.18 B. As the suction phase initiates it pulls fluid from the shear-layer traveling around the CCW vortex towards the cylinder, this results in the cross-flow destroying the CCW vortex (fig. 6.18 C).

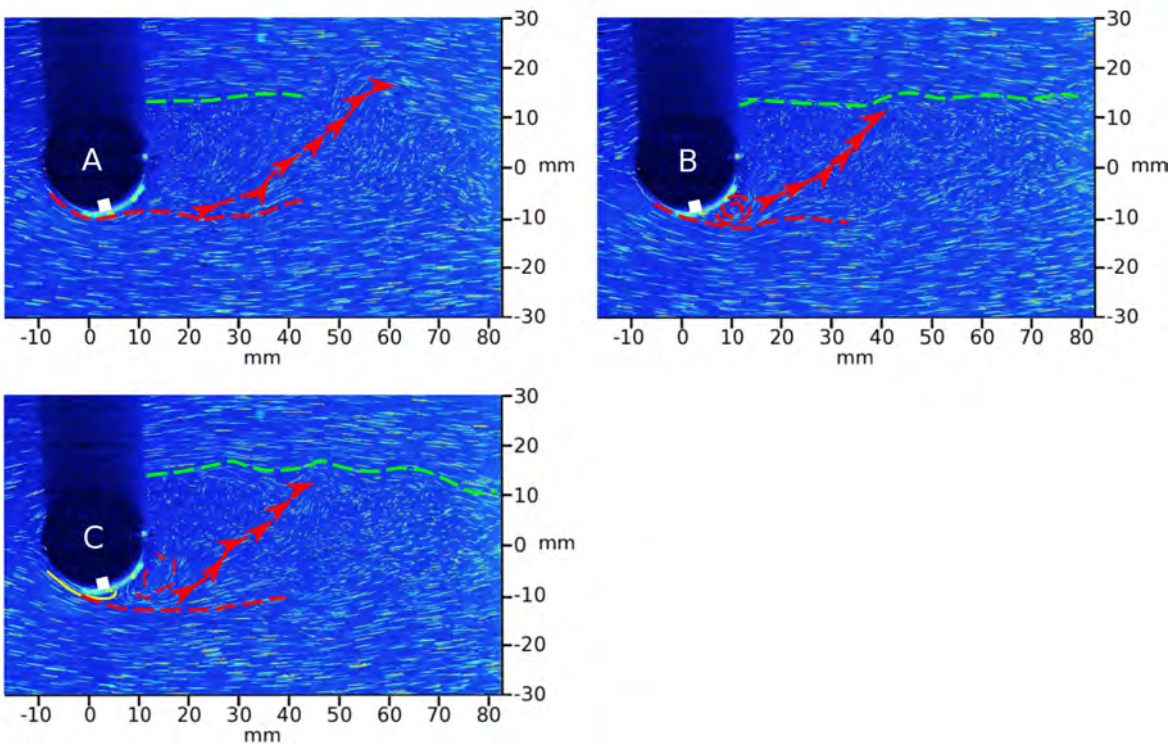

Figure 6.18: Wake structures when L_{SJA} is 0.5mm, α_{SJA} is 100°, and f_{SJA} is 8Hz where: A) suction phase, B) formation of SJA CCW, and C) breaking down of CCW vortex by shear layer. Red = CCW vorticity and Green = CW vorticity

As with a jet stroke length of 0.25mm (f_{SJA} = 9Hz, V_R = 0.28) the CCW vortex's vorticity pulls fluid into the wake diagonally from the cross-flow. This fluid prevents vortices from

forming at the top of the wake and as such, no significant oscillation take place.

The most significant difference of having a larger stroke is in the effect that the suction phase has on the boundary layer. With an increase in vortical strength the CCW vortex causes a larger separation in the boundary layer, but the vortex is not able to travel far along the surface of the cylinder, as the suction phase is strong enough to pull the shear-layer back to the surface. This results in the shear-layer overpowering the CCW vortex, as seen in figure 6.18 C.

6.5 Discussion on flow visualization

FV was used to determine the interactions of the SJA with the shear-layers over a cylinder, to establish the mechanism that produce the drag modification seen in chapter 5. To best show the range of interactions three primary angles, where looked at due to their particular attributes:

1. α_{SJA} 140° for an L_0/D_O of 0.5
    - SJA produces both an increase and a reduction in drag from the no-jet condition.
2. α_{SJA} 100° for an L_0/D_O of 0.25
    - SJA produces a stable drag reduction.
3. α_{SJA} 80° for an L_0/D_O of 0.5
    - SJA produces large peaks of drag increase.

6.5.1 Shift in synthetic jet actuator drag effect from increase to reduction at high stroke length after the separation point (L_0/D_O = 0.5, α_{SJA} = 140°)

Looking firstly at 140^o it was seen in figure 6.2 that at lower jet frequencies a spike in drag increase from the no jet conditions was seen, followed by a sudden plummet in drag levels to

20% below the no jet condition.
In the case of figure 6.8 an increase in drag at 6Hz (V_R = 0.38) is due to the production of large counter rotating vortices. The vortex produced by the SJA results in the formation of a large CCW vortex, that remains attached to the surface of the cylinder due to the collapsing of the shadowing effect from the CW vortex. The CCW vortex grows exponentially, pulling fluid from the far wake and the top surface, resulting in the formation of a CW vortex from the top surface as the CCW vortex travels down-stream. The CCW vortex is broken down by the CW vortex, allowing the CCW vortex to travel down-stream into the far wake. This results in large oscillations forming directly behind the cylinder and allowing high levels of turbulence to be transmitted down-stream into the far wake, while also increasing the average wake with.

The three drag reduction cases of 9 (V_R = 0.56), 10 (V_R = 0.63), and 11Hz (V_R = 0.69) show how jet interaction at this angle is able to reduce drag bellow the 10% barrier experienced by 100°, 110°, and 120°. At the jet frequencies of 9Hz (V_R = 0.59) and 10Hz (V_R = 0.63) it is seen that streamlined wakes are produced, with a suction effect from the suction phase moving the separation point down-stream along the cylinder.
For 9Hz (V_R = 0.56) there is a small amount of oscillation, but these oscillations take place around 1.5 cylinder diameters down-stream and usually dissipate by 2.5 cylinder diameters. This means that the bubble of separation has ended by around 3 cylinder diameters, but with turbulent perturbations being shed regularly from the back of the separation bubble. The suction phase of the SJA results in a narrowing of the wake structure and the interactions of the CCW vortex produced trips turbulence in the shear-layer, stopping swelling in the boundary layer.

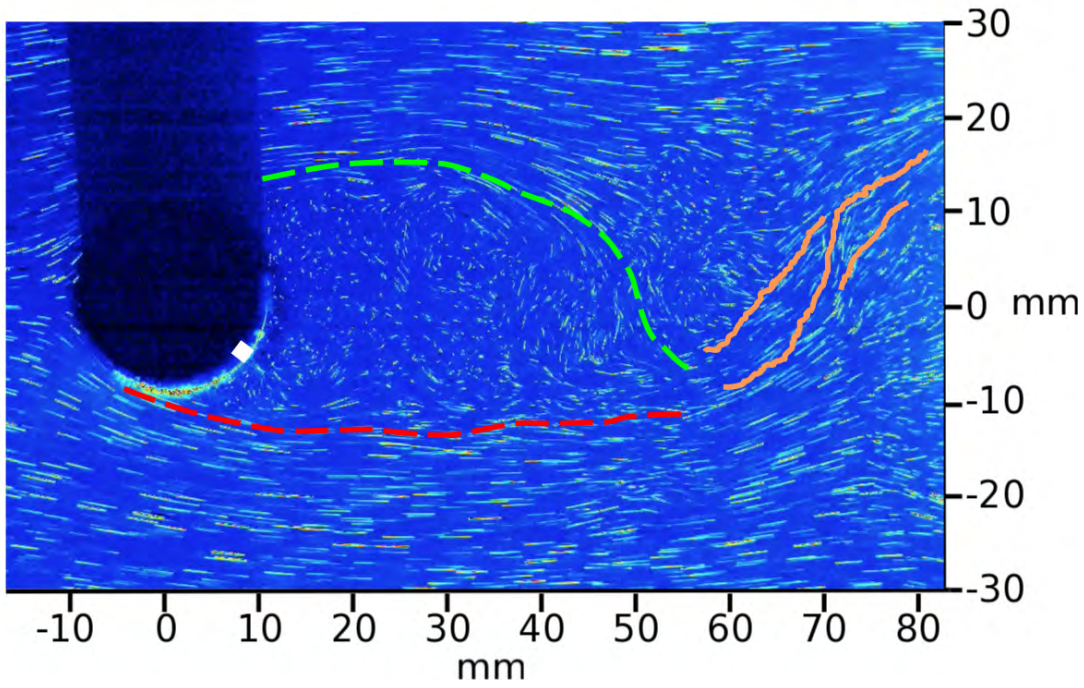

Figure 6.19: Steam-lining effects of and SJA with an L_0/D_O of 0.5 at a jet angle of 140° when jet frequency is 9Hz. Red = CCW vorticity, Green = CW vorticity, and Orange = downstream turbulence from the wake

At 10Hz (V_R = 0.63) only a CCW vortex is able to form, as the CW vortex is unable to overcome the Boundary layer vorticity. However, a slug of fluid breaks through the boundary-layer, resulting in the point of separation not being pushed backwards as the CCW vortex grows. As the slug passes quickly thought the shear-layer, the shear-layer is able to impart CCW vorticity on the CCW vortex, resulting in quick growth, producing a swelling in the wake at around 1.5 diameters down-stream of the cylinder. The large CCW vortex produces significant turbulent mixing in the wake, reducing the pressure differential between the front and rear stagnation points. It is also seen that there are less turbulent perturbations shed from the back of the wake.

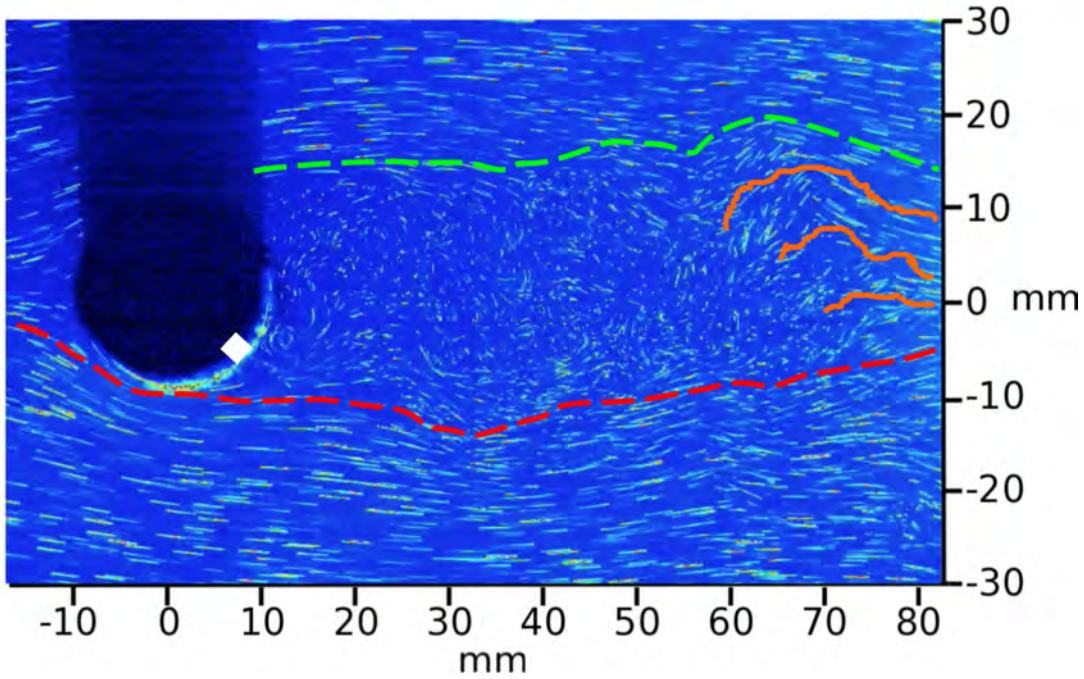

Figure 6.20: Steam-lining effects of and SJA with an L_0/D_O of 0.5 at a jet angle of 140° when jet frequency is 10Hz. Red = CCW vorticity, Green = CW vorticity, and Orange = downstream turbulence from the wake

For both cases, the separation bubble ends few diameters down-stream of the cylinder, both trip turbulence in the shear-layer and their suction phases pull the separation point down-stream. The short streamlined bubble of separation result in the cross-flow fluid smoothly merging, reducing the pressure drag by artificially streamlining the wake. Pressure recovery is hampered by the shedding of turbulence, increasing the magnitude of the pressure differential.

When the jet frequency is increased to 11Hz (V_R = 0.69), the SJA interacts in a manner similar to both of the previous frequencies. In which CW vortex is formed and both CCW and CW (shed form top surface of cylinder) vortices are present in the wake. As a result of the CW vortex emanating from the orifice shadowing the CCW vortex, the CCW does not grow rapidly. This allows a CW vortex to shed for the top surface. As a result, a return flow is formed centrally in the wake between the counter rotating vortices, this energizes and supplies the formation of further vortices. This regulated structure prevents oscillations in the near wake, and produces a stable wake structure and separation bubble. The primary turbulence of the separated bubble has ended by around 3 cylinder diameters down-stream.

This uniformity of wake shape, lack of turbulent perturbations forming at the end of the separated bubble, and high levels of mixing in the separated bubble, result in a large reduction in pressure drag.

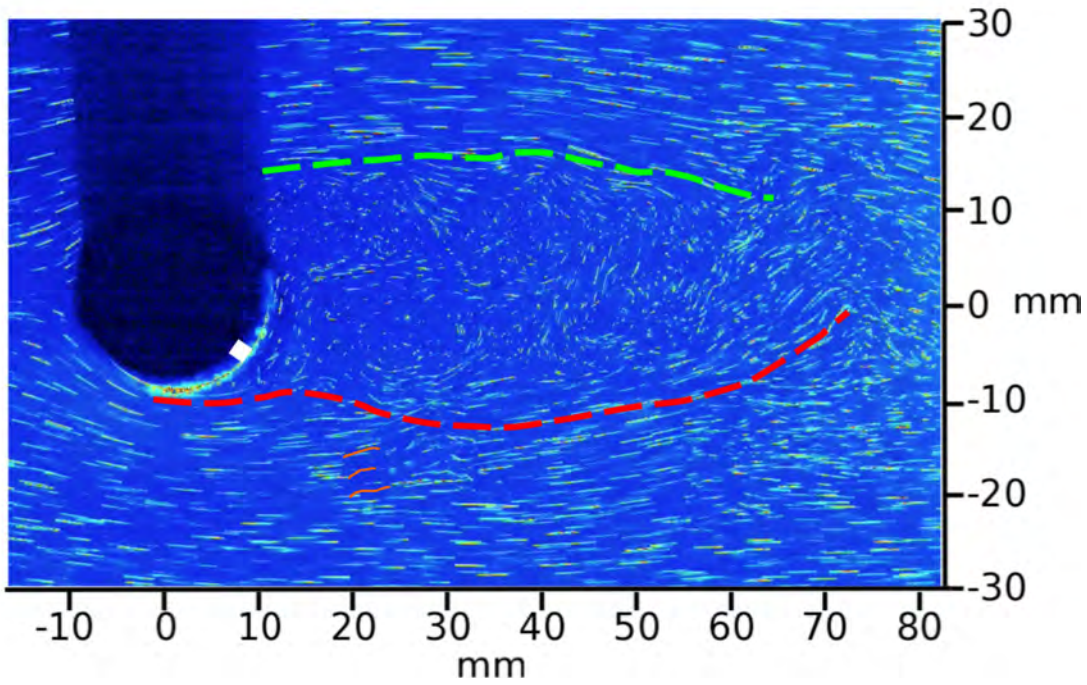

Figure 6.21: Steam-lining effects of and SJA with an L_0/D_O of 0.5 at a jet angle of 140° when jet frequency is 11Hz. Red = CCW vorticity, Green = CW vorticity, and Orange = downstream turbulence from the wake

Figure 6.21 shows how this profile reduces drag over the cylinder, thought virtual streamlining. Fluid hitting the front of the cylinder is at a high pressure (low velocity), as the fluid comes off the shoulder of the cylinder its velocity increases. This velocity increase results in an area of low pressure at the thickest part of the wake. As the fluid moves towards the end of the separated bubble, the velocity is reduced, increasing pressure. This increase in pressure after the separation bubble minimizes the differential in pressure between it and the front stagnation point, reducing the pressure drag. One of the primary reasons that 11Hz is able to double the drag reduction levels of 9Hz and 10Hz is due to the stability of the wake shape allowing for a minimizing of pressure differential, and in the lack of regular turbulent perturbations effecting the levels of drag recovery.

6.5.2 Sustained synthetic jet actuator drag reduciton at low stroke length at around the separation point ($L_0/D_O = 0.25$, α_{SJA} = 110°)

L_0/D_O is 0.25

In this setup the SJA is able to produce and maintain a level of consistent drag reduction over a 5Hz range of jet frequencies. At the 9Hz (V_R = 0.28) a distinctly shaped separation bubble is seen (Fig. 6.22 A). Fluid being entrained by the CCW vortex produced by the SJA results in short separation bubble that is highly angles on one side. This profile reduces the levels of pressure drag, but it does not achieve the same levels as 140^o at L_0/D_O of 0.5. In figure 6.22 A, the flow over the top surface has a straight trajectory not allowing for effective pressure recovery. The flow traveling past the SJA has an overly abrupt angle change to overcome without pressure loss, reducing drag recovery. As such, this results in small separation bubble, a significant narrowing of the wake, and turbulence injected into the boundary layer and shear-layer, resulting in a reduction in pressure and frictional drag.

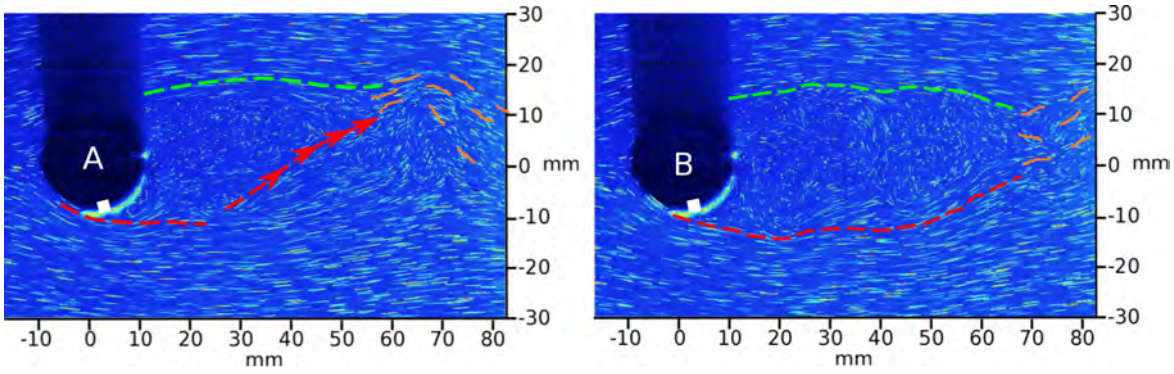

Figure 6.22: Steam-lining effects of and SJA with an L_0/D_O of 0.5 at a jet angle of 100° when jet frequency is: A) 9Hz and B) 8Hz. Red = CCW vorticity, Green = CW vorticity, and Orange = downstream turbulence from the wake

From figure 6.13 when the jet frequency is 8Hz (V_R = 0.25) the average wake has a longer separation bubble that resembles a traditional hydrofoil as shown in figure 6.22 B. It would be expected that this shape would produce a larger drag reduction compared the 9Hz (V_R = 0.28), due to having a better pressure recovery potential. However, as the wake structure undergoes a periodic change from a smooth separated bubble to a brief period of oscillation in the far wake, resulting in a period of a higher pressure differential increasing the pressure drag.

6.5.3 Large drag spike caused by an synthetic jet actuator at high stroke length before the separation point (L_0/D_O = 0.5, α_{SJA} = 80°)

At 80° only a increases drag over the range of frequencies. The two spikes in drag are produced by very different mechanism. At the lower jet frequencies, drag increase is like that of 140, with an increase in wake instabilities. At higher jet frequencies, drag increase is as a result of large blockages produced by the SJA vortices.

Looking initially at the 4Hz (V_R = 0.25) it is seen from figure 6.9 that as only a CCW vortex is able to form, that remains attached to the surface of the cylinder. This vortex is unable to grow, but is able to pull the flow around the shoulder of the cylinder. This results in the Vortex being released from the cylinder at sharp angle into the wake. This results in the formation of sharp oscillations directly behind the cylinder. Giving an unstable wake structure and high levels of turbulence in both the near and far wake. This results in a large increase of pressure drag compared to that of the no-jet.

At 11Hz (fig. 6.10) drag increase is caused by separation taking place early on both sides of the cylinder, and by the large blockage produced by the SJA vortices increasing the wake to around 3.5 cylinder diameters. The large vortices in the wake produce a strong backflow in the core of the cylinder. This increase the separation potential of the wake, by increasing the backpressure along the surface of the cylinder forcing the separation point to move upstream. These mechanisms result in a large increase of drag of 40% above the no-jet condition, due to an increase in pressure and frictional drag.

6.5.4 Comparison of drag reduction values looked at

From the test conducted it was seen that when a drag increase was present there was either large oscillations that resulting form vortical interaction or due to a large blockage in the wake (fig. 6.23 A). These interactions result in a significant difference in pressure between the front and rear stagnation points of the cylinder. In the case of the L_0/D_O of 0.5 the increase in wake results in a virtual reshaping of the cylinders' hydrodynamic profile to act like that of a cylinder with a considerably larger diameter.

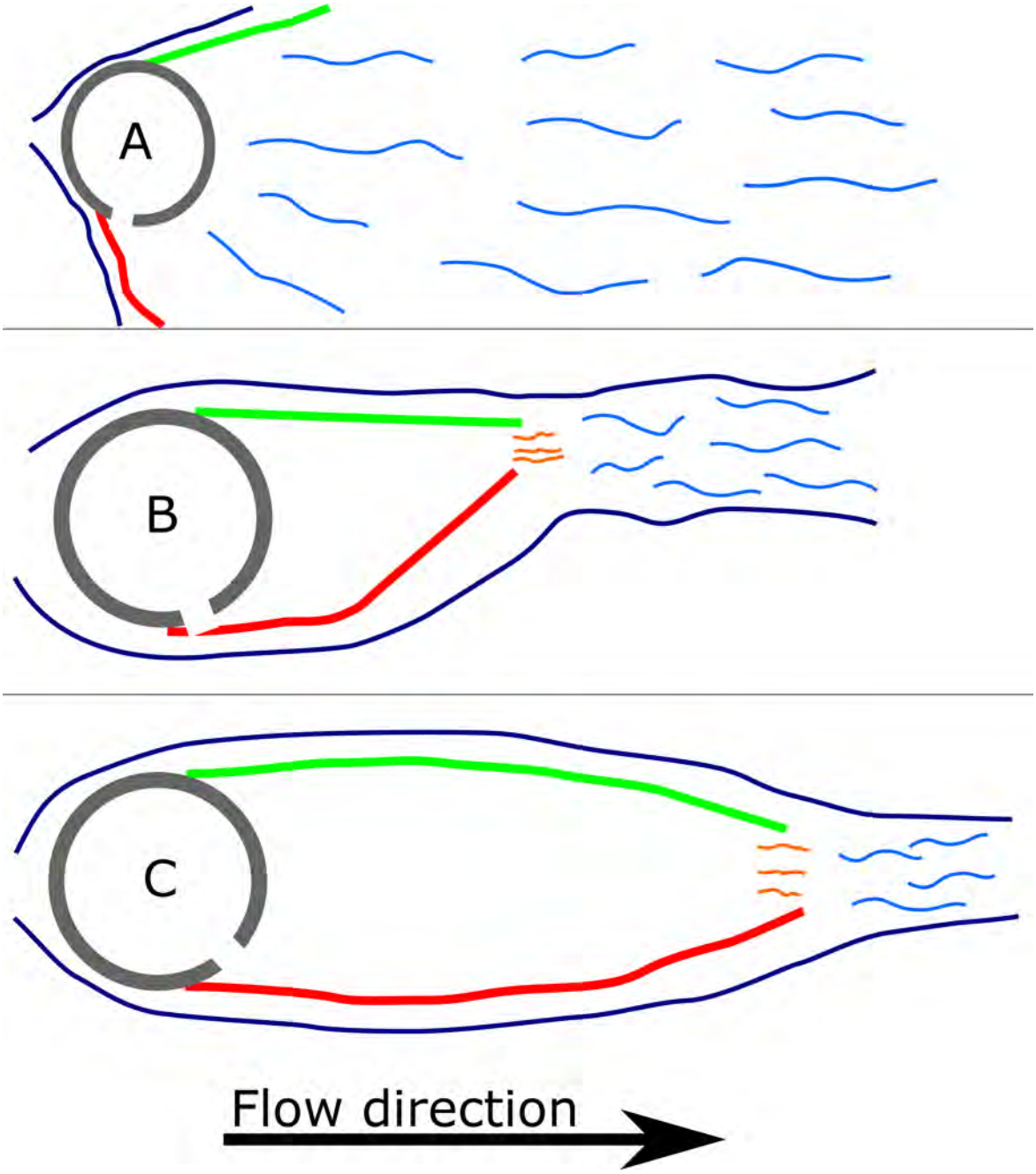

Figure 6.23: Virtual reshaping of the cylinders' hydrodynamic profile though the use of a synthetic jet actuator. Hydrodynamic profiles when: A) drag is increased, B) Drag reduction type 1, and C) drag reduction type 2. Red = CCW vorticity, Green = CW vorticity, and Blue = cross-flow

Interestingly the SJA produces a drag reduction by virtually streamlining the wake structure, allowing for greater pressure recovery, minimising the pressure differentials and so reducing the pressure drag. This is achieved through the reshaping of the bubble of separation to resemble that of a rudimentary hydrofoil. There are two particular types of reshaping seen,

that of a short high angles asymmetric hydrofoil (fig. 6.23 B) and a hydrofoil with a long chord length with gradual angles and a greater symmetry (fig. 6.23 C).

Figure 6.23 B represents the typical highly angle separation bubble as seen for L_0/D_O 0.25 at the velocity ratios of 0.31 (10Hz) and 0.28 (9Hz) for the jet angles of 110^o (fig. 6.16) and 100^o (fig. 6.14) respective. Both cases display a very similar shape, but with 110^o achieving 5% more drag reduction, this is due to primarily to:

- As the angle for 110° is at a larger offset, it allows for a stronger vortex to interact with the shear-layer. Tis vortex is able to travel further down-stream, and penetrate deeper into the shear-layer. This result in a larger quantity of fluid being drawn into the wake, at a less steep angle.

- The produces a longer profile that has a less abruptness angle, allowing fluid to circulate around the cylinder and separation bubble more naturally as shown in figure6.23 B. This allows for better pressure recovery, as the fluid transitions from the thickest part of the separation bubble to the end, minimizing the pressure differential.

Figure 6.23 C shows the separation bubble for the jet angle of 140^o with an L_0/D_O of 0.5 at a V_R of 0.69. It can be seen that the separation bubble is shaped like that of a traditional hydrofoil, with a slight thickening in the wake, followed by a gradual tapering to the tail. This allows for a efficient pressure recovery, and is responsible for the 20% drag reduction from the no-jet case.
In comparing the two drag reduction profiles it may seem that figure 6.23 B would achieve the higher levels of drag reduction as it has a smaller separation bubble. However due to having a less optimal ratio of thickness to chord length, and its harsh angle on one side, and flat surface on the other it is not as effective at pressure recovery as that of figure 6.23 C.

In order to better understand the effects an SJA has on drag PIV will be used to investigate the differences between the two primary types of virtual hydrodynamic profile's, by looking at:

- Average velocity profiles, to determine wake shape

- Average turbulence intensity, to determine the effect size of the separation bubble and amount of turbulence reaching the far wake.
- Average vorticity. To determine how vorticity is altered when drag is reduced.

6.6 Conclusion of flow visualisation results

In this chapters the mechanism that influence drag modification where analysed through flow visualisation. It was found that through complex interactions of the vortices with the shear-layer and wake, the SJA was able to modify drag thought virtual reshaping of the hydrodynamic profile of the cylinder.

At lower jet frequencies (*flow regimes II and III.a*) the SJA primarily has a negative effect on drag, particularly when L_0/D_O is 0.5. It is seen that the wakes in these zones tend to produce large oscillation, that start from the back of the cylinder, as well as large levels of turbulence in the far-wake

At higher jet frequencies, there is a wider variety of drag modifications, from large increase to large decreases. The large increases at this point tend to be as a result of blockages caused by the vortex or due to the production of large oscillations stemming from large movement of the separation point up and down-stream between the ejection and suction phases of the SJA. The large reduction in drag where found to be a result of the SJA re-shaping the hydrodynamic profile of the cylinder, the behave more like that of a hydrofoil. This allowed for considerable gains in pressure recovery between the front and rear stagnation points, resulting in a large reduction in pressure drag. To better understand these interactions and to obtain average wake shapes, PIV results are detailed in the next chapter.

Chapter 7

Synthetic Jet Actuated Cylinder in Cross-Flow: Particle Image Velocimetry in the Wake

7.1 Aims

Having used flow visualization to look at the mechanism responsible for the drag modifications seen in section 6.23, PIV will be used to validate these mechanism and to gain a better understanding of how an SJA alters the wake structures to achieve these drag modification through synthetic jet actuation. PIV is used to give the average flow fields for velocity, turbulence intensity and vorticity. These flow field where analysed to determine how an SJA is able to alter the natural flow state and to provide a virtual hydrodynamic profile behind the cylinder, capable of mimicking the drag modifications of a physical object.

7.2 Introduction

In the pervious chapters the synthetic jet actuator operating conditions responsible for drag modification where established using strain readings (chapter 5), and the mechanism responsible for these modifications where examined through the use of flow visualization (chapter 6.). Flow visualization only allowed for an instantaneous qualitative image, with

velocity changes presented by streak lengths. PIV is used to quantitatively analyse the effects of the SJA on wake structures, through the use average flow profiles. Flow will be looked at in terms of:

- Average velocity
- Average turbulence intensity
- Average vorticity

In the previous section it was found that the SJA appeared to be capable of modifying the hydrodynamic profile of the cylinder, either reducing or increasing the drag forces experienced by the cylinder from that of the no-jet condition. With regard to drag reduction two primary wake structures responsible for the apparent virtual hydrodynamic profile modifications were identified and characterised as *type I* (Fig. 6.23 B) & *Type II* (Fig. 6.23 C). The proper identification and analysis of these structures is the primary focus of the PIV. PIV allows these structures to by analysed, to determine how they alter the flow states from the no-jet condition, and how these structures are capable of reducing drag. In these tests the no-jet condition, a drag increase condition, and the *type I* and *type II* drag reduction cases will be looked at. The setups looked are laid out in table:

Table 7.1: Particle image velocimetry results looked at

Modification	No-jet	Drag increase	Drag reduction		—
α_{SJA}	NA	80	100	140	Degrees
L_0/D_O	NA	0.5	0.25	0.5	—
f_{SJA}	0	6	9	11	Hz
V_R	0.	0.	0.	0.	—

7.3 Test setup and procedure

Test where set up as in section 4.1.3. The Camera was positioned normal to the viewing window, with a light sheet ($f = -6$ cylindrical lens) in positioned centrally (spanwise) and parallel to the flow. The camera had a 105 lens set to an aperture of 2.8, and the laser power was set to its maximum of 1W. The recording rate was set to 185Hz and recordings where taken for 50 seconds.

7.4 Results for particle image velocimetry

The primary focus of this section is to determine and further understand how the interaction of a synthetic jet affects the drag forces acting on a cylinder through the apparent virtual hydrodynamic profile reshaping identified in section 6. In order to get a more complete understanding of how this is archived the results section is broken down into the following sections.

1. Average velocity
2. Average turbulence intensity
3. Average vorticity

7.4.1 Average velocity flow profiles

Average velocity flow profiles are looked at to determine and better understand the shape, size, and velocity of the cylinder wake structures. In particular, to better establish the velocity differential between the cross-flow and wake as well as the size, location, and magnitude of the differentials. This establishes the first step in understanding how the pressure differential is modified.

7.4.1.1 Average velocity for the no-jet condition

In figure 7.1 the average velocity profile for the *no-jet* condition is shown. In this profile a 10mm long by 20mm wide area of low velocity flow is seen directly behind the cylinder, followed by a secondary teardrop bubble of low-velocity flow. The bubble behind the cylinder has a core velocity of between 0 and 0.05m/s, where the secondary bubble has a primary core velocity of between 0.15 to 0.2m/s. These areas of low velocity show a velocity differential is present between the front and rear stagnation points. The thickest part of the separating bubble behind the cylinder is roughly 1 cylinder diameter. By the time the wake has travelled to an X/D of 6 down-stream, the velocity differential begins to break down and is almost gone by an X/D of 10. Symmetrical areas of high-velocity fluid (dark red) are seen around each shoulder of the cylinder, due to the flow being channelled around the cylinder, with both areas having a similar speed (0.4m/s) shape and an advection length 2 diameters down-stream.

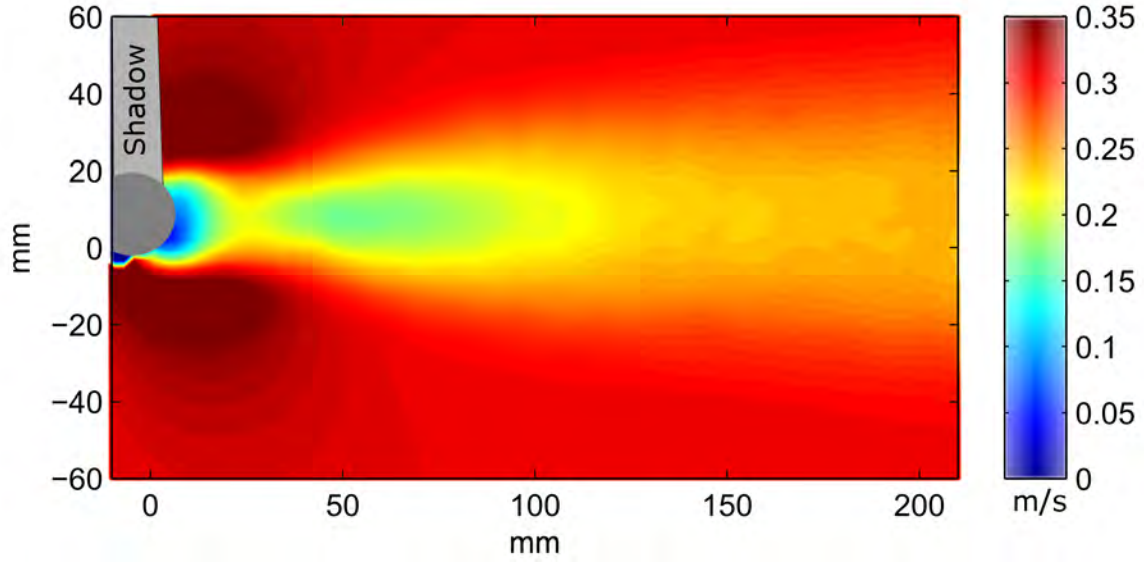

Figure 7.1: Average velocity profile for the no-jet condition

7.4.1.2 Average velocity for the drag increase condition

Figure 7.2 shows the velocity profile for the increased drag-condition. A long detached teardrop area of velocity between 0.14 and 0.21 m/s, forming at an X/D of 1 down-stream from the cylinder. This area has a maximum thickness of roughly 1.3 diameters. At around an X/D of 7 the area of low-velocity begins to slightly reduce, but continues into the far-field wake beyond the interrogation window. It can be seen that there is a sudden transition along the length of this area from low-velocity flow to near-regular cross-flow velocity in comparison to the no-jet condition. This large wake structure, though narrow, produces a large pressure drag. The area of high velocity around the shoulders are asymmetric in shape, with the lower having a longer profile, suggesting a level of lift modification is taking place.

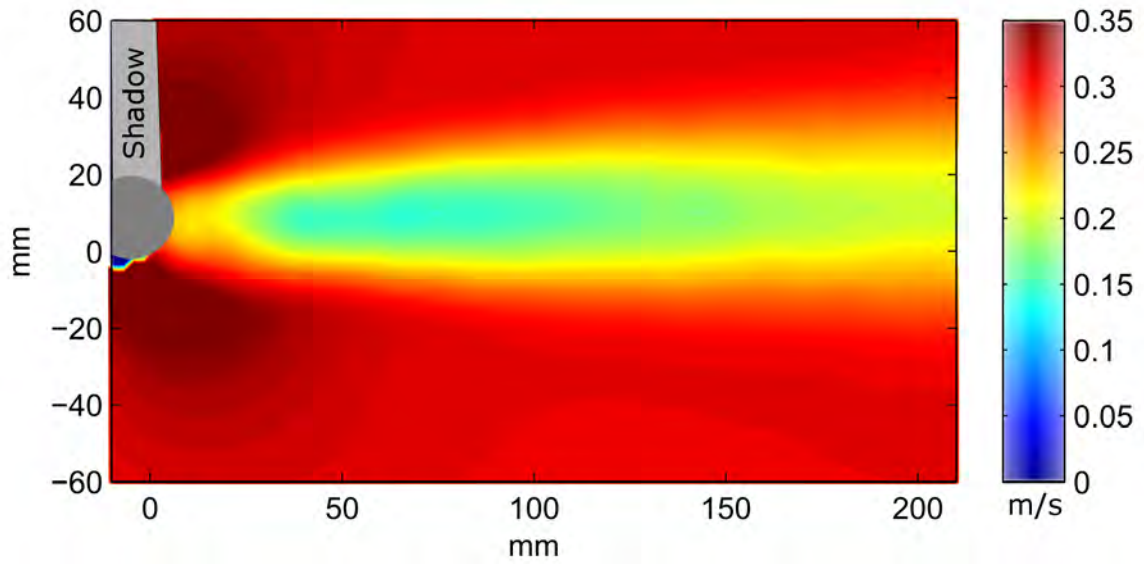

Figure 7.2: Average velocity profile of cylinder wake when L_0/D_O is 0.5, V_R is 0.25 and α_{SJA} is 80^o

7.4.1.3 Average velocity for the type I drag reduction

Figure 7.3 shows the average velocity profile for the **type I** drag reduction profile (see fig. 6.23 B). The small bubble of low-velocity fluid attached to the cylinder is highly tilted, as would be expected from the wake vectoring looked at in FV (Fig. 6.14). The bubble and wake have both been reduced significantly in size from the no-jet and drag increase cases, with the max thickness of the low-velocity area being roughly 0.5 cylinder diameters, half that of the no-jet. The velocity differential between the wake and the cross-flow have been reduced, with the small bubble having a velocity of around 0.23m/s and the larger bubble having a velocity between 0.2s to 0.22m/s. By X/D of 7 the velocity differential begins to rapidly break down, and has almost fully dissipated by an X/D of 10.

Around the shoulders of the cylinder the areas of high velocity (dark red) are asymmetric, with the lower being tilted inwards and traveling further down-stream. This higher velocity around the lower surface of the cylinder suggests an element of lift is present, as was shown in section 5.11.

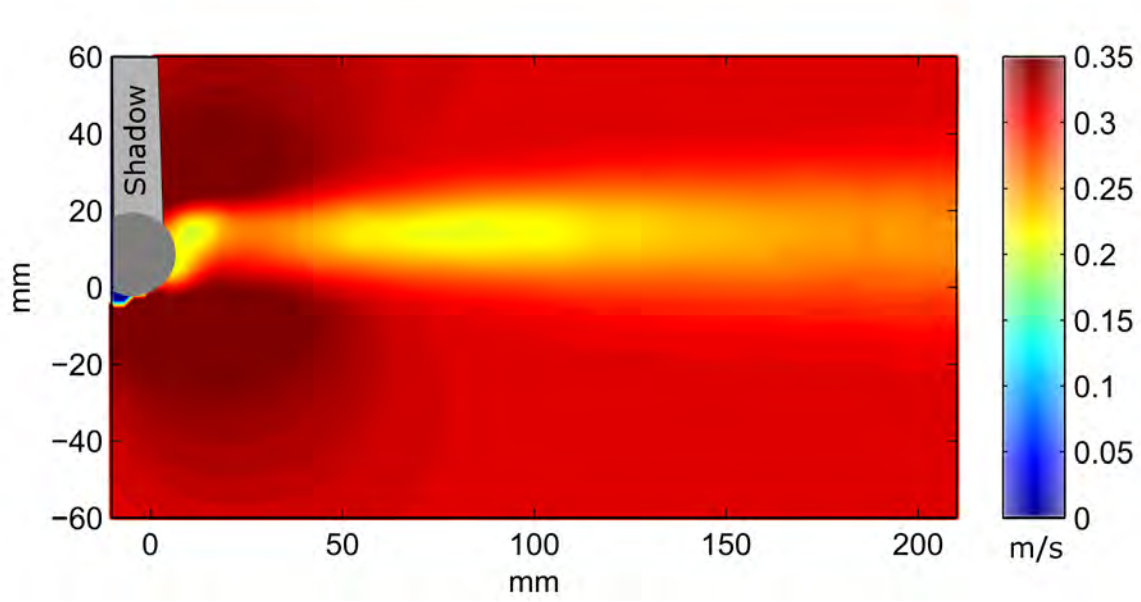

Figure 7.3: Average velocity profile of cylinder wake when L_0/D_O is 0.25, V_R is 0.28 and α_{SJA} is 100^o

7.4.1.4 Average velocity for the type II drag reduction

Figure 7.4 shows the average velocity profile for the **type II** drag reduction profile (Fig. 6.23 C). The average velocity difference between the wake structures and cross-flow has been reduced significantly, as is seen with a wake velocity of around 0.17m/s directly behind the cylinder and a narrow area of velocity around 0.2 m/s in the mid-wake (X/D from 3 to 5). At around an X/D of 6 the wake structure has begun to break down with a minimum velocity of 0.25m/s. The bubble of low velocity fluid behind the cylinder is more symmetric than that of the *type I*, and has a core velocity of roughly 0.2m/s. The main core of the mid-wake is seen to have a core with a higher velocity to that of the *type I*.

The wake is slightly tilted shown by the slight deformation of the low-velocity bubble and by the asymmetry of the high-velocity flow regions around the shoulders of the cylinder, again suggesting an element of lift (Fig. 5.10).

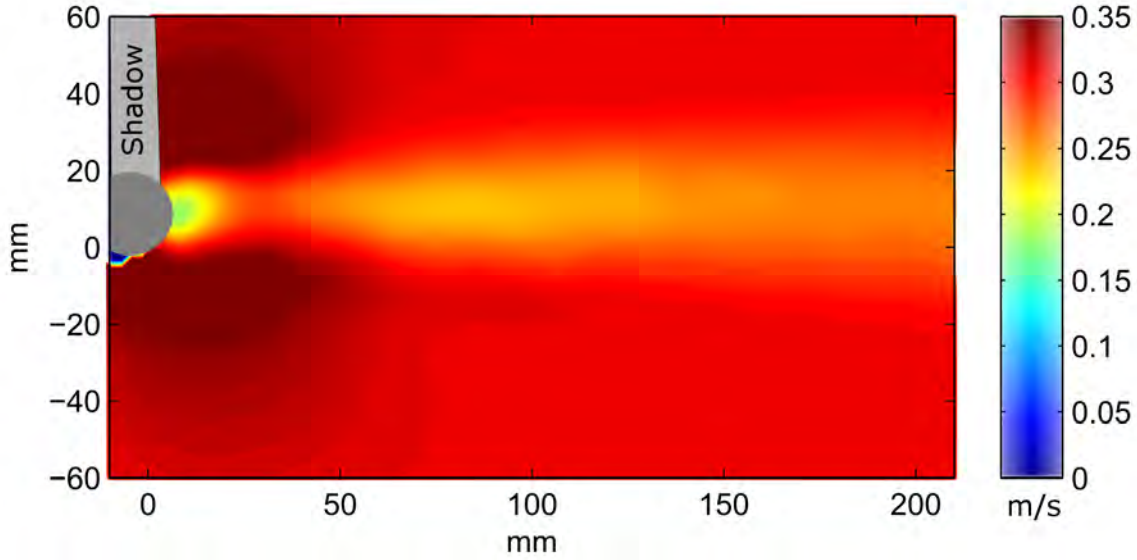

Figure 7.4: Average velocity profile of cylinder wake when L_0/D_O is 0.25, V_R is 0.34 and α_{SJA} is 140^o

7.4.2 Average Turbulence

Turbulence intensity is used to show the wake structures in terms of turbulence.

7.4.2.1 Turbulence intensity of No-Jet condition

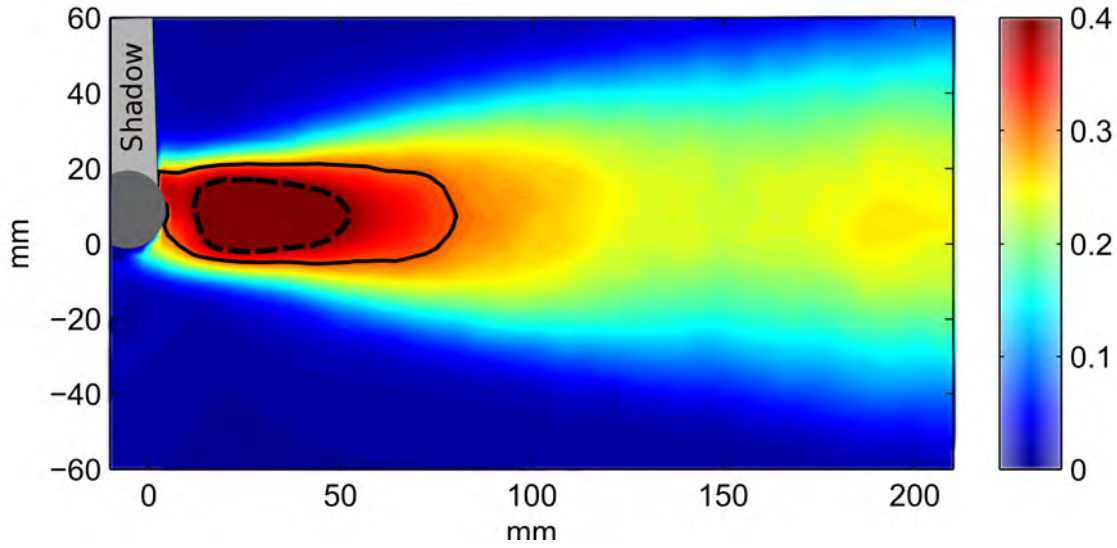

Figure 7.5: Average turbulence intensity profile of cylinder wake with no synthetic jet actuation

Figure 7.1 shows the average turbulence intensity around a cylinder for the no-jet condition. There is a large detached central core of high-level turbulence that travels down-stream to roughly an X/D of 2.5. The core has a bluntly trailing edge that undergoes a gradual reduction in turbulence. The wake experiences a small growth at around an X/D of 6 down-stream, where turbulence remains at around the same level of roughly 0.22, apart from a small area of increase at an X/D of 9 to around 0.28. The wake is seen to have a smooth profile with a max thickness of over 4 cylinder diameters.

7.4.2.2 Turbulence intensity of Drag increase condition

Figure 7.1 shows the average turbulence around a cylinder when the jet it set to produce a drag increase. It can be seen that there is a long central core of high-level of turbulence, one cylinder diameter thick, spanning down-stream to an X/D of roughly 5. This lower-turbulence core has a flat trailing edge that sees a sudden drop-off in turbulence intensity. The wake undergoes a small growth at an X/D of around 6mm, whereafter turbulence remains at around the same level of roughly 0.22. The wake is seen to have a smooth profile with a max thickness of roughly 3 cylinder diameters.

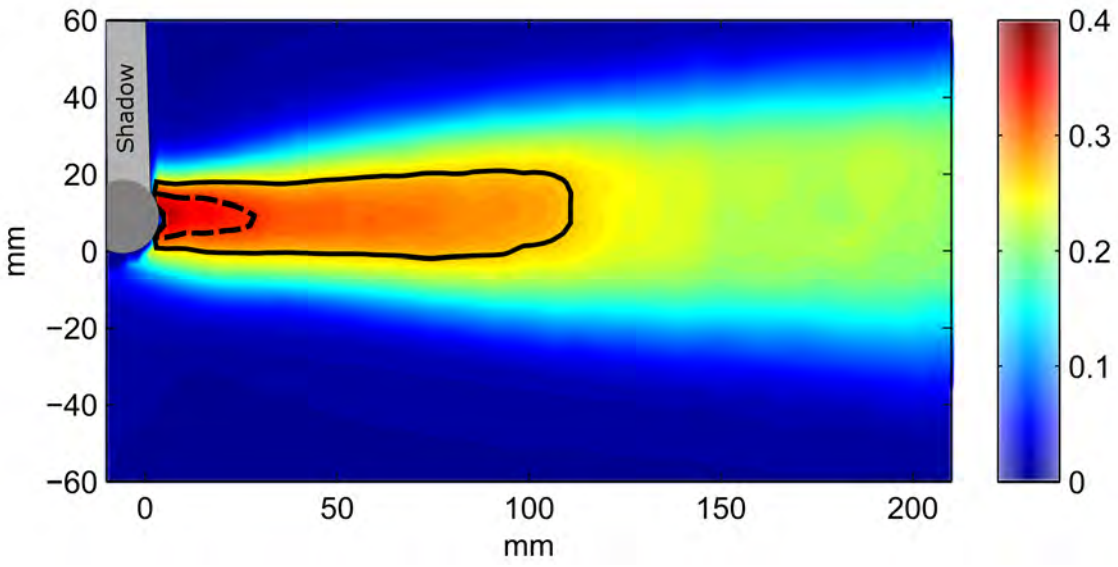

Figure 7.6: Average turbulence intensity profile of cylinder wake, when L_0/D_O is 0.5, V_R is 0.25 and α_{SJA} is 80^o

7.4.2.3 Turbulence intensity of drag reduction Type I

The turbulence experienced by drag reduction *type I* in figure 7.7 differs significantly from the no-jet and drag increase profiles, with a short, narrow and asymmetric wake (an upwards tilt). A long gradually sloping sharp turbulent bubble it formed directly behind the wake. This bubble has a turbulence intensity of around 0.4 to 0.5 and an asymmetry as the lower shear layer slopes diagonally upwards, compared to that of the flatter top surface.

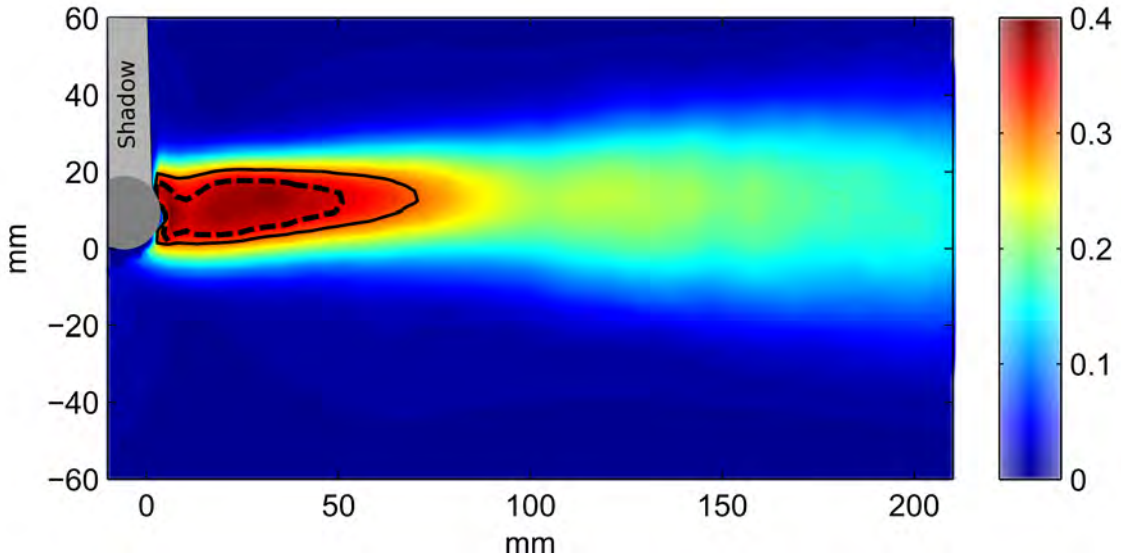

Figure 7.7: Average velocity profile of cylinder wake, when L_0/D_O is 0.25, V_R is 0.28 and α_{SJA} is 100^o

7.4.2.4 Turbulence intensity of drag reduction Type II

In figure 7.8 the turbulence profile for the wake structure responsible for the largest drag reduction of 20% from the no-jet condition is shown. The wake has a long narrow asymmetric (a downward tilt) turbulent bubble with gradually sloping profile. This smooth profile should allow for better pressure recovery, which is seen by the flows turbulence having almost dissipated by an X/D of 7. *Type II* average turbulence levels are less than that of *type I*, in particular within the high-turbulence core.

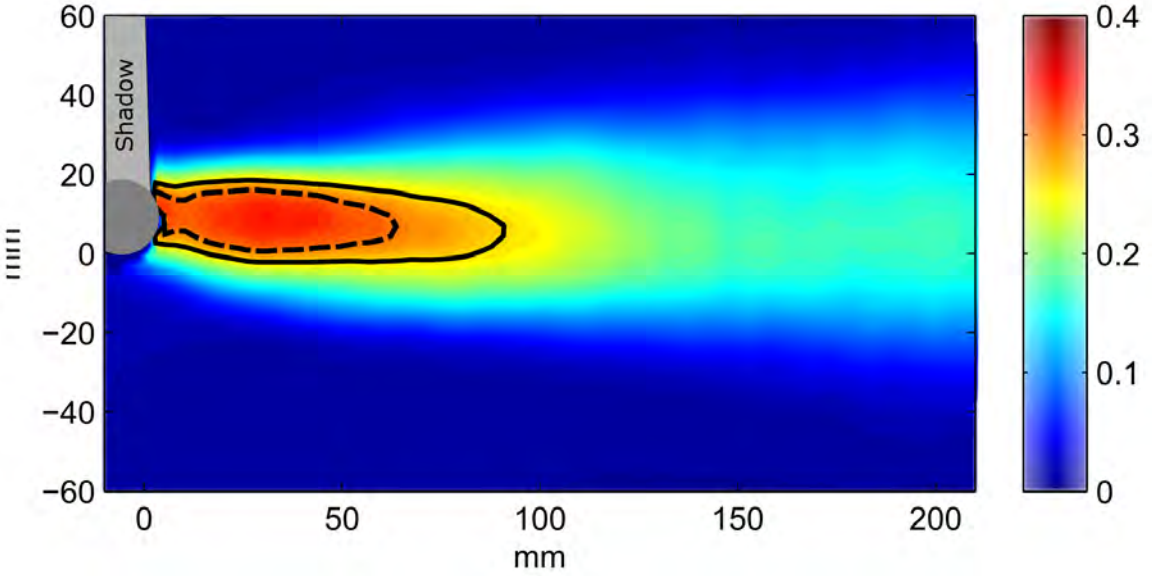

Figure 7.8: Average velocity profile of cylinder wake when L_0/D_O is 0.25, V_R is 0.28 and α_{SJA} is 100^o

7.4.3 Average Vorticity

7.4.3.1 Average vorticity of no-Jet condition

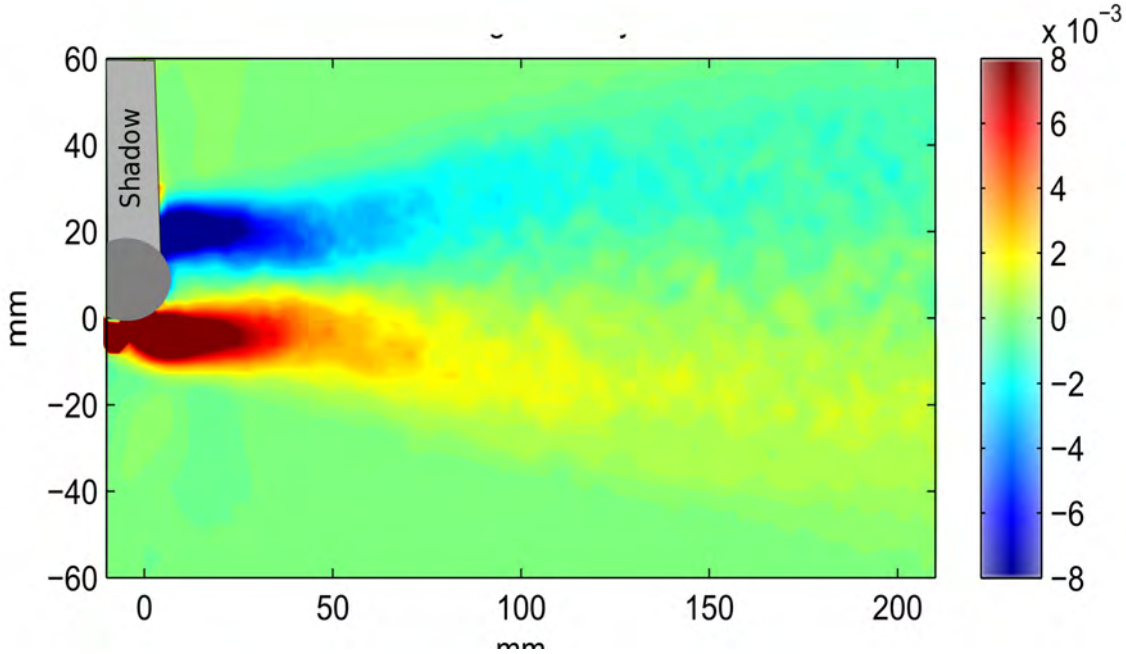

Figure 7.9: Average vorticity profile of cylinder wake with no synthetic jet actuation

Figure 7.9 shows that without SJ actuation, vorticity is concentrated within the first 50mm down-stream of the cylinder. These areas of vorticity thicken the wake to approximately 2 cylinder diameters. Beyond this point the levels of vorticity drop rapidly.

7.4.3.2 Average vorticity of drag increase condition

In figure 7.10 the vortical structures are seen to grow significantly in length to an X/D of 8.5 and 9.5 for the CW and CCV vortical components respectively. The initial width of the vortical wake is about 1.5 cylinder diameters, but it gradually expands to 3 cylinder diameters by and X/D of 5.

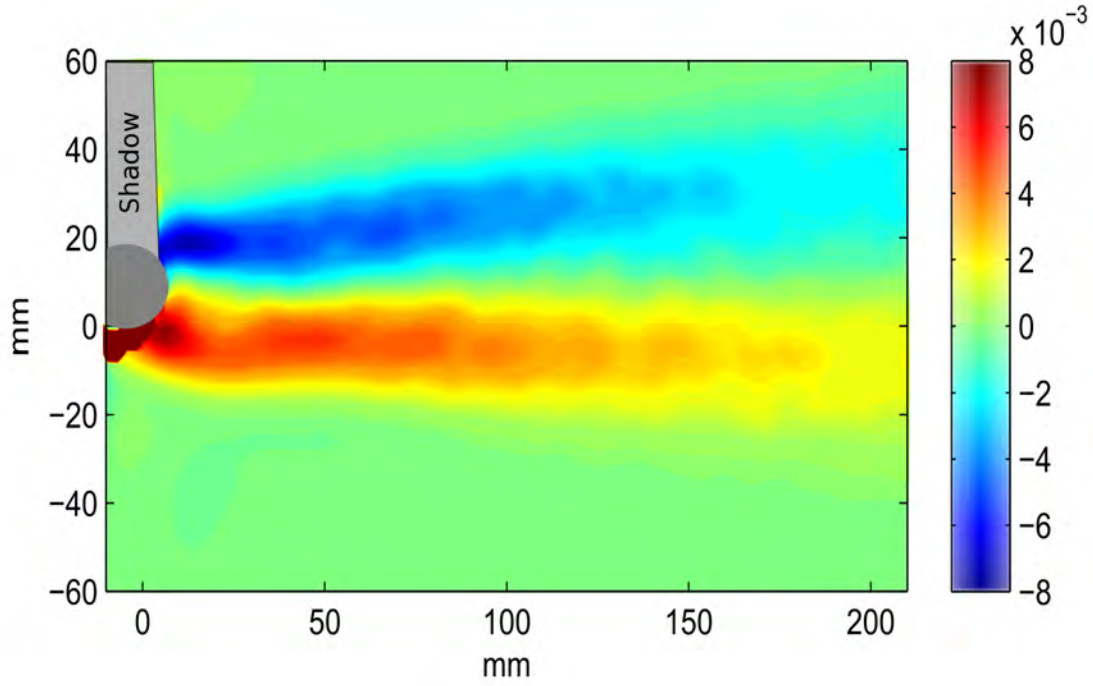

Figure 7.10: Average vorticity of cylinder wake when L_0/D_O is 0.5, V_R is 0.25 and α_{SJA} is 80^o

7.4.3.3 Average vorticity of drag reduction Type I

Type I drag reduction produces a wake that is very different from that of the no-jet condition. The vortical arms travel down-stream to around an X/D of 8 and 6.5 for the CW and CCW vortices. The vortical arms produce a wake thickness of 2 cylinder diameters, that remain constant along the length of the high-turbulence areas. The CW vortical arm is narrower, but has a higher level of vorticity. The extra thickness of the CCW vortical arm, with less

turbulence, is due to the entrainment of fluid from the cross-flow by the CCW vortex produced by the SJA and the strong free-stream CW shear layer show in section 6.4.4.3 figure 6.14

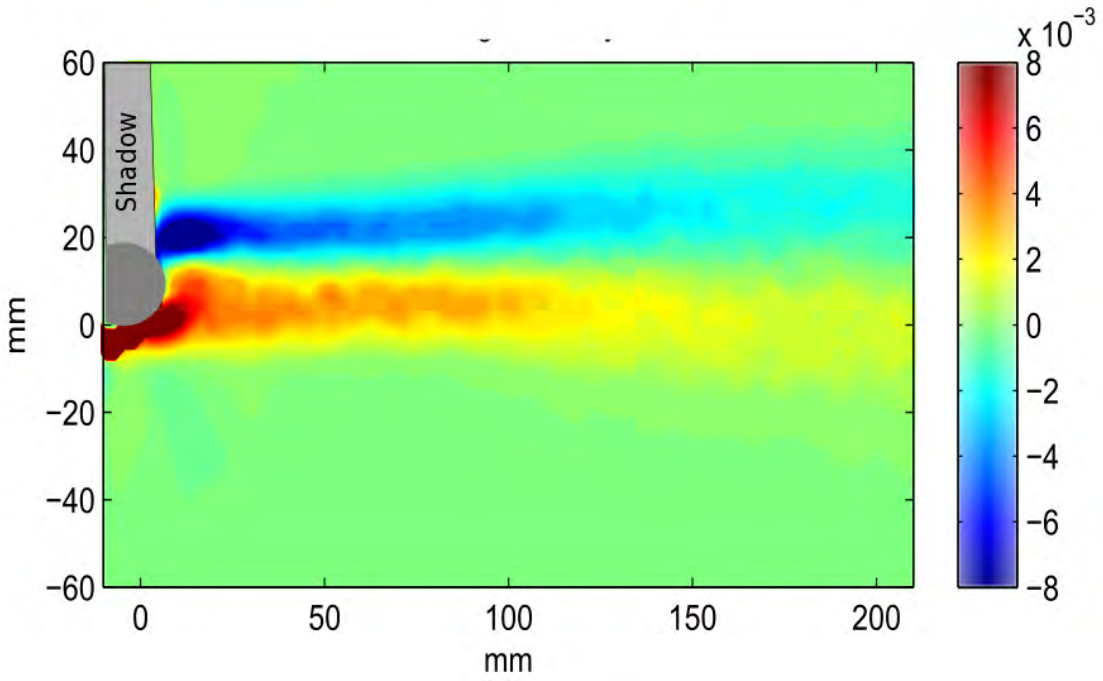

Figure 7.11: Average vorticity profile of cylinder wake when L_0/D_O is 0.25, V_R is 0.28 and α_{SJA} is 100^o

7.4.3.4 Average Vorticity of drag reduction Type II

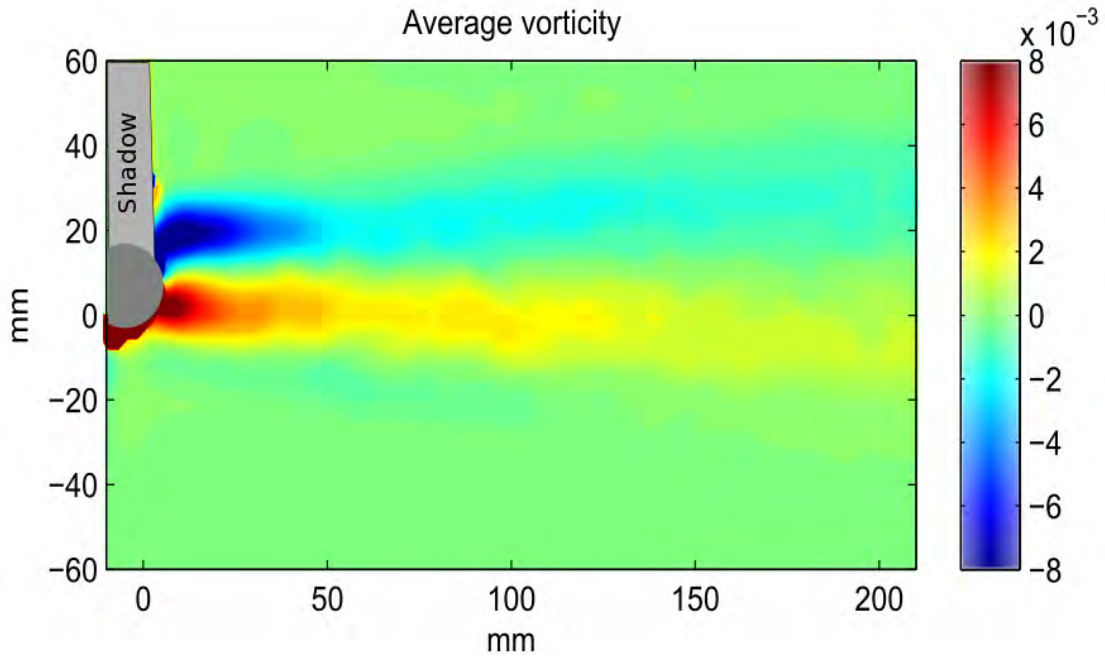

Figure 7.12: Average vorticity profile of cylinder wake when L_0/D_O is 0.25, V_R is 0.28 and α_{SJA} is 140^o

In Figure 7.12 the length of vortical components break down at 50mm where CCW vorticity does not break down fully until 130mm. The width of the vortical wake is seen to be similar to *type I*, at around 1.2D.

7.5 Discussion of particle image velocimetry results

Looking firstly at the the velocity profiles it can be seen that when drag reduction is present (Fig 7.3 & 7.4), the differential between the wake velocity and cross-flow velocity is minimised, with only small areas of low-velocity fluid are present. This minimizing of the velocity differential indicates a reduction in the pressure differential between the front and rear stagnation points, resulting in a reduction in pressure drag. On the other side of this, when looking at the drag increase (Fig. 7.2), the bubble of low velocity fluid directly behind the cylinder has also been reduced. However, in the wake beyond this point the velocity differential between the wake and the cross-flow has increased. The reason for the higher velocity behind the cylinder is primarily due to the synthetic jet perturbations reducing the

formation length of the shedding vortices, resulting in a large increase in drag pressures. The gradual widening of the wake from behind the cylinder to roughly 5 cylinder diameters, produces a large blockage. This blockage can be seen in the shortening of the high velocity bubbles around each shoulder of the cylinder, furthering the pressure differential. In order to better understand the mechanisms that have produced these velocity profiles, the wake needs to be looked at in terms of turbulence intensity and vorticity. As the physical interactions were covered in detail in the last chapter (chapter 6.), the manner in which the average wake structure influence drag modification was the primary focus of the analysis.

The no-jet condition (Fig. 7.14 A) experiences a large area of turbulence intensity at around an X/D of 0.5 that continues on until an X/D of 2.5, whereas the drag-increase condition (Fig. 7.14 B) has its highest level of turbulence attached directly to the cylinder that continues down-stream to an X/D of 6. This shows again the reaction in vortex shedding formation distance. It should also be noted that it has a flat end profile. This profile will likely result in a poor pressure recovery, and so would explain the large increase in drag, which was shown in figure 7.2 where the core velocity in the far wake is significantly lower than that of any setups looked at.

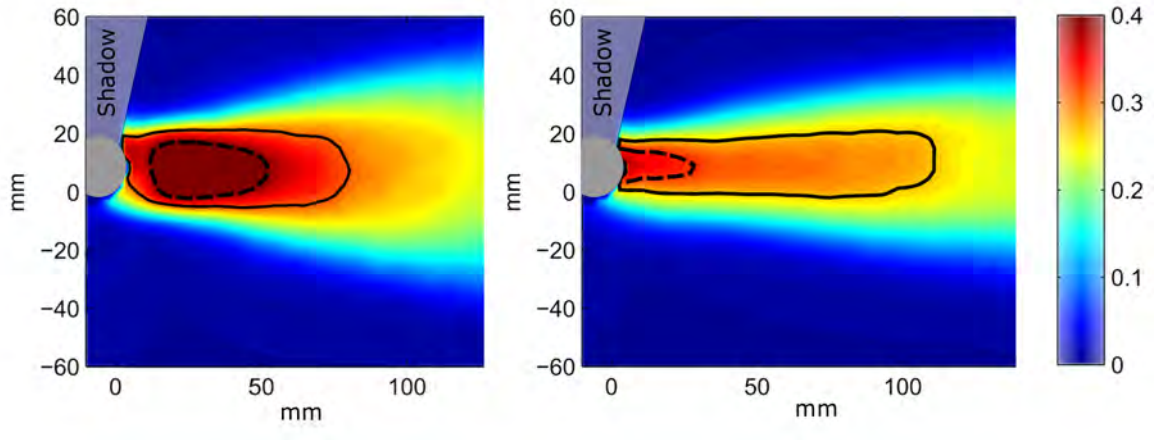

Figure 7.13: Comparison turbulence intercity of the wakes for A) the no-jet condition, and B) drag increase when L_0/D_O is 0.5, V_R is 0.25, and α_{SJA} is 80^o

In looking at the drag reduction profiles *type I* and *type II* the average turbulence intensity

can be used to show how the SJA virtually remodels the hydrodynamic profile of the cylinder through the remodelling of the separation bubble attached to the cylinder. In both cases the separation bubble can be seen to resemble that of a rudimentary aerofoil or a cylinder with fairing added.

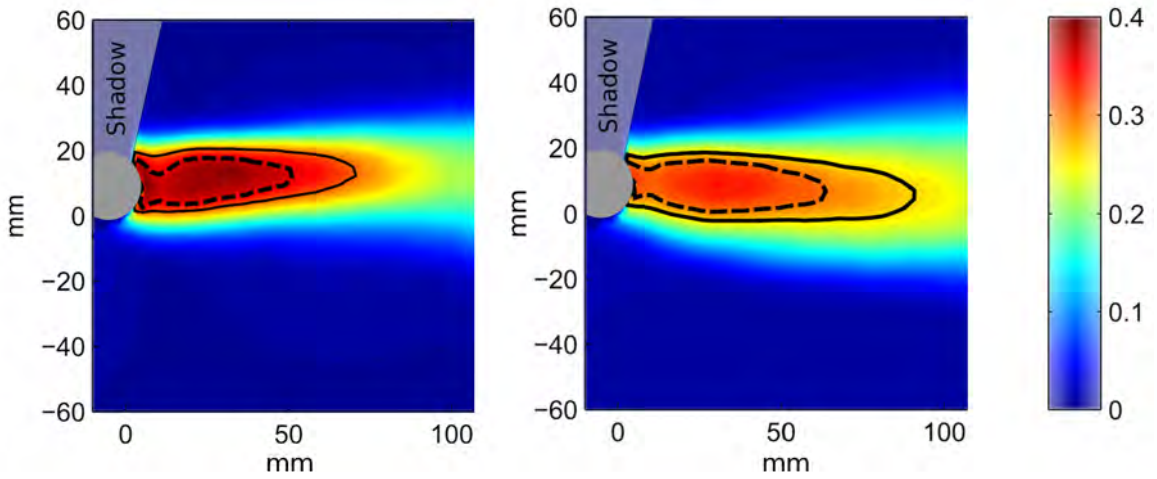

Figure 7.14: Overlaying of average turbulent intensity separation bubble on average velocity profile for drag reduction A) type I , and B) type II

Type II (Fig. 7.14 B) produces a longer, less turbulent and more gradual swooping separation bubble, that gradually reduces turbulence. Unlike in *type I* (Fig. 7.14 A) the separation bubble for *type II* has a more gradual reduction in turbulence levels from X/D of 3 to 5. The separation bubble for *type I* has a core with a greater turbulence intensity, that undergoes a more sudden drop in turbulence as travels downstream. This is due to the manner in which the turbulent structure was formed as laid out in section 6.4.4.3. These differences in formation results in a *type II* having a smoother far-field wake with a narrow band of low turbulence. How this profile emulates a hydrofoil can be seen in figure 7.17, where the turbulence intensity profile is overlaid on the average velocity profile.

Figure 7.9 shows that at no-jet, there are short vortical arms with a high-level of vorticity attached to the cylinder spanning to an X/D of around 2. This is due to a short formation region prior to the roll-up of large counter rotating vortices producing high levels of vorticity. These vortices quickly break down into turbulence as they travel down-stream, hence the low levels of turbulence after an X/D of 3.5. In figure 7.10 vorticity is less concentrated,

but remains at a high-level up to an X/D of 8 and 9 for the CW and CCW vortical arms respectively. A level of asymmetry between the vortical arms is present, due to the SJA causing perturbations in the shear layer, that suppress the formation of naturally shedding vortices. This is seen with longer and thicker vortical arm, resulting from the formation of multiple CCW vortices from the blockage caused by the SJA vortex formation, and the CCW vortex that is produced by the SJA (see section 6.4.3.3 more details). The increased length of vorticity is due to the formation of stronger more concentrated counter rotating vortices that are able to travel further down-stream, prior to breaking down into turbulence at around an X/D of 8. A reduction in the formation length coupled with an increase in the strength of the free-stream shear layer as in figure 7.10, can result in a significant increase in drag forces, as the magnitude between the front and rear stagnation points and the length of the wake structure is increased.

In vorticity the largest difference between the types of drag modification in seen between drag reduction *type I & II*, with:

- **Type I** (Fig. 7.11) producing long narrow asymmetric vortical arms, with the CCW shear layer's high-vorticity area experiencing a significant amount of tilting and thickening in the near-wake, directly behind the cylinder. Vorticity is seen to drop off significantly after around an X/D of 6
- **Type II** (Fig. 7.12) producing short asymmetric vortical arms, where the CCW arms have a shorter high-vorticity area. Vorticity is seen to drop off significantly after an X/D of 2.5.

Type I's CCW tilt and thickening of the vortical arm is due to the entrainment of cross-flow fluid diagonally into the wake as detailed in section 6.4.4.3. In this section two defined free-stream shear layers developed, as the roll-up of vortices were suppressed in the upper free-shear layer. This suppression of roll-up resulting in the formation of strong free-stream shear layers that controlled the fluid motion of the cross-flow fluid around the cylinder and wake structure. These shear layers behave as a physical barrier producing a virtual hydrodynamic profile as indicated in figure 7.7.

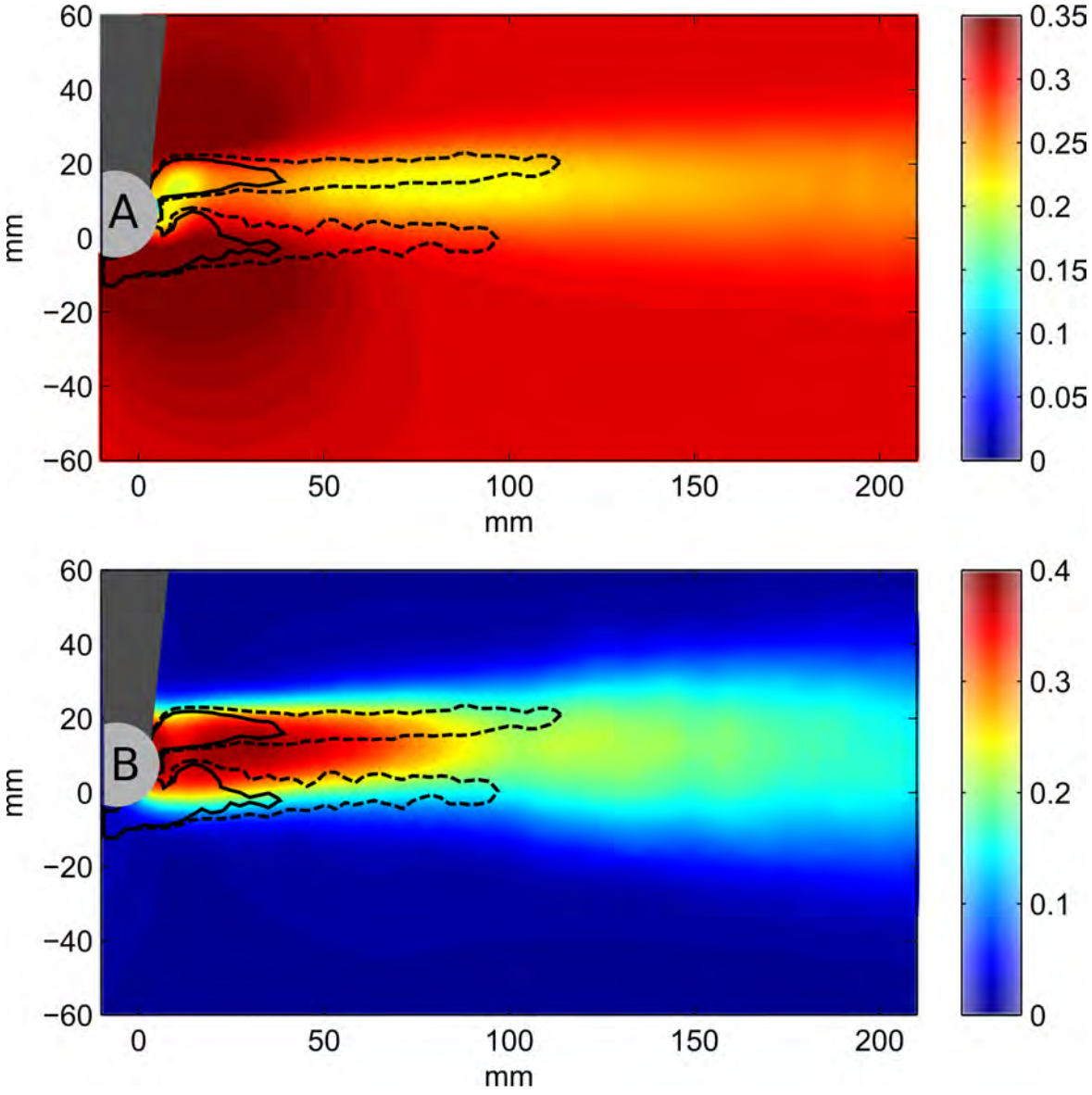

Figure 7.15: Overlaying of average vorticity on A) Average velocity, and B) average velocity profile for drag type I. where the solid black line represents strongest primary vorticity, and the dashed represents the lesser primary vorticity

Figure 7.15 A and B show the average velocity and average turbulence profiles for drag reduction *type I & II*, with the primary vorticity cores overlain on them. In figure 7.15 A the more intense CCW vorticity tilts the wake upwards towards the upper free-shear layer, suppressing the formation of CW shedding vortices, but adding a CW vorticity to the wake fluid, resulting in high levels of vorticity in the near wake. At an X/D of 1 where the thickness of the high-vorticity area ends, the wake experiences its highest velocity and highest level of turbulence for A and B respectively. This is due to the high energy cross-flow fluid

being entrained into the wake. It can also be seen that at around an X/D of 5, where the weaker primary vorticity ends for the CCW vortical arm, turbulence intensity tapers off as the differential between wake and cross-flow velocity is at its highest level. This level of cross over would suggest that the SJA interaction has created a virtual hydrodynamic surface, responsible for the drag reduction levels form section 5.5.3, through pressure recovery.

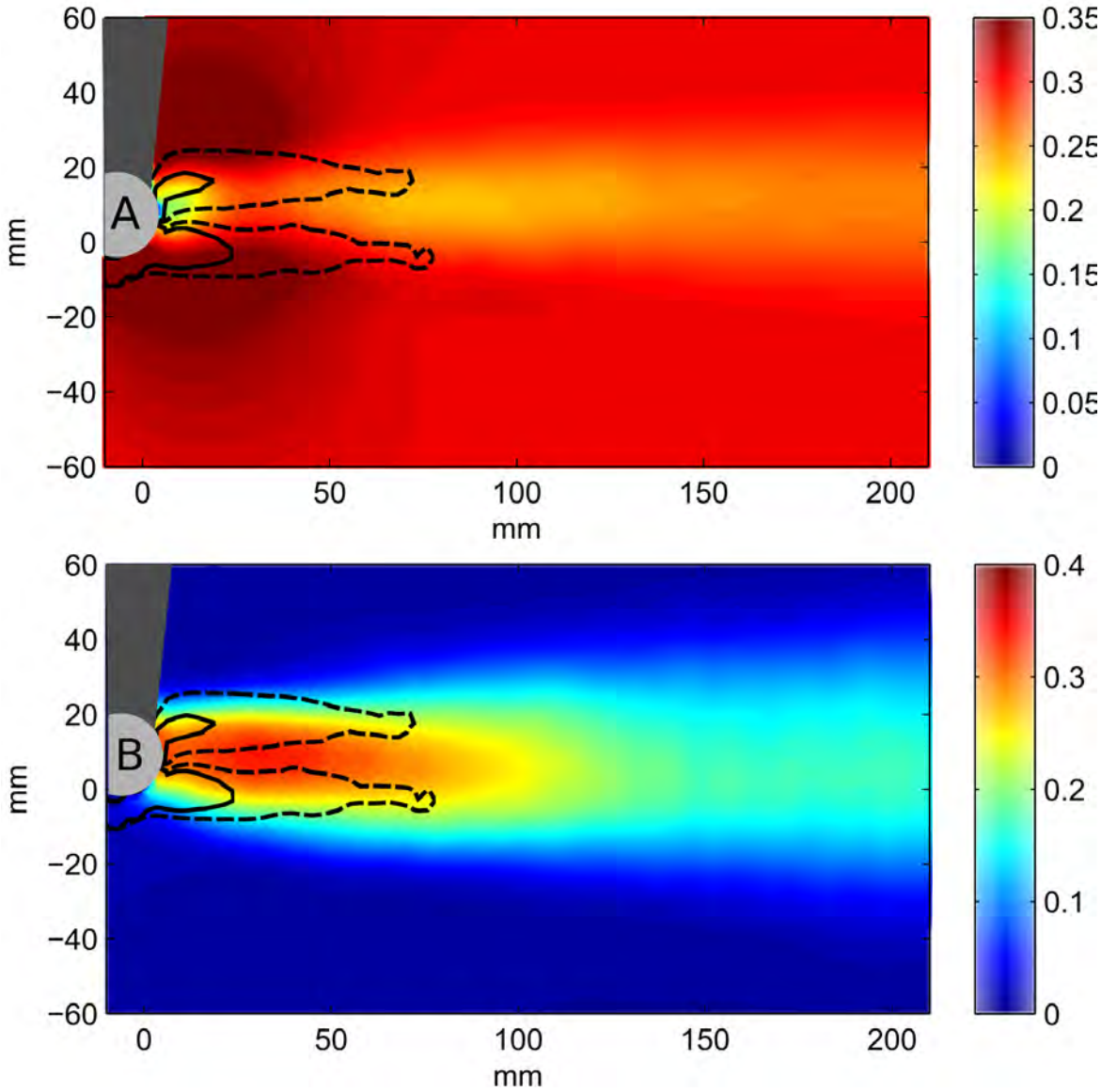

Figure 7.16: Overlaying of average vorticity on A) Average velocity, and B) average velocity profile for drag type II

Type II vorticities (Fig. 7.16) profile differs significantly from *type I* in shape but accomplishes a similar result by reducing drag via pressure drag reduction through pressure

recovery, but to a greater degree. The reason for the shorter vortical arms was seen in section 6.4.2.3 figure 6.7, where natural vortical shedding was suppressed, but a large short lived CCW vortex was formed along with a small CW vortex from the upper free-shear layer, that resulted in a central stream of backflow. This is responsible for the reduced spacing between the CW and CCW vortical arms compared to *type I*. Unlike *type I* the separation bubbles lowest velocity takes place between the area of highest vorticity, and it should be noted that *type II* has a lower velocity within the separation bubble. It can be seen that as the high-vorticity areas break down so to does the initial bubble of low-velocity. As the lesser areas of vorticity narrows turbulence levels are reduced. At this point velocity reduction begins, where the largest velocity differential in the far-wake after an X/D of 4 is present.
The significant differential between the vortical structures of *type II & I* is primarily due to type II producing a self-sustaining core within its separation bubble, that does not rely on the entraining fluid directly from the cross-flow. *Type II* (20% drag reduction) is shown to be capable of reducing drag by around double that of *type I* (10% drag reduction). This suggests that *type II* produces a more robust virtual hydrodynamic profile, that allows for a more efficient recovery of pressure, through the production of a smoother, more consistent turbulent free-shear layer. This allows the fluid traveling around the virtual profile to more effectively increase it velocity as it reaches the thickest section, followed by a smooth reduction in velocity towards the tail of the virtual profile as seen in figure 7.17.

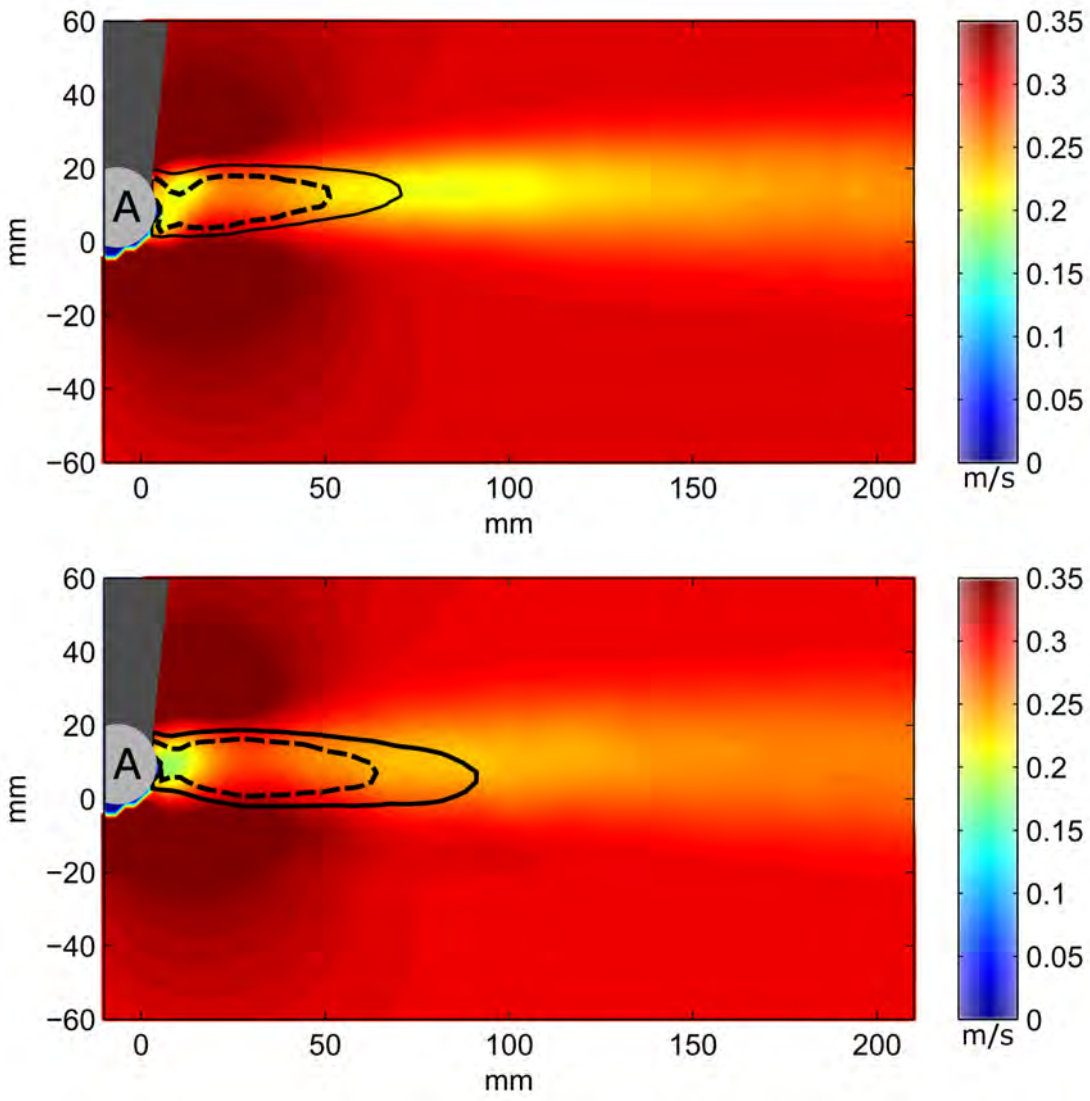

Figure 7.17: Velocity profile with turbulent structures overlain for: A) is type I drag reduction, and B is type II drag reduction). Where the dashed black lines indicate the high-turbulent core and the dashed black lines indicate the area of lower turbulence, depicting the boundaries of the wake structure

The fact that the low-velocity bubbles directly behind the cylinder for *type II* has a lower average velocity and larger size than that of *type I*, would suggest that *type II* has a larger differential between the stagnation points. It would be expected that *type I* would achieve a greater reduction in pressure drag. However, pressure is being recovered by another means. when the turbulent structures identified are taken to produce a virtual hydrodynamic profile, then the degree of pressure recovery shown in section 5 can be explained

When the virtual profiles identified through the analysis of turbulence intensity are overlain on their respective average velocity profiles in figure 7.17, the streams of fluid passing over the

cylinder are seen to accelerate towards the thickest part of the separation bubble and gradually reduces its velocity as it reaches the trailing edge. This gradual reduction in velocity would suggest that some form of streamlining is taking place allowing pressure to be recovered. To determine how *type II* is able to reduce drag to a greater degree the effect that the virtual hydrodynamic profile has on the fluid streams must be analysed.

In the velocity profile produced by *type I* (Fig 7.17 A), the upper CCW free-shear layer has a flat profile, which could be attributed to the reduction in pressure recovery. This can be seen in the flat inner profile of the upper high-velocity area for *type I*, whereas a gradually curved profile is seen for *type II* (Fig 7.17 B). When comparing the high-velocity areas beneath the cylinder, it can be seen that *type I* has a more abrupt curvature, which is a result of fluid being entrained from the cross-flow by the SJA vortex (Sec. 6.4.4.3). *Type II*'s high-velocity areas profile has a smoother, more gradual profile, allowing fluid to pass around the cylinder more favourably than *type I*.

In looking at the tails of the vortical structures, it is seen that as the primary core of turbulence breaks down for both cases, the start of the second bubble of low-velocity fluid is forms. For the lower-turbulence area, the lowest velocity point of the secondary bubble occurs at its tail. This suggest that these cores are producing a virtual structure, that allows for pressure recovery by allowing both streams to merge at its training edge.

Type II's ability to better recover pressure between the front stagnation point and the rear stagnation point of the virtual profile, would appear to be due to it having a more streamlined virtual profile. With this profile allowing for a smother more symmetric (pressure recovery taking place over both the CW and CCW free-shear layers) transition of fluid from a high velocity to low velocity as it approaches the trailing edge, without having to overcome any sudden angles as identified for *type II*. This is seen when the wake velocities at the end of each profile are compared. *Type II* produces a narrower, higher velocity wake, that's velocity has broken down significantly by an X/D of 8 (this can't be seen happening for *type I* within the viewing window). From these results it would seem that the high levels of drag reduction achieved by *type I & II* are due to their ability to produce an effective virtual hydrodynamic profile that is able to mimic that of a physical structure, with *type II* producing a more pronounced virtual profile that is more effective at reducing pressure drag.

7.6 Conclusion of particle image velocimetry results

In this section the average result for velocity, *turbulence intensity*, and *vorticity* were analysed to further determine how the synthetic jet actuator could create a virtual hydrodynamic profile to control drag modification. It was found that by looking at the two drag reduction types identified in chapter 6 , that the SJA was able to produce a virtual hydrodynamic profile capable of mimicking the behaviour a physical structure.

It was found that *type I* produced a highly turbulent virtual profile, that relied on the entrainment of high energy fluid for cross-flow, where as *type II* produced a self sustaining virtual profile. This resulted in *type I* having a profile that is less smooth and less streamlined than that of *type II*. This in turn meant that *type II* was able to recover pressure more effectively, resulting in it having a far-wake, with less velocity differential between the wake and cross-flow, less vorticity, and less turbulence. This accounts for the near doubling of drag reduction between *type I* (-10%) and *type II* (-20%) from that of the no-jet condition.

Chapter 8

Discussion: Interpretation of the Findings of the Drag Force and Wake Flow Studies

Previously the results of lift and drag (chapter 5), flow visualisation (chapter 6), and PIV (chapter 7) were discussed individually. This chapter's focus is on discussing them as a whole.

It was found in chapter 5, that a change in L_0/D_O has a significant effect on drag modification. This is particularly evident when considering the optimal angle for drag reduction. For an L_0/D_O of 0.5 it was found that optimum drag reduction took place between the range $140^\circ < \alpha_{SJA} < 180^\circ$, whereas optimum drag reduction for an L_0/D_O of 0.25 took place between the range $90^\circ < \alpha_{SJA} < 120^\circ$. The optimum jet angles for L_0/D_O of 0.25 is more akin to that of Amitay *et al.* [47] and Niam *et al.* [48]. However, Feng & Wang [49] found the optimum jet angle to be at an angle closer to 180^o , which was similar to the results for *type II* drag reduction (Chapeter 5), where the jet angle was at 140°, L_0/D_O was 0.5, and V_R was 0.69. The change of optimal jet-angle between dimensionless stroke lengths was due primarily to the changes in stroke length altering advection distance and strength of the forming vortices. Using an axisymmetric orifice Jabbal & Zhong [9] demonstrated that as the strength of vortices emanating from synthetic jet actuator (SJA) increases the ability of that vortex to penetrate deeper into the boundary layer, to a point at which it is capable of

breaking through. This was seen in figure 6.10 where the formation of a large CCW vortex is able to penetrate the boundary layer and produced a blockage that redirected the shear layer, which caused a significant blockage to the flow. The increasing of blockage with an increase in V_R was similar to the results found by Sahni *et al.* [13], where increase V_R resulted in an increase in blockage size over a flat plate. For these reasons, the stroke lengths have a different optimum jet angle.

When the drag reduction cases of *type I* and *type II* where examined, it was found that *Type II* produces a smooth virtual profile with a closed recirculation zone, whereas *type I* produced a highly turbulent core to the virtual structure. textitType II produced a recirculation zone with a long central reversed flow and a low turbulence intensity, suggesting a lower kinetic energy in the wake, which resembled the structures identified by Fujisawa & Takeda [15]. The high levels of turbulence in *type I* suggested a poor drag reduction, however due to the manner in which *type I* was formed (section 6.16), with the primary core of high-level turbulence dethatched from the cylinder. This turbulence resulted in a complete suppression of the naturally-shedding vortices. The suppression of these vortices resulted in the separation point of both the forced and unforced side of the cylinder being moved down-stream and held at a constant point. Similarly, for *type II* the virtual cylinder wake structure saw the fixing of the separation point at a down-stream location.

For both types of drag reduction average velocity profiles showed an element of lift was present, that was more pronounced for higher levels of drag reduction. This was in line with the findings of Ametay *et al.* [14], and Niam *et al.* [48], where lift was higher at larger drag reduction levels due to actuation causing a larger differential between the forced and unforced separation points.

When the two stroke lengths are looked at in relation to the drag results, patterns of flow control are found. When the jet angles of 90° at an L_0/D_O of 0.25 (*type I*) and the jet angles of 140° at an L_0/D_O of 0.5 (*type II*), two different drag profiles are produced. Using these profiles, simple methods for drag reduction are presented. At an Re of 6215, when the jet is at an angle of 140° between the jet frequencies of 6Hz to 11Hz using the equation 8.1

(based on the average slope), rough drag modification values can be obtained. For example, if the frequency changed from 6.4Hz to 10.5Hz then drag will be modified from a drag value of 17% to -16%. When the jet angle is changed to 100^o and L_0/D_O is reduced to 0.25 (Fig. 8.1 II), drag modification remains at around a value of then it is know that between the frequencies of 8Hz to 11Hz drag reduction can be maintained at a value of roughly -10%.

$$Drag modification(\%) = (-0.0787 \times f_{sja} + 0.6688) \times 100\% \tag{8.1}$$

Each of these setups allowed for different types of fluidic control to be achieved. L_0/D_O of 0.5 had a more pronounced effect on the shear layer due to its stronger vorticity, which resulted in drag modification for 140^o (Fig. 8.1) going form a high level of drag (20%) to a high level of drag reduction (-20%) with a near linear slope. This setup allows for a large range of fluidic control, however as this system was sensitive to small changes in V_R, maintaining the maximum level of drag reduction of -20% would be difficult as a change in V_R of 0.06 could result drag being modified by 8%. This would require an accurate measuring system, with a quick response to any changes. An L_0/D_O of 0.25 produced lesser drag-reduction compared to an L_0/D_O of 0.5, with two types of drag reduction profiles seen. The first being for the angle of 110°, which produced a maximum drag reduction of 15%, with a profile similar to that of 140°. The second being for the angles of 90° and 100° where a smaller maximum drag reduction of around 12% was achieved, but were capable of sustaining a more consistent level of drag reduction over a larger V_R range. This in turn resulted in a more stable drag reduction, that was not as sensitive to V_R, in particular with 100° remaining at around -10% from 7Hz to 11Hz. This would require less monitoring, potentially reducing the complexity of the systems. When comparing the drag profiles, the lower drag reduction produced a more stable profile. This stability could be more beneficial in terms of safety, as a system sensitive to changes in V_R could lead to a steep drop-off in drag reduction or flip to drag increase, which could result in a large change in drag forces, which could lead to structural failure or increased structural fatigue.

From these results it was found that a synthetic jet actuator could achieving fluidic control thought simple actuation, with a potential to do so with a low power input, as drag could be reduced significantly at low V_R, This is seen with a drag reduction of value of 12% at a

low V_R of 0.22 and maximum drag reduction values for the low and high stroke lengths of 15% at a low V_R of 0.31 and up 20% at a higher V_R of 0.69 respective. This study was also able to show in detail the structures responsible for drag modification over a broad range of conditions and a map of how altering actuator parameters can produce vastly different drag modification (Fig. 5.2 & Fig. 5.3). This study established good foundations from which to produce a more effective method of reducing drag thought simple actuation.

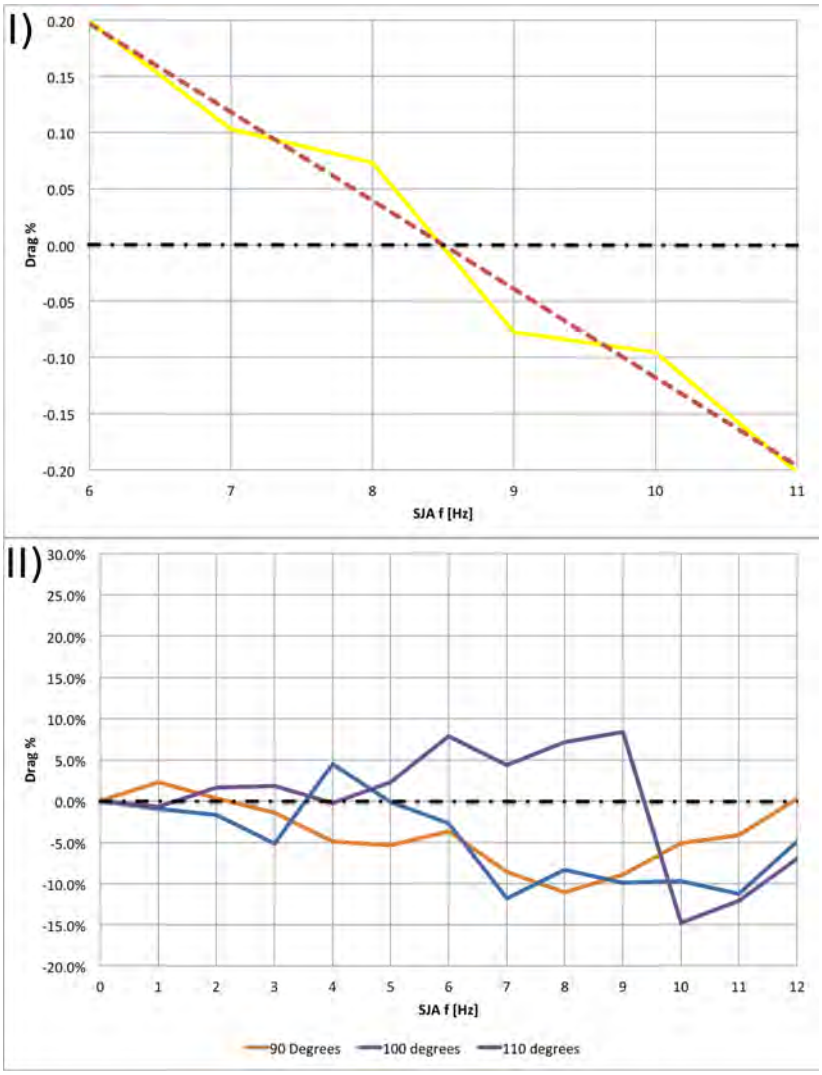

Figure 8.1: Drag values for I) Drag profile type II ($L_0/D_O = 0.5$ when $_{SJA} = 140^\circ$ for the range $6Hz < f_{SJA} < 11Hz$) , and II) Drag profile type I ($L_0/D_O = 0.25$ when $_{SJA} = 90^\circ$, 100°, and 110° for the range $1Hz < f_{SJA} < 12Hz$

Chapter 9

Conclusions

In this thesis the effects of an embedded synthetic jet on the drag forces experienced by a cylinder in a cross-flow were investigated experimentally. This was achieved using direct force measurements, flow visualisation, and particle image velocimetry.

The direct force measurements used strain readings to determine the effects the synthetic jet had on the drag and lift forces acting on the cylinder. This allowed for the identification of the potential for drag modifications achievable using a 20mm diameter cylinder, with a cross flow giving a Reynolds number of 5.62×10^3. It was found that drag could potentially be reduced (with respect to the case without jet actuation) by a maximum of 20% at a velocity ratio of 0.69, and by as much as 12% at a velocity ratio of as low as 0.22. It was also found that drag could be significantly increased to value of up to 30%, and that these large spikes in drag levels could take place over a change in jet frequency of as little as 1 to 2Hz.

Flow visualisation allowed for the identification of the mechanism involved in the drag modifications found in the force analysis. In this analysis two primary cylinder wake structures responsible for drag reduction were identified. These structures were seen to behave as virtual hydrodynamic profile, displacing local streamlines well outside the undisturbed shear layer. These structures were labelled as either *type I* or *type II* drag reduction profiles. *Type I* completely suppresses the formation of naturally shedding vortices, through the diagonal entraining of high-energy fluid from the cross flow, resulting in a highly asymmetric wake

structure. *Type II* was found to suppress the formation of naturally shedding vortices from the forced side, while controlling the formation of vortices from the unforced side of the cylinder, resulting in a reversed flow in the central wake, that was ultimately rolled up by the vortices formed at bother the top and bottom of the cylinder. This lead to the formation of a stable self-sustaining recirculation zone.

Particle image velocimetry allowed the wake to be examined quantitatively in terms of time-averaged flow velocity, turbulence intensity, and vorticity. Turbulence intensity was used to characterise the cylinder wake structures identified by flow visualisation, where it was found that *type I* produced a highly turbulent wake structure and *type II* produced a less turbulent elongated recirculation zone. Vorticity fields were used to investigate the strength and lengths of the vortical arms of the wake, showing that *type I* had longer vortical arms compared to that of *type II*. This increase in vorticity was due to the formation of a stronger shear layer on both the forced and unforced sides of the cylinder, as a result the suppression of fully forming vortices from the unforced side and the entrainment of fluid form the forced side of the wake. A potential element of lift was also identified in the asymmetry of the vortical arms. The velocity profiles characterised the effects that these virtual profiles have on the flow around the cylinder, showing how *type I & II* recover pressure similarly to that of an aerofoil. This was particularly evident when the virtual profiles identified through turbulence intensity were overland on the velocity profiles, where the velocity profiles show the flow passing over the virtual profile in a similar similar manner to that of a physical profile.

9.1 Achievements to date

9.1.1 List of modules and ECTS attained

- Core Module One of the Innovation Academy: Creative thinking and innovation (10 ECTS)
- Core Module two of the Innovation Academy: Opportunity generation and recognition (5 ECTS)

- Fluid Induced Vibrations (5 ECTS)
- Energy Technical Seminars (5 ECTS)
- Reflective teaching assistantship (5 ECTS)

9.1.2 Publishing

9.1.2.1 To date

- D. Jackson and T. Persoons, Feasibility study and cost benefit analysis of tidal energy: a case study for Ireland, Fourth International Conference on Ocean Energy October, 2012.

9.1.3 Future

- D. Jackson and T. Persoons, Optimal Positioning of a Synthetic Jet Actuator to Control Separation from a Cylinder in Cross-Flow, (in preparation)

9.1.4 Research projects undertaken to date

- Hydrofoil Anchoring of tidal Turbines; Project Leaders: Dr. Tim Persoons and Diarmuid Jackson in collaboration with Prof. William Kinston; MAI student: Tom Burke, September 2013 - April 2014
- Wake Control Using Synthetic Jets Emanating form the Surface of a Circular Cylinder in a Cross-Flow; Project Co-Ordinator: Dr. T. Persoons; MAI student Antoine Queffelec, September 2014 - April 2015
- Impact of Synthetic Jet Actuating on Flow Control Bluff Bodies; Project Co-Ordinator: Dr. T. Persoons; MAI student Cormac Bourke, September 2015 - April 2016

As part of the Hydrofoil Anchoring of Tidal Turbines in November 2013 I attended MARINEt 1st user-Workshop at the CNR-INSEAN in Rome as a representative for the project collaboration. The purpose of the visit was to meet up with experts in the field of ocean energy devices to ascertain the level of research and the viability of the tidal anchoring

system, and to meet with the managers of the test facilities in Den Oever, to establish what would be required to make the best use of the facilities provided.

My role in the 'Wake Control Using Synthetic Jets Emanating form the Surface of a Circular Cylinder in a Cross-Flow' project was to give advice on the use of synthetic jets in a cross flow and to advise on the best test types required to achieve the most useful data.

My role within the masters project 'Impact of Synthetic Jet Actuating on Flow Control Bluff Bodies' was to provide advice and guidance on the use of synthetic jets as a fluidic control. The project was set up based on the parameters laud out in this thesis.

9.2 Future work

Even though this thesis has been able produce a state-of-the-art water tunnel and contribute to the understanding of the interactions of a spanwise rectangular synthetic jet embedded in a cylinder with a boundary layer and wake, there is still a great deal to be learnt. As such some suggestions for future works will be presented in this section.

In this thesis a wide range of jet operating conditions were looked at, with the goal of characterising the drag and lift behaviour over that range. As such optimisation of drag reduction was not looked at in detail. Therefore a good start point would be to look more closely at the maximum drag reduction cases to establish if they can be improved upon. This would require looking at three major aspects I) the jet actuation frequency, II) the jet orifice angle, and III) the dimensionless stroke length.

As the tests in this thesis only looked at the drag reduction values at a single cylinder Reynolds number, a study on the effects of modifying the cylinder Reynolds number while maintain the same velocity ratios, jet angles and dimensionless stoke lengths, would produce some interesting values.

The particle image velocimetry results in this thesis where taken along the central plane

of the spanwise length of the cylinder, giving a 2*D* view of the SJA interaction. A project should be undertaken to dissect the spanwise length of the cylinder into several streamwise planes to determine the three-dimensional interaction of the jet with the cross-flow such as done by Sahni *et al.* [13].

9.2.1 Experimental optimization

After concluding of tests it was found that both the water tunnel and test equipment could be optimised for future testing. As the water tunnel was designed to be modular, each section can be removed and modified without the need to disassemble the entire tunnel. As such a good start point in optimising the water tunnel would be to further improve the flow conditions of the water tunnel. This could be achieved by improving the mitre bends, as the turning vanes used were made by hand on a budget. Another step would be to add stator vanes before and after the propeller.

In terms of imaging, optimisations can be made by reducing the reflections from the cylinder surface. this could be achieved by coating the cylinder in luminous paint (e.g. containing Rhodamine B dye)) and a filter will be placed on the camera, filtering out the reflections. This could further reduce the distance from the surface that particles can be accurately traced, improving the quality of particle image velocimetry results.

In the future, the test section can easily be modified to allow for different types of testing to be performed, such as analysing the wake effects further downstream or for the testing of different bodies, such an aerofoil or a bluff body.

Bibliography

[1] T. Brome. Wyoming turbine collapse, Nov 25 2010.

[2] C. A. Yunus and J. Cimbala. Fluid mechanics: fundamentals and applications. *International Edition, McGraw Hill Publication*, pages 185–201, 2006.

[3] J. M. Shuster and D. R. Smith. Experimental study of the formation and scaling of a round synthetic jet. *Physics of Fluids (1994)*, 19(4):045109, 2007.

[4] J. Zhou, H. Tang, and S. Zhong. Vortex roll-up criterion for synthetic jets. *AIAA Journal*, 47(5):1252–1262, 2009.

[5] A. Crook, W. J. Crowther, and N. J. Wood. A parametric study of a synthetic jet in a cross flow. In *Proceedings of the 22nd International Congress of Aeronautical Sciences*, 2000.

[6] M. Jabbal and S. Zhong. The near wall effect of synthetic jets in a boundary layer. *International Journal of Heat and Fluid Flow*, 29(1):119 – 130, 2008.

[7] A. Michael and G. Ari. Controlled transients of flow reattachment over stalled airfoils. *International Journal of Heat and Fluid Flow*, 23(5):690 – 699, 2002.

[8] S. Zhang and S. Zhong. Experimental investigation of flow separation control using an array of synthetic jets. *AIAA Journal*, 48(3):611–623, 2010.

[9] M. Jabbal and S. Zhong. Particle image velocimetry measurements of the interaction of synthetic jets with a zero-pressure gradient laminar boundary layer. *Physics of Fluids (1994)*, 22(6):063603, 2010.

[10] A. Bridges and D. R. Smith. Influence of orifice orientation on a synthetic jet-boundary-layer interaction. *AIAA Journal*, 41(12):2394–2402, 2003.

[11] D. R. Smith. Interaction of a synthetic jet with a crossflow boundary layer. *AIAA Journal*, 40(11):2277–2288, 2002.

[12] Y. Elimelech, J. Vasile, and M. Amitay. Secondary flow structures due to interaction between a finite-span synthetic jet and a 3-d cross flow. *Physics of Fluids (1994)*, 23(9):094104, 2011.

[13] O. Sahni, J. Wood, K. E. Jansen, and M. Amitay. Three-dimensional interactions between a finite-span synthetic jet and a crossflow. *Journal of Fluid Mechanics*, 671:254–287, 2011.

[14] M. Amitay, A. Honohan, M. Trautman, and A. Glezer. Modification of the aerodynamic characteristics of bluff bodies using fluidic actuators. *AIAA paper*, 2004, 1997.

[15] N. Fujisawa and G. Takeda. Flow control around a circular cylinder by internal acoustic excitation. *Journal of Fluids and Structures*, 17(7):903–913, 2003.

[16] R. Gordon and M. S. Imbabi. Cfd simulation and experimental validation of a new closed circuit wind/water tunnel design. *Journal of Fluids Engineering*, 120(2):311–318, 1998.

[17] D. S. Miller. *Internal Flow System*. BHRA, Bedford, United Kingdom, 1990.

[18] M. Raffel, C. E. Willert, and J. Kompenhans. Particle image velocimetry: a practical guide. *Springer-Verlag Berlin Heidelberg*, 1998.

[19] M. M. Zdravkovich. Flow around circular cylinders, vol. 1. fundamentals. *Journal of Fluid Mechanics*, 350:377–378, 1997.

[20] D. Jackson and T. Persoons. Feasibility study and cost-benefit analysis of tidal energy: a case study for ireland. In *the 4th International Conf. on Ocean Energy*, 2012.

[21] J. D. Vasile and M. Amitay. Interactions of an array of finite span synthetic jets and a crossflow. *AIAA Journal*, 51(10):2503–2512, 2013.

[22] M. Zhang, W. Yu, and J. Xu. Aerodynamic physics of smart load control for wind turbine due to extreme wind shear. *Renewable Energy*, 70:204–210, 2014.

[23] C Lee, G. Hong, Q. P. Ha, and S. G. Mallinson. A piezoelectrically actuated micro synthetic jet for active flow control. *Sensors and Actuators A: Physical*, 108(1-3):168 – 174, 2003. Selected Papers from the Pacific Rim Workshop on Transducers and Micro/Nano Technologies.

[24] A. Glezer. Some aspects of aerodynamic flow control using synthetic-jet actuation. *Philosophical Transactions of the Royal Society A: Mathematical, Physical and Engineering Sciences*, 369(1940):1476–1494, 2011.

[25] M. Jahanmiri. Active flow control: A review. Technical report, Chalmers University of Technology, Gothenburg, Sweden, 2010.

[26] J. Tensi, I. Boue, F. Paille, and G. Dury. Modification of the wake behind a circular cylinder by using synthetic jets. *Journal of Visualization*, 5(1):37–44, 2002.

[27] N. J. Farnsworth, J. C Vaccaro, and M. Amitay. Active flow control at low angles of attack: stingray unmanned aerial vehicle. *AIAA Journal*, 46(10):2530–2544, 2008.

[28] K. Calsoyds and D. G. Calley. Truck after-body drag reduction device, jul 22 2003. US Patent 6,595,578.

[29] B. R. Munson, D. F. Young, and T. H. Okiishi. *Fundamentals of fluid mechanics*. New York, 1990.

[30] A. Abbas, J. De Vicente, and E. Valero. Aerodynamic technologies to improve aircraft performance. *Aerospace Science and Technology*, 28(1):100–132, 2013.

[31] F. M. White and I. Corfield. *Viscous fluid flow*, volume 3. McGraw-Hill New York, 2006.

[32] B. L. Smith and A. Glezer. The formation and evolution of synthetic jets. *Physics of Fluids (1994)*, 10(9):2281–2297, 1998.

[33] A. Glezer and M. Amitay. Synthetic jets. *Annual Review of Fluid Mechanics*, 34(1):503–529, 2002.

[34] R. Holman, Y. Utturkar, R. Mittal, B. L. Smith, and L. Cattafesta. Formation criterion for synthetic jets. *AIAA Journal*, 43(10):2110–2116, 2005.

[35] N. Didden. On the formation of vortex rings: rolling-up and production of circulation. *Zeitschrift fur angewandte Mathematik und Physik ZAMP*, 30(1):101–116, 1979.

[36] R. Mittal, P. Rampunggoon, and H. S. Udaykumar. Interaction of a synthetic jet with a flat plate boundary layer. *AIAA Paper*, 2773(200):1, 2001.

[37] B. L. Smith and G. W. Swift. Synthetic jets at large reynolds number and comparison to continuous jets. *AIAA Paper*, 3030:2001, 2001.

[38] C. Y. Lee and D. B. Goldstein. Two-dimensional synthetic jet simulation. *AIAA Journal*, 40(3):510–516, 2002.

[39] D. J. Nani and L. B. Smith. Effect of orifice inner lip shape on synthetic jet efficiency. In *Mechanical and Aerospace Engineering, Utah State University, Logan, Utah 84322, USA*, 2012.

[40] P. Valiorgue, T. Persoons, A. McGuinn, and D. B. Murray. Heat transfer mechanisms in an impinging synthetic jet for a small jet-to-surface spacing. *Experimental Thermal and Fluid Science*, 33(4):597–603, 2009.

[41] T. Persoons and T. S. O'Donovan. A pressure-based estimate of synthetic jet velocity. *Physics of Fluids (1994)*, 19(12):128104, 2007.

[42] M. Amitay and A. Glezer. Role of actuation frequency in controlled flow reattachment over a stalled aerofoil. *AIAA Journal*, 40(2):209 – 216, 2002.

[43] S. Zhong, F. Millet, and N. J. Wood. The behaviour of circular synthetic jets in a laminar boundary layer. *The Aeronautical Journal*, 109(1100):461–470, 2005.

[44] S. Zhong, F. Millet, and N. J. Wood. The behaviour of circular synthetic jets in a laminar boundary layer. *The Aeronautical Journal*, 109(1100):101–111, 2014.

[45] M. Jabbal and S. Zhong. The near wall effect of synthetic jets in a boundary layer. *International Journal of Heat and Fluid Flow*, 29(1):119–130, 2008.

[46] A. Glezer, M. Amitay, and A. M. Honohan. Aspects of low-and high-frequency actuation for aerodynamic flow control. *AIAA Journal*, 43(7):1501–1511, 2005.

[47] M. Amitay, Barton L. Smith, and A. Glezer. Aerodynamic flow control using synthetic jet technology. *AIAA paper*, 208:1998, 1998.

[48] A. Naim, D. Greenblatt, A. Seifert, and I. Wygnanski. Active control of a circular cylinder flow at transitional reynolds numbers. *Flow, turbulence and combustion*, 78(3-4):383–407, 2007.

[49] L. Feng and J. Wang. Synthetic jet control of separation in the flow over a circular cylinder. *Experiments in fluids*, 53(2):467–480, 2012.

[50] J. Hwang and K. Yang. Drag reduction on a circular cylinder using dual detached splitter plates. *Journal of Wind Engineering and Industrial Aerodynamics*, 95(7):551–564, 2007.

[51] Je. Bera, M. Michard, M. Sunyach, and G. Comte-Bellot. Changing lift and drag by jet oscillation: experiments on a circular cylinder with turbulent separation. *European Journal of Mechanics-B/Fluids*, 19(5):575–595, 2000.

[52] G. Mehta, Rabindra, and P. D. Bradshaw. Design rules for small low-speed wind tunnels. *The Aeronautical Journal*, 83(827):443–449, 1979.

[53] J. L. Lumley and J. F. McMahon. Reducing water tunnel turbulence by means of a honeycomb. *Journal of Fluids Engineering*, 89(4):764–770, 1967.

[54] J. B. Barlow, W. H. Rae, and A. Pope. *Low-speed wind tunnel testing*. John Wiley Sons, 1999.

[55] V. Kulkarni, N. Sahoo, and S. D. Chavan. Simulation of honeycomb–screen combinations for turbulence management in a subsonic wind tunnel. *Journal of wind engineering and industrial aerodynamics*, 99(1):37–45, 2011.

[56] K. Ghorbanian, M. R. Soltani, and M. D. Manshadi. Experimental investigation on turbulence intensity reduction in subsonic wind tunnels. *Aerospace science and Technology*, 15(2):137–147, 2011.

[57] J. Scheiman. Considerations for the installation of honeycomb and screens to reduce wind-tunnel turbulence, technical report, nasa langley research center; hampton, va, united states. 1981.

[58] G. N. Patterson. Note on the design of corners in duct systems. Technical report, DTIC Document, 1936.

[59] R. I. Loehrke and H. M. Nagib. Experiments on management of free-stream turbulence. Technical report, DTIC Document, 1972.

[60] Aeronautical Research Council (Great Britain). *Comparative Tests of Thick and Thin Turning Vanes in the Royal Aircraft Establishment 4 X 3-ft Wind Tunnel*. HM Stationery Office, 1952.

[61] G. Johl, M. A. Passmore, and P. M. Render. Design and performance of thin, circular arc, wind-tunnel turning vanes. 2007.

[62] J. Westerweel. Fundamentals of digital particle image velocimetry. *Measurement science and technology*, 8(12):1379, 1997.

[63] R. O'R. Meehan, B. Donnelly, K. Nolan, T. Persoons, and D. B. Murray. Flow structures and dynamics in the wakes of sliding bubbles. *International Journal of Multiphase Flow*, 84:145–154, 2016.

[64] Davis product-manual. 2008.

[65] T. Persoons and T. S. O'donovan. High dynamic velocity range particle image velocimetry using multiple pulse separation imaging. *Sensors*, 11(1):1–18, 2010.

[66] F. Scarano. Iterative image deformation methods in piv. *Measurement science and technology*, 13(1):R1, 2001.

[67] C. Tropea, A. L. Yarin, and J. F. Foss. *Springer handbook of experimental fluid mechanics*, volume 1. Springer Science and Business Media, 2007.

[68] A. Melling. Tracer particles and seeding for particle image velocimetry. *Measurement Science and Technology*, 8(12):1406, 1997.

[69] J. H. Kim, T. W. Simon, and R. Viskanta. Journal of heat transfer policy on reporting uncertainties in experimental measurements and results. *Journal of Heat Transfer*, 115(1):5–6, 1993.

[70] T. Persoons, D. Murray, and R. Farrelly. High dynamic range whole-field turbulence measurements in impinging synthetic jets for heat transfer applications. 2010.

[71] K. Kahler C. J. Westerweel J. Stanislas, M. Okamoto. Main results of the second international piv challenge. *Experiments in Fluids*, 39(2):170–191, 2005.

[72] B. H. Timmins, B. W. Wilson, B. L. Smith, and P. P. Vlachos. A method for automatic estimation of instantaneous local uncertainty in particle image velocimetry measurements. *Experiments in Fluids*, 53(4):1133–1147, 2012.

[73] B. M. Wilson and B. L. Smith. Uncertainty on piv mean and fluctuating velocity due to bias and random errors. *Measurement Science and Technology*, 24(3):035302, 2013.

[74] Z. Xue, J. J. Charonko, and P. P. Vlachos. Particle image velocimetry correlation signal-to-noise ratio metrics and measurement uncertainty quantification. *Measurement Science and Technology*, 25(11):115301, 2014.

[75] J. J. Charonko and P. P. Vlachos. Estimation of uncertainty bounds for individual particle image velocimetry measurements from cross-correlation peak ratio. *Measurement Science and Technology*, 24(6):065301, 2013.

[76] A. Sciacchitano, B. Wieneke, and F. Scarano. Piv uncertainty quantification by image matching. *Measurement Science and Technology*, 24(4):045302, 2013.

[77] A Sciacchitano, F. Scarano, and B. Wieneke. Multi-frame pyramid correlation for time-resolved piv. *Experiments in fluids*, 53(4):1087–1105, 2012.

[78] T. Persoons. Time-resolved high-dynamic-range particle image velocimetry using local uncertainty estimation. *AIAA Journal*, pages 1–10, 2014.

[79] T. Morel. Comprehensive design of axisymmetric wind tunnel contractions. *Journal of Fluids Engineering*, 97(2):225–233, 1975.